This is to certify that the

dissertation entitled

A STUDY
OF THE MECHANISM OF ^{16}O-INDUCED
REACTIONS BETWEEN 140 AND 315 MeV
INCIDENT ENERGIES

presented by

Terry Clayton Awes

has been accepted towards fulfillment
of the requirements for

_____PhD_____ degree in __Physics__

Harald Gelbin
Major professor

Date _Nov. 20, 1981_

O-12771

A STUDY OF THE MECHANISM OF ^{16}O-INDUCED
REACTIONS BETWEEN 140 AND 315 MeV INCIDENT ENERGIES

By

Terry Clayton Awes

A DISSERTATION

Submitted to
Michigan State University
in partial fulfillment of the requirements
for the degree of

DOCTOR OF PHILOSOPHY

Department of Physics

1981

ABSTRACT

A STUDY OF THE MECHANISM OF ^{16}O-INDUCED
REACTIONS BETWEEN 140 AND 315 MeV INCIDENT ENERGIES

By

Terry Clayton Awes

Reactions induced by ^{16}O ions on ^{238}U at incident
energies of $E/A = 20$ MeV have been studied. In coincidence
with fission fragments, projectile residues (Li,...,O) have
been measured near the grazing angle and double differential
cross sections have been measured for energetic p,d,t, and
α-particles. The folding-angle between the two coincident
fission fragments is shown to provide information on the
linear momentum transfer to the target nucleus.

The emission of energetic light particles into the
forward direction is shown to be an important aspect of the
mechanism of projectile residue emission. However, light
particles emitted in coincidence with projectile residues
are not the result of a simple quasi-elastic breakup of the
projectile. This is shown by a kinematical analysis which
demonstrates that a large amount of linear momentum is
transferred to the target residue prior to fission. Using
the folding-angle information in coincidence with the
observation of energetic light particles, it is concluded

that the majority of these particles result from fusion-like
"central" collisions with no projectile residue in the exit
channel. It is suggested that these particles most likely
are emitted during the early stages of the reaction.

Double differential cross sections have also been
measured for energetic p,d,t, and α-particles emitted in
^{16}O-induced reactions on targets of Al, Zr, and Au at
incident energies of 140, 215, and 310 MeV. The energy and
angular distributions are well described by isotropic
emission from a moving thermal source. The extracted
temperature and velocity parameters are found to vary
systematically with the incident energy per nucleon above the
Coulomb barrier. The observed trend cannot be explained by
compound nucleus emission but instead suggest emission from
a source which consists of comparable contributions from
target and projectile. Alternatively, the proton energy
spectra are compared with a rotating hot spot model, a
precompound model, and with a simple knock-out model. The
d,t, and α-particle cross sections are also described using
the proton cross sections in terms of a generalized
coalescence relation which takes into account Coulomb
repulsion from the target nucleus.

Dedicated to Theresa and Jennifer

ACKNOWLEDGEMENTS

of the results presented here.

I also thank Dr. Marshall Blann for making his precompound code available and for many helpful suggestions concerning the precompound calculations.

I would like to thank Drs. Henry Blosser and Walter Benenson for the extensive travel support which I have received throughout my graduate career.

I am most grateful to Dr. David Scott for his interest in this project and for arranging my financial support during my stay at Lawrence Berkeley Laboratory. The financial support of LBL during this period is gratefully acknowledged.

Financial support in the form of an MSU Graduate Tuition Scholarship and various research assistanceships funded by the Department of Energy and the National Science Foundation is greatly appreciated.

I wish to thank my office-mate, Arno Ledebuhr, for his friendship and unending interest in all aspects of the subject of physics. I also wish to express my thanks to the rest of the Nuclear Beer Group for those memorable Friday evenings and all of the good times of the last four years.

I especially thank my parents for their encouragement, support, and love.

Most of all, I thank my wife, Theresa, for typing this thesis (equations and all!), for her understanding and sacrifices, and especially for her love.

TABLE OF CONTENTS

iv

LIST OF TABLES

LIST OF FIGURES

xi

CHAPTER I

INTRODUCTION

A. Motivation

Heavy ion reactions have been studied intensively in
recent years at bombarding energies below 10 MeV/nucleon
and at relativistic energies above 200 MeV/nucleon. At low
energies of a few MeV/nucleon above the Coulomb barrier
processes known as deeply inelastic collisions have been
shown to make a major contribution to the reaction cross
section [Ar 73, Sc 77, Vo 78, Go 80]. These reactions are
collisions of a two-body nature with a large overlap of
target and projectile and cover the range between compound
nucleus formation and direct reactions. They are typically
characterized by a partial memory loss of the incident
channel due to extensive kinetic energy dissipation and
substantial diffusion of nucleons between the interacting
nuclei. As a result of the dissipative nature of these
reactions, the outgoing nuclei exhibit a high degree of
equilibration. At relativistic energies, on the other hand,
the interaction time is short preventing any substantial

1

communication between target and projectile. In particular, peripheral collisions are largely associated with fragmentation process in which the surviving target and projectile fragments act as mere spectators in the reaction while the overlapping participant nuclear matter becomes a highly excited subsystem moving independent of the target and projectile [Gr 75, Gu 76].

In the intermediate energy region between 10 and 200 MeV/nucleon a transition is expected to occur from the mean field description of low energy interactions to the nucleon-nucleon scattering behavior characteristic of high energy collisions [Sc 81a]. This transition is expected to result when the velocity of the colliding nucleons surpasses both the Fermi velocity and the velocity of nuclear sound. Indications of the onset of such a transitional behavior have been reported for reactions of ^{16}O on ^{208}Pb already at incident energies of $E/A = 20$ MeV [Ge 78]. Here, the element production cross sections for projectile fragments were observed to resemble more closely the production cross sections at $E/A = 2.1$ GeV incident energy than at $E/A = 10$ MeV incident energy. In addition, the main features of the projectile residue energy spectra could be explained in terms of intrinsic motion of the excited projectile in a manner similar to the projectile fragmentation interpretation formulated for relativistic energies [Ge 77]. These observations suggest that the transition to high energy behavior might begin already at

incident energies of only a few tens of MeV per nucleon.
The current generation of nuclear accelerators now nearing
completion, including the super-conducting cyclotron
facility here at Michigan State University, will be well
suited to study this region of transition between 10 and
200 MeV/nucleon.

A useful method for studying the development of the
heavy ion reaction mechanism from energies just above the
Coulomb barrier up to relativistic energies is through the
observation of energetic light particles (n,p,d,t, and α).
At relativistic energies several systematic studies of
inclusive light particle emission [Go 77, Sa 80, Na 81]
have resulted in a great deal of theoretical interest. The
models which have been proposed to explain the light
particle spectra range from single scattering knock-out
models [Ko 77, Ha 79] to the fireball [We 76] or firestreak
[My 78] models in which thermal emission is assumed to
occur from the highly excited and independently moving
participant matter. The inclusive data are found to carry
sufficient information to rule out either single scattering
or thermal emission as the sole source of light particles
[Na 81]. Instead the data suggest a model in which both
direct and thermal components are included either explicitly
[Ch 80] or by including contributions from single and
multiple collisions as in linear cascade models [Hü 77,
Ra 78, Cu 81] or in fully three-dimensional cascade models
[Ya 79a, Cu 80, Ya 81].

At low energies (E/A $\gtrsim$ 5 MeV above the Coulomb barrier) detailed studies of neutron emission in heavy systems have shown that the neutrons are explained by statistical evaporation from the compound nucleus or from fully accelerated reaction partners of deeply inelastic collisions [Ey 78, Hi 79, Ta 79, Go 80a]. At somewhat higher energies there exists evidence for nonequilibrium neutron emission [Hi 78, We 78, Ge 80, Ga 81, Ts 81, Be 81, Yo 81]. Non-equilibrium charged particle emission has also been observed in inclusive measurements [Br 61, Ba 78, Sy 80] as well as in various coincidence experiments. Many of these coincidence studies have involved the observation of light particles in coincidence with projectile fragments [Ha 77, Ho 77, Ge 77a, Ga 78, Bh 79, Ho 80]. Unfortunately, the interpretation of these experiments is dependent upon assumptions about the origin of the light particles. For example, if they are assumed to result from the sequential decay of excited projectile fragments, then one must also make assumptions about the primary distribution of the projectile fragments [Bi 80]. As a result, systems similar to those which have been associated with nonequilibrium effects have also been shown to be consistent with equilibrium emission from excited reaction partners [Bi 80, Yo 80, Sc 81]. In less kinematically restrictive experiments in which coincident fusion products were identified using γ-ray techniques [In 77, Zo 78, Ya 79, Si 79a, Ba 80a] it has been demonstrated that energetic light particles

are emitted in processes that cannot be associated with equilibrium emission from either the compound nucleus or from fully accelerated reaction partners. Instead, it has been shown that reactions in which a major portion of the projectile mass is transferred to the target nucleus make an important contribution to the light particle emission. These reactions have been termed "massive transfer" [Zo 78, Ya 79] or "incomplete fusion" [Si 79a] reactions.

The models which have been developed to explain the light particle spectra observed in low-energy heavy ion induced reactions are closely analogous to the models used at relativistic energies. Following the original suggestion of Bethe [Be 38], there exist several models which assume thermal emission from a locally heated region or "hot spot" on the nuclear surface [Ho 77, We 77, Go 77a, No 78, Go 79, Ut 80, Ga 80, Ga 80a, Mo 80, Mo 81]. Such a "hot spot" corresponds directly to the highly excited participant matter in a relativistic collision but at low-energies does not have sufficient translational energy to become dissociated from the target and projectile nuclei. This heated region of the nuclear surface would attain much higher temperatures than the compound nucleus and, immediately after its formation, would decay by thermal diffusion into the adjacent nuclear matter or by the emission of energetic light particles. Rather good agreement with experimental data has been obtained using such an

interpretation in several instances [No 78, Ut 80, Ga 80].
Alternatively, it has been proposed that promptly emitted
particles or "PEPs" resulting from a nucleon-nucleon single
scattering process might explain the energetic light
particles as the result of a velocity addition effect in
which the Fermi velocity couples with the relative velocity
to yield the observed high energies [Bo 79, Bo 80]. In
between these two extreme points of view are models which
consider the time development of the approach to equilibrium
such as the cascade [Be 76] and precompound [Bl 75, Bl 81]
models. Most of these theories are formulated to predict
single particle inclusive cross sections. On the other
hand, as noted above, most of the experimental effort in
low-energy light particle emission has been devoted to
coincidence studies which are generally very phase space
selective. The resulting coincidence cross sections are
very difficult to relate to the inclusive cross sections.
As a result, it has not been possible to provide a
sufficiently stringent test to differentiate between the
various models.

B. Scope

The emphasis of the present study has been in two
directions. In the first place, it has sought to determine
the degree to which the reaction mechanism operating in
heavy ion reactions at 20 MeV/nucleon is comparable to the

mechanism of relativistic energies. Previous results at
this incident energy [Ge 78] have suggested that the energy
and element distributions of projectile-like fragments have
features which are characteristic of relativistic collisions.
In order to investigate this similarity further we have
obtained information on the momentum transferred to the
target residue and its excitation energy. With this infor-
mation it is possible to determine whether the role of the
target residue is that of a mere spectator, as believed for
relativistic energies, or whether it is actively involved in
the reaction. The other direction of emphasis in the
present research has been toward understanding the
characteristics of light particle emission in heavy ion
reactions in the range of incident energies between 10 and
20 MeV/nucleon. The present results should help to
discriminate between the various models proposed to explain
light particle production in this range of incident energies.

The research described here is the result of four
experiments, each of which has been published previously
[Dy 79, Aw 79, Ba 80, Aw 80, Aw 81, Ka 81, Aw 81a, Aw 82].
In the first three experiments reactions resulting from the
bombardment of a ^{238}U target with ^{16}O ions of E/A = 20 MeV
incident energy have been studied. In these studies one or
both fission fragments were observed in coincidence with
other reaction products. For this reason, we have chosen
an actinide target because of its low fission threshold.

As a consequence, fission is the dominant decay mode of the target residue and only the most quasi-elastic collisions will be excluded by the fission coincidence requirement. Furthermore, because the fission fragment distribution is dominated by the inherent kinetic energy release of the fission process and not the kinematics of the reaction, only a small kinematic bias is imposed on the reaction by the coincidence requirement. This allows the study of rather global features of the reaction. In particular, the folding-angle between the two outgoing fission fragments is closely related to the amount of linear momentum transferred to the fissioning system [Si 62, Vi 76]. This information can be used to discriminate between "peripheral" collisions such as inelastic scattering, breakup, or transfer reactions and "central" collisions, such as massive transfer, complete and incomplete fusion. In addition, the fission fragment mass distribution can be used to some degree as a measure of the excitation energy of the fissioning system.

In the first of these three experiments, projectile-like fragments were observed in coincidence with both fission fragments [Dy 79, Aw 79, Ba 80]. This enabled a rather complete kinematic understanding of those reactions which produce projectile-like residues. In the second experiment both fission fragments were again observed but in coincidence with light particles (protons, deuterons,

tritons, and alphas) [Aw 80, Aw 81]. It was thereby possible to determine the relative contributions of processes such as breakup or incomplete fusion to the emission of light particles. The third experiment involved the observation of either protons or neutrons in coincidence with a single fission fragment [Ka 81]. The purpose here was to compare proton and neutron spectra directly in order to better understand the mechanism through which composite particles such as the deuteron are produced. The fourth and final experiment of this study was an investigation of the incident energy and target dependence of light particle production. For this purpose inclusive measurements were made of light particles emitted in ^{16}O induced reactions on targets of ^{27}Al, ^{90}Zr, and ^{197}Au at incident energies of 140, 215, and 310 MeV [Aw 81a, Aw 82].

C. Organization

The next two chapters of this dissertation present the experimental details of the current study. In Chapter II the experimental setup of each of the four experiments and the calibration procedures are described. Chapter III describes the method of data analysis including kinematic considerations and normalization procedures. The results and interpretation of reactions involving the emission of projectile-like residues are described in Chapter IV.

At the present time there exists no satisfactory theoretical framework for the description of light particle emission in heavy ion induced reactions. Instead, the theoretical approaches tend to be rather phenomenological drawing motivation from specific features of the light particle spectra. For this reason, the theoretical models are discussed in the context of the experimental results in Chapter V. In this chapter we discuss four different models of light particle emission, including a single scattering knock-out model, two models making assumptions of thermal emission, and a precompound model which considers the time development of the approach to equilibrium. Chapter VI discusses the production of the various composite particles. A coalescence description is applied in which the composite particles are assumed to result from a condensation or coalescence of free nucleons [Sc 63, Gu 76]. The last chapter is a summary of the present results. In addition, five appendices are included to provide detailed information about experimental corrections and the models applied.

CHAPTER II

EXPERIMENTAL PROCEDURES

A. Introduction

The general objective of the present study was to
investigate details of the reaction mechanism operating in
heavy ion collisions at $E/A = 20$ MeV. The experiments have
been performed at the 88-inch cyclotron of the Lawrence
Berkeley Laboratory (LBL) where an $^{16}O^{6+}$ beam of 315 MeV
incident energy is available. Four experiments have been
performed with the following specific objectives:
1) to investigate those reactions in which a projectile-
like fragment is emitted, 2) to determine which processes
result in light particle emission, 3) to make a direct
comparison of proton and neutron spectra, and 4) to study
the systematics of light particle production. All of these
experiments except the neutron comparison experiment were
performed using the LBL 36-inch scattering chamber. The
neutron experiment was completed using the spectrograph
vault. A detailed summary of the experimental arrangements

in the first three experiments is given in Tables II-1, II-2, and II-3. Included here are estimates of the dynamic ranges of the various particle telescopes. In each of the four experiments the raw data were recorded event by event on magnetic tape using the LBL Modcomp computer system. The data were analyzed off-line on the Sigma-7 computer system at MSU using the program SCANDIA.

B. Experimental Arrangement

1. Projectile-like Fragment Experiment

This experiment was performed using ^{16}O beams of 140 MeV and 315 MeV incident energy. The target consisted of 200 $\mu g/cm^2$ of $^{238}UF_4$ evaporated onto a 50 $\mu g/cm^2$ carbon foil. The detector arrangement is illustrated in Figure II-1 and details of the experimental arrangement are presented in Table II-1. The emphasis in this experiment was toward detecting projectile-like fragments (PLFs) in coincidence with fission fragments. For this purpose two commercially available ORTEC position sensitive solid state detectors (PSDs) of 8 mm x 47 mm active area were placed on opposite sides of the beam axis at $\theta_B^o = -\theta_A^o = 80°$. These detectors allowed the measurement of the energy and angle of the two coincident fission fragments resulting from the sequential fission decay of the target residue. A heavy ion telescope placed at $\theta = 15°$ relative to the beam axis was used to detect projectile residues in coincidence with
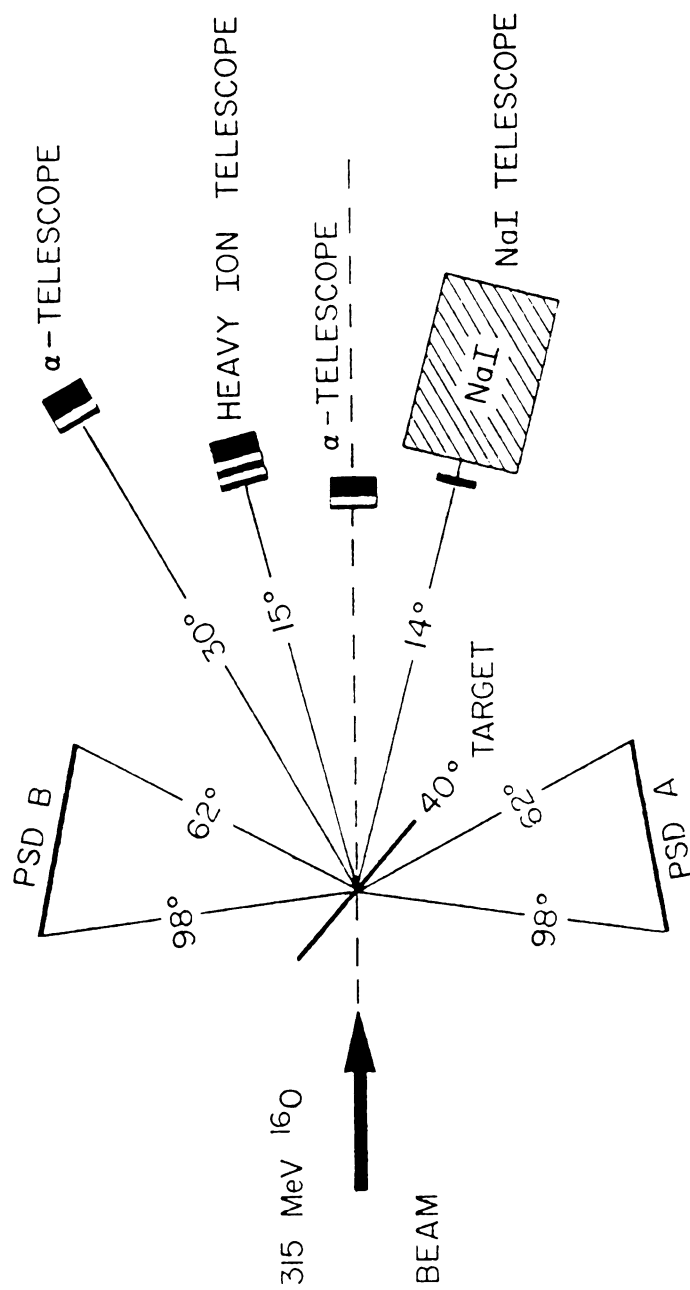
Figure II-1. Experimental geometry used in the experiment in which projectile-like fragments and light particles were measured in coincidence with fission fragments.

Table II-1. Summary of experimental setup for measuring projectile-like fragments in coincidence with fission fragments (140, 315 MeV ^{16}O onto 200 μg/cm^2 ^{238}UF$_4$ on 50 μg/cm^2 carbon backing)

Particles Detected	Angle	Solid Angle	$\Delta E_1^\dagger$	$\Delta E_2^\dagger$	$E^\dagger$	Comment (Designation)
fission fragments	-80°	8 mm x 47 mm at 6.4 cm	—	—	—	position sensitive(PSDA)
"	80°	"	"	"	"	" (PSDB)
(Li,...,O)[a]	15°	7.5 msr	68 μm	95 μm	5 mm	(HI telescope)
(p,d,t,α)[b]	-14°	7.6 msr	400 μm Al	375 μm	3.8 cm NaI(Tl)	Al absorber foil (NaI telescope)
α-particles[c]	30°	3.9 msr	—	200 μm	5 mm	(α$_1$ telescope)
α-particles[d]	26°, φ=90°	9.1 msr	—	250 μm	5 mm	(α$_2$ telescope)

†Thickness of Si surface barrier detector unless otherwise noted.
a) Dynamic range Li: 35-315 MeV, O: 140-315 MeV.
b) Dynamic range p: 9-130 MeV, α: 40-315 MeV.
c) Dynamic range α: 20-120 MeV.
d) Dynamic range α: 22-120 MeV.

fission fragments. In addition to projectile-like fragments, light particles were observed in three light particle telescopes. One telescope consisted of a 375 μm thick surface barrier solid state detector backed by a 3.8 cm deep NaI(Tl) scintillation detector. This NaI-telescope was located at an angle of $\Theta_{NaI} = -14°$ relative to the beam axis and subtended a solid angle of $\Omega_{NaI} = 7.6$ msr. An Al cover foil of 400 μm thickness was placed in front of this telescope to stop elastically scattered particles in order to reduce the count rate and prevent radiation damage. A second telescope, used for detecting alpha-particles, consisted of a 200 μm thick ΔE-detector and a 5 mm thick E-detector. This telescope was placed at $\Theta_{\alpha_1} = 30°$. An additional alpha-particle telescope was located out of the reaction plane at the angles $\Theta_{\alpha_2} = 26°$, $\Phi_{\alpha_2} = 90°$. The light particle results of this experiment will be discussed only superficially, however, since the second experiment of the present study deals with the question of light particle emission more thoroughly.

A valid coincidence event consisted of a coincidence between both fission detectors and a projectile residue or a light particle (detected in any of the four telescopes). For each event, 17 parameters were measured and recorded on magnetic tape. The parameters are: the energy signals of all eleven detectors, the two position dependent signals for the position sensitive fission detectors and

the time to amplitude converter outputs that correspond to
the time spectra measured between the fission detector
PSDA and the four particle telescopes. In addition, the
relative time spectra between the two fission detectors
were monitored. Since these spectra contained only a
negligible number of events corresponding to random
coincidences ($\sim 10^4$ real-to-random ratio), this parameter
was not stored on magnetic tape.

2. Light Particle Coincidence Experiment

In this experiment a self-supporting metallic ^{238}U
target of approximately 500 μg/cm^2 areal density was
bombarded by ^{16}O^{6+} ions at 315 MeV with a beam current of
~ 3 nA. A schematic drawing of the experimental layout is
shown in Figure II-2 and experimental details are presented
in Table II-2. Four ΔE-E light particle telescopes were
mounted in the plane of two position sensitive solid state
fission detectors. All detectors were mounted on a
movable table inside the scattering chamber. Each of the
four ΔE-E telescopes consisted of a 400 μm surface barrier
Si detector and a 7.6 cm thick NaI detector. Two experi-
mental geometries were used. In geometry I, shown in
Figure II-2, the light particle telescopes were placed at
the scattering angles of -95°, -25°, 70°, and 140°. The
position sensitive detectors were located at $\Theta_A^\circ = -60°$ and
$\Theta_B^\circ = 100°$ with each subtending an angular range of about
$\pm 20°$. For geometry II, the entire arrangement was rotated
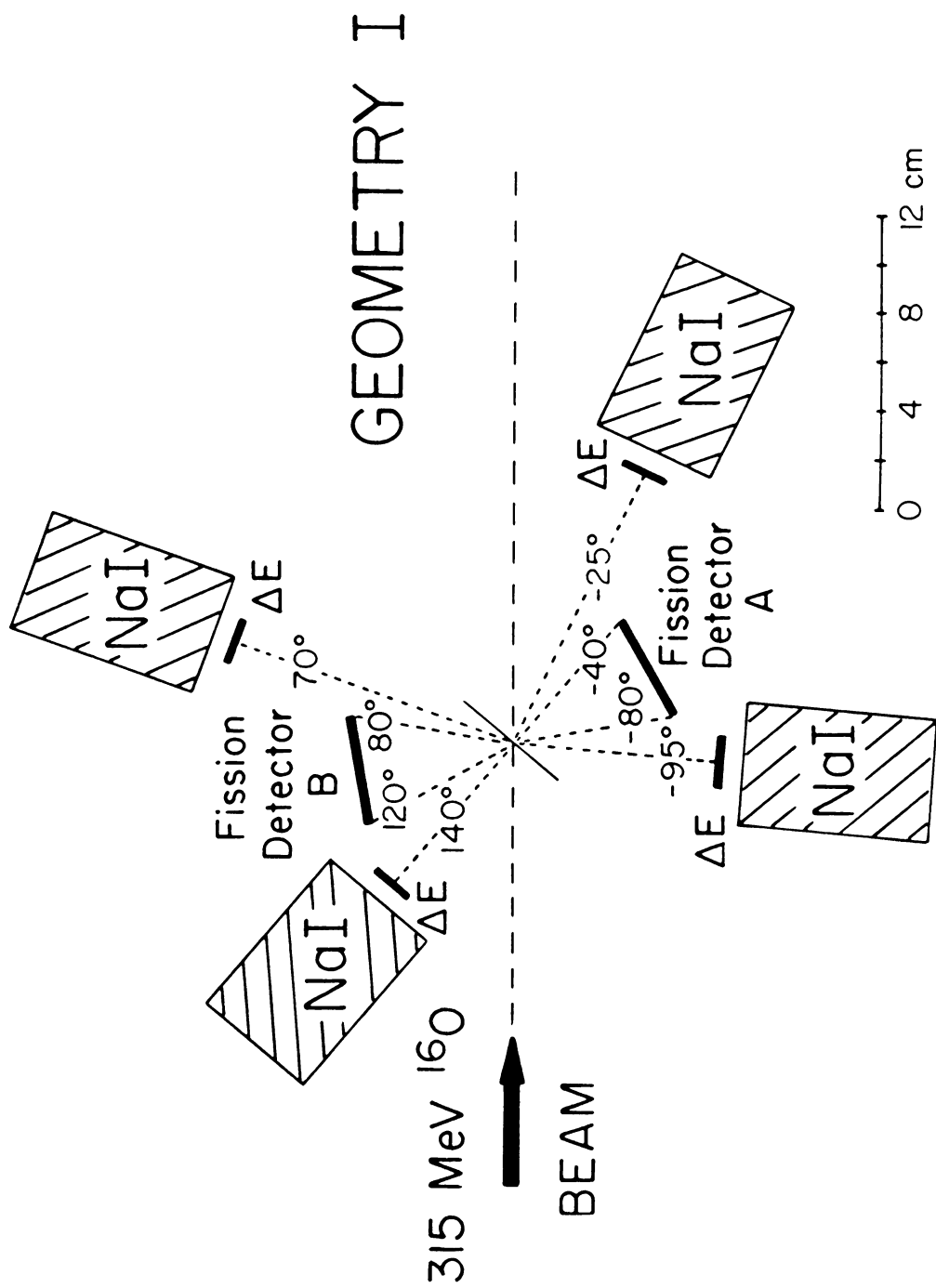
Figure II-2. Experimental geometry used in the experiment in which light particles were measured in coincidence with fission fragments.

Table II-2. Summary of experimental setup for measuring light particles in coincidence with fission fragments. (315 MeV 16O onto 500 μg/cm² 238U)

Particles Detected	Angle	Solid Angle	$\Delta E^{\dagger}$	$E^{\dagger}$	Comment	Geometry #
fission fragments	-60°	±20°	—	—	position sensitive(PSDA)	I
"	100°	"	"	"	" (PSDB)	"
(p,d,t,α)[a]	-95°	49 msr	400 μm	7.6 cm NaI(Tl)	—	"
"	-25°	23 msr	"	"	—	"
"	70°	24 msr	"	"	—	"
"	140°	59 msr	"	"	—	"
(p,d,t,α)[b]	15°	15 msr	"	"	640 μm Al absorber	"
fission fragments	-75°	±20°	—	—	position sensitive(PSDA)	II
"	85°	"	"	"	" (PSDB)	"
(p,d,t,α)[a]	-110°	49 msr	400 μm	7.6 cm NaI(Tl)	—	"
"	-40°	23 msr	"	"	—	"

Table II-2. (con't.)

Particles Detected	Angle	Solid Angle	$\Delta E^\dagger$	$E^\dagger$	Comment	Geometry #
(p,d,t,α)a)	55°	24 msr	400 μm	7.6 cm NaI(Tl)	—	II
"	125°	59 msr	"	"	—	"

†Thickness of Si surface barrier detector unless otherwise noted.
a) Dynamic range p: 7-200 MeV, α: 30-315 MeV.
b) Dynamic range p: 11-200 MeV, α: 55-315 MeV.

by -15° to give four additional angles (-110°, -40°, 55°,
125°) for light particle observation. Accordingly, the
fission detectors were then centered at $\Theta_A^0 = -75°$ and
$\Theta_B^0 = 85°$. In geometry I, one telescope was moved for a
portion of the run to the forward angle of 15°. At this
angle an aluminum absorber of 640 μm thickness was placed
in front of the telescope to prevent pile-up and radiation
damage by the high flux of elastically scattered ^{16}O
nuclei.

In this experiment, sixteen parameters were recorded
on magnetic tape: the energy signals of all ten detectors,
the two position dependent signals of the position
sensitive fission detectors, and the four timing signals
corresponding to the time separation between fission
detector A and the four light particle telescopes. In
addition the coincidence time signal between the two
fission detectors was monitored and used to gate the
computer to ensure that two fission fragments were detected
for each event. Since only a negligible number of random
coincidences between the two fission detectors were
observed, this parameter was not recorded on tape.

A "coincidence event" was defined as a coincidence
between the two fission fragments and at least one of the
light particle telescopes. In addition to coincidence
events, "inclusive fission events" were recorded on tape
at a downscaled rate for normalization purposes. An

inclusive fission event was defined as a coincidence between two fission fragments.

3. Neutron Experiment

The emission of energetic neutrons and protons was measured in coincidence with fission fragments for the reactions ^{238}U $(^{16}O, nf)$ and ^{238}U $(^{16}O, pf)$. A $^{238}UF_4$ target of 320 $\mu g/cm^2$ thickness, mounted on an 80 $\mu g/cm^2$ carbon backing was irradiated by $^{16}O^{6+}$ ions of 310 MeV incident energy. The experiment was performed in a large experimental area in order to have long neutron flight paths for improved energy resolution and also to minimize the background due to the rescattering of neutrons from the walls. Details of the experimental setup are given in Table II-3. To minimize the rescattering of neutrons, a thin-walled aluminum scattering chamber was used [Hi 79]. Fission fragments were detected inside this chamber with a surface barrier detector mounted at an angle of $\theta_f = 90°$ with respect to the beam axis and at a distance of 1.5 cm from the center of the target. The primary purpose of the fission detection was to provide a time signal with which to perform the neutron time-of-flight measurement. This was necessary because the time structure of the cyclotron beam pulse was not sufficient for this purpose.

In the first part of the experiment, four liquid scintillation detectors (NE 213) were used to detect neutrons emitted at angles with respect to the beam of

Table II-3. Summary of measurement[†] of neutrons and protons in coincidence with fission fragments. (310 MeV [16]O onto 320 μg/cm² [238]UF₄ on 80 μg/cm² carbon backing)

Particles Detected	Angle	Distance	Area/diameter	Solid Angle	ΔE[††]	E[††]
fission fragments	90°	1.5 cm	450 mm²	—	—	60 μm
neutrons	-25°	2.05 cm	11.4 cm	—	400 μm	6.0 cm (NE 213)
"	-40°	"	12.7 cm	—	"	5.1 cm (NE 213)
"	-55°	"	"	—	"	7.6 cm (NE 213)
"	-95°	"	"	—	"	"
protons[a)]	-25°	—	—	6.6 msr	400 μm	7.6 cm NAI(Tl)
"	-55°	—	—	10.1 msr	"	"

[†]All detectors except fission detector mounted in air.
[††]Thickness of Si surface barrier detector unless otherwise noted. For the neutron telescopes the ΔE detectors served to reject charged particles.
a)Dynamic range p: 7-200 MeV, α: 30-310 MeV.

-25°, -40°, -55° and -95° respectively, in coincidence with fission fragments. The flight paths were 2.05 m. In order to reduce the background due to extraneous sources and due to scattering in the experimental vault, these detectors were placed inside shields constructed of lead, concrete and paraffin. The background remaining was determined by measurements with a tapered steel bar of 60 cm length placed halfway between the target and each detector. This "shadow bar" completely filled the detector solid angle so that neutrons originating in the target were absorbed but extraneous neutrons were allowed to reach the detector. Energetic charged particles were discriminated by an anticoincidence requirement using transmission-mounted solid state detectors placed outside the scattering chamber. Pulse shape information from each scintillator was obtained by means of Canberra Model 2160 pulse shape discriminators [Sp 74].

In the second part of the experiment, coincident protons were detected with two ΔE-E telescopes positioned at angles of $\theta_p = -25°$ and $-55°$. Each of these telescopes consisted of a 400 μm thick surface barrier detector and a 7.6 cm thick NaI(Tl) detector. The detectors were placed outside two exit ports of the scattering chamber which were covered with 50 μm thick mylar windows.

Downscaled fission singles data were recorded simultaneously with the coincidence data. For each event,

the pulse heights of all detector signals were recorded on magnetic tape; in addition, the time difference between light particle and fission detector signals was recorded together with the output of the pulse shape information circuit for each neutron detector.

4. Inclusive Light Particle Experiment

The aim of this experiment was to study the energy and target dependence of inclusive light particle cross sections. For this reason, ^{16}O beams of 140, 215, and 310 MeV incident energies were used with typical intensities of 20, 1, and 0.5 nA, respectively. Measurements were made using three different targets spanning a large mass range. An ^{27}Al target of 1.6 mg/cm^2 thickness was used at all three bombarding energies. A ^{90}Zr foil of 20.9 mg/cm^2 thickness and a 10.6 mg/cm^2 thick ^{197}Au foil were each irradiated at 215 and 310 MeV incident energies. In addition, a thin ^{197}Au target of 1.2 mg/cm^2 thickness was bombarded at 140 MeV incident energy. This target was found to have a hydrogen contaminant which gave rise to a distant peak in the forward angle proton spectra. This contribution has been removed in the analysis.

Light particles (p,d,t, and α) were detected with two ΔE-E telescopes mounted on a movable table inside the scattering chamber. Each telescope subtended a solid angle of 22 msr and consisted of a 400 μm thick surface barrier detector and a 7.6 cm thick NaI(Tl) detector.

The entrance window of the NaI detector consisted of a
Havar foil of about 75 μm thickness. The ΔE and E energy
signals of the two telescopes were recorded event by event
on magnetic tape for off-line analysis.

C. Calibration Procedures

1. Energy Calibration of Fission Fragment Detectors

The energy calibration of the position sensitive
fission detectors used in the PLF and light particle experi-
ments was obtained by recording the pulse height spectrum
from the spontaneous fission of ^{252}Cf and using the Schmitt
calibration procedure [Sc 65]. This procedure takes into
account the mass dependent response (known as the pulse
height defect or mass defect) of surface barrier detectors
to heavy ions and fission fragments by employing a mass
dependent energy calibration of the form

$$E = (a + a'M) P + (b + b'M) \quad . \qquad (II-1)$$

Here E and M are the ion energy and mass, respectively, and
P is the corresponding pulse height. For a given detector
the constants a, a', b, and b' may be obtained directly by
making a minimum of two measurements of pulse height
versus energy for at least two different ion masses.
However, such a calibration procedure would be difficult
and time consuming to perform in every experiment.

Schmitt et. al. have overcome this problem by using the pulse height spectrum from ^{252}Cf spontaneous fission fragments to uniquely define two pulse heights P_L and P_H. Due to the dominance of asymmetric fission, the ^{252}Cf pulse height spectrum is a bi-modal distribution with the peak at large pulse height corresponding to the light fission fragment and the peak at low pulse height corresponding to the heavy fragment. The pulse height P_L is then defined as the midpoint between the 3/4-maximum points in the light fragment peak and the pulse height P_H corresponds to the midpoint between the 3/4-maximum points in the heavy fragment peak.

The pulse height locations P_L and P_H are uniquely defined independent of the detector response. As a result, the energies $E_{L,M}$ and $E_{H,M}$ associated with these pulse height positions for a fragment of mass M and for a given detector will be associated with the same pulse height positions in any similar detector. Having once determined the energies $E_{L,M}$ and $E_{H,M}$ for a fragment of mass M it is never necessary to do so again. It is only necessary to determine the actual pulse height values P_L and P_H which will depend on a particular detector's response. By using any four energies E_{L,M_1}, E_{H,M_1} and E_{L,M_2}, E_{H,M_2}, associated with any two fragment masses M_1 and M_2, it is possible to solve for the four constants of Eq. (II-1). In particular, Schmitt et. al. [Sc 65] determined the Br (M = 80) and

I ($M = 127$) energies corresponding to each pulse height location P_L and P_H. Using these four energies in Eq. (II-1) the resulting four simultaneous equations may be solved in terms of P_L and P_H to obtain

$$a = 24.0203/(P_L - P_H),$$
$$a' = 0.03574/(P_L - P_H),$$
$$b = 89.6083 - aP_L,$$
$$b' = 0.1370 - a'P_L.$$

$$(II-2)$$

This procedure allows the energy calibration of surface barrier fission detectors to be performed quickly and efficiently.

The surface barrier fission detector used in the neutron experiment was not energy calibrated since its only purpose was to provide a timing signal when a fission fragment was observed. The pulse height resolution was sufficient to distinguish alpha-particles from fission fragments and to observe the light and heavy fragment components of the fission pulse height spectrum.

2. Position Calibration of Position Sensitive Detectors

The position calibration of the PSDs was obtained by viewing a ^{252}Cf source through a mask with 15 equally spaced slits of 0.8 mm width placed over each detector. A third order calibration polynomial was used with the form

$$s = a_0 + a_1 x + a_2 x^2 + a_3 x^3 \qquad (II-3)$$

where s is the position along the detector and x is the position signal defined by the ratio x = (position x energy signal)/(energy signal) for each detected particle. Due to the pulse height defect of the PSDs (see II.C.1) it was necessary to allow for the energy dependence, viz. mass dependence, of the parameters a_i of Eq. (II-3) according to

$$a_i = b_i + b_i' P \qquad \text{(II-4)}$$

where P is the pulse height of the energy signal. The constants b_i and b_i' were obtained by gating the ^{252}Cf energy pulse height spectrum with several energy windows and fitting the centroids of the slit locations in the position spectrum to the known mask positions.

This calibration procedure gave good position resolution of $\Delta s \leq 0.5$ mm corresponding to a typical angular resolution of better than 0.3 degrees in our experimental geometry. However, in order to achieve good efficiency for the detection of fission coincidences, it was necessary to mount the fission detectors close to the target (see Figures II-1 and II-2). This close geometry renders the angle calibration quite sensitive to systematic errors resulting from small uncertainties in the beam and target positions. To minimize such systematic errors we have measured the folding-angle distributions in each experiment for four different target positions. (The fission fragment

folding-angle, Θ_{AB}, is defined as the angle of emission between two coincident fission fragments). As shown in Appendix A, this allows measurement and correction for displacements of the beam and target from the center of the scattering chamber. In the projectile-like fragment experiment the folding-angle calibration was further verified by requiring that the fission fragment folding-angle (and hence target recoil momentum) observed in coincidence with inelastically scattered ^{16}O ions (Q > -15 MeV) be consistent with a pure two-body reaction followed by the fission decay of the target nucleus. With these corrections taken into account, it is estimated that the fission fragment folding-angle is measured with an accuracy of $\Delta\Theta_{AB} \leq 1°$ (see Appendix A).

3. Energy Calibration of NaI Detectors

Previous observations [Ba 78, Sy 80] of energetic light particle emission in heavy ion reactions have shown that protons are emitted at forward angles with energies of up to four times the incident energy/nucleon of the beam. These protons, having energies greater than 80 MeV, would require over 2.5 cm of Si in order to be stopped. The expense of such thick Si surface barrier detectors prohibits their use as stopping detectors but makes thick NaI(Tl) detectors appear highly attractive. Unfortunately, the large amount of energy deposited by these energetic particles would quickly saturate a photomultiplier tube at

normal operating voltages. Therefore, in order to prevent saturation, we have shortened the dynode chain of the photomultiplier tubes used in the present study. For a typical NaI detector the energy signals were taken from the fifth dynode of the photomultiplier tube.

In all four experiments except the neutron experiment, the NaI detectors were placed in the scattering chamber under vacuum. Since the NaI detectors were electrically insulated and therefore in poor thermal contact with the scattering chamber it was necessary to monitor them for possible gain shifts due to resistive heating in the photomultiplier tube base. In the experiment emphasizing projectile fragment emission, the NaI detector stability was monitored by observing the peak position of elastically scattered ^{16}O ions which entered the detector through a 1.6 mm diameter hole in the aluminum cover foil. In the light particle coincidence experiment and the light particle inclusive experiment the gain stability was monitored by recording the γ-ray spectra of ^{22}Na and ^{60}Co, respectively, during ion source changes. Due to the long term gain shifts, the overall accuracy of the NaI energy calibrations is estimated to be about 3%.

In the experiment in which light particles were measured inclusively, the energy calibration of the NaI detectors for hydrogen isotopes was established by measuring the elastic scattering of protons on a ^{197}Au target

at the incident energies of 10, 20 and 45 MeV. The result-
ing energy calibration was found to be linear over this
energy range and was extrapolated toward high energies. An
independent energy calibration was established for alpha-
particles by measuring the elastic scattering of alpha-
particles on ^{197}Au at 40, 80 and 120 MeV. The resulting
energy calibration was found to be slightly non-linear
with a decreasing response toward high energies. These
calibration points and the chosen calibration curves are
shown in Figure II-3 for one of the NaI(Tl) detectors.
From this figure the rather large pulse height defect of
these detectors is evident. The pulse height defect
between the various hydrogen isotopes has been assumed to
be negligible [Wa 60].

In the three fission coincidence experiments the NaI
detectors were not calibrated as thoroughly due to beam
time constraints. In the light particle coincidence
experiment the energy calibration for hydrogen isotopes was
established by measuring the elastic scattering of protons
on a ^{197}Au target at incident energies of 20 MeV and
45 MeV. The energy calibration for alpha-particles was
obtained by measuring the elastic scattering of alpha-
particles on a ^{197}Au target of 80 MeV. This gave a fixed
point for the calibration. The energy deposited in the ΔE
detector was then used to determine the thickness of the
ΔE detector. The response of the NaI detector to
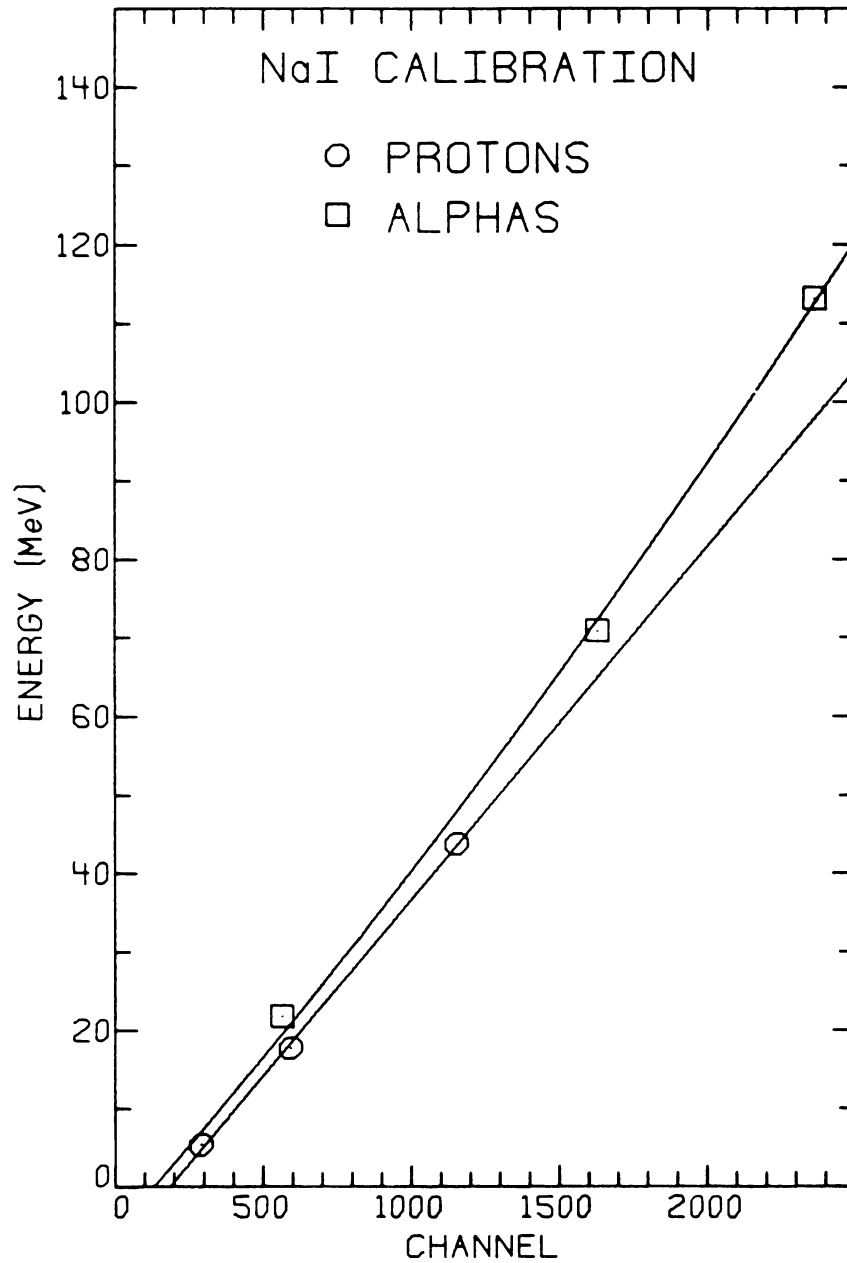
Figure II-3. Energy calibration for a typical NaI(Tl) detector used in the present study. The calibration shown is for one of the two detectors used in the experiment in which light particles were measured inclusively.

alpha-particles was then established from a continuum
spectrum by setting gates on the ΔE signal and calculating
[CMap] the alpha-particle energy corresponding to the
measured ΔE signal. The overall accuracy of this procedure
is about 5%.

In the neutron experiment, the energy calibration of
the NaI detectors was established by observing 45 MeV
protons elastically scattered from a gold target. The
shapes of the high energy tails of the proton spectra
measured in coincidence with fission fragments were con-
sistent with the spectra of the previous light particle
coincidence experiment. In the projectile-like fragment
experiment the energy calibration of the NaI telescope for
hydrogen isotopes was obtained by measuring the elastic
scattering of protons on gold at 21 MeV and measuring the
$p(\alpha,p)$ reaction at 79 MeV incident energy using a hydro-
carbon target. The alpha-particle energy calibration was
assumed to be parallel to the calibration for hydrogen
isotopes and to pass through the fixed point obtained by
measuring the elastic scattering of alpha-particles on
^{238}U at 79 MeV.

4. Energy Calibration of Solid State Detectors

Solid state silicon detectors were used in the present
study as ΔE detectors in front of the NaI detectors and
also as both ΔE and E detectors in the alpha-particle and
heavy ion telescopes of the projectile-like fragment

experiment. These detectors were energy calibrated and the linearity of the electronics was checked by injecting a known amount of charge using a calibrated pulser into the input stage of the detector preamplifiers. From the measured value of the ionization energy of silicon (3.67 eV/ion pair) this amount of charge can be directly related to an equivalent amount of energy deposited in the detector. These pulser calibrations were verified by measuring the alpha-particle energy spectra resulting from the decay of ^{228}Th, ^{241}Am, or ^{252}Cf sources and/or by calculating [CMap] the energy lost in the ΔE detectors corresponding to the measured ΔE signals of the elastically scattered proton and alpha beams.

5. Neutron Time-of-Flight Calibration

In the neutron coincidence experiment the neutron energy was determined by measuring the neutron flight-time. The flight times were recorded using time to amplitude converters (TACs) with start signals derived from the anode signal of the neutron detector photomultiplier tubes and with a stop signal derived from the fission detector. The TAC spectra were calibrated using a pulser system with a set of calibrated delays. A time calibration of the form

$$T = c_0 + c_1 t + c_2 t^2 + c_3 t^3 \qquad \text{(II-5)}$$

was assumed where T is the calibrated time corresponding to the channel t of the TAC spectrum. The coefficients c_2

and c_3 of the non-linear terms were relatively small. The neutron time-of-flight, T_n, is then given by

$$T_n = T_\gamma - T + d/c \qquad\qquad \text{(II-6)}$$

where T_γ is the arrival time of the prompt γ-rays which was used as a reference time and, d/c, the flight path divided by the speed of light, is the time-of-flight of the γ-rays. The neutron energy was calculated according to

$$E = mc^2 (\gamma - 1) \qquad\qquad \text{(II-7)}$$

where mc^2 is the neutron rest mass and $\gamma = (1 - \beta^2)^{-\frac{1}{2}}$ with $\beta = (d/T_n)/c$.

In order to improve the time resolution and hence the energy resolution, the neutron-fission timing signals were corrected for the flight time of the fission fragments. This was accomplished by gating the fission fragment pulse height spectrum into four bins. These bins of increasing pulse height then correspond to four bins of decreasing fragment mass. Since the heavier fragments have longer flight times their time spectra will be shifted relative to the light fragment time spectra. By using separate reference times T_γ for each of the four fission pulse height gates it was thereby possible to achieve an overall time resolution of 1.0 nsec (fwhm), corresponding to an energy resolution of 5 MeV (fwhm) at 50 MeV.

CHAPTER III

DATA ANALYSIS

A. Normalizations and Corrections

1. Projectile-like Fragment Experiment

The coincidence spectra and calculated quantities of
this experiment have been corrected for accidental coinci-
dences. The spectra for accidental events were obtained by
gating the relative time spectrum between the fission
detector and particle telescope on the random coincidence
peaks. The envelope of the random coincidences has a max-
imum at the real coincidence peak. It is therefore necessary
to renormalize the random spectra obtained from the random
peaks to the maximum of the envelope. The relative contri-
bution of accidentals in the real coincidence peak was
deduced from the contribution of elastically scattered ^{16}O
which cannot occur as a true coincidence with fission. The
spectrum of the accidentals, N_{ac}, in the real coincidence
peak was then calculated as

$$N_{ac} = \frac{(N_{el.})_{ac}}{(N_{el.})_{rn}} N_{rn} \qquad \text{(III-1)}$$

where $(N_{el.})_{ac}$ and $(N_{el.})_{rn}$ are the elastic contributions in the real and random coincidence peaks, respectively, and N_{rn} is the spectrum of random events obtained from the random coincidence peaks. The resulting random corrections were typically less than 3%. In addition, the fission fragment folding-angle distributions have been corrected for the geometrical detection efficiency. The coincident cross sections are presented as the raw number of counts.

2. Light Particle Coincidence Experiment

The fission fragment folding-angle distributions, Θ_{AB}, have been corrected for the geometrical efficiency of the fission detection system. The coincident light particle spectra were also corrected for the fission detection efficiency on an event by event basis. The detection efficiency, shown in Figure III-1, was determined by a computer simulation of the fission decay of ^{254}Fm (Appendix B). In this simulation, the total momentum vector of the recoiling ^{254}Fm nucleus was assumed to be directed parallel to the beam axis. This assumption is necessarily fulfilled for compound nucleus reactions. For noncompound reactions, however, the recoil momentum components perpendicular to the beam axis could be appreciable. In this case, the momentum vectors of the fission fragments could span a plane that does not contain the beam axis and our calculations would overestimate the detection efficiency. Since the transverse momentum
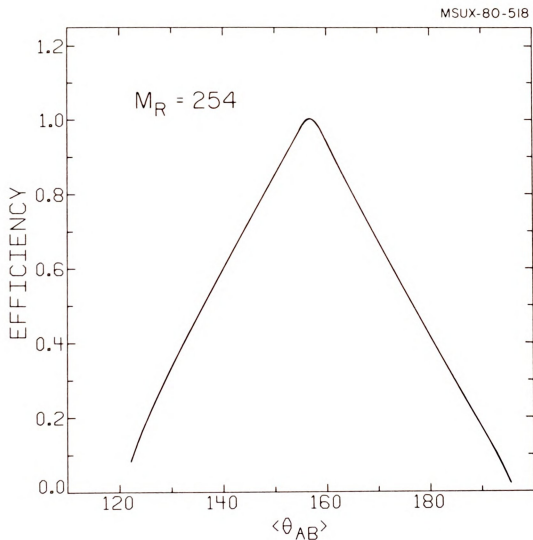
Figure III-1. Fission fragment detection efficiency as a function of the fission fragment folding-angle θ_{AB} obtained by simulation of the fission of ^{254}Fm with the experimental geometries I and II of the present study.

distribution of the target residue is not known, a correction for this effect could not be made.

The coincident spectra have also been corrected for accidental coincidences. The coincident light particle cross sections are presented as the differential multiplicity per fission event, that is, as the number of light particle coincidences normalized to the number of inclusive fission events N_f.

3. Neutron Experiment

In the off-line analysis, two-dimensional gates were set in the pulse height versus pulse-shape spectra to distinguish γ-rays from neutrons. The neutron detection efficiency was calculated with a modified version of a computer code originally developed by Kurz [RJKu]. For a given detector thickness, the efficiency depends primarily on the threshold set on the pulse height distribution. The threshold for each detector was chosen to be higher than the electronic threshold, and two different values of threshold for each detector were tried to check the calculated efficiency. The accuracy of the absolute neutron efficiency is estimated to be ±15%.

A 10-15% contribution of background neutrons was subtracted from the neutron spectra. The background was determined during runs in which the "shadow bars" were in place. The spectra were also corrected for accidental coincidences. The coincident neutron and proton cross

sections are presented as the number of coincidence events normalized to the number of inclusive fission events N_f.

4. Inclusive Light Particle Experiment

Differential cross sections were determined using the measured target thicknesses and integrated beam current. The dead time of the system was monitored by injecting a pulse into the detector preamplifiers at a rate which was proportional to the beam current. The resulting dead time corrections were usually less than 4%. The absolute magnitude of the cross sections is estimated to be accurate to within 35%.

B. Particle Identification

Mass and charge identification of the particles observed in each telescope was obtained by using a standard particle identification (PI) function of the form [Go 75]

$$PI \propto (E + \Delta E)^{\gamma} - E^{\gamma} . \qquad \text{(III-2)}$$

Here ΔE and E are the measured energy loss and residual energy of the particle and γ is a parameter which is optimized to give minimum energy dependence of the PI function. Generally, γ varies from 1.6 to 1.8.

A typical PI spectrum observed in the inclusive light particle experiment is shown in Figure III-2. Here the NaI energy calibration for hydrogen isotopes was used to
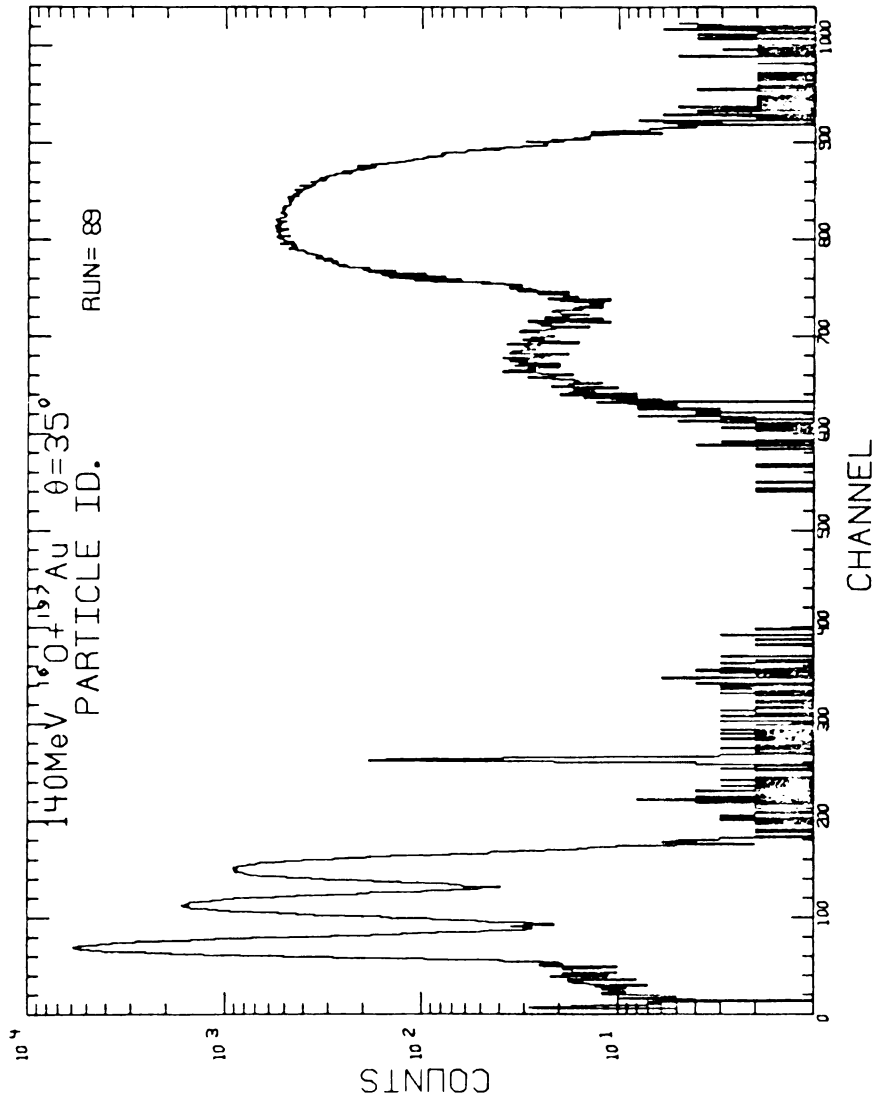
Figure III-2. Typical particle identification spectrum as observed in the present study. The spectrum shown was obtained at 35° in the 16O+197Au reaction at 140 MeV incident energy. The p,d, and t peaks are clearly observed in the region below channel 200 while 3He and α-particles are separated at about channels 700 and 800, respectively. The narrow peak at channel 250 is the pulser used for monitoring the system dead time.

separate the individual hydrogen isotopes and identify helium. When a helium particle was identified, the alpha-particle energy calibration was applied and a new PI was calculated which allowed resolution of ^{3}He and alpha-particles. However, the spectra of ^{3}He have not been analyzed in the present study due to non-negligible contributions from the abundant alpha-particles. In the light particle coincidence experiment a contribution of approximately 10% ^{3}He was included in the ^{4}He spectra.

C. Fission Reaction Kinematics

The projectile-like fragment coincidence data have been analyzed off-line on an event by event basis in order to extract the amount of linear momentum transferred to the target residue prior to fission. In this experiment, the energy and outgoing direction were the only parameters determined for each fission fragment. Because the fragment masses were not measured the reconstruction of the kinematics of the fission reaction is not possible unless two further assumptions are made to determine these two parameters. In our analysis we have made specific assumptions about the sum mass of the primary fission fragments and about the target residue momentum component $P_R^\perp$ perpendicular to the beam axis. In this section we give a detailed discussion of our kinematical analysis and the validity of our approximations.

We consider the fission decay of the recoiling nucleus as an isolated event, i.e., we assume a truly sequential fission process. Momentum conservation in the laboratory system then gives the following two equations

$$P_R^{\parallel} = P_A \cos \Theta_A + P_B \cos \Theta_B, \qquad \text{(III-3)}$$

and

$$P_R^{\perp} = P_A \sin \Theta_A - P_B \sin \Theta_B, \qquad \text{(III-4)}$$

where $P_R^{\parallel}$ and $P_R^{\perp}$ denote the parallel and perpendicular momentum components of the recoiling system with respect to the beam axis. The magnitude and angle of the momentum of fragment A with respect to the beam axis are denoted P_A and Θ_A, respectively. A similar notation is adopted for the momentum of fragment B. Mass conservation during the fission decay can be expressed as

$$M_R = M_A + M_B \qquad \text{(III-5)}$$

where M_R, M_A and M_B are the masses of the recoil nucleus and the primary fragments A and B, respectively. The momenta of the primary fission fragments are given by

$$P_A = (2 \ M_A \ E_A)^{\frac{1}{2}} \qquad \text{(III-6a)}$$

$$P_B = (2 \ M_B \ E_B)^{\frac{1}{2}} \qquad \text{(III-6b)}$$

where E_A and E_B denote the primary fragment kinetic energies. (For the discussion of the corrections for neutron

evaporation from the primary fragments, see below). It is clear that two more equations are needed to determine the momentum of the target residue.

If the primary reaction between the projectile and target residue were a pure two body process we would have the additional relations

$$P_R^\| = P_1^\| - P_3^\| \qquad\qquad \text{(III-7a)}$$

$$P_R^\perp = -P_3^\perp \qquad\qquad \text{(III-7b)}$$

$$M_R = M_1 + M_2 - M_3 \qquad\qquad \text{(III-7c)}$$

where the indices 1, 2 and 3 denote the projectile, the target and the outgoing projectile residue, respectively. Since only two relations are needed to determine the kinematics unambiguously, we have measured one redundant parameter in this case, which can then be used to test the assumption of a primary two-body reaction.

In the general case we are dealing with more than three particles in the exit channel and Equations (III-7) are no longer fulfilled. If we denote the total mass and momentum of all undetected particles by the "missing mass", M_m, and the "missing momentum", P_m, we have instead (see Figure III-3)

Figure III-3. Schematic diagram of momentum balance in the heavy ion reaction followed by fission of the target residue.

$$P_R^{\parallel} = P_1 - P_3^{\parallel} - P_m^{\parallel} \qquad \text{(III-8a)}$$

$$P_R^{\perp} = -P_3^{\perp} - P_m^{\perp} \qquad \text{(III-8b)}$$

$$M_R = M_1 + M_2 - M_3 - M_m. \qquad \text{(III-8c)}$$

In the following we will show that the momentum components parallel to the beam axis, $P_R^{\parallel}$ and $P_m^{\parallel}$, are quite well determined by the present measurements, whereas the momentum components perpendicular to the beam axis are only poorly known. This is primarily a result of placing the position sensitive detectors symmetrically about the beam axis, which gives $<\theta_A> \simeq <\theta_B>$. For an average event we can therefore write (see Equations (III-3) and (III-4)).

$$P_R^{\parallel} \simeq \left[\sqrt{2M_A E_A} + \sqrt{2M_B E_B} \right] \cos<\theta_A> \qquad \text{(III-9a)}$$

and

$$P_R^{\perp} \simeq \left[\sqrt{2M_A E_A} - \sqrt{2M_B E_B} \right] \sin<\theta_A> \qquad \text{(III-9b)}$$

The energies E_A and E_B are measured directly, but the masses M_A and M_B are in principle unknown. An increase in the first term in Eq. (III-9a), due to the assumption of a large M_A, will be compensated by a decrease in the second term via M_B due to mass conservation. For the same reason, the perpendicular component of the recoil momentum, $P_R^{\perp}$, is very sensitive to the fragment masses M_A and M_B, see Eq. (III-9b).

For events that were detected in coincidence with a projectile residue (Li,...,O) we have made the following assumptions in order to be able to calculate the complete kinematics for each event

$$M_R = M_2 \quad (\text{i.e., } M_m = M_1 - M_3) \qquad \text{(III-10)}$$

and

$$P_R^{\perp} = -P_3^{\perp} \quad (\text{i.e., } P_m^{\perp} = 0) \qquad \text{(III-11)}$$

The first assumption introduces only minor uncertainties in the mass of the target residue prior to fission. The sensitivity to the second assumption was investigated in more detail by replacing it by the more general assumption of a constant value, Θ_m, of the direction of the missing momentum vectors

$$P_m^{\perp}/P_m^{\parallel} = \tan \Theta_m = \text{const.} \qquad \text{(III-12)}$$

Defining

$$\vec{P}_4 = \vec{P}_1 - \vec{P}_3 = \vec{P}_R + \vec{P}_m \qquad \text{(III-13)}$$

and using Equations (III-8) we can rewrite Equation (III-12)

$$P_R^{\perp} = P_R^{\parallel} \tan \Theta_m + P_4 (\sin \Theta_4 - \cos \Theta_4 \tan \Theta_m). \qquad \text{(III-14)}$$

By inserting the expressions for $P_R^{\parallel}$ and $P_R^{\perp}$ from Eq. (III-3) and Eq. (III-4) we find

$$P_B^2 C_B^2 = P_A^2 C_A^2 + P_4^2 C_4^2 - 2C_A C_4 P_A P_4, \qquad \text{(III-15)}$$

where

$$C_A = \sin \Theta_A - \cos \Theta_A \tan \Theta_m,$$

$$C_B = \sin \Theta_B + \cos \Theta_B \tan \Theta_m, \qquad \text{(III-16)}$$

$$C_4 = \sin \Theta_4 - \cos \Theta_4 \tan \Theta_m.$$

Rewriting Eqs. (III-5) and (III-6) gives

$$P_B = \sqrt{(2M_R - P_A^2/E_A)E_B} \ , \qquad \text{(III-17)}$$

and with Eq. (III-15)

$$\left(C_A^2 + C_B^2 \frac{E_B}{E_A} \right) P_A^2 - 2C_A C_4 P_4 P_A + C_4^2 P_4^2 - 2C_B^2 M_R E_B = 0. \quad \text{(III-18)}$$

The solution to this equation is

$$P_A = \frac{C_A C_4 P_4 + C_B \sqrt{2M_R E_B (C_A^2 + C_B^2 \frac{E_B}{E_A}) - C_4^2 P_4^2 \frac{E_B}{E_A}}}{C_A^2 + C_B^2 \frac{E_B}{E_A}} \ . \qquad \text{(III-19)}$$

The remaining unknown quantities can then be obtained from the following relations

$$M_A = P_A^2/2E_A \qquad \text{(III-20a)}$$

$$M_B = M_R - M_A \qquad \text{(III-20b)}$$

$$P_B = \sqrt{2M_B E_B} \qquad \text{(III-20c)}$$

and from Eqs. (III-3), (III-4), and (III-8).

Mass dependent corrections for pulse height defects in the position sensitive detectors and for neutron evaporation from the fission fragments are performed by means of an iterative procedure for each event. In this procedure, an initial guess is made for the post-neutron evaporation fission masses and the pulse height defect correction described in Section II.C.1. is applied to determine the fragment energies. These energies are used to calculate the primary fission fragment masses according to the kinematic relations described above. The average number of neutrons emitted from each fragment is then calculated to obtain a better approximation for the post-neutron evaporation masses. These steps are repeated until convergence is attained. The average number of neutrons emitted per fission is assumed to be

$$\bar{\nu}(M_R, E^*) = 0.118 \ (M_R - 220) + 0.133 \ E^* \qquad (III-21)$$

where E^* is the excitation energy of the fissioning system. This formula represents a reasonable average fit to experimental data [Va 73].

The number of neutrons emitted from each fragment is furthermore assumed to be proportional to the primary fragment mass

$$\bar{\nu}(M_R, E^*, M_A) = \frac{M_A}{M_R} \ \bar{\nu}(M_R, E^*) \qquad (III-22)$$

The dependence of the extracted mean values of $P_m^{\parallel}$ and $P_R^{\parallel}$ on the correction for neutron evaporation from the fragments is rather insignificant. However, it should be kept in mind that the widths of the $P_R^{\parallel}$ distributions are artificially widened because neutron evaporation introduces random fluctuations on the angles Θ_A and Θ_B and on the final fragment energies and masses.

The momentum component $<P_R^{\parallel}>$ is rather insensitive to the choice of Θ_m while the $<P_R^{\perp}>$ component has a rather strong dependence. This is illustrated in Figure III-4 where the dependence of the average momentum components $<P_R^{\perp}>$ and $<P_R^{\parallel}>$, on Θ_m is shown for the reaction ^{238}U (^{16}O, ^{10}Bf). It is seen that only momentum components parallel to the beam axis are relatively independent of our kinematic assumptions. The range of acceptable choices of Θ_m can be determined from the requirement that, on the average, both detectors should see equal amounts of light and heavy fission fragments, i.e., $<M_B - M_A> = 0$. This requirement is a consequence of assuming that the fission decay occurs as a truly sequential process. This dependence of $<M_B - M_A>$ on Θ_m is shown in the upper part of Figure III-4. Within the accuracy of this experiment, the range of acceptable values for Θ_m falls between $-30°$ and $+5°$. Very similar observations are made for other exit channels in which a projectile residue was detected in coincidence with two fission fragments. In all cases the
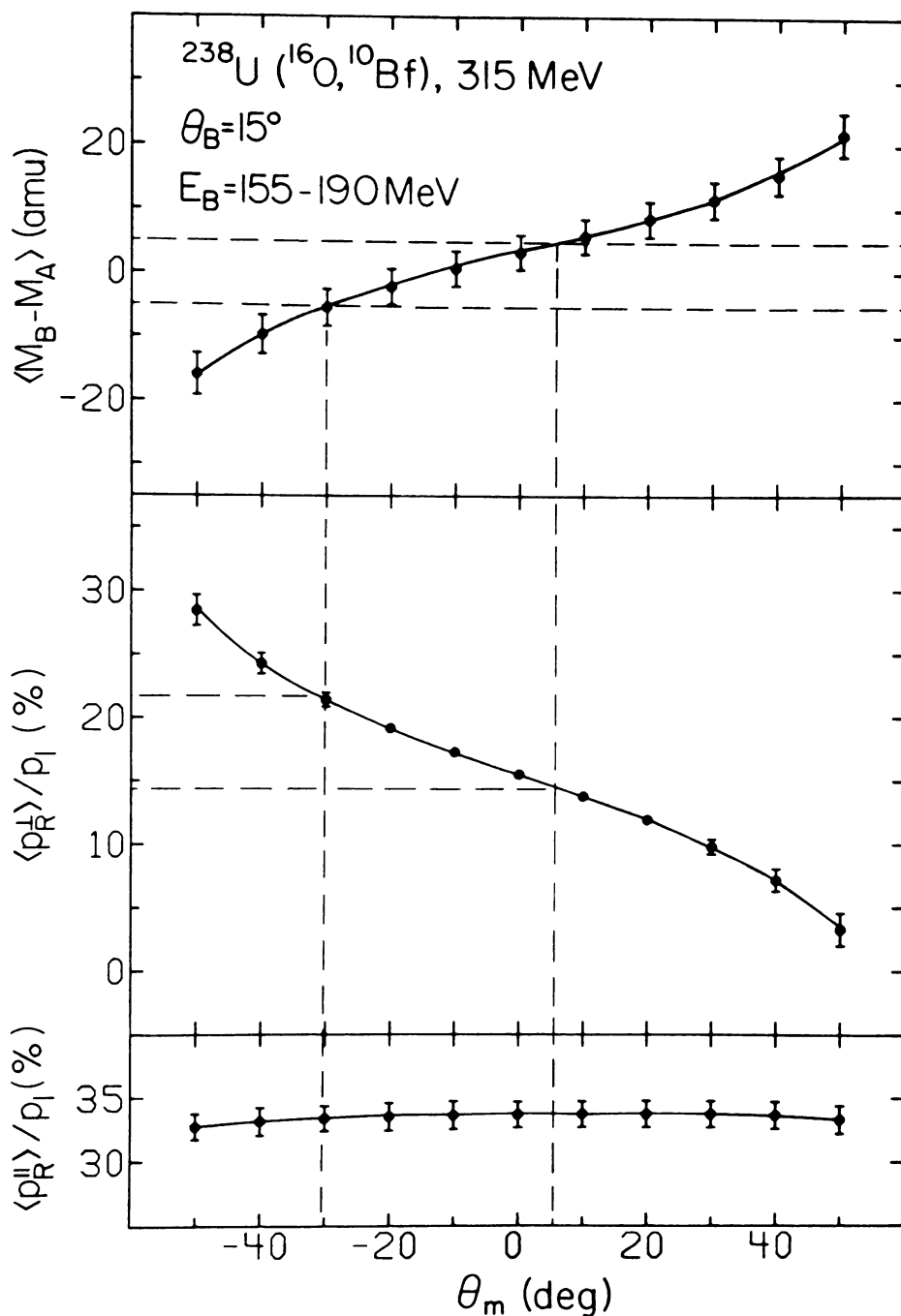
Figure III-4. The average mass difference $\langle M_B - M_A \rangle$ of fission fragments detected in the two fission counters, the average transverse momentum of the recoiling nucleus $\langle P_R^\perp \rangle$ and the average longitudinal recoil momentum $\langle P_R^\| \rangle$ are shown as a function of the assumed angle of emission of the missing mass. Note the extreme insensitivity of $\langle P_R^\| \rangle$ on Θ_m over the range of Θ_m, where approximate balance of fission fragment masses in the two detectors is achieved.

value $\Theta_m = 0$ was found to lie within the range of acceptable values of Θ_m, as deduced from the requirement $\langle M_B - M_A \rangle = 0$.

We have, therefore, proceeded by using $\Theta_m = 0$, i.e., Eq. (III-11), for the analysis of projectile residue - fission fragment coincidences. The uncertainties in the deduced momenta were estimated by varying the value of Θ_m in the range between $-30°$ and $+30°$.

The fission fragment folding-angle is defined as the angle of emission between two coincident fission fragments, $\Theta_{AB} = \Theta_A + \Theta_B$. The folding-angle is mainly determined by the projection, $P_R^{\parallel}$, of the target recoil momentum onto the beam axis. This is illustrated in Figure III-5 where the experimental data are shown in a two-dimensional contour plot of $P_R^{\parallel}$ versus Θ_{AB} for reactions in which a coincident projectile residue (Li,...,O) is observed. (For the calculation of $P_R^{\parallel}$, assumptions corresponding to Eqs. (III-10) and (III-11) have been made). For comparison, the expected average values of Θ_{AB} have been calculated (solid curves of Figure III-5) by computer simulation (Appendix B) for the fission decay of either ^{238}U or ^{254}Fm nuclei moving parallel to the beam axis. The average folding-angles are seen to be approximately linearly related to $P_R^{\parallel}$. The finite width of the distribution of folding-angles for a given recoil momentum is partially due to the distribution of fission momenta which results from the fission fragment mass distribution. The folding-angle
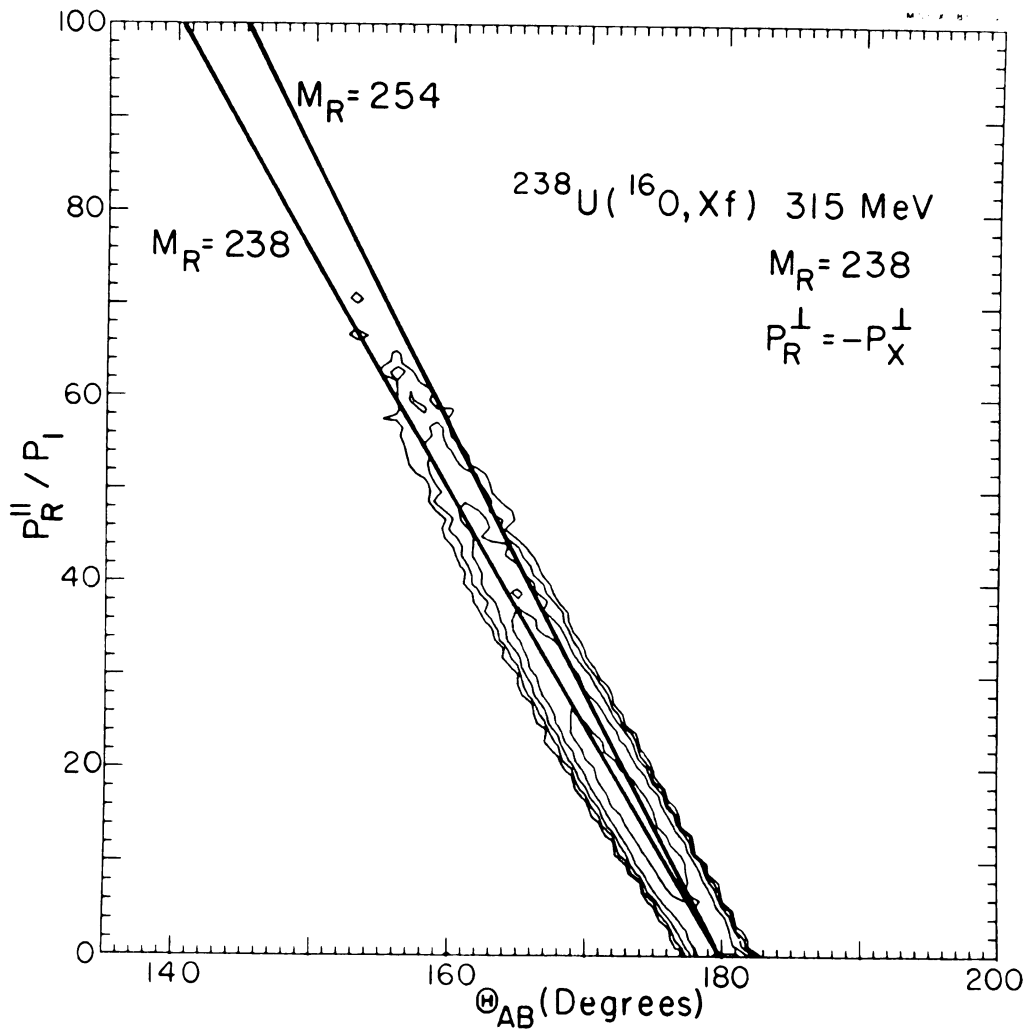
Figure III-5. Distribution of projectile residue - fission coincidence events in the $P_R^{\parallel}$ vs. Θ_{AB} plane. The assumptions of Eqs. (III-10) and (III-11) have been used for the analysis. The solid lines correspond to the calculated average quantities for the fission of ^{238}U and ^{254}Fm nuclei moving parallel to the beam axis.

distribution is also broadened as a result of neutron evaporation from the fission fragments.

The relatively small difference between the two calculated curves illustrates the small uncertainty that is introduced by the assumption of Eq. (III-10). The two curves are expected to provide limiting cases of the actual relationship between $P_R^{\|}$ and $<\Theta_{AB}>$. The curve for the fission of ^{254}Fm will be valid for the case of complete fusion of target and projectile and the ^{238}U curve will hold in the event that no mass is transferred to the target. Consequently, the curve for ^{238}U will be more realistic for small momentum transfers ($P_R^{\|}/P_1 \approx 0$) as in Figure III-5. On the other hand, the curve for ^{254}Fm will be more realistic for large momentum transfers ($P_R^{\|}/P_1 \approx 1$). This is illustrated in Figure III-6 where the calculated curves are compared with the $P_R^{\|}$ versus Θ_{AB} distribution of inclusive fission events. For the analysis of inclusive fission events and of events involving only a coincident light particle (p,d,t,α) the assumptions of Eqs. (III-10) and (III-11) have been replaced by the relations

$$P_R^{\perp} = 0 \qquad\qquad\qquad\qquad \text{(III-23a)}$$

$$M_R = M_1 + M_2 \qquad\qquad\qquad \text{(III-23b)}$$

These assumptions are in fact exact if a compound nucleus is formed. They are good for reactions involving large transfers of linear momentum and mass, but are poor for
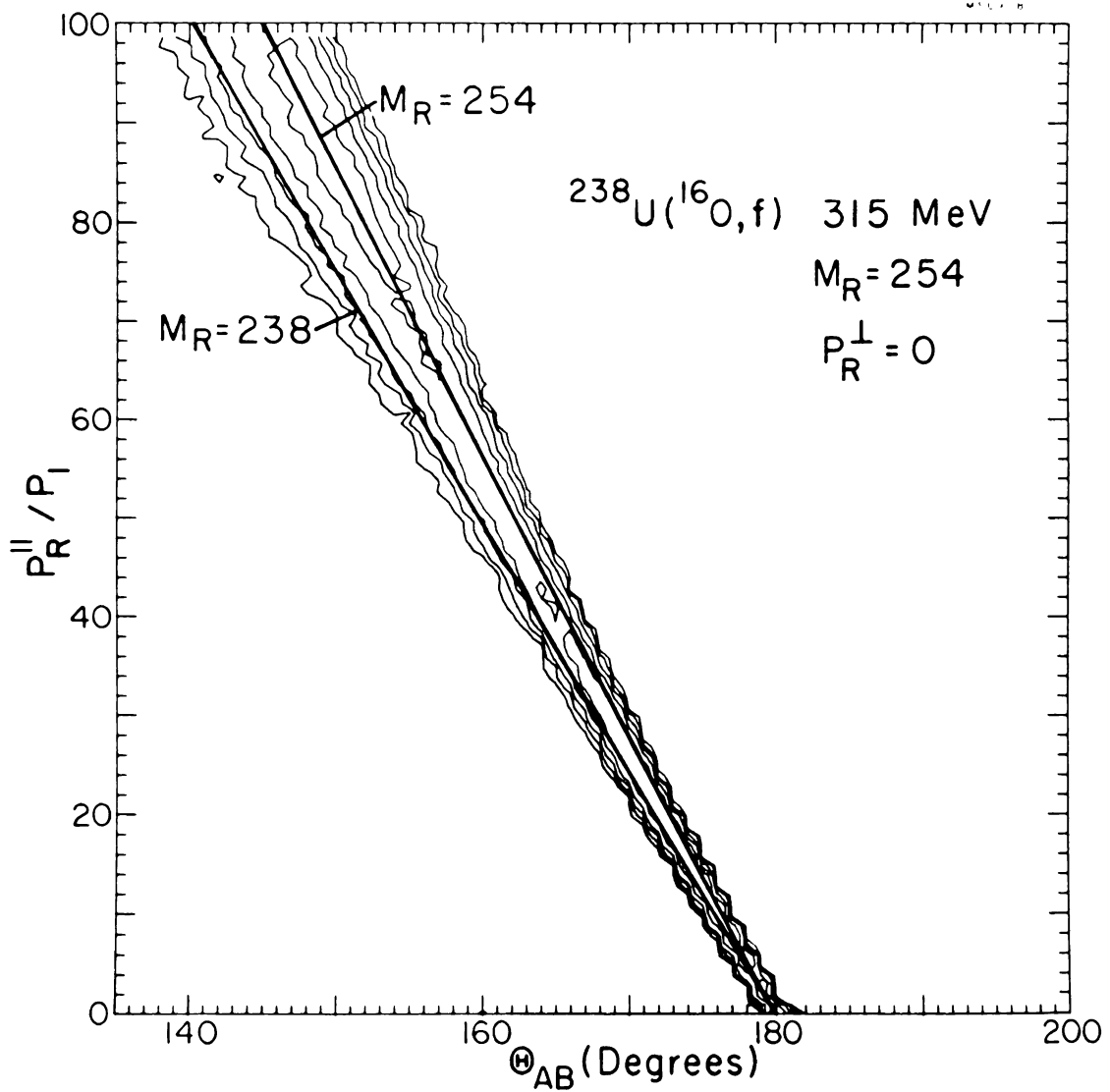
Figure III-6. Distribution of inclusive fission events in the $P_R^{\parallel}$ vs. Θ_{AB} plane. The assumptions of Eqs. (III-23a) and (III-23b) have been used for the analysis. The solid lines correspond to the calculated average quantities of ^{238}U and ^{254}Fm nuclei moving parallel to the beam axis.

peripheral reactions.

The results shown in Figures (III-5) and (III-6) illustrate that the simple measurement of the folding-angle between coincident fission fragments provides a good estimate of the mean momentum transferred to the target residue. In what follows in this study we shall use the solid curve corresponding to fission of ^{254}Fm to establish an approximate relationship between the measured value of Θ_{AB} and $<P_R^{\parallel}>$.

CHAPTER IV

PROJECTILE-LIKE FRAGMENT RESULTS

A. Projectile Residue Energy Spectra

Energy spectra of projectile-like fragments observed at 15° in coincidence with fission fragments are shown in Figure IV-1. These spectra were recorded close to the grazing angle of $\Theta_g \approx 19°$ and exhibit close similarities to inclusive spectra of projectile residues [Ge 78] observed at 15° in ^{16}O induced reactions on ^{208}Pb at 315 MeV. From this qualitative similarity we conclude that the requirement of a fission coincidence does not impose a serious kinematical bias on the spectra. Such a bias is only present in the ^{16}O spectrum which, of course, exhibits a sharp cut-off corresponding to the fission threshold of ^{238}U.

The energy spectra shown in Figure IV-1 have maxima which correspond to projectile residue velocities near to the beam velocity (marked by arrows). The widths of the energy spectra increase with decreasing atomic numbers of the outgoing projectile residues. These
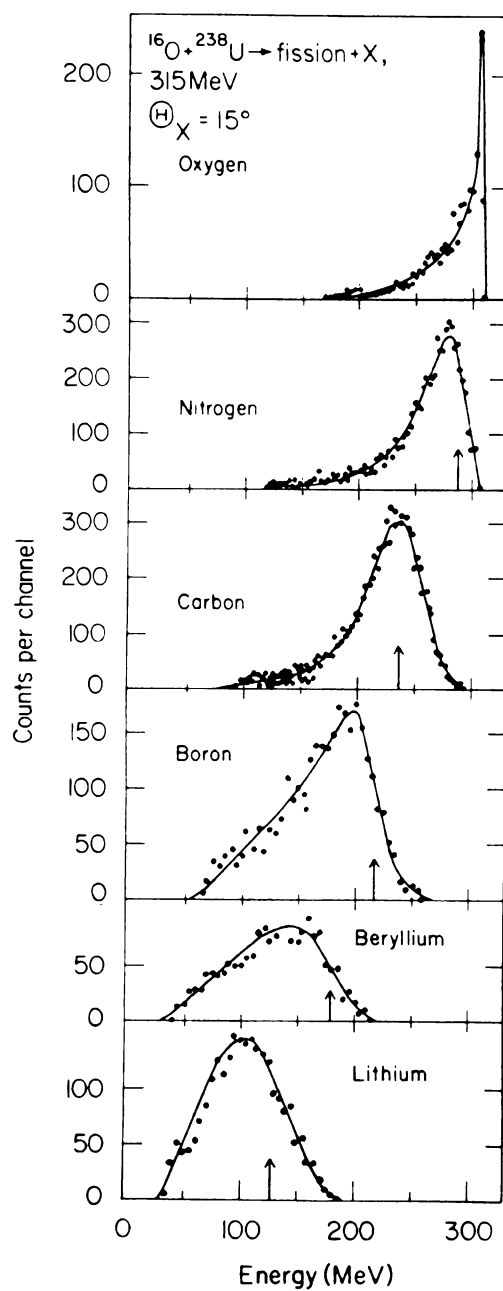
Figure IV-1. Laboratory energy spectra of projectile frag-
ments (Li - O) detected in the heavy ion tele-
scope at $\theta = 15°$, in coincidence with fission
fragments.

observations are similar to the ones for inclusive spectra
[Ge 78] which could be explained within the framework of a
simple model for projectile fragmentation. It has been
shown [Ge 77, Go 74] that the widths of these energy spectra
can either be explained in terms of the Fermi momenta of
the nucleons in the projectile if a fast breakup process is
assumed or they can be explained in terms of the thermal
kinetic energy of the nucleons in the projectile if the
reaction proceeds via the sequential decay of an excited
and completely thermalized projectile.

Such inclusive energy spectra have prompted explana-
tions in terms of several partially conflicting models
[Al 79, Ud 79, Mc 80] ranging from simple transfer reactions
to breakup processes. Recent measurements of light
particles in coincidence with projectile fragments
[Ha 77, Ho 77, Ge 77a, Ga 78, Bh 79, Ho 80] have sought to
limit the possible interpretations of these reactions.
Unfortunately, these experiments cannot distinguish
kinematically between sequential decay and projectile break-
up unless the final state is completely determined or unless
in- and out-of-plane angular correlations are obtained. As
a result, the interpretation of these experiments is often
model dependent [Bi 80, Yo 80]. Although such measurements
can provide detailed information, this is not necessarily
advantageous in the early stages of investigating the
reaction mechanism since focus might be placed on rather

uncharacteristic processes [Fr 81] due to the strong phase space selections which result simply from the placement of the detectors. Furthermore, from these measurements it is difficult to estimate the significance of processes with only a projectile fragment or only a light particle in the exit channel. From such investigations it has become apparent that the type of experiments required are those which will provide more detailed information than simple inclusive measurements and yet allow overall features of the reactions to be observed in a manner characteristic of an inclusive measurement.

B. Fission Fragment Folding-Angle Distributions

Several aspects of the reaction mechanism operating in reactions of $^{16}O + ^{238}U$ at 315 MeV are directly observable by studying the folding-angle distribution of fission fragments as illustrated in Figure IV-2. The folding-angle, Θ_{AB}, is defined as the angle of emission between the two fission fragments measured in the laboratory system. The upper scale of the figure gives the corresponding values of the recoil momentum $P_R^{\parallel}$ expressed in units of the beam momentum P_1. This scale has been calculated assuming fission of the compound nucleus ^{254}Fm and corresponds to the solid lines marked as ^{254}Fm in Figures III-5 and III-6. The mean folding-angle expected for fission of the compound nucleus ($P_R^{\parallel} = P_1$) is $\Theta_{AB} = 144.4°$. The folding-angle
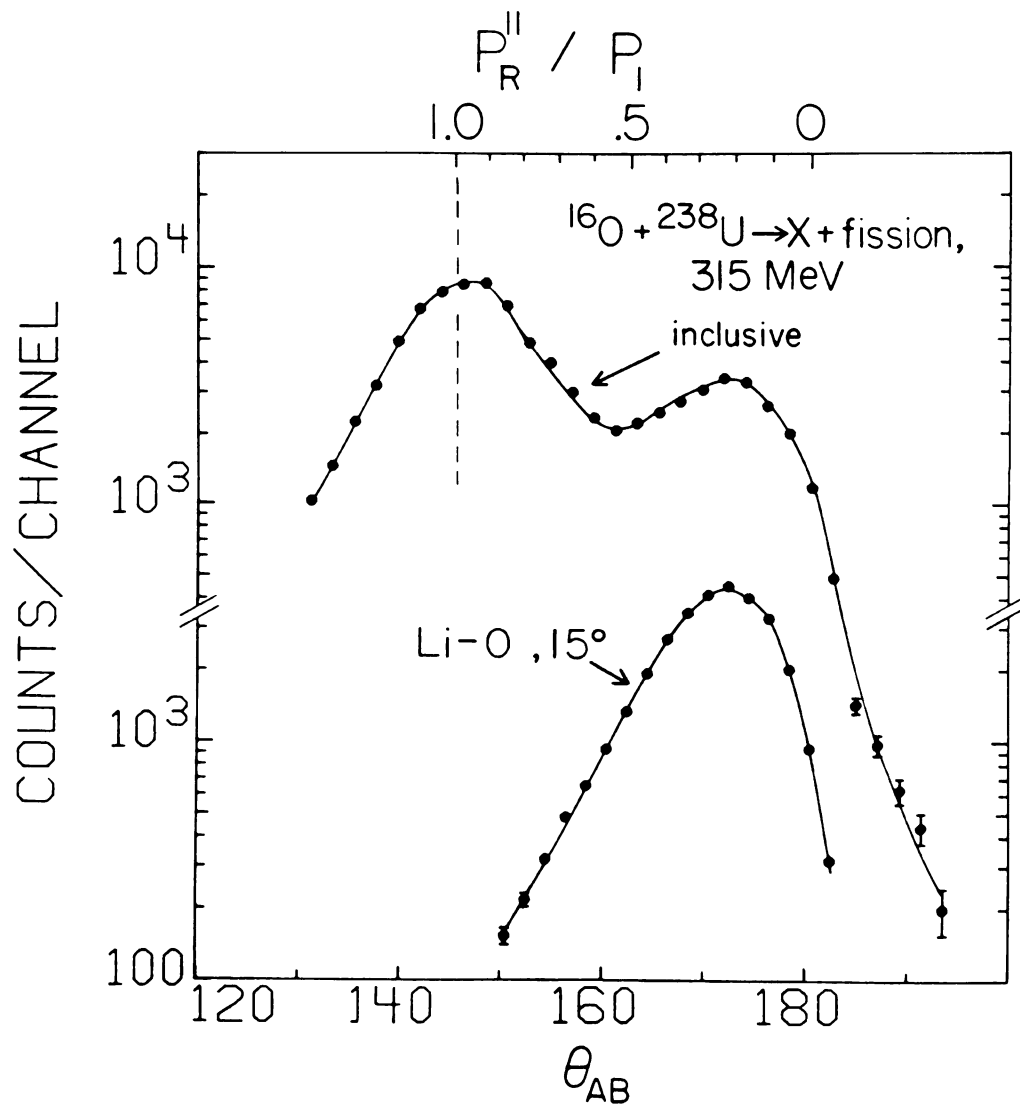
Figure IV-2.   Folding-angle distributions of fission frag-
ments measured inclusively (top) and in coin-
cidence with projectile residues (Li - O) in
the heavy ion telescope at $\theta = 15°$.   The
momentum scale at the top of the figure
corresponds to the solid curve of Figures
III-5 and III-6.

distribution for inclusive fission events exhibits two
clearly separated components. The strongest component
centered at $\Theta_{AB} = 148°$ corresponds to $\sim 92\%$ of the beam
momentum being transferred to the fissioning system. At
incident energies of 140 MeV for the same system this
component of the folding-angle distribution is centered at
$\sim 100\%$ of the full momentum transfer limit (see Appendix A).
This shift away from full momentum transfer with increasing
energy suggests the increasing importance of processes
such as "incomplete fusion" [Si 79a] and "massive transfer"
[Ya 79] in which a portion of the projectile escapes the
fusion process. (This observation raises doubt about the
method of calculating the fusion cross section by measuring
evaporation residues since an incomplete fusion product is
indistinguishable from an evaporation residue unless the
accompanying light particle distributions are measured).
The deviation from complete fusion has recently been
observed to become even more pronounced at higher energies
[Sa 81]. We shall associate this component of the folding-
angle distribution with "central" collisions corresponding
to a large overlap of target and projectile.

The second component in the folding-angle distribu-
tion, centered around $\Theta_{AB} \simeq 173°$, we attribute to
"peripheral" reactions in which the major part of the
projectile momentum is carried off by heavy projectile
residues emitted at small angles [Ge 78]. The minimum in

the folding-angle distribution reflects the fact that, for
peripheral reactions, the largest cross sections are
observed for nitrogen and carbon fragments and larger mass
transfers are less likely. This is seen in Figure IV-3 in
which folding-angle distributions measured in coincidence
with projectile-like fragments (Li,Be,B,C,N,O) at 15° are
shown. With decreasing mass of the outgoing projectile
residue the folding-angle distributions have maxima at
angles further from $\Theta_{AB} = 180°$. This is expected from
simple momentum conservation requirements if a sizeable
fraction of the momentum lost by the projectile is
transferred to the target. This observation immediately
rules out an extreme participant-spectator model in which
the projectile fragments after minimal interaction with the
target.

In the following section a more detailed analysis of
the data shows that the momentum carried off by the
projectile-like fragment is not sufficient, however, to
account for the difference between the beam momentum and
the recoil momentum of the fissioning system. This
"missing momentum" is very likely carried off by light
particles emitted into the forward direction. Possible
evidence for such an interpretation is given in Figure IV-4
where the folding-angle distributions observed in
coincidence with light charged particles (p,d,t,α) at
$\Theta = 14°$ are shown. For reference the inclusive distribution
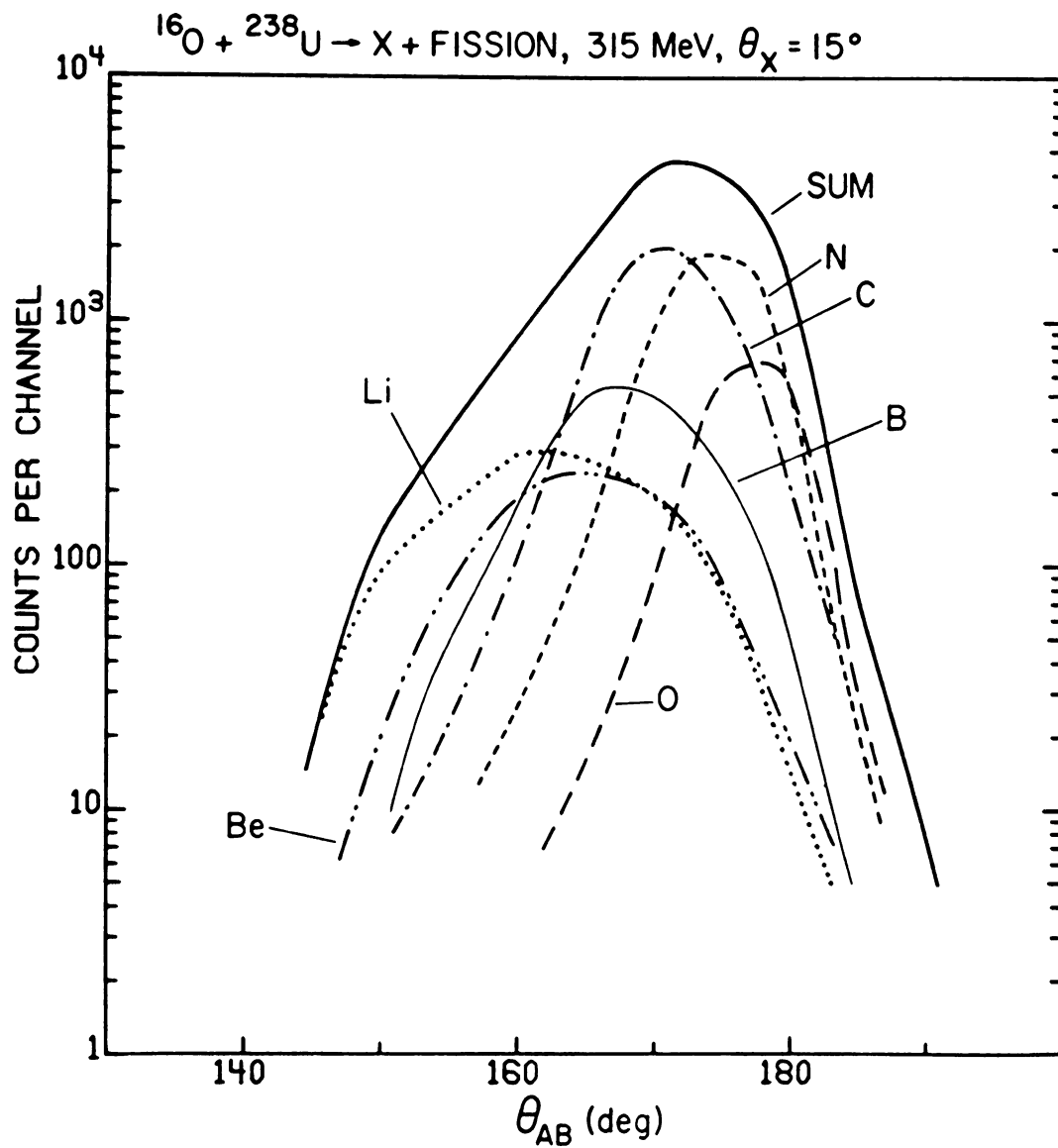
Figure IV-3. Folding-angle distributions of fission frag-
ments measured in coincidence with projectile
residues (Li,Be,B,C,N,O) in the θ = 15° heavy
ion telescope. The sum over all products
from Li to O is shown as a solid line.

65
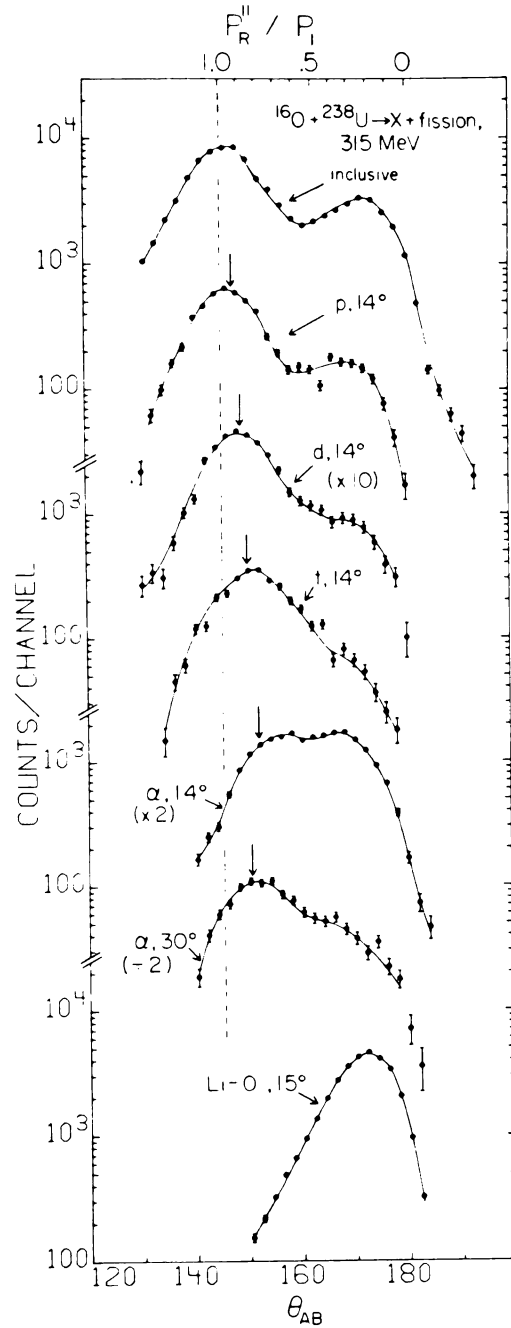
Figure IV-4. Folding-angle distributions of fission frag-
ments measured inclusively (top), in coin-
cidence with protons, deuterons, tritons, and
α-particles in the Θ = 14° Si-NaI telescope,
in coincidence with α-particles in the
Θ = 30° in-plane telescope and in coincidence
with heavy projectile residues (Li - O) in the
heavy ion telescope at Θ = 15°. The momentum
scale at the top of the figure corresponds to
the solid curve of Figures III-5 and III-6.

and the distribution measured in coincidence with
projectile-like fragments are also shown. Light particles
are seen to be emitted at forward angles in events with
momentum transfers ($\Theta_{AB} \sim 170°$) similar to the ones in
which a projectile residue is observed. More intriguing
is the observation that most of the p,d, and t's near the
grazing angle result from processes with large momentum
transfers ($\Theta_{AB} \sim 150°$) which cannot be interpreted as
projectile breakup or sequential decay reactions. This
result was investigated further in the second experiment
where only light particles were detected in coincidence
with fission fragments and will be discussed in detail in
Chapter V. (The arrows in Figure IV-4 are discussed in
Section V.A).

C. Kinematical Analysis

1. Missing Momentum Distributions

A more detailed description of the reaction mechanism
can be obtained by performing an event by event recon-
struction of the kinematics of the reaction using the
method described in Section III.C. This type of analysis
has been applied to reactions in which a projectile-like
fragment (Li,...,0) was detected at $\Theta = 15°$ in coincidence
with both fission fragments. Through this analysis it is
possible to obtain momentum distributions of the

unobserved particles and mass distributions of the fission fragments.

Missing momentum distributions are shown in Figures IV-5, IV-6, IV-7, and IV-8 for various projectile residues and cuts in the energy spectra. The missing momentum distribution for the highest energy cut on inelastically scattered ^{16}O ions is centered around zero since only pure inelastic scattering (followed by fission) is energetically possible. However, the missing momentum distributions for the two lowest energies of the scattered ^{16}O-ions show a clear shift away from zero missing momentum. Similar trends are observed for lighter projectile fragments as illustrated in Figures IV-6, IV-7, and IV-8. Arrows in the figures represent the missing momentum expected for quasi-elastic projectile break-up reactions in which the projectile breaks up into two or more fragments which all continue with the beam velocity. The missing momentum distributions are peaked between the pure two-body reaction limit $\langle P_m^{\parallel} \rangle = 0$ and the quasi-elastic projectile break-up limit $\langle P_m^{\parallel} \rangle = \dfrac{M_1 - M_3}{M_1} P_1$. The rather narrow widths of the $P_m^{\parallel}$ distribution indicate that the main reaction mechanism is not simply a superposition of simple transfer reactions and quasi-elastic break-up reactions.
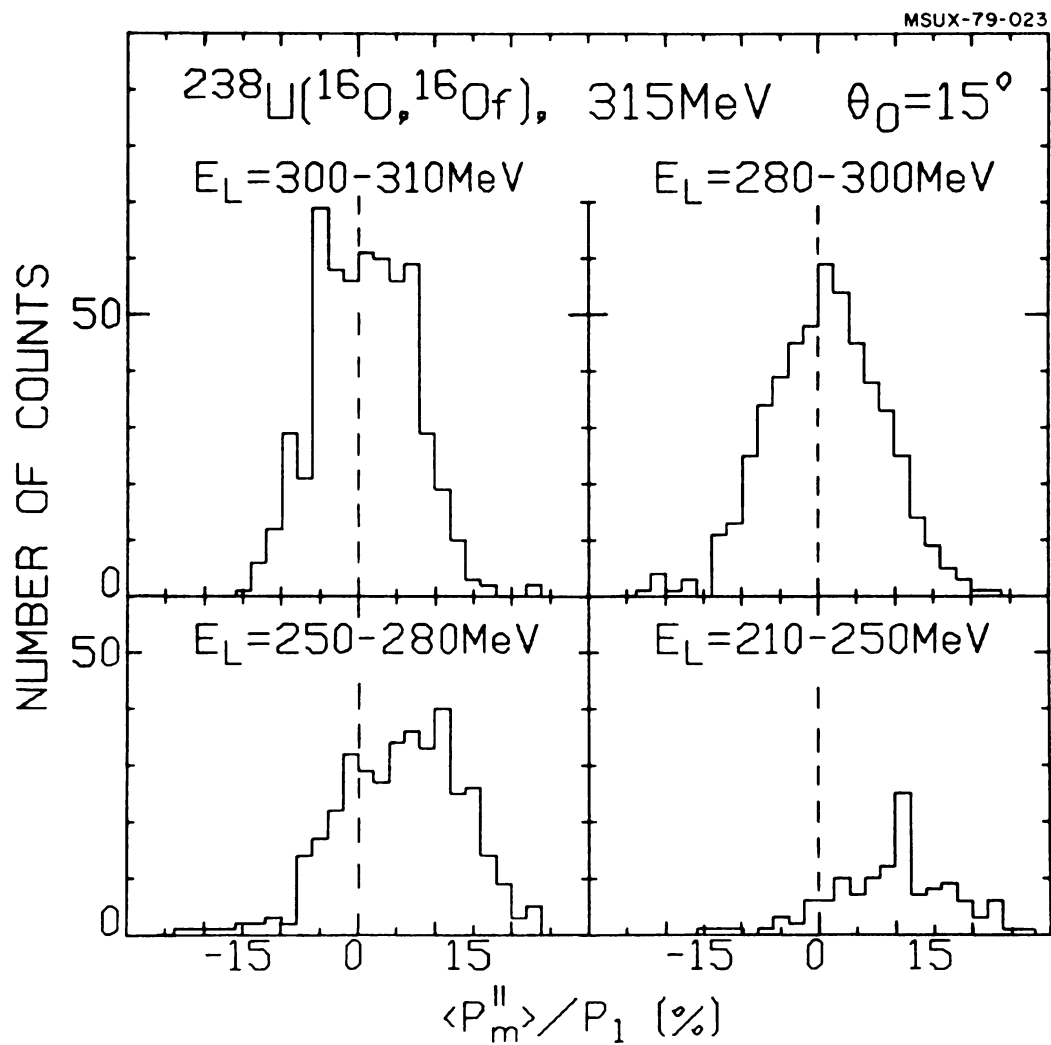
Figure IV-5. Missing momentum distributions for 4 different gates on the laboratory energy of outgoing ^{16}O ions. $\langle P_m^{\parallel} \rangle$ is positive in the beam direction.
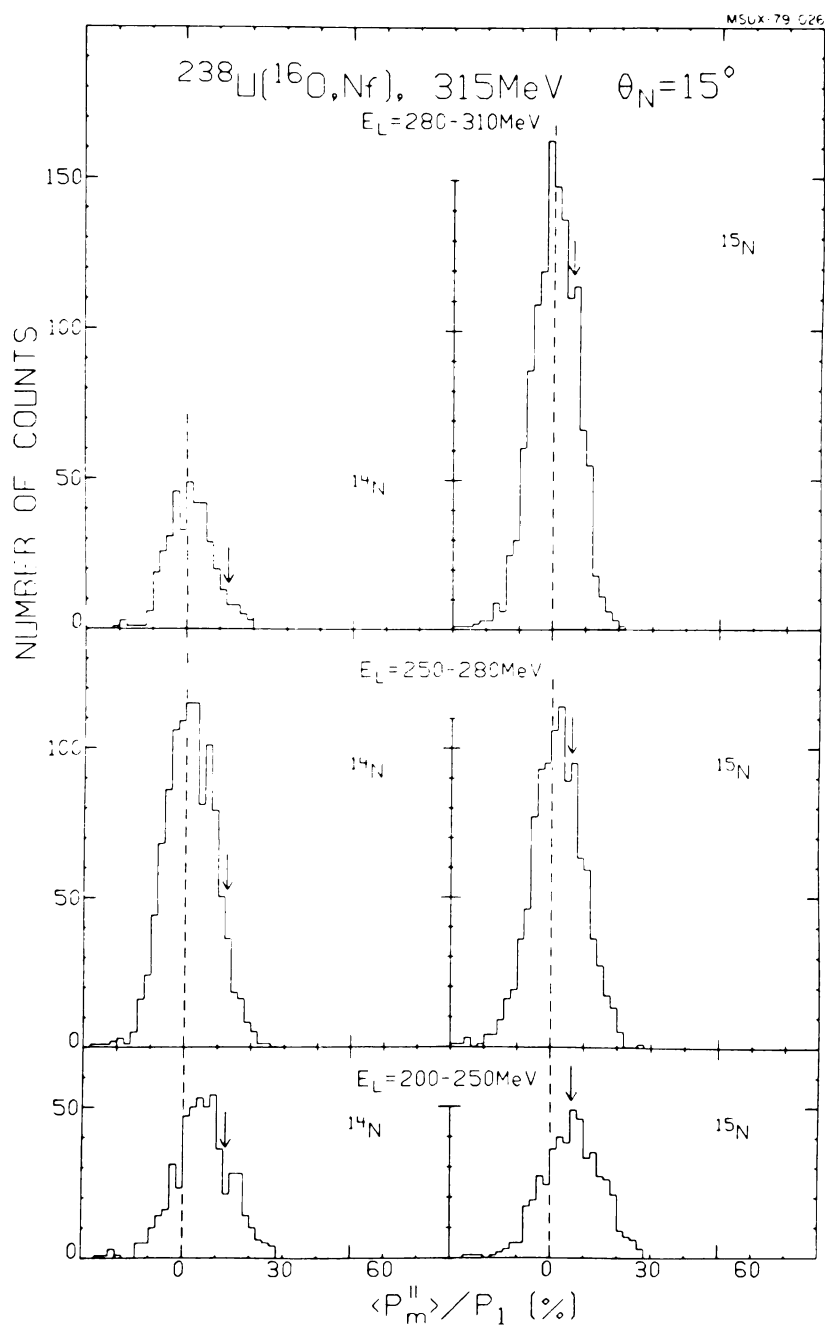
Figure IV-6. Missing momentum distributions for 3 different gates on the laboratory energy of ^{14}N and ^{15}N projectile residues. $\langle P_m^{\parallel}\rangle$ is positive in the beam direction.
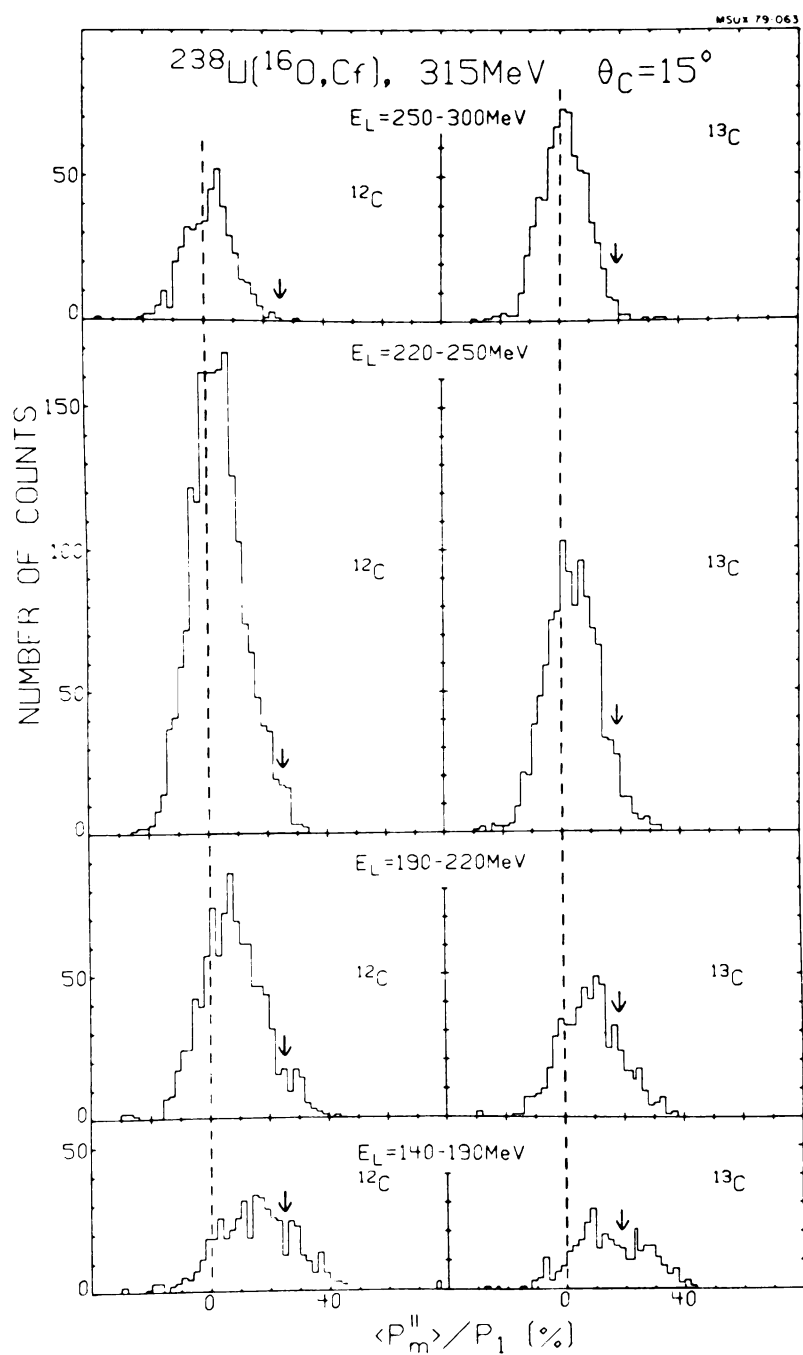
Figure IV-7. Missing momentum distributions for 4 different gates on the laboratory energy of ^{12}C and ^{13}C projectile residues. $\langle P_m^{\parallel} \rangle$ is positive in the beam direction.
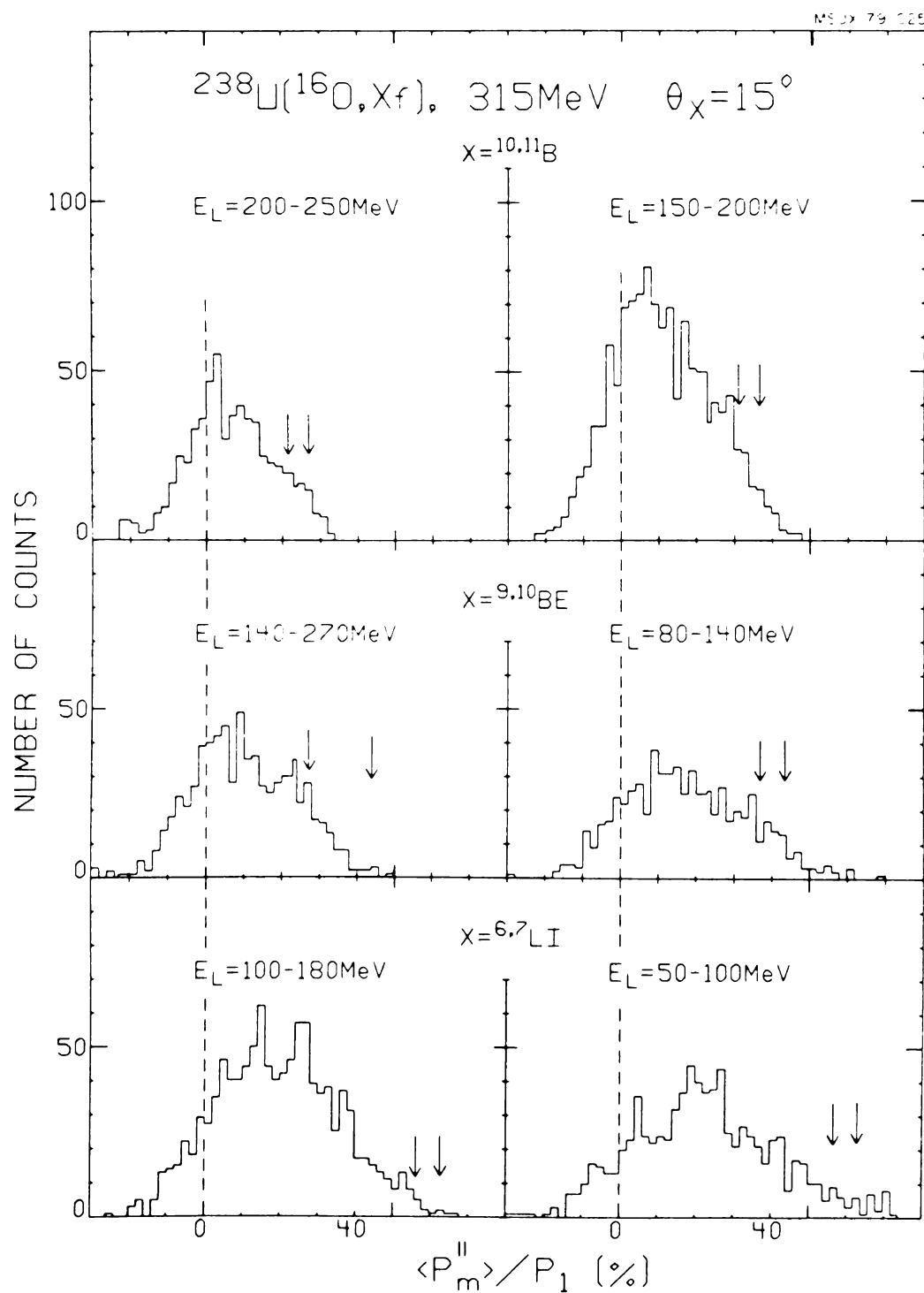
Figure IV-8. Missing momentum distributions for 2 different gates on the laboratory energy of $^{10,11}B$, $^{9,10}Be$ and $^{6,7}Li$ projectile residues. $\langle P_m^{||} \rangle$ is positive in the beam direction.

2. Systematics of Momentum Transfer

The systematics of the average missing momentum as a function of the energy of the projectile residue are shown in Figure IV-9. The data points are scattered around a line with a negative slope of $\langle P_m^{\parallel}\rangle/P_1\langle E_3\rangle = 1.0 \times 10^{-3}$ MeV^{-1}. The missing momentum increases with increasing energy loss of the projectile residue. Such a behavior is consistent with any mechanism that associates the energy loss with the emission of light particles into the forward direction. In particular, the sequential decay of the projectile residue by light particle emission would be consistent with the trends observed in Figure IV-9. In this case, larger energy losses would be associated with higher excitation energies of the projectile residue which would lead to the emission of a higher multiplicity of light particles.

The dependence of the average value of the recoil momentum $\langle P_R^{\parallel}\rangle$ on the average momentum of the projectile residue $\langle P_3^{\parallel}\rangle$ is shown in Figure IV-10. For a pure two-body reaction (followed by fission of the target residue) one has: $P_1 = P_R^{\parallel} + P_3^{\parallel}$. For orientation, this limit is shown by the solid line in the figure. The data clearly rule out this limit as was already obvious from Figures IV-5, IV-6, IV-7, and IV-8. The extreme limit of quasi-elastic projectile breakup, where the target nucleus acts as a mere spectator, corresponds to negligibly small values of $P_R^{\parallel}$, similar to the ones observed for inelastic
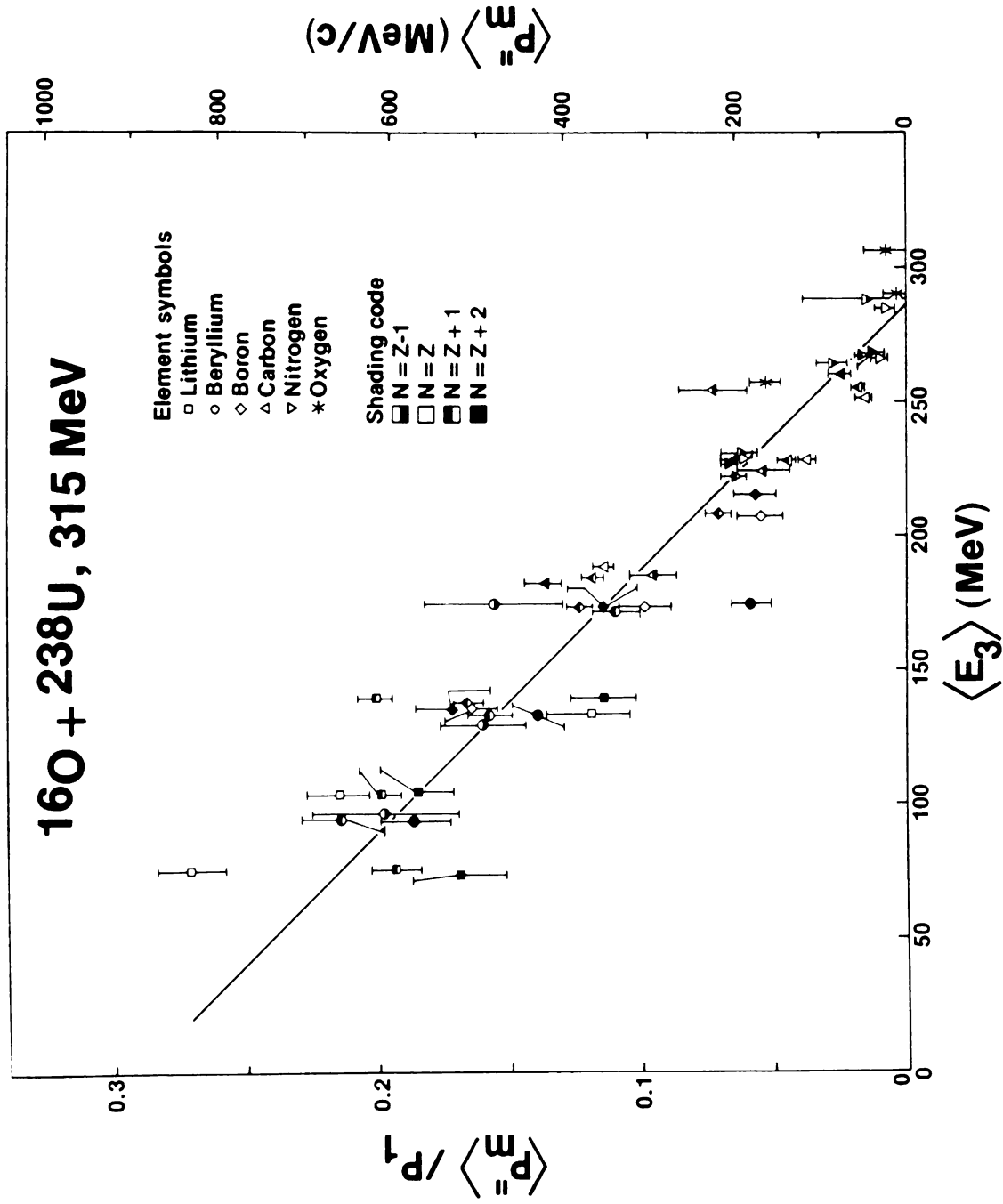
Figure IV-9. Dependence of the average missing momentum on the laboratory energy of the projectile residue.
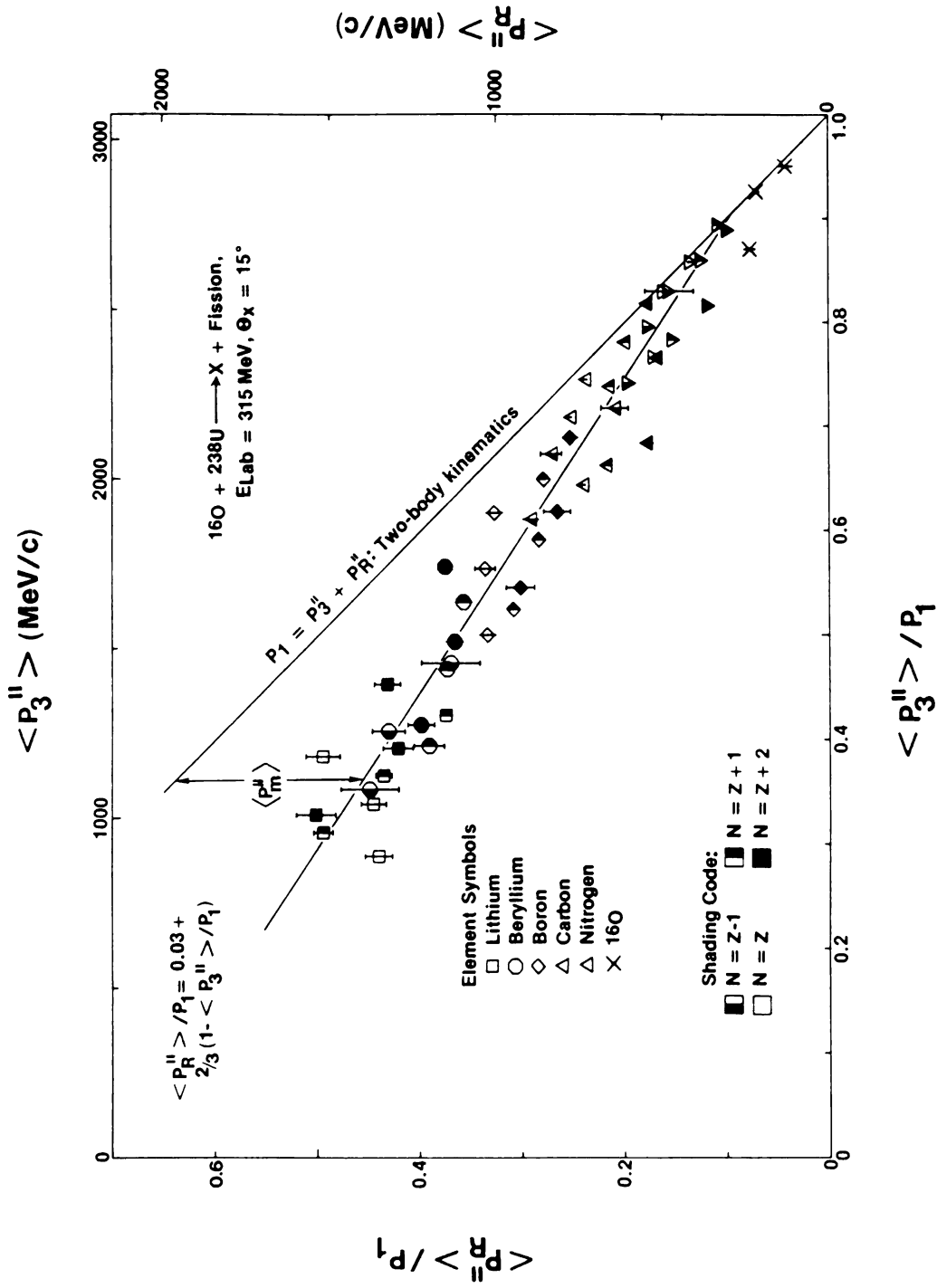
Figure IV-10. Dependence of the average parallel component of the recoil momentum on the average parallel component of the momentum of the projectile residue. The limit expected for pure two-body reactions is indicated and the average missing momentum can be derived as the distance from this line to the data points.

scattering. This interpretation was consistent with the single particle inclusive spectra [Ge 77], but it is not consistent with the rather large values of $P_R^\parallel$ observed here. The reaction, instead, involves significant interaction between projectile and target. Therefore, our results cannot support the participant-spectator model [We 76] at incident energies of E/A = 20 MeV. Similar conclusions have been reached in recent measurements [Eg 81] of the momentum widths of projectile residues in the reaction $^{20}Ne + ^{197}Au$. However, this study concentrated on the ^{16}O exit channel which may be strongly influenced by the α-cluster nature of the projectile. Other recent results [Na 81a] suggest that the pure fragmentation model is still valid at energies as low as E/A = 43 MeV. Further coincidence investigations at these energies will be necessary to determine whether the momentum transfer to the target residue is in fact small, as suggested by the extreme participant-spectator model, or whether it is rather large as we have shown for reactions at E/A = 20 MeV.

3. Fission Fragment Mass Distributions

An estimate of the excitation energy of the fissioning system can be obtained from the mass distribution of fission fragments. The mass distributions measured in coincidence with the projectile residues Li,...,O are shown in Figures IV-11, IV-12, IV-13 and IV-14 for several regions of the outgoing particle energies. For the high
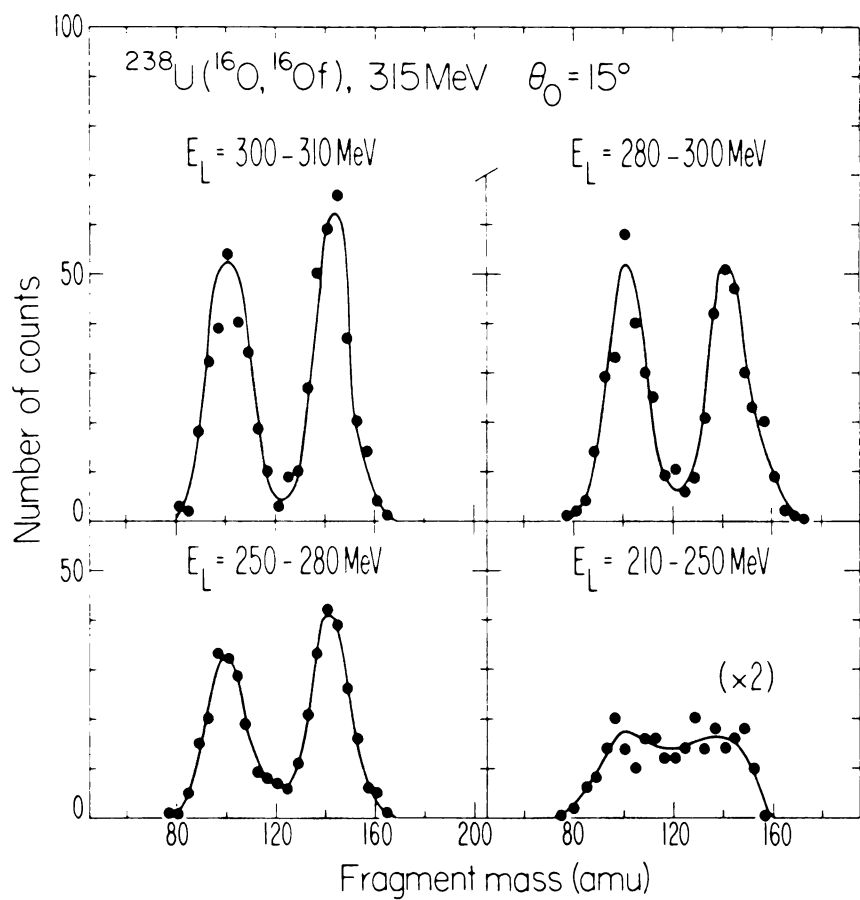
Figure IV-11. Mass distributions of fission fragments for 4 different gates on the [16]O laboratory energy.
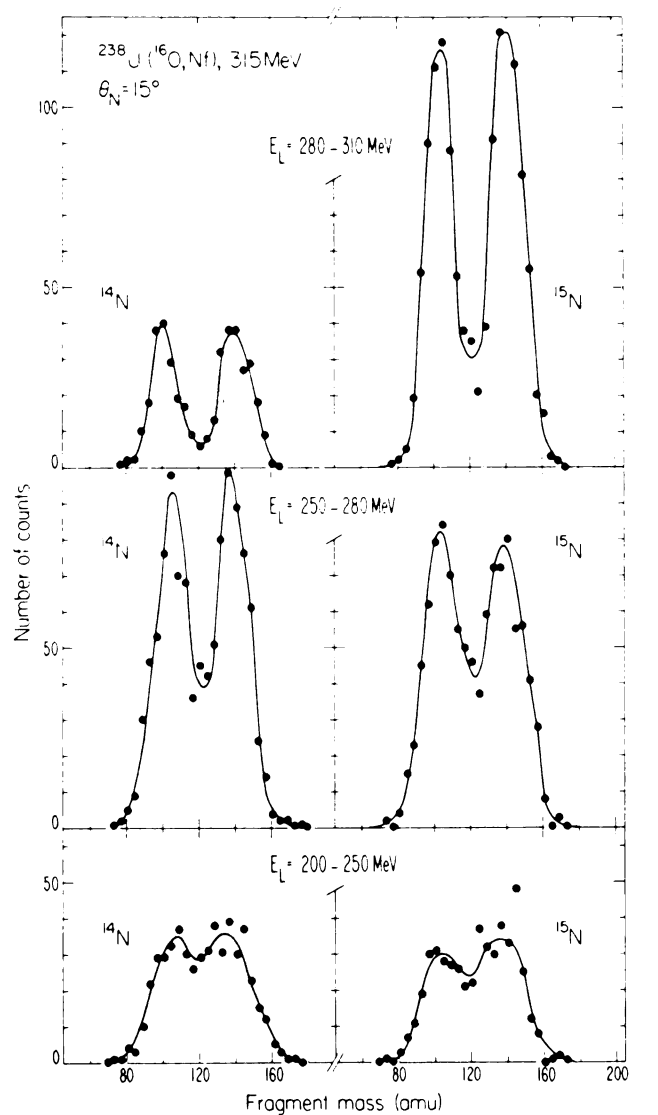
Figure IV-12. Mass distributions of fission fragments for 3 different gates on the ^{14}N and ^{15}N laboratory energy.
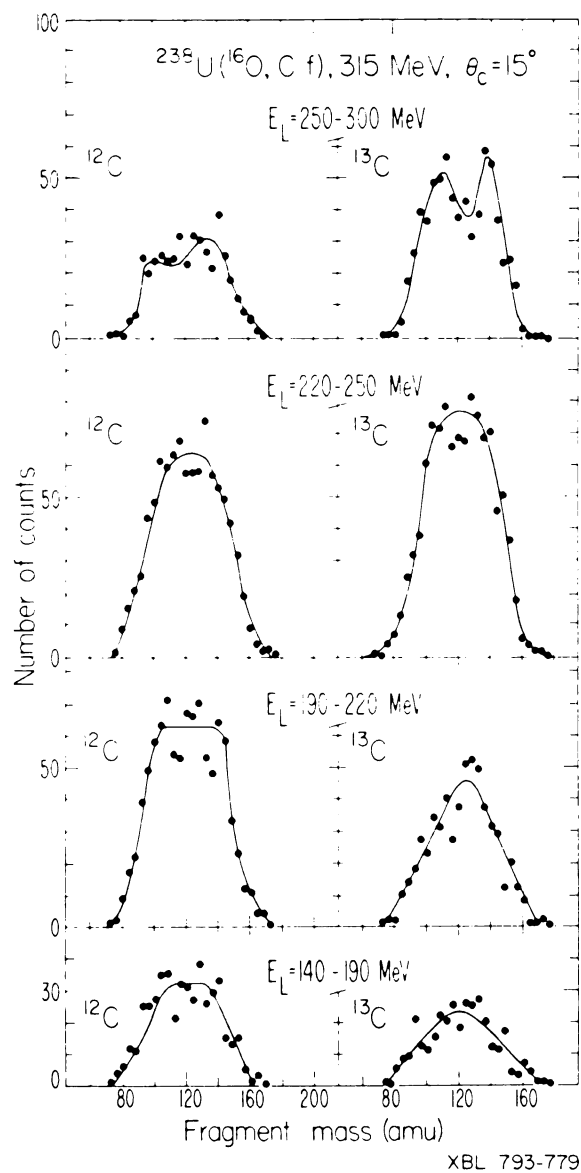
Figure IV-13. Mass distributions of fission fragments for 4 different gates on the ^{12}C and ^{13}C laboratory energy.
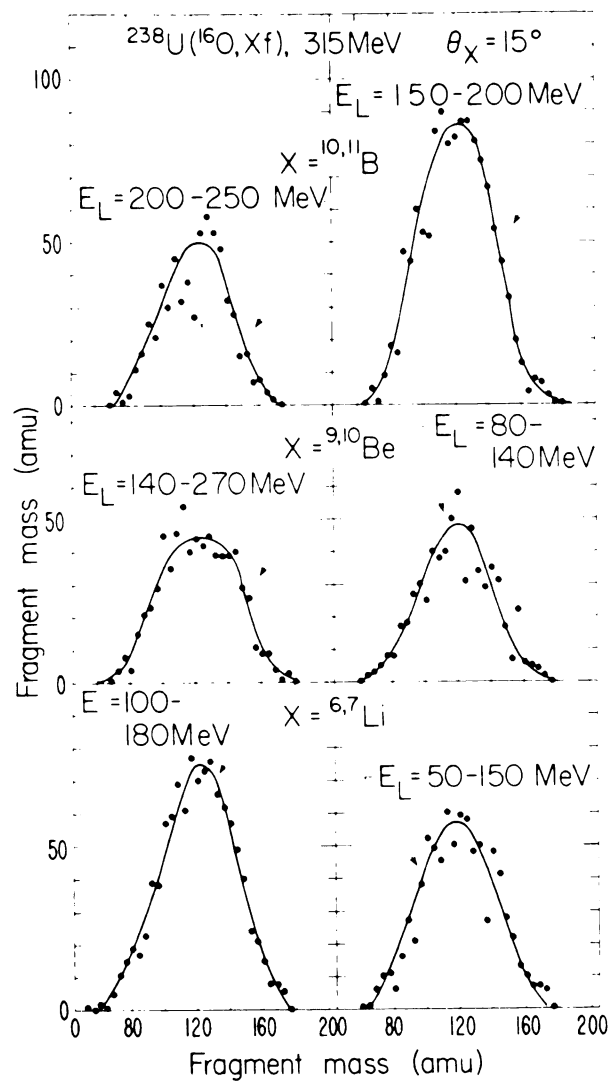
Figure IV-14. Mass distributions of fission fragments for two different gates on the laboratory energy of 10,11B, 9,10Be and 6,7Li projectile residues.

kinetic energy region of the oxygen and nitrogen spectra we observe very asymmetric mass distributions, with large (>20) peak-to-valley ratios. Such asymmetric mass distributions are typical for the fission of actinide nuclei at relatively low excitation energies. The valley corresponding to symmetric fission (the mass of the fissioning nucleus was assumed to be $M_R = 238$ in this analysis) is seen to fill in for increasing energy losses. This indicates that fission takes place from a more highly excited nucleus. One can put this qualitative observation on a more quantitative basis by comparing the peak-to-valley ratios of these asymmetric mass distributions with the ones observed in reactions where the excitation of the fissioning nucleus is known, and thus obtain an estimate of the excitation energy for each ejectile energy bin. This provides one of the few direct measurements of the target excitation energy. The results of such a comparison with mass distributions obtained in measurements of fission following compound nucleus formation in the α-bombardment of a ^{238}U target [Co 61] (see Figure IV-15) are presented in Table IV-1.

For the smallest energy losses, as observed for high energy oxygen and nitrogen nuclei, the target residue excitation energy, which is deduced from the fission fragment mass distributions, is slightly larger than allowed even for a two-body reaction. The reason for this is the
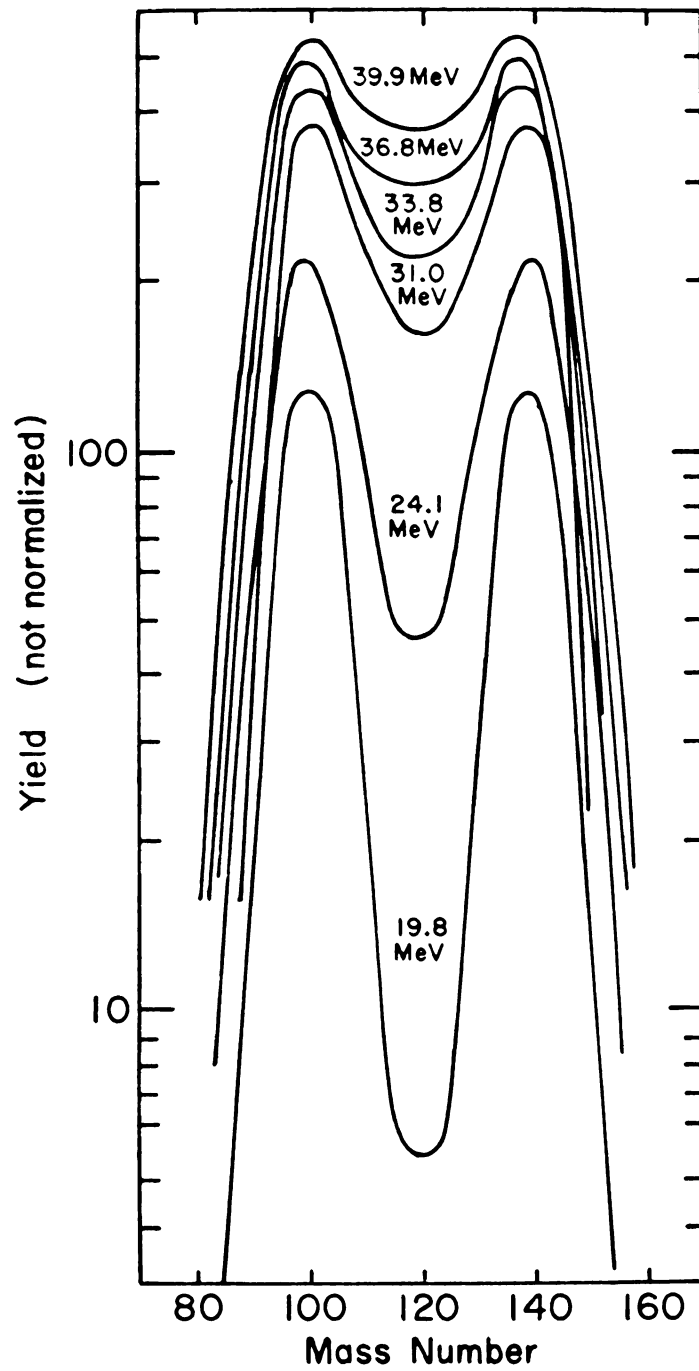
Figure IV-15. Fission fragment mass distributions for α-induced fission of ^{238}U at projectile energies indicated in the figure. The data are taken from Colby et. al. [Co 61].

Table IV-1. Estimates of excitation energy of the
fissioning nucleus.

Ejectile	E_3 (MeV)	$<E^*(E_3)>$[a] (MeV)	$<E^*(P/V)>$[b] (MeV)
^{16}O	300-310	7.4	14
	280-300	22.2	16
	250-280	46.6	18
	210-250	78.7	35
^{15}N	280-310	16.5	20
	250-280	39.0	28
	200-250	75.3	33
^{14}N	280-310	14.0	17
	250-280	34.3	25
	200-250	67.7	35
^{13}C	250-300	38.7	33

[a] Average excitation energy of the fissioning system
estimated from the ejectile energy assuming two-body
kinematics.

[b] Average excitation energy of the fissioning system
estimated from the peak/valley ratio of the mass
distribution when compared to $\alpha + ^{238}U$ data of Colby et. al.
[Co 61].

relatively poor energy resolution of the position sensitive
fission detectors, which fills in the valley between the
two mass peaks. However, for larger energy losses of the
outgoing projectile residues the fission fragment mass
distributions observed experimentally are more asymmetric
than expected from an estimate of the excitation energy on
the basis of two-body kinematics. In fact, the assumption
of two-body kinematics can lead to a significant over-
estimate of the target residue excitation energy. On the
other hand, it is also clear that the amount of excitation
energy deposited in the target residue is by no means
negligible. This corroborates the conclusion drawn from
the large momentum transfers to the target residue that
inelastic interactions with the target are an important
aspect of the reaction mechanism. Quasi-elastic breakup
is not the dominant reaction mechanism. Similar con-
clusions had been drawn [Ge 77a] from the measurement of
alpha-particle projectile residue coincidences. The
analysis of that experiment, however, had to rely on the
validity of three-body kinematics in order to deduce the
excitation energy of the target residue.

CHAPTER V

LIGHT PARTICLE RESULTS

A.   Fission Fragment Folding-Angle Distributions

1.   Inclusive Folding-Angle Distributions

The fission fragment folding-angle, Θ_{AB}, is defined as the angle of emission between two coincident fission fragments measured in the laboratory system. The distribution of folding-angles measured for inclusive fission events is shown in Figure V-1. The distributions are shown for the two experimental geometries of the light particle coincidence experiment and also for the geometry of the projectile-like fragment experiment $(\Theta_B^0 = -\Theta_A^0 = 80°)$. The inclusive distributions exhibit two clearly distinct components. As discussed in Section IV.B, the strongest component centered in the region of $\Theta_{AB} \sim 150°$ corresponds to large recoil momenta and is therefore associated with "central" collisions. The location of this maximum shifts with fission detector geometry in exactly the manner predicted by computer simulation. This is shown in Figure V-2 where the average values of Θ_{AB} have been
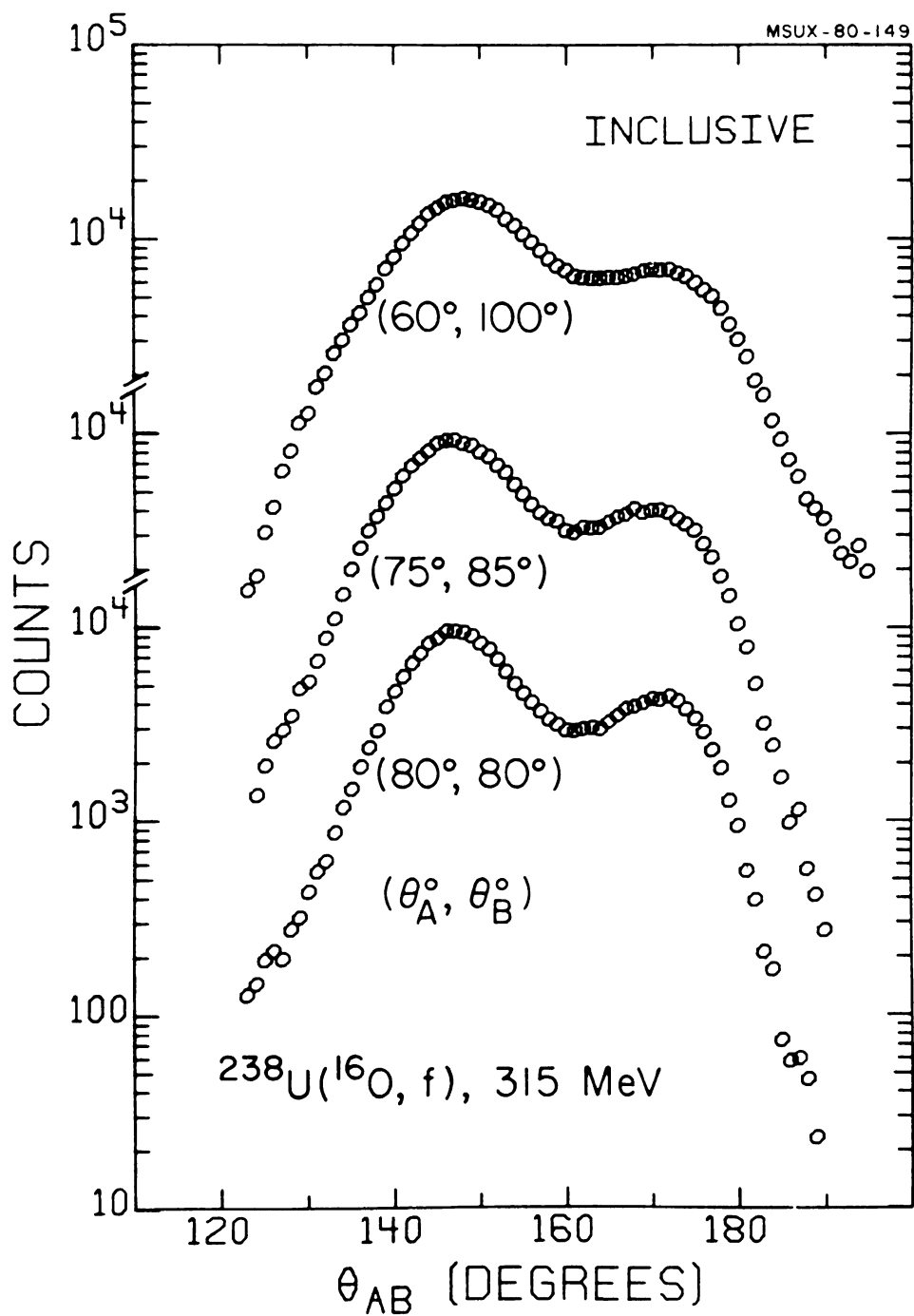
Figure V-1. Folding-angle distributions of fission frag-
ments measured inclusively for the experimental
geometries of this study ($\theta_A^o = 60°$, $\theta_B^o = 100°$;
$\theta_A^o = 75°$, $\theta_B^o = 85°$; and $\theta_A^o = \theta_B^o = 80°$).

MSUX-80-515
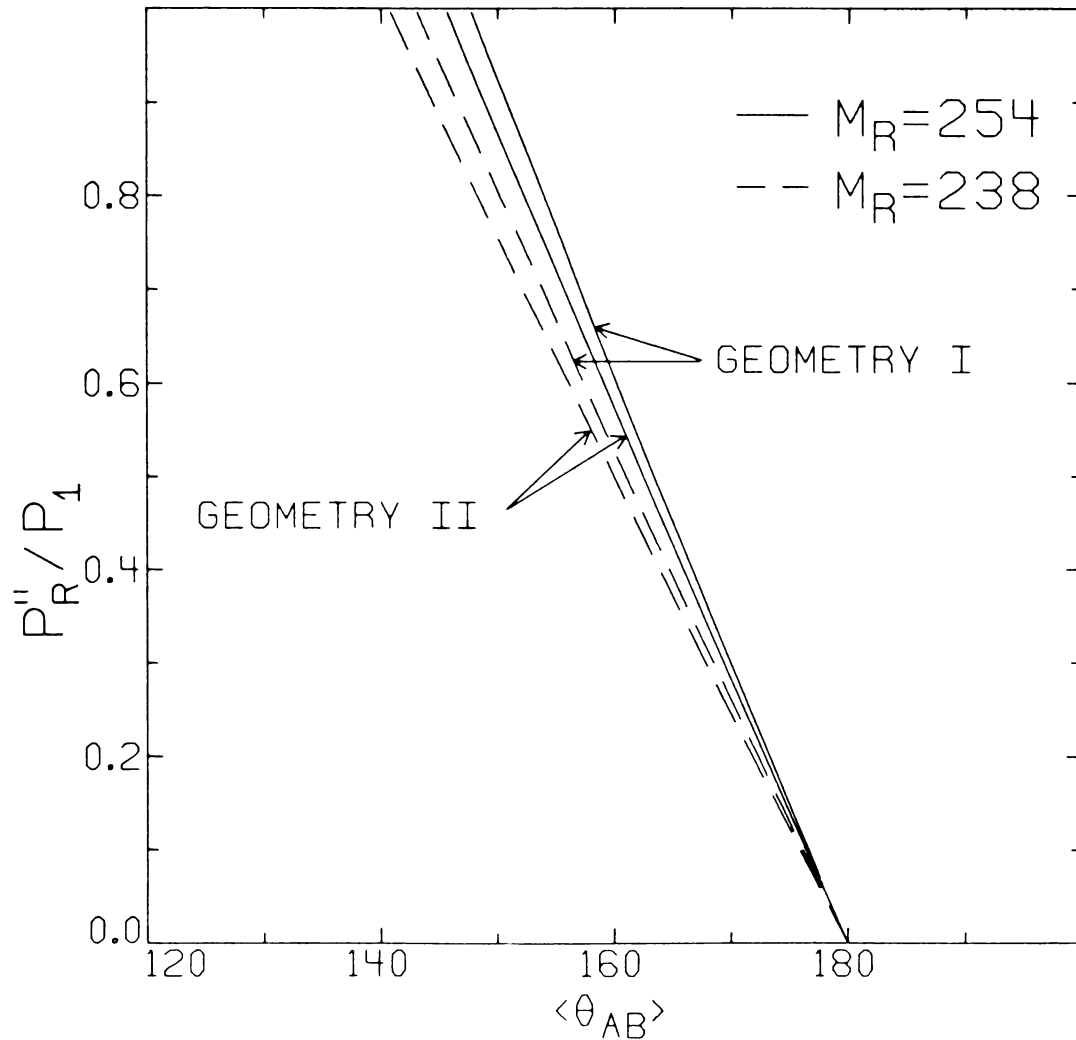
Figure V-2.   Dependence of the average folding-angle Θ_{AB} on $P_R^{\parallel}$ as calculated from the simulated fission of ^{238}U and ^{254}Fm nuclei moving parallel to the beam axis.   The relationship is shown for experimental geometries I and II.   (P_1 is the beam momentum).

calculated for geometry I ($\Theta_A^o = -60°$, $\Theta_B^o = 100°$) and geometry II ($\Theta_A^o = -75°$, $\Theta_B^o = 85°$) by simulation of the fission of either ^{238}U or ^{254}Fm nuclei moving parallel to the beam axis. (These calculations are analogous to those shown in Figures III-5 and III-6 for the geometry $\Theta_B^o = -\Theta_A^o = 80°$). It is seen from the calculation that, exactly as observed, a shift of approximately 2° is expected in the region of full momentum transfer when going from geometry I to geometry II.

The other component in the folding-angle distribution peaks in the region of $\Theta_{AB} \simeq 173°$. We attribute this component to "peripheral" collisions (Section IV.B) such as inelastic scattering, breakup, and transfer reactions in which a projectile residue escapes. As noted previously, the minimum in the folding-angle distribution is a consequence of the fact that, for peripheral collisions, the largest cross sections are observed for nitrogen and carbon fragments. For the very asymmetric detector arrangement this minimum is less pronounced, mainly due to pileup in the forward fission detector which extended forward to 40° and was subjected to high count rates.

2. Folding-Angle Distributions in Coincidence with Light Particles

The distribution of fission fragment folding-angles measured in coincidence with light charged particles (p,d,t,α) are shown in Figures V-3, V-4, V-5, and V-6. For reference, the inclusive distributions for geometries I
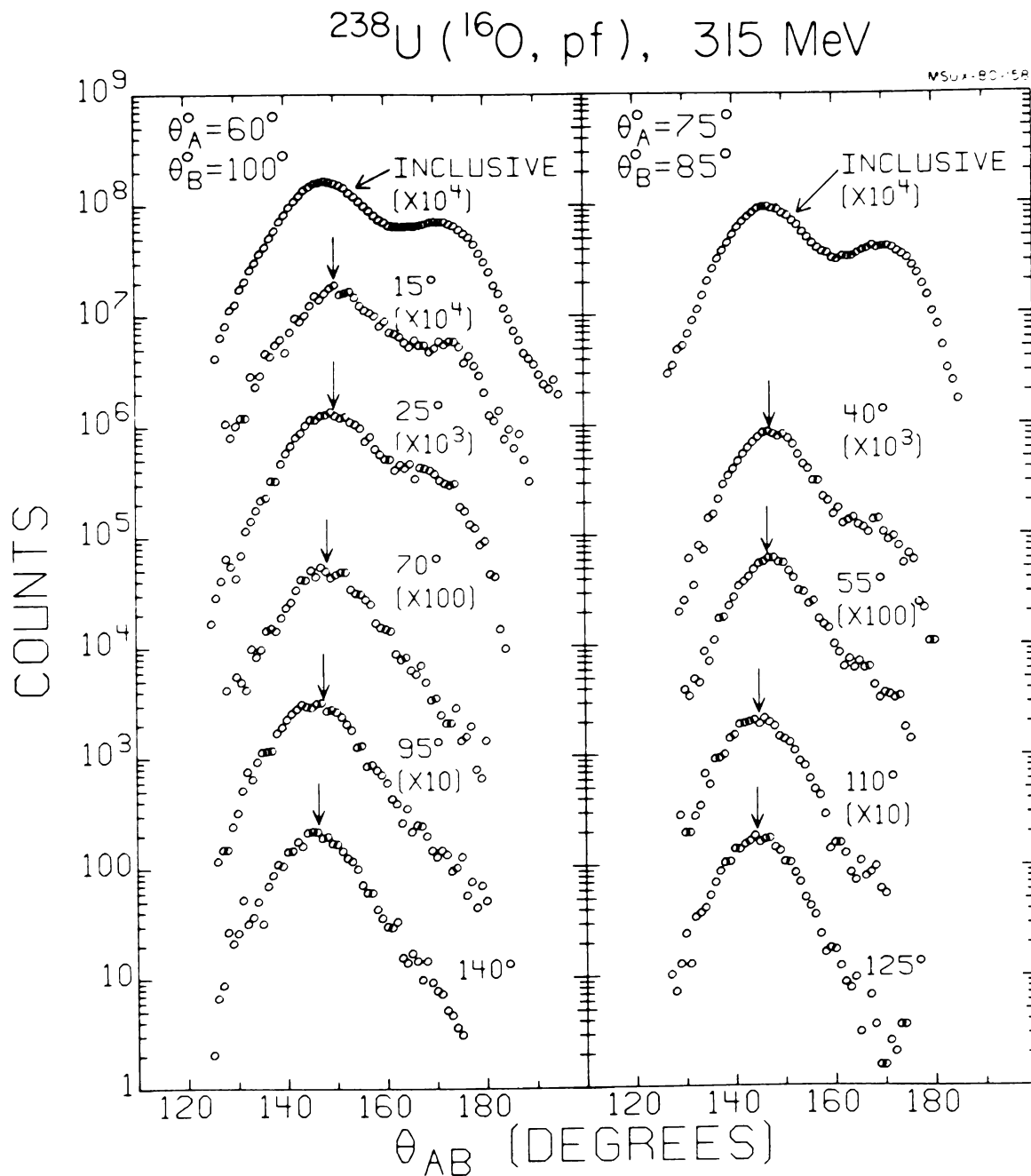
Figure V-3. Folding-angle distributions of fission fragments measured inclusively and in coincidence with protons for experimental geometries I and II. The detection angles of the coincident protons are given in the figure.
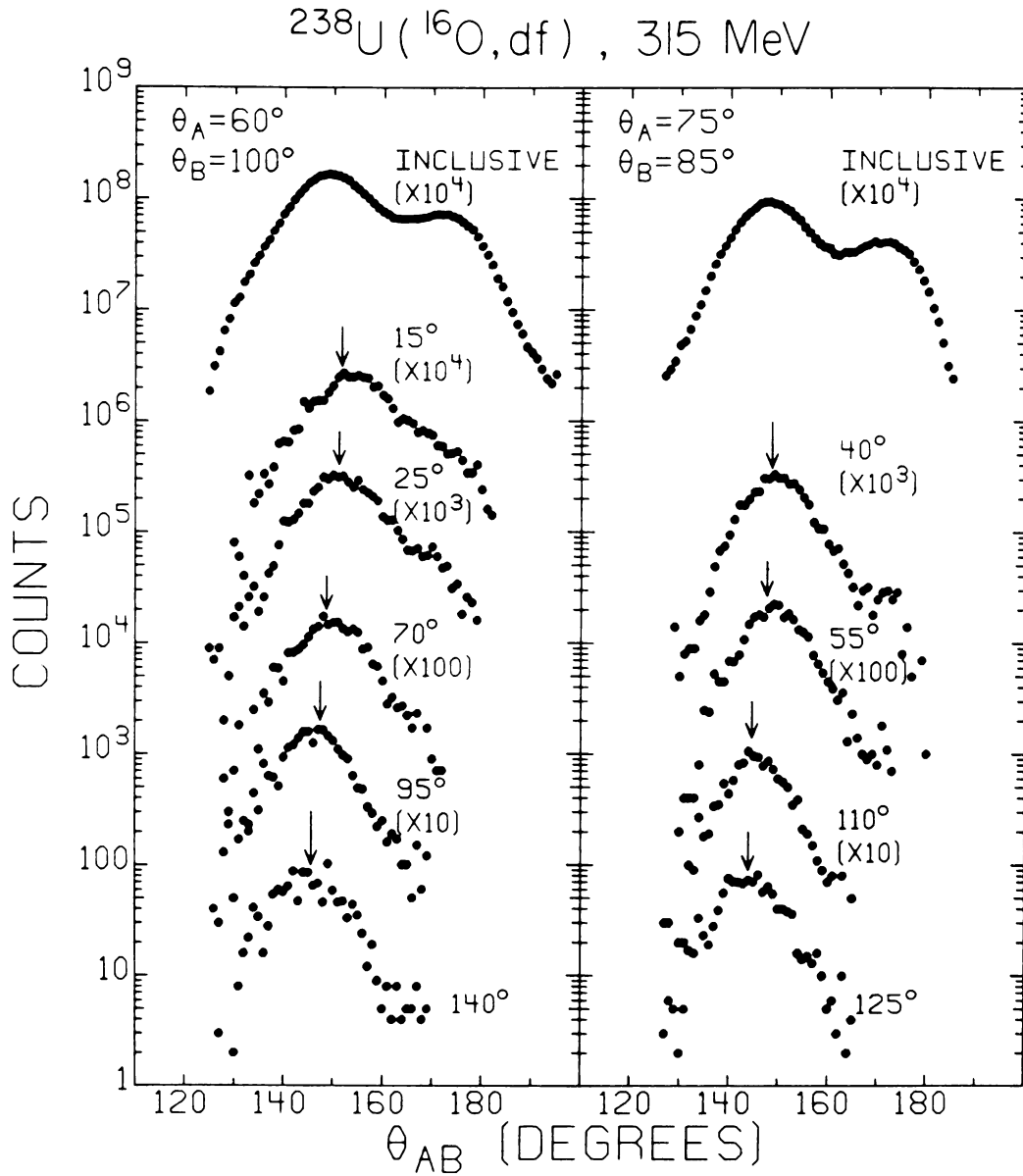
Figure V-4. Folding-angle distributions of fission frag-
ments measured inclusively and in coincidence
with deuterons for experimental geometries I
and II. The detection angles of the coincident
deuterons are given in the figure.
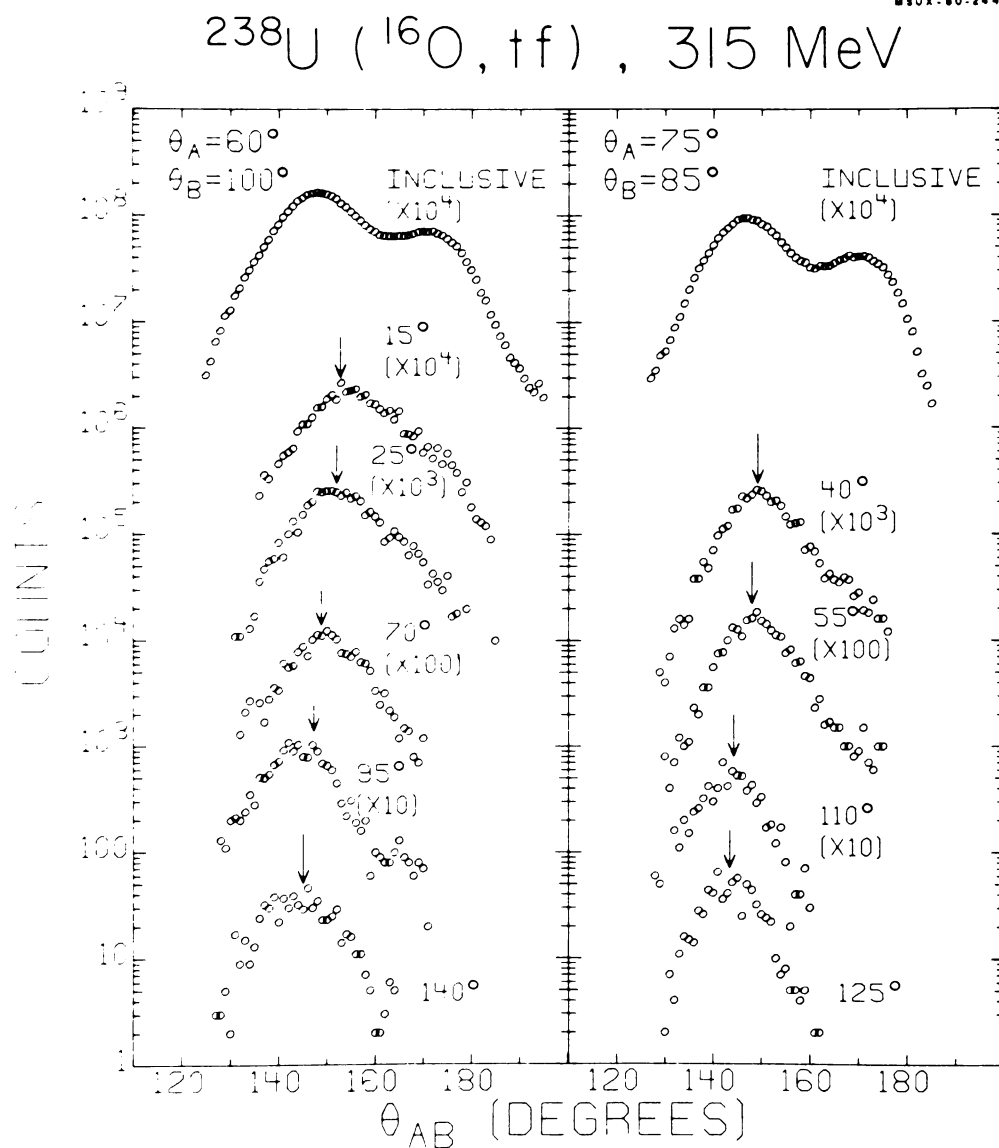
Figure V-5. Folding-angle distributions of fission frag-
ments measured inclusively and in coincidence
with tritons for experimental geometries I and
II. The detection angles of the coincident
tritons are given in the figure.
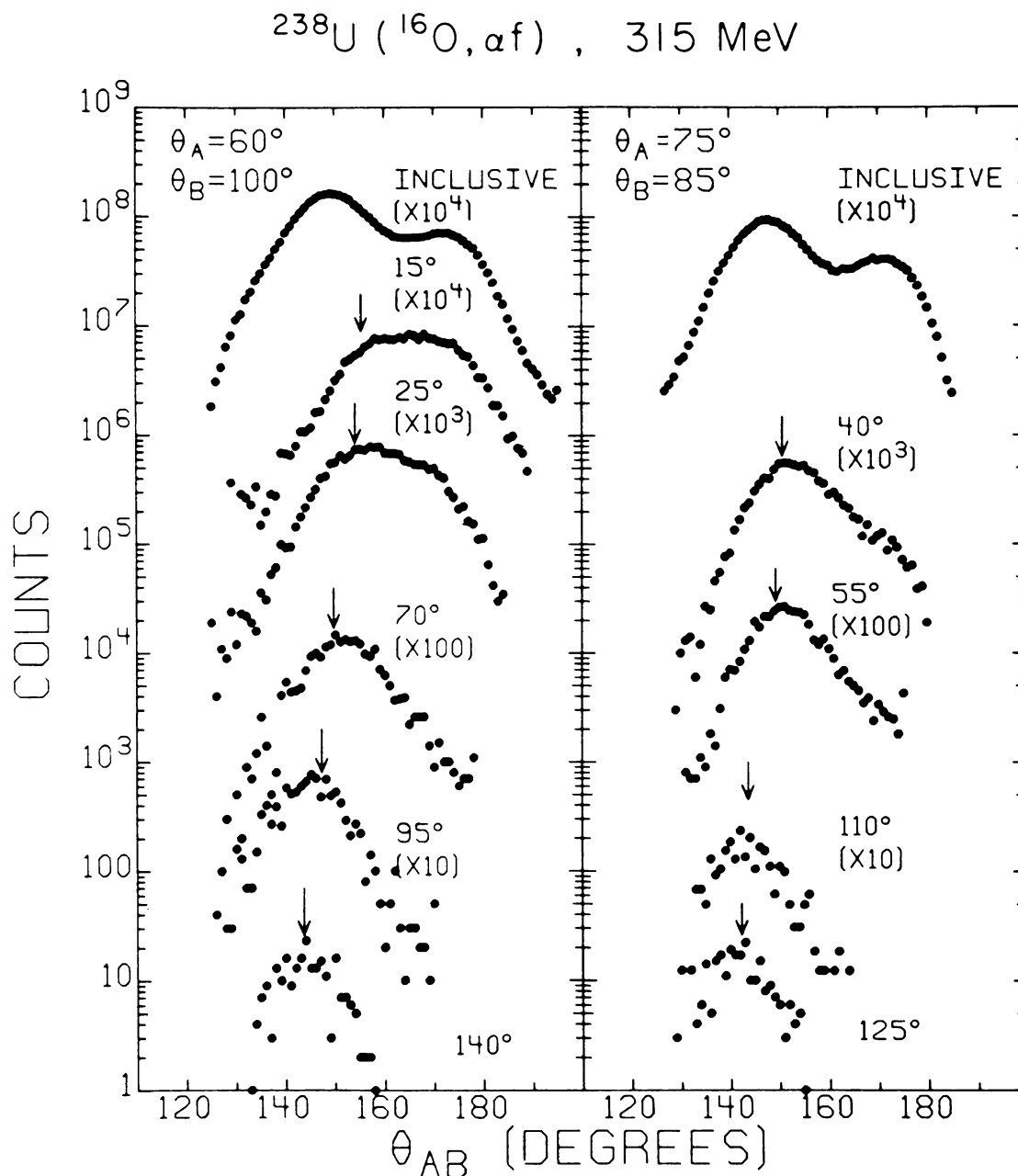
Figure V-6. Folding-angle distributions of fission fragments measured inclusively and in coincidence with alpha-particles for experimental geometries I and II. The detection angles of the coincident alpha-particles are given in the figure.

and II (from Figure V-1) are shown at the top of each figure. The folding-angle distributions observed in coincidence with light particles are shown below the inclusive distribution for the same geometry. The detection angle of the coincident light particle is indicated.

When light particles are observed at forward angles, the coincident fission fragment folding-angle distribution exhibits both central and peripheral components. This indicates that light particles are produced not only in massive transfer or incomplete fusion reactions, but also in peripheral reactions where a major portion of the beam momentum is carried off by projectile-like fragments. Protons, deuterons, and tritons are produced predominantly in central collisions whereas alpha-particles have about equal contributions from both central and peripheral reactions. The large alpha-particle cross sections observed for peripheral collisions at forward angles may be explained as due to significant contributions from α-particle breakup of the ^{16}O projectile [Ge 77a]. As the detection angle is increased, the contribution from peripheral processes is observed to decrease rapidly to the point of being insignificant beyond about 50°, as expected intuitively for breakup reactions.

If we assume that any unobserved particles are emitted isotropically, (as is the case for thermal emission at low angular momenta) then the average recoil momentum can be

calculated as the difference between the beam momentum and the average momentum of the observed light particle. The relationship between recoil momentum and folding-angle (see Figure V-2) can then be used to determine the average folding-angle which would be expected in this case. These average folding-angles are marked by arrows in Figures IV-4, V-3, V-4, V-5, and V-6. They coincide with the corresponding peak locations of the large momentum transfer component. Therefore this component must be associated with a low multiplicity of precompound light particles. Since this component dominates the light particle distributions at all angles the emission of light particles is dominated by processes in which the target residue absorbs the major part of the beam momentum. This is in accordance with the pictures implied by the terms "incomplete fusion" or "massive transfer".

B. "Central" Versus "Peripheral" Reactions

1. Light Particle Angular Distributions

The folding-angle between the two fission fragments can be used to classify "central" (or fusion-like) and "peripheral" (or transfer-like) collisions and study the corresponding light particle spectra. For this purpose a cut corresponding to $P_R^{\parallel}/P_1 \simeq 50\%$ (see Figure V-2) has been introduced in the inclusive folding-angle distributions. Those events with larger recoil momenta (smaller Θ_{AB}) were

defined as "central" collisions and events with smaller
recoil momenta (larger Θ_{AB}) as "peripheral" collisions.
For the different detector geometries of this experiment
this cut on Θ_{AB} was adjusted to keep the ratio of central
to peripheral components in the inclusive distributions
constant. The light particle angular distributions, gated
on central and peripheral collisions are shown in
Figure V-7. The contribution from central collisions
dominates the light particle cross sections at all angles
with the exception of the forward angle α-particle
emission. Here comparable cross sections are observed for
peripheral and central processes. For central collisions
the cross sections for the emission of deuterons and
tritons are comparable in magnitude to the ones for proton
and alpha-particle emission. This is in contrast to
expectations for compound nucleus evaporation in which
deuteron and triton emission is generally considered to be
of minor importance [Pü 77]. The angular distributions for
light particles produced in peripheral collisions exhibit
a significantly steeper falloff toward large angles than
the corresponding cross sections for central collisions.

2. Light Particle Multiplicity

The multiplicity of light particles per fission event
can be estimated by assuming the angular correlations to be
symmetric about the beam axis. Integrating the angular
distributions of Figure V-7, rather low multiplicities of

MSUX-80-344
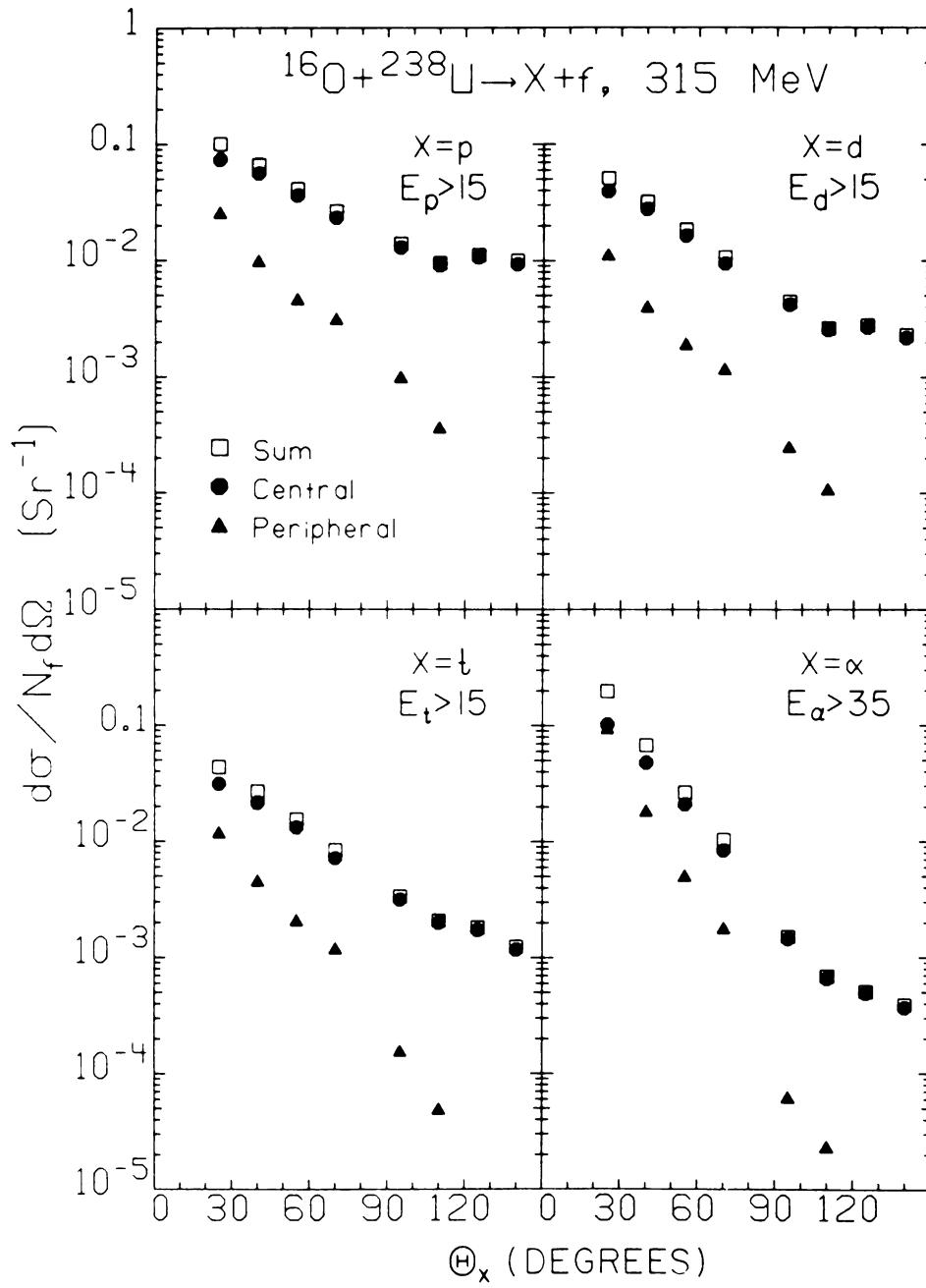
Figure V-7. Angular distributions of light particles, p,d,
t, and α, in coincidence with fission fragments
produced in central and peripheral collisions.
The sum of the two contributions is also shown.
The lower energy cutoffs are given in the
figure. The cross-sections are normalized to
fission singles.

$M(p) = 0.39$, $M(d) = 0.18$, $M(t) = 0.15$ and $M(\alpha) = 0.44$ are obtained. This is consistent with the qualitative conclusions reached by consideration of the momentum balance (see Section V.A.2). The multiplicities of hydrogen isotopes that are observed in peripheral reactions are lower by about a factor of two than the ones observed in central reactions. For our particular choice of gates we obtain: $M_p(p) = 0.21$, $M_c(p) = 0.47$; $M_p(d) = 0.09$, $M_c(d) = 0.21$; $M_p(t) = 0.10$, $M_c(t) = 0.16$, where the subscripts p and c denote peripheral and central events. This observation might be explained by the fact that the peripheral gate includes inelastic scattering and rearrangement reactions that do not involve preequilibrium emission of light particles. The alpha-particle multiplicity of peripheral reactions, on the other hand, is larger than that of central reactions: $M_p(\alpha) = 0.67$ versus $M_c(\alpha) = 0.33$. This again indicates the importance of breakup reactions or sequential alpha-particle decay of the projectile residue for peripheral reactions induced by ^{16}O ions.

3. Light Particle Energy Spectra

As noted above, we can use the folding-angle between the fission fragments to classify "central" and "peripheral" collisions and study the corresponding spectra of coincident light particles. Energy spectra of light particles (p,d,t, and α) emitted at $\Theta_{NaI} = 14°$ are shown in Figure V-8 for both "central" ($\Theta_{AB} < 160°$) and "peripheral" ($\Theta_{AB} > 160°$) events.
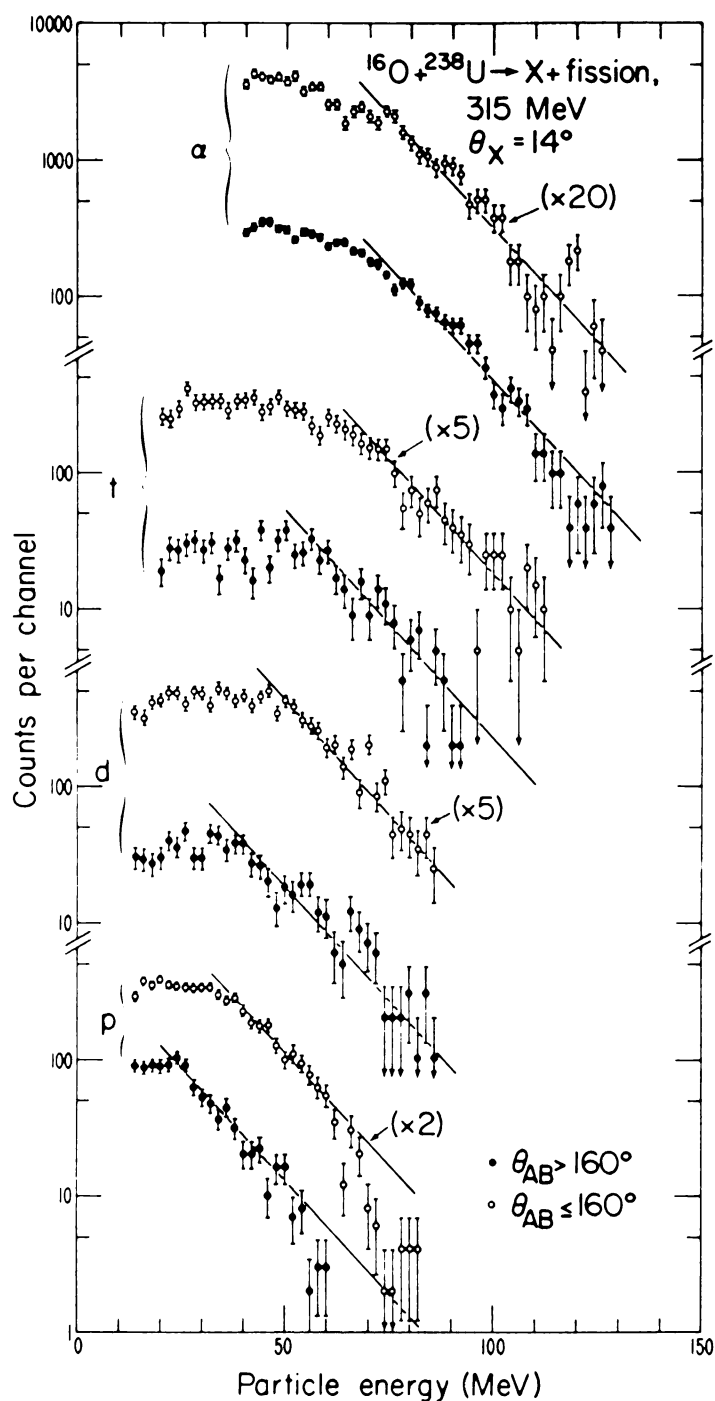
Figure V-8. Laboratory energy spectra of protons, deuterons, tritons, and α-particles detected in the θ = 14° Si-NaI telescope in coincidence with fission fragments with folding angles Θ_{AB}<160° (open circles, central collisions) and with folding angles Θ_{AB}>160° (filled circles, peripheral collisions).

Although there are differences in the low energy regions of
these spectra, it is remarkable that the slopes of the high
energy regions are very similar for central and peripheral
collisions and for all light particle species. This ob-
servation was verified to be independent of the particular
choice of division between central and peripheral events.
In Figure V-9 it is demonstrated that the similarity of
spectral shapes for central collisions and peripheral
collisions persists over the full angular range of observa-
tion. This similarity in the spectra strongly suggests that
light particles observed in central and peripheral collisions
are of similar origin. A natural explanation is that the
light particles originate from the early stages of the
collision before the final fate of the projectile residue
has been determined. Thus after the light particle is
emitted, the projectile residue could either fuse with the
target nucleus, resulting in a large momentum transfer, or
interact relatively weakly by inelastic scattering or few
nucleon transfer. We can not, however, rule out the possi-
bility that the light particles observed in peripheral
collisions result from sequential decay of the excited pro-
jectile residue (as suggested in Section IV.C.2). In fact,
both direct and sequential breakup processes are known to
contribute [Sh 81]. If sequential decay were the dominant
mechanism, however, it would require that the similarly
shaped energy spectra of central collisions be produced by
an entirely different process (since there is no projectile
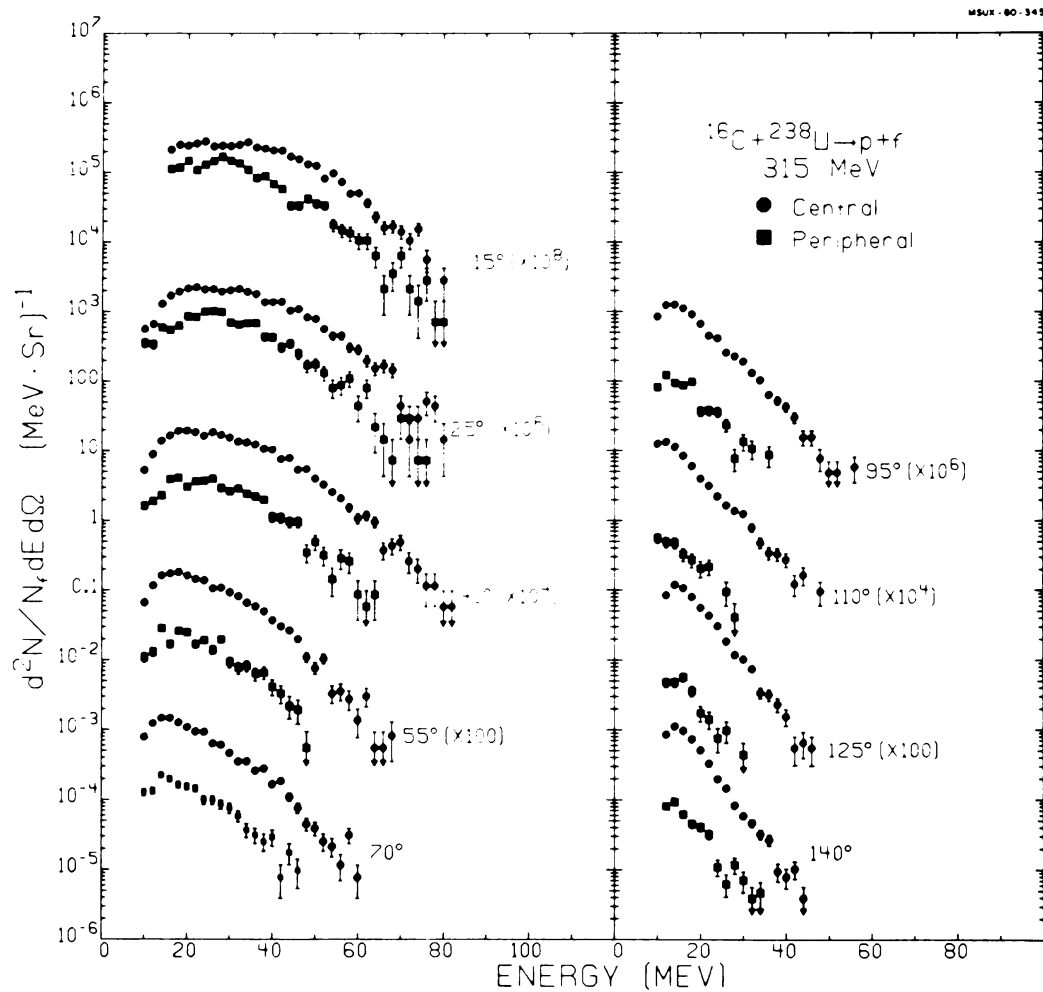
Figure V-9. Energy spectra of protons detected in the reaction ^{238}U (^{16}O, pf) at 315 MeV gated by "central" and "peripheral" collisions. The spectra are labeled by the detection angle of the coincident protons. The cross-sections are normalized to fission singles.

residue to decay sequentially in a central collision. Although this is entirely possible it would seem to be rather unlikely.

Since we find that the central contribution typically dominates the light particle energy spectra and since there are no characteristics unique to either component of the light particle energy spectra, we shall henceforth make no distinction between the two components and simply sum their contributions. After using the fission coincidence technique to demonstrate the dominant role of central collisions (or incomplete fusion reactions) in light particle emission, we then made an investigation of the energy and target dependence of inclusive light particle production.

C. Energy and Target Dependence

1. Light Particle Angular Distributions

The light particle angular distributions from the present study are shown in Figures V-10, V-11, and V-12 for reactions of ^{16}O on ^{197}Au, ^{90}Zr, and ^{27}Al at three incident energies. The distributions were obtained by summing over all energies with the lower threshold set at 12 MeV for the hydrogen isotopes and at 30 MeV for alpha-particles. The cross sections increase with increasing incident energy. The angular distributions are forward peaked at all energies and for all light particles. The slope of the angular distributions increases monotonically
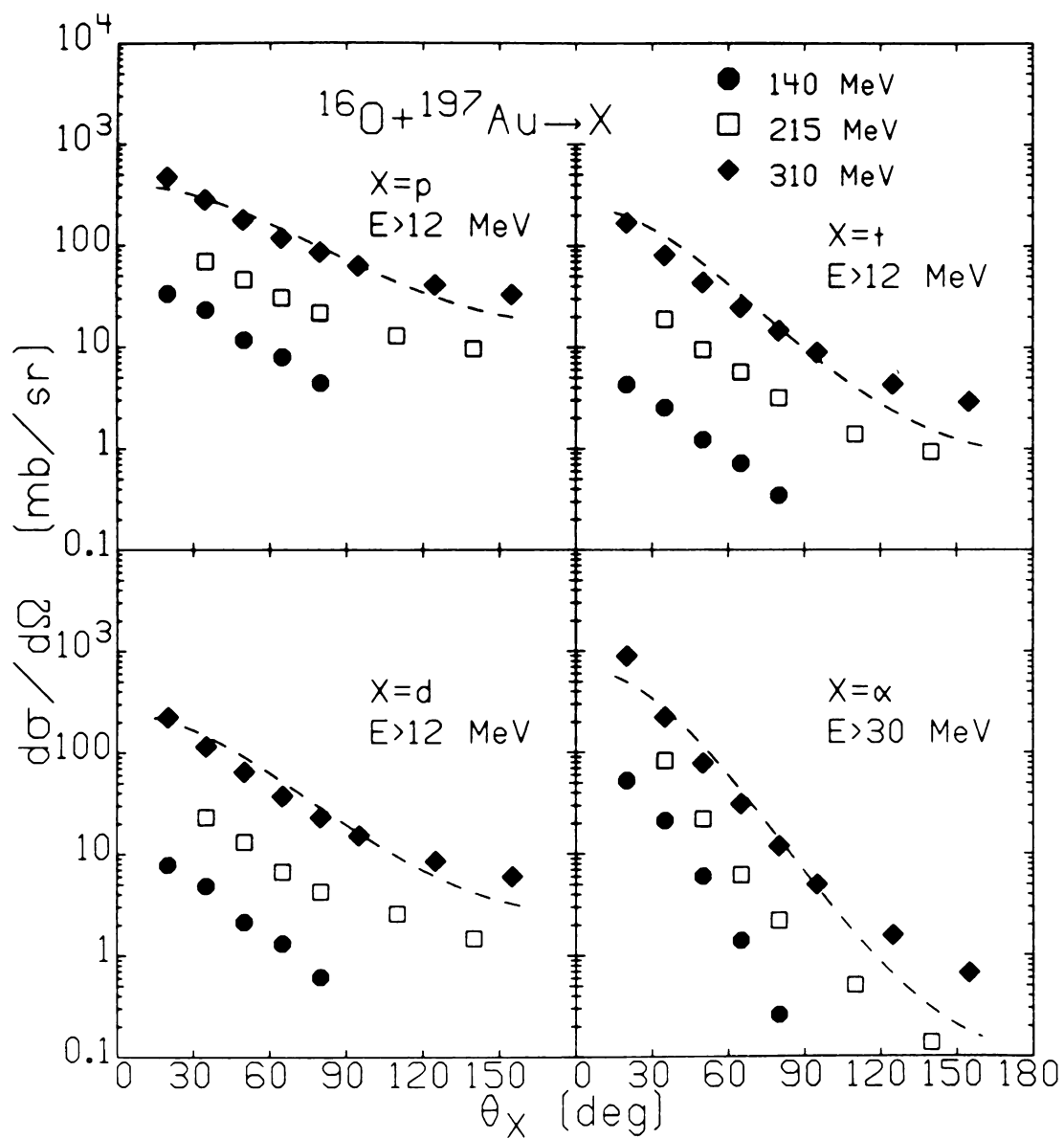
Figure V-10. Light particle angular distributions for reactions on ^{197}Au at 140, 215, and 310 MeV incident energies. The low-energy cut-offs for the energy integration are indicated. The dashed curves correspond to emission from a moving source with v = 0.071c and T = 5.9 MeV.
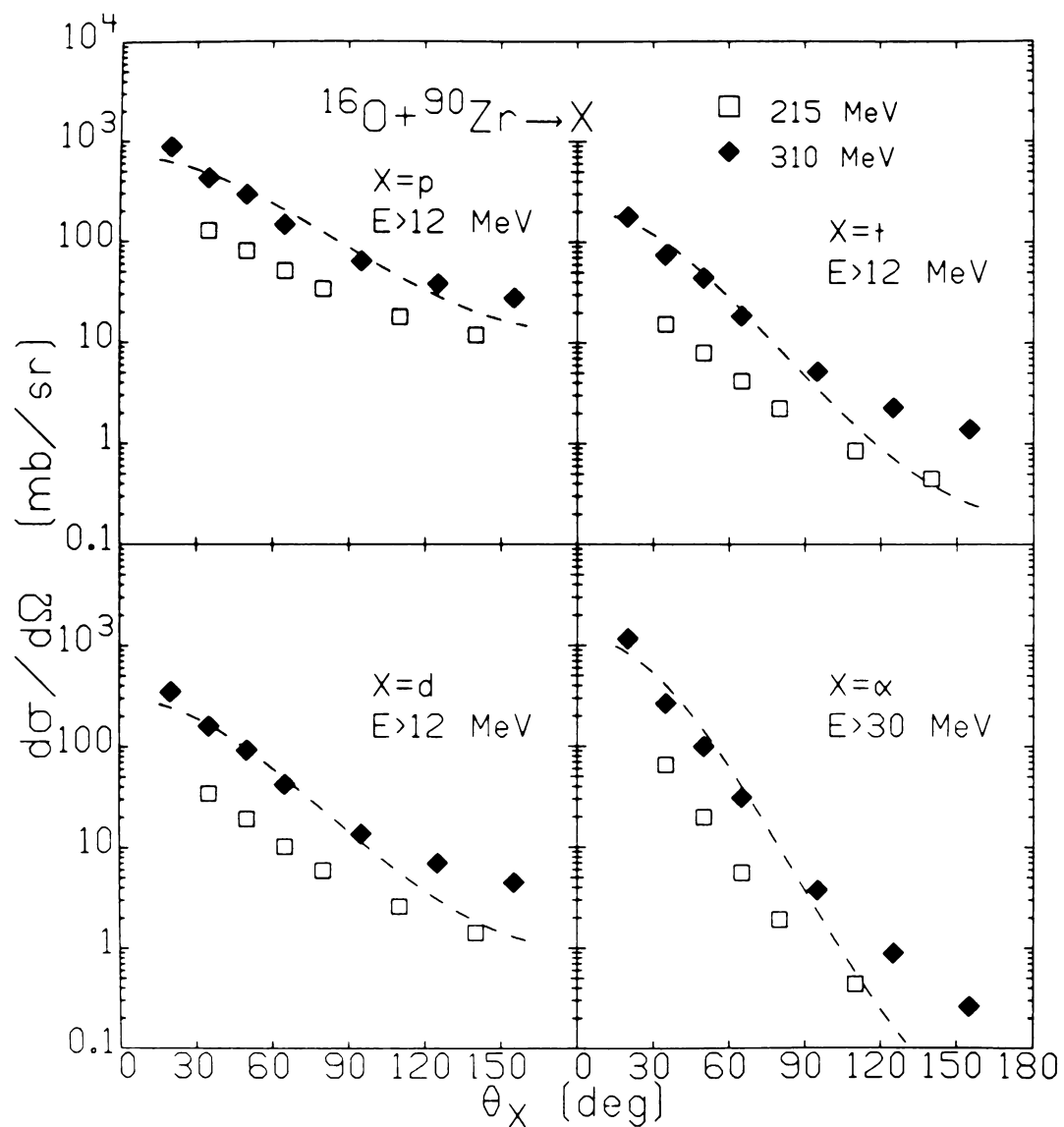
Figure V-11. Light particle angular distributions for reactions on ^{90}Zr at 215 and 310 MeV incident energies. The low-energy cut-offs for the energy integration are indicated. The dashed curves correspond to emission from a moving source with $v = 0.072c$ and $T = 5.73$ MeV.
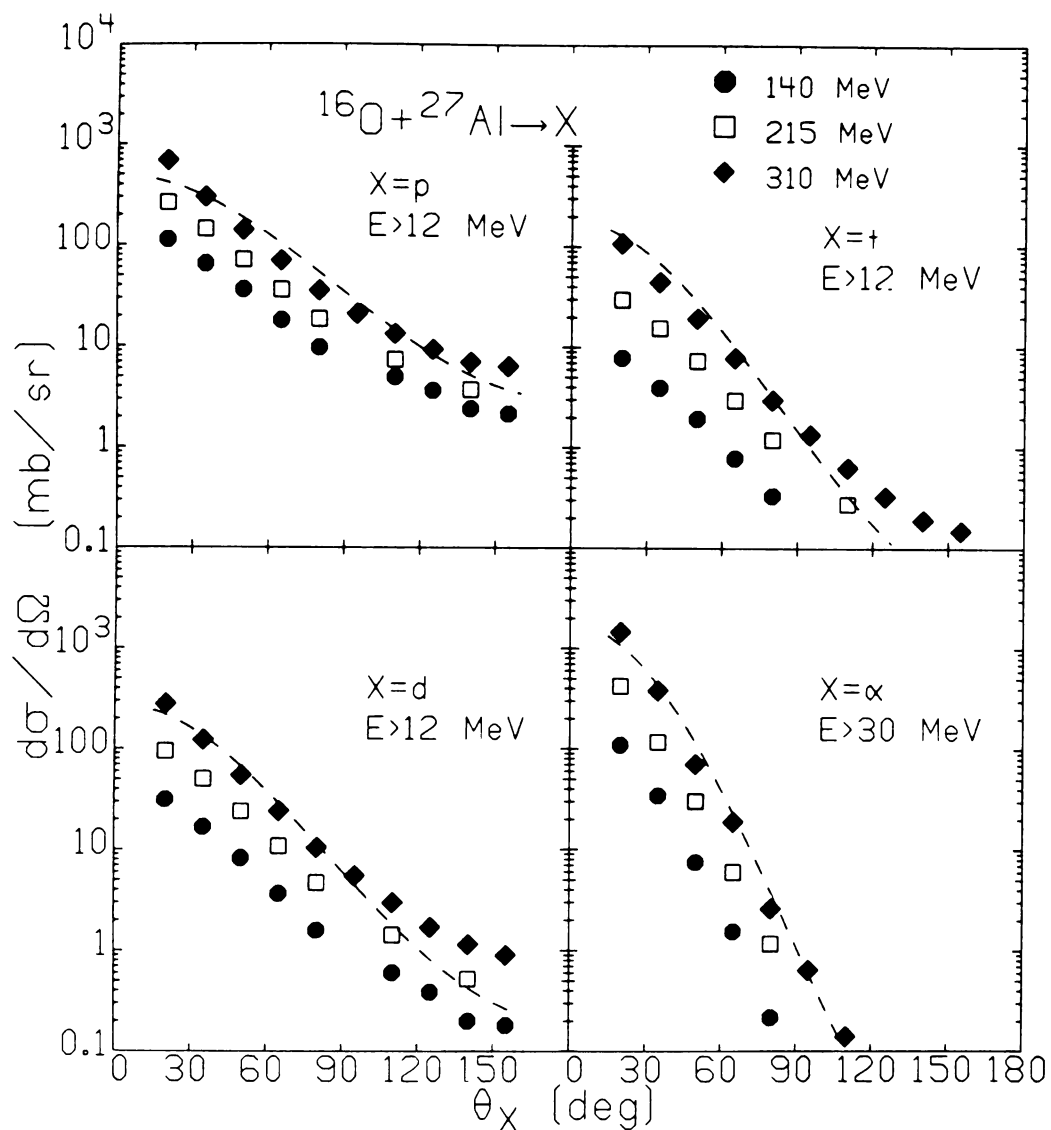
Figure V-12. Light particle angular distributions for reactions on ^{27}Al at 140, 215, and 310 MeV incident energies. The low-energy cut-offs for the energy integrations are indicated. The dashed curves correspond to emission from a moving source with v = 0.085c and T = 6.25 MeV.

with the mass of the outgoing light particle. The shape
of the angular distributions appears to be nearly
independent of the incident energy, but become progressively
more isotropic with increasing mass of the target nucleus.
An interpretation of some of these features as well as a
description of the dashed curves in Figures V-10, V-11,
and V-12 will be given in Section V.E.2.

2. Light Particle Integrated Cross Sections

Total inclusive cross sections integrated over light
particle energy and angle are listed in Table V-1. The
integration over energy has been made with a 12 MeV
threshold for hydrogen isotopes and a 30 MeV threshold for
alpha-particles and thereby emphasizes the nonequilibrium
contributions to the cross sections. Also shown in
Table V-1 are the total reaction cross sections as
calculated using the heavy-ion optical model code HOP II
[JGCr] with the optical potentials [Ba 75, Re 75, Cr 76]
listed in Table V-2. The calculated reaction cross
sections were found to be rather independent of the details
of the optical potential parameters. For example, inter-
changing potentials between the targets resulted in only
10% changes in the calculated total reaction cross
sections. From Table V-1 it is seen that the cross
sections for producing protons and alpha-particles are
comparable for each target and incident energy. On the
other hand, the cross section for the production of

Table V-1. Total inclusive cross sections (mb) for light particle emission. Systematic errors of absolute values are about 35%. Relative errors between light particle species are about 10%.

Target	Energy (MeV)	Protons[a]	Deuterons[a]	Tritons[a]	Hydrogen Isotopes[a]	Alphas[b]	σ_R[c]
^{197}Au	140	76	15	8	99	72	2259
	215	327	85	65	477	241	3075
	310	1414	497	340	2251	1162	3520
^{90}Zr	215	545	119	49	713	191	2487
	310	1971	649	304	2924	1448	2642
^{27}Al	140	253	58	14	325	140	1742
	215	528	172	52	752	524	1820
	310	1155	437	158	1750	1781	1846

a) Integrated over E>12 MeV.
b) Integrated over E>30 MeV.
c) Total reaction cross sections calculated using the optical model code HOP II [JGCr] with the parameters of Table V-2.

Table V-2. Optical model potential parameters used in calculation of total reaction cross sections (units of MeV and fm). The optical potential was parameterized in the form:

$$U(r) = V_o\{1+\exp[(r-R_o)/a_o]\}^{-1} + W_o\{1+\exp[(r-R_I)/a_I]\}^{-1}, \text{ with}$$

$$R_o = r_o(A_1^{1/3} + A_2^{1/3}), \quad R_I = r_I(A_1^{1/3} + A_2^{1/3}).$$

Target	V_o	r_o	a_o	W_o	r_I	a_I
197Au[a]	40	1.226	.634	35	1.226	.634
90Zr[b]	100	1.148	.635	20	1.245	.521
27Al[c]	10	1.35	.618	23.4	1.23	.552

a) Potential for elastic scattering of 16O on 208Pb[Ba 75].
b) Potential for elastic scattering of 16O on 92Mo[Re 75].
c) Potential for elastic scattering of 16O on 28Si[Cr 76].

deuterons is typically inhibited over proton emission by a factor of 3 to 4 with triton emission inhibited by another factor of about 2. The cross sections for light particle emission are observed to constitute a significant fraction of the total reaction cross section and even exceed it at the highest energies indicating mean multiplicities comparable to one.

The dependence of the average proton multiplicity, σ_p/σ_R, on target mass and incident energy per nucleon above the barrier is shown in Figure V-13. Also included in the figure is the multiplicity of the summed hydrogen isotopes. The Coulomb barrier in the laboratory was calculated according to

$$V_c = \frac{(A_p + A_t)}{A_t} \; \frac{Z_p \, Z_t \, e^2}{r_o (A_p^{1/3} + A_t^{1/3})} \qquad \text{(V-1)}$$

where A_p, A_t and Z_p, Z_t are the mass and atomic numbers of the projectile and target and $r_o = 1.44$ fm. The proton multiplicity is observed to be essentially independent of target and to increase smoothly with increasing available energy per nucleon. Therefore, we may conclude that the light particle multiplicities, excluding low energy contributions, depend only little on the details of the target nucleus but mainly on the incident energy per nucleon above the Coulomb barrier.
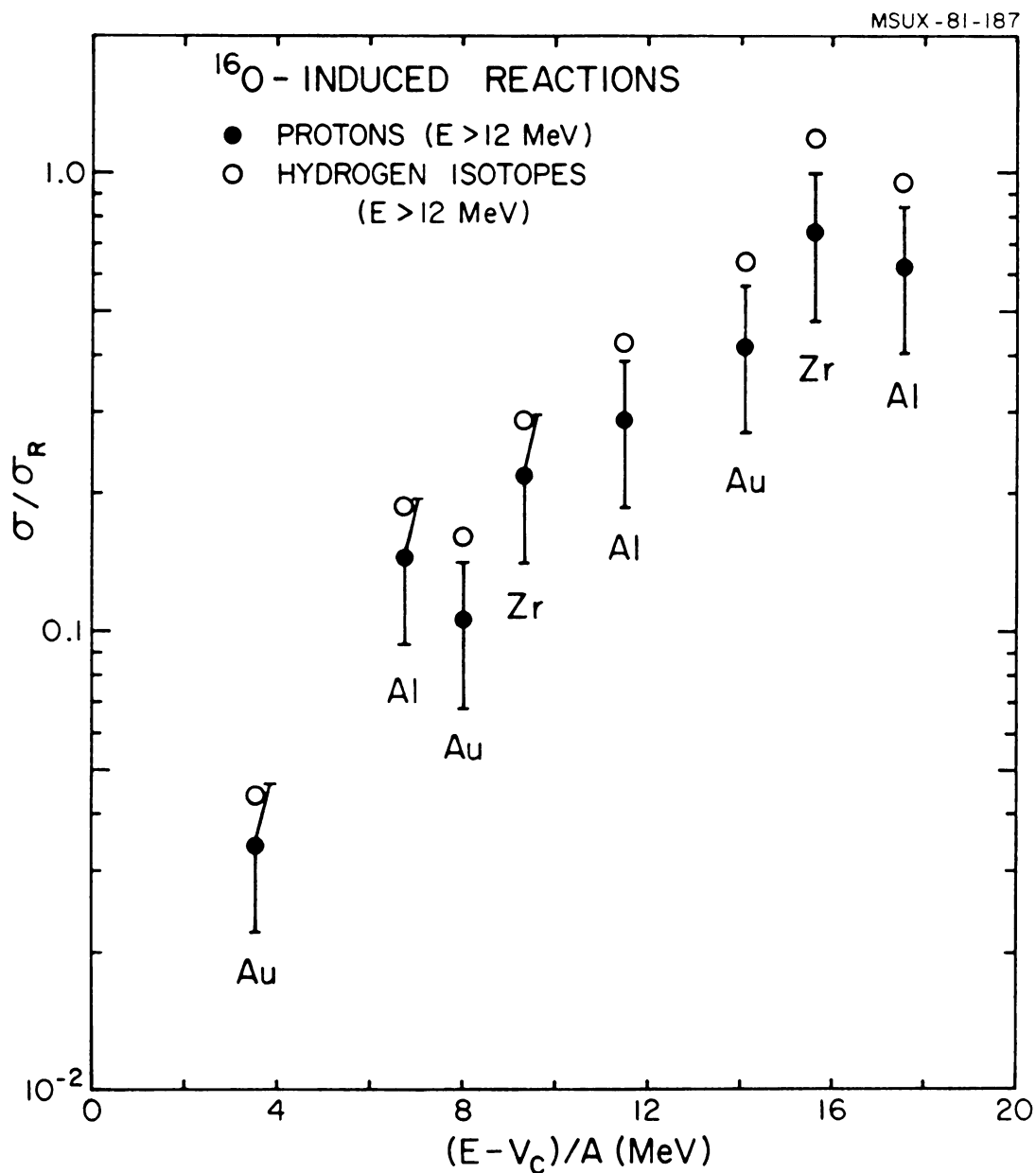
Figure V-13.   Dependence of proton and hydrogen multiplicity on target and incident energy. Multiplicities are taken from Table V-1 of text. Errors reflect the 35% uncertainty of the absolute cross sections. The Coulomb barrier V_c has been calculated using Eq. (V-1).

3. Light Particle Energy Distributions

Some of the general features of the light particle energy spectra observed in the present study may be seen in Figures V-14, V-15, and V-16. In Figure V-14, the light particle spectra for reactions of 140 MeV ^{16}O on ^{197}Au are shown by solid points at three selected angles which span the full angular range of observation. Also shown are the corresponding energy spectra for reactions on ^{27}Al. In order to facilitate a comparison of the spectral shapes, the ^{27}Al cross sections have been renormalized for each angle at 20 MeV for the isotopes of hydrogen and at 40 MeV for alpha-particles. In Figures V-15 and V-16 similar comparisons are made for the incident energies of 215 and 310 MeV, respectively. (Although the features of the energy spectra for the $^{197}Au(^{16}O,p)$ reaction at 310 MeV are qualitatively similar to those reported by Symons et. al. [Sy 80] for the same system, our data are observed to differ in slope. The reason for this difference is not understood, however we were able to reproduce our results at 310 MeV in two independently calibrated experiments). It is observed that these different target nuclei give rise to light particle spectra with very similar character- istics. Reactions on both ^{27}Al and ^{197}Au targets show smooth structureless energy spectra which extend well beyond the incident energy per nucleon of the beam and show a distinct shouldering at the most forward angles.

MSUX-8-060
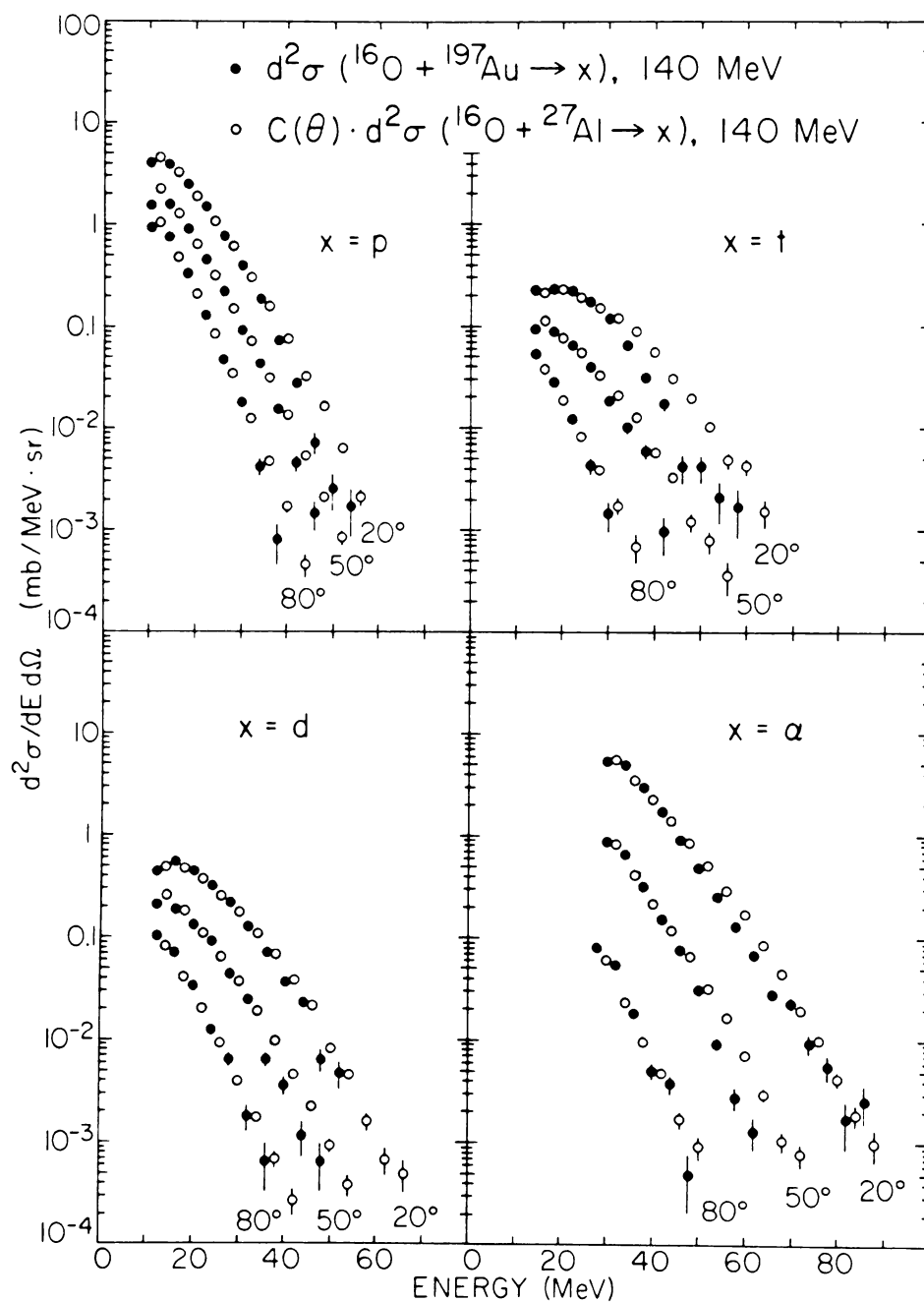
Figure V-14. Comparison of light particle energy spectra for reactions on ^{197}Au and ^{27}Al targets at 140 MeV incident energy. At each angle, the ^{27}Al data have been normalized to the ^{197}Au data at 20 MeV for the hydrogen isotopes and at 40 MeV for alpha-particles.

MSUX-8-009
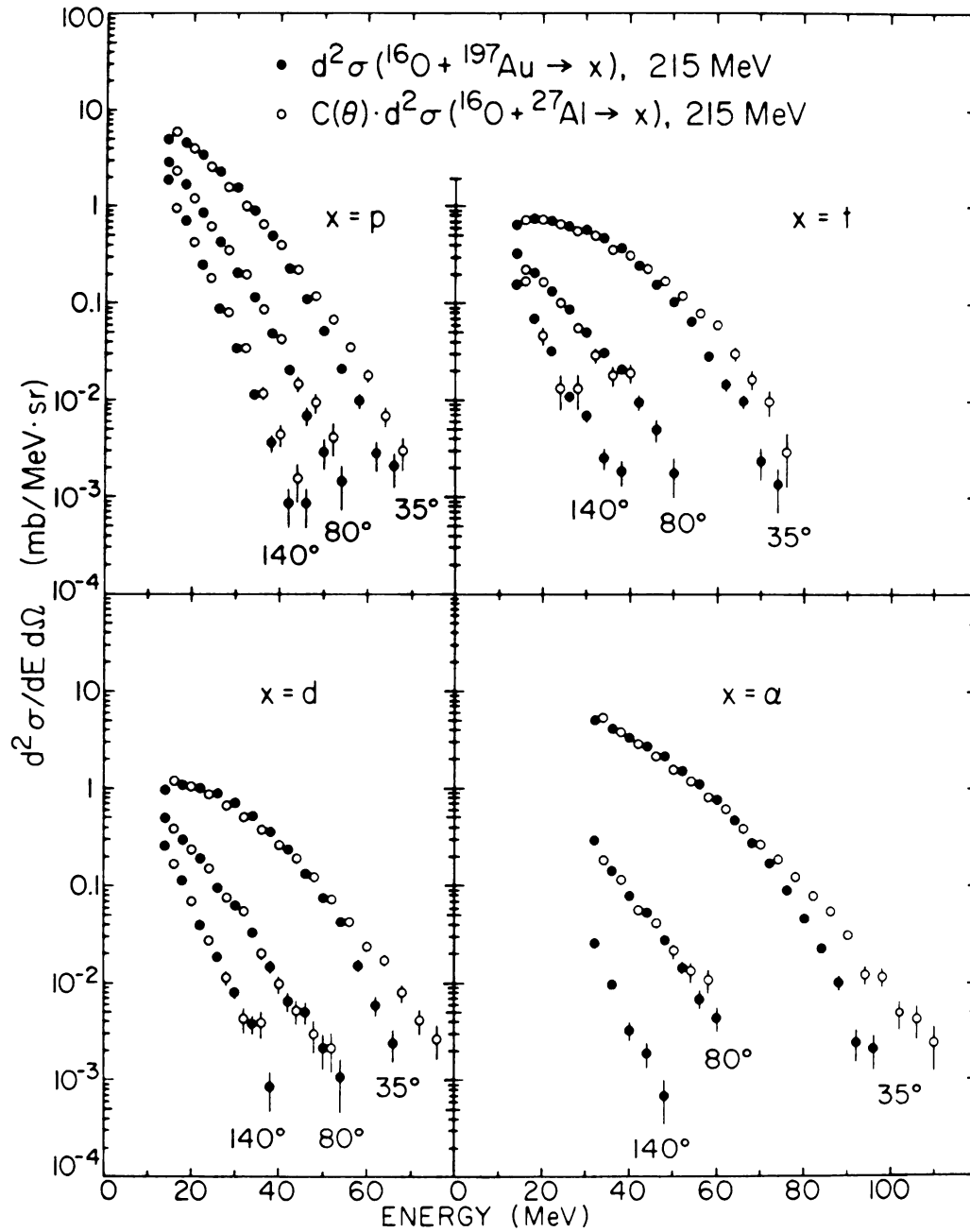
Figure V-15. Comparison of light particle energy spectra for reactions on ^{197}Au and ^{27}Al targets at 215 MeV incident energy. At each angle, the ^{27}Al data have been normalized to the ^{197}Au data at 20 MeV for the hydrogen isotopes and at 40 MeV for alpha-particles.
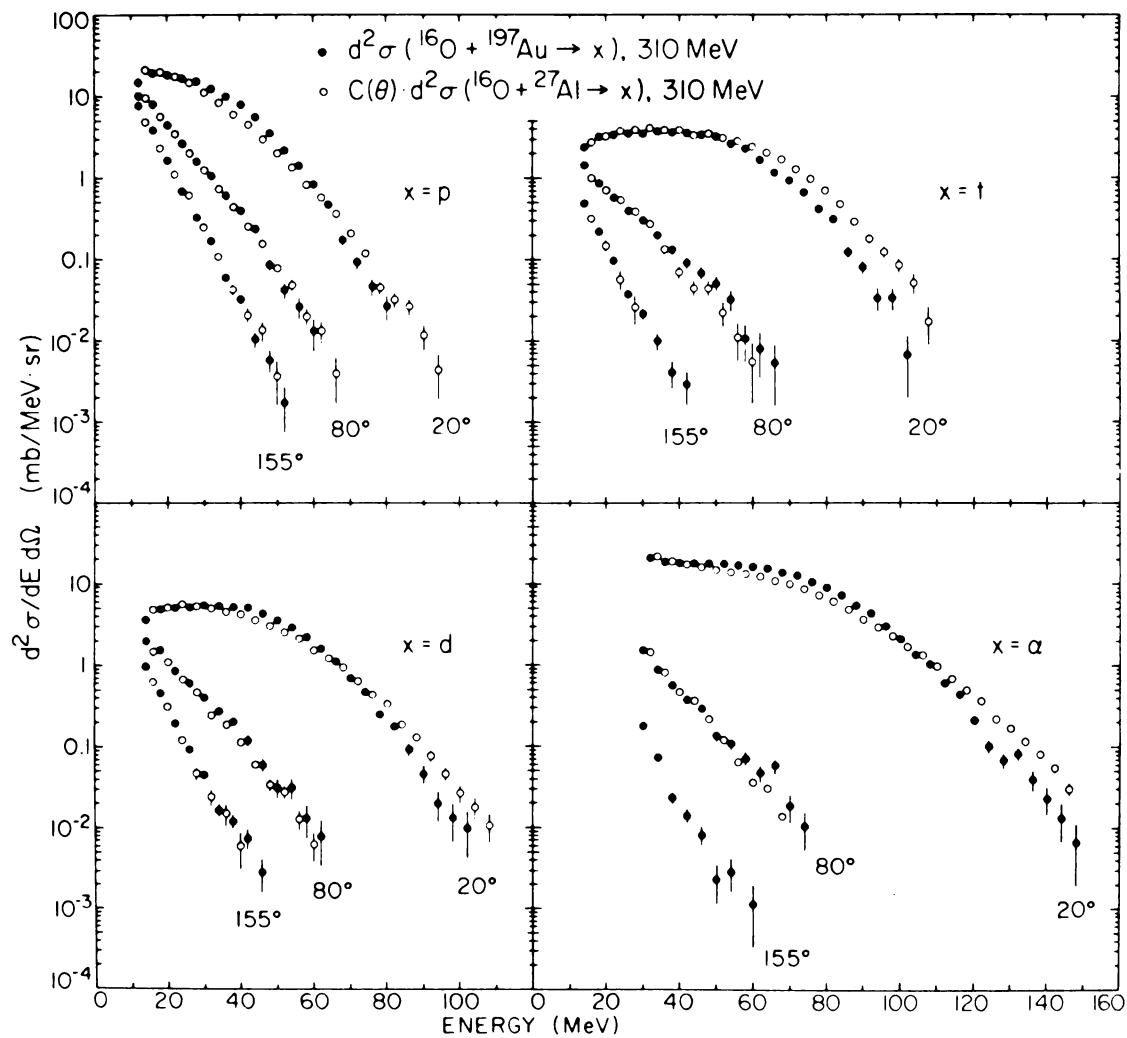
Figure V-16. Comparison of light particle energy spectra for reactions on [197]Au and [27]Al targets at 310 MeV incident energy. At each angle, the [27]Al data have been normalized to the [197]Au data at 20 MeV for the hydrogen isotopes and at 40 MeV for alpha-particles.

Both targets also display nearly exponential tails which are very similar at each angle for all light particle species and which become progressively steeper toward backward angles. The only persistent difference between the light particle energy spectra resulting from reactions on the two targets is that in the case of ^{27}Al the energy spectra have slightly flatter slopes. This might be explained by the fact that the incident energy per nucleon above the Coulomb barrier is slightly higher for reactions on Al than on Au due to the lower Coulomb barrier of the Al target. These observations suggest that the light particle spectra depend mainly on the available energy per nucleon above the Coulomb barrier rather than on the characteristics of the target nucleus.

D. Rotating Hot Spot Model

It has been proposed [Ho 77, No 78, Ut 80] that light particle energy spectra having exponential slopes which are angle dependent may be understood in terms of emission from a nuclear "hot spot" which cools as it rotates. In this model, large frictional forces rapidly convert the relative motion of target and projectile into the excitation of internal degrees of freedom. This causes local heating in the region of contact. Simultaneously, part of the tangential motion of the system is transformed into collective rotational energy. Particle emission is

assumed to occur from the heated region in the average
direction of the tangential velocity at the surface.
Because the emission angle can be related to the reaction
time, the nuclear temperature deduced from the energy
spectra will show an increasing degree of energy relaxation
as the scattering angle is increased.

Particle evaporation in the frame of the composite
system is assumed to occur from the hot spot following the
statistical formula of Erickson [Er 60]

$$\frac{d^2N}{d\Omega_{cm}dE_{cm}} \propto E_{cm} \ \sigma_{inv} \ (E_{cm}) \ \exp \ (-E_{cm}/T) \qquad (V-2)$$

where E_{cm} is the kinetic energy of the evaporated
particle, σ_{inv} the inverse cross section, and T the nuclear
temperature. Since the major energy dependence of σ_{inv}
is a cutoff at the Coulomb barrier we have simply included
the effect of Coulomb repulsion from the target residue and
treated σ_{inv} as a normalization constant. After trans-
forming to the laboratory frame and including the effects
of the Coulomb barrier we obtain

$$\frac{d^2N}{d\Omega dE} = N_0 E'^{\frac{1}{2}}(E' - 2E'^{\frac{1}{2}}E_1^{\frac{1}{2}}\cos\theta + E_1)^{\frac{1}{2}} \qquad (V-3)$$

$$x \exp[-(E' - 2E'^{\frac{1}{2}}E_1^{\frac{1}{2}}\cos\theta + E_1)/T] \ .$$

Where N_0 is a normalization constant for each spectrum,
$E' = E - ZE_c$ is the energy before acceleration in the Coulomb
field, E_c the Coulomb energy per unit charge, Z the charge

of the emitted particle, T_Θ the angle dependent nuclear temperature and $E_1 = mv^2/2$ is the kinetic energy of the particle of mass m at rest in the center of mass frame moving at velocity v.

Using Eq. (V-3) with the compound nucleus velocity $v = .013c$ and with $E_c = 10$ MeV it is possible to obtain quite satisfactory fits to the data (Figures V-17, V-18, V-19, and V-20). At forward angles the agreement is somewhat worse, possibly due to contributions from nonthermal processes which are not included in this picture. The normalizations and temperatures used for the calculations of Figures V-17 through V-20 are displayed in Table V-3. Except at forward angles, there is little variation of normalization with angle (Nomura et. al. [No 78] assumed the normalization to be constant with angle). The angle dependent temperatures T_Θ extracted from the fits are shown in Figure V-21.

As a simple illustration of how such a model might be extended we assume that the "hot spot" is at a uniform temperature and cools predominantly by convection with the surrounding nuclear matter. Classically, according to Newton's Law of Cooling, the rate of heat loss, dQ/dt, is proportional to the temperature difference, $\Delta T = T - T_0$, between the hot region and its surroundings

$$\frac{dQ}{dt} \propto \Delta T. \qquad (V-4)$$
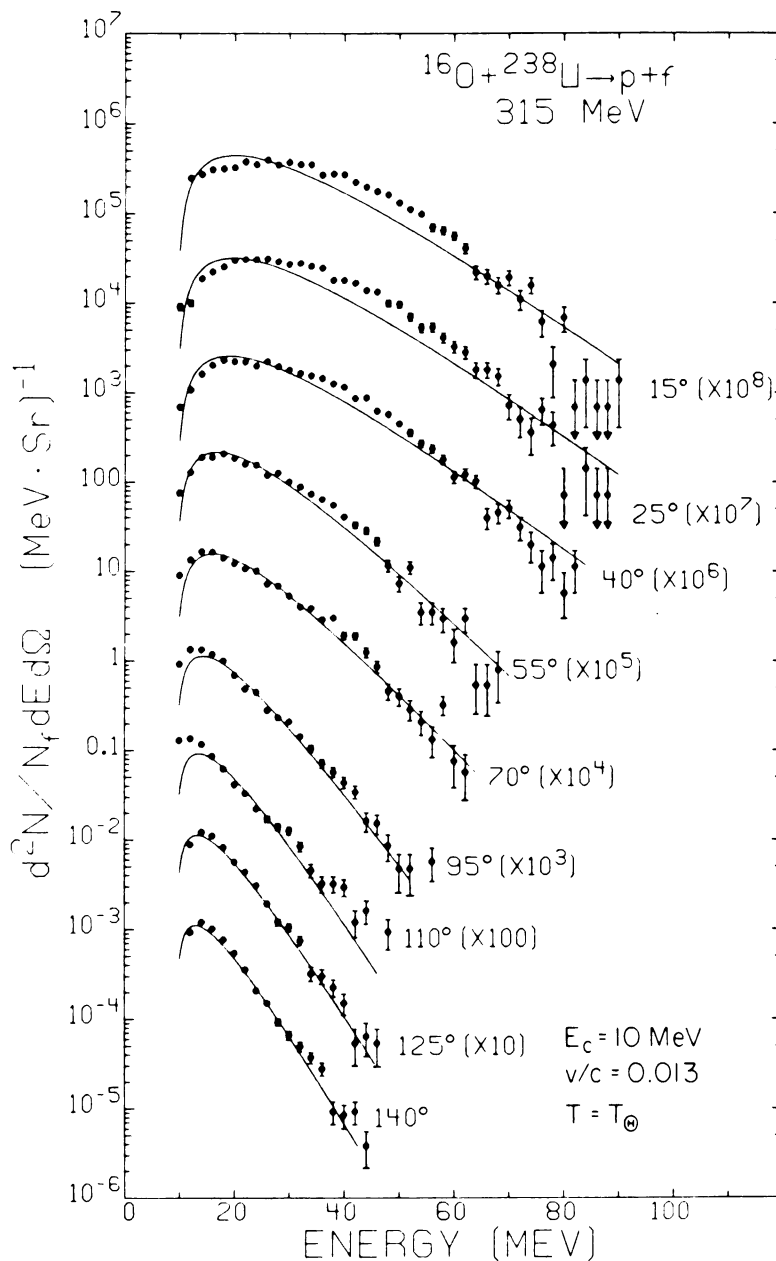
Figure V-17. Energy spectra of protons detected in the
reaction ^{238}U (^{16}O, pf) at 315 MeV. The
spectra are labeled by the detection angle of
the coincident protons. The cross sections
are normalized to fission singles. The data
are fit with the rotating hot spot model of
Eq. (V-3).
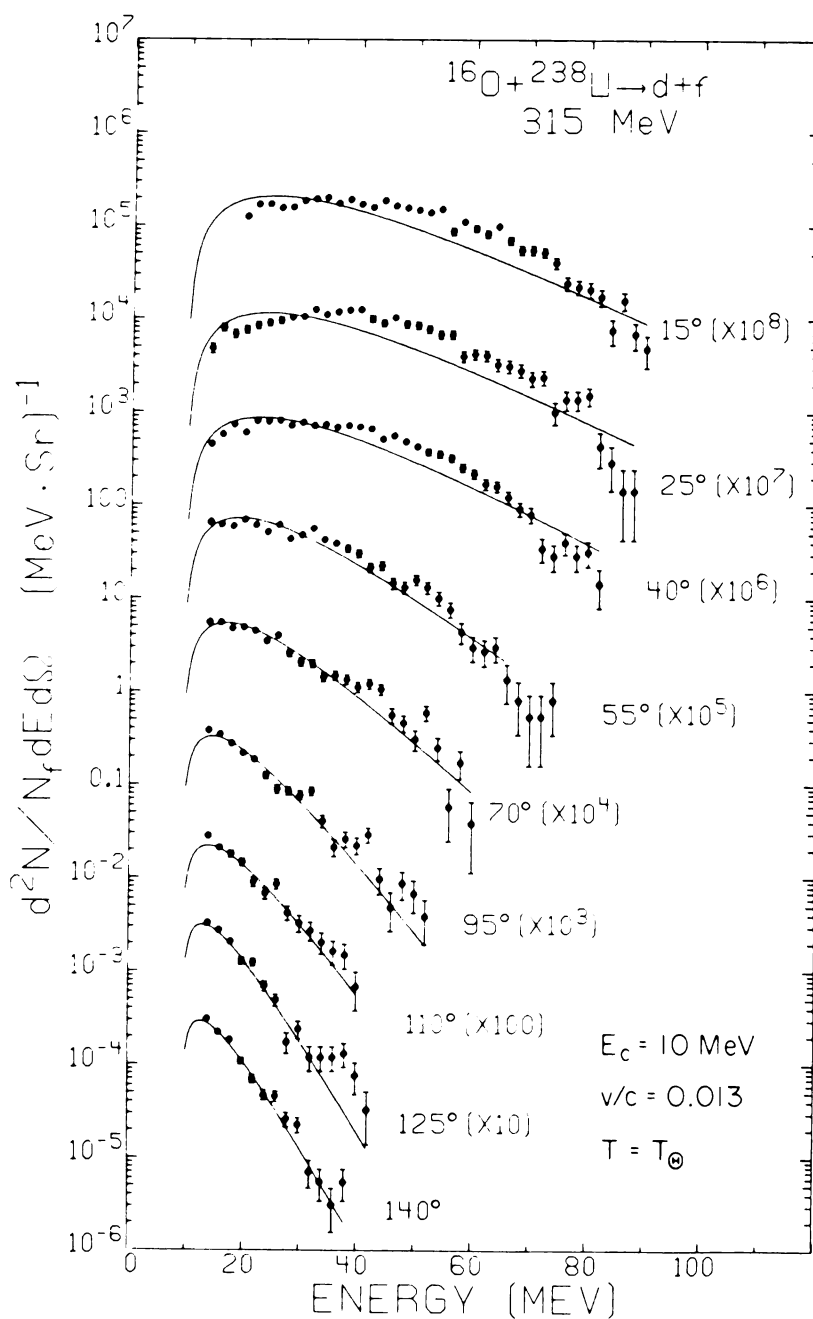
Figure V-18. Energy spectra of deuterons detected in the
reaction ^{238}U (^{16}O, df) at 315 MeV. The
spectra are labeled by the detection angle of
the coincident deuterons. The cross sections
are normalized to fission singles. The data
are fit with the rotating hot spot model of
Eq. (V-3).
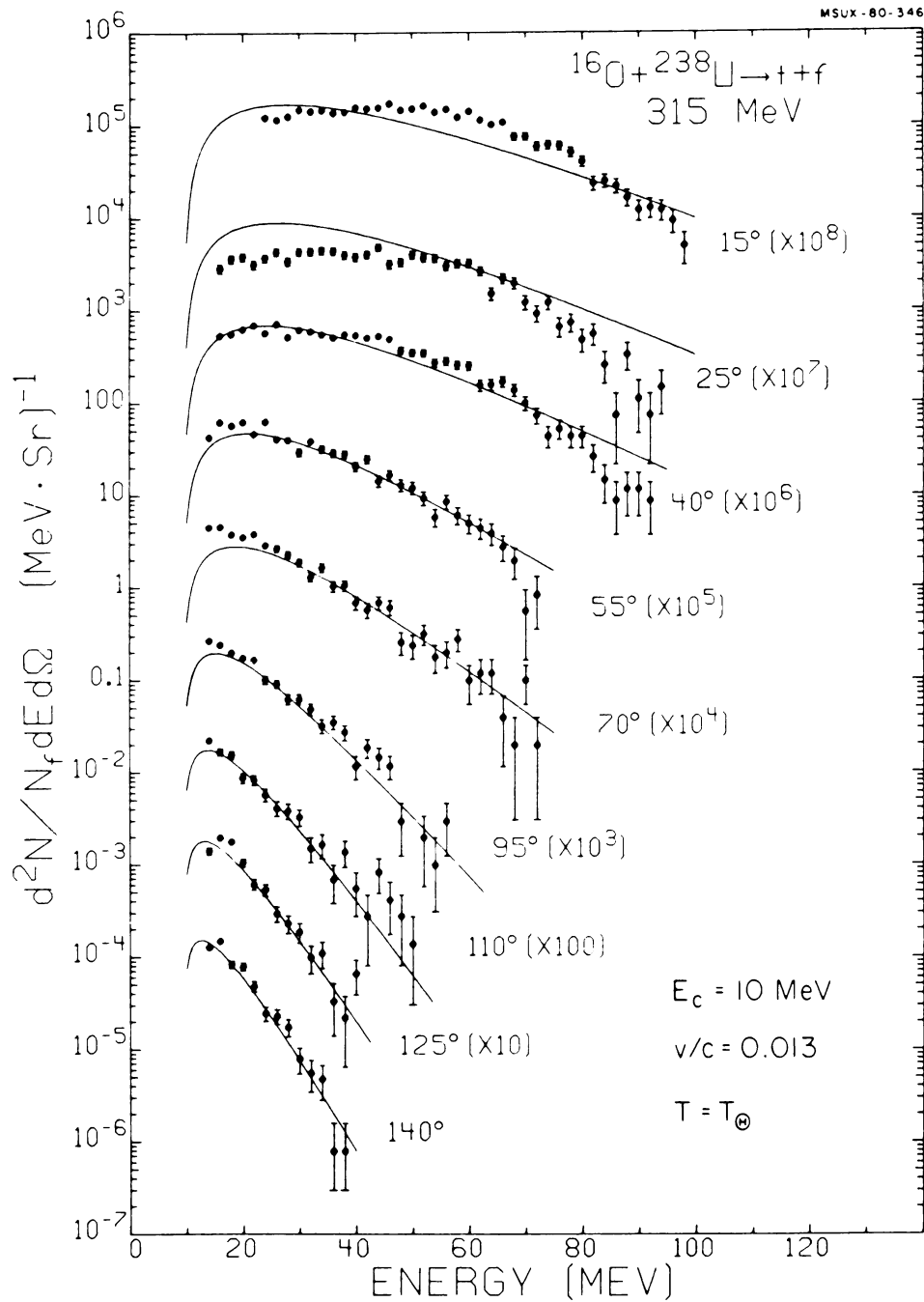
Figure V-19. Energy spectra of tritons detected in the reaction ^{238}U (^{16}O, tf) at 315 MeV. The spectra are labeled by the detection angle of the coincident tritons. The cross sections are normalized to fission singles. The data are fit with the rotating hot spot model of Eq. (V-3).
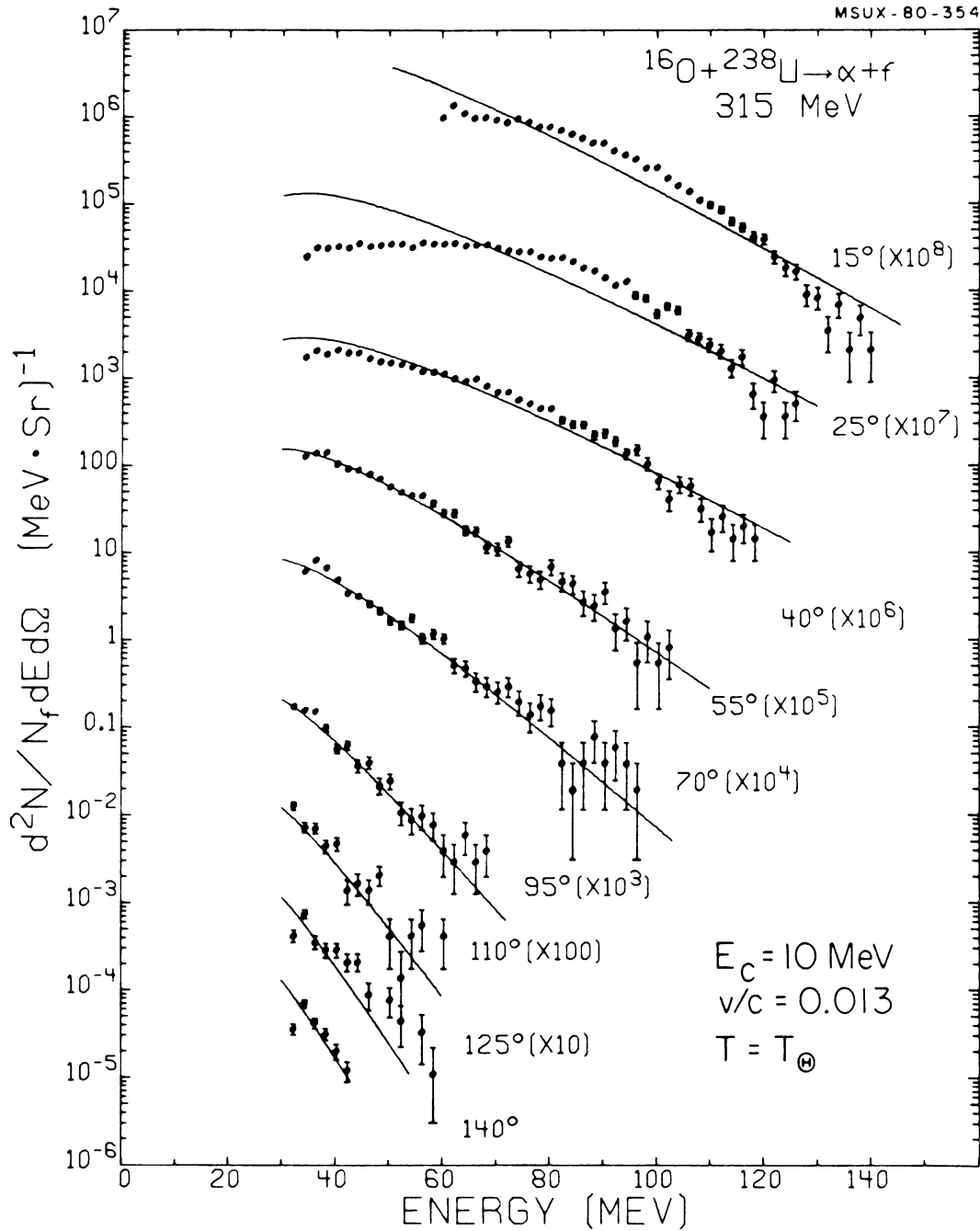
Figure V-20. Energy spectra of alpha-particles detected in the reaction ^{238}U (^{16}O, αf) at 315 MeV. The spectra are labeled by the detection angle of the coincident alpha-particles. The cross sections are normalized to fission singles. The data are fit with the rotating hot spot model of Eq. (V-3).

Table V-3. Normalizations and temperatures used in "rotating hot spot" calculations of Figures V-17 through V-20.

Angle	Normalization, N_o (MeV^{2}sr)$^{-1}$				Temperature, $T_\odot$ (MeV)			
	Protons	Deuterons	Tritons	Alphas	Protons	Deuterons	Tritons	Alphas
15°	124	40	28	1350	8.96	12.6	14.8	10.7
25°	92	23	16	268	8.74	12.1	13.6	11.5
40°	78	19	14	60	8.34	11.2	12.3	11.5
55°	86	22	12	42	6.51	8.36	9.76	8.88
70°	68	20	9.0	29	6.05	6.84	8.18	7.44
95°	67	18	9.6	13	4.76	5.18	5.83	5.72
110°	63	13	11	12	4.24	4.86	4.81	4.97
125°	82	25	13	19	4.15	4.00	4.41	4.41
140°	86	25	13	29	3.97	3.87	4.07	4.16

Figure V-21. Angular dependence of the temperature T_Θ, obtained by fitting the p,d,t, and α energy spectra (Figures V-17 through V-20) with the rotating hot spot model.

Ignoring the time and temperature dependence of the proportionality constant we find that after a time, Δt, the temperature difference, ΔT, is related to the initial temperature difference, ΔT_i, by

$$\Delta T = \Delta T_i \exp(-\Delta t/\tau) \qquad (V-5)$$

where τ is the characteristic decay time. The relaxation time, τ_R, is related to the decay time by integrating Eq. (V-4) [Ch 67, Lu 68, We 77]

$$Q = \int_0^{\tau_R} dQ(t) = Q_0[1 - \exp(-\tau_R/\tau)] \quad . \qquad (V-6)$$

Thus for practical purposes the relaxation time is a few times the decay time.

Classically, the decay time is given by [Ch 67, Lu 68] $\tau = \rho c R^2/\kappa N_{Nu}$ where ρ is the density, c the heat capacity, κ the thermal conductivity, R a characteristic length, and N_{Nu} a dimensionless number dependent on geometry known as Nusselt's number. Substituting the thermal conductivity of nuclear matter [We 77], $\kappa \sim \rho c v_F \lambda$, where v_F is the Fermi velocity and λ the nucleon mean free path, we obtain [Sc 78]

$$\tau_R \sim \frac{R^2}{v_F \lambda} \qquad (V-7)$$

in agreement with Weiner and Weström [We 77].

Substituting $\omega = \Delta\Theta/\Delta t$ into Eq. (V-5) we find

$$\Delta T = \Delta T_i \exp[-\Delta\Theta/(\omega\tau)] \qquad (V-8)$$

which is in accord with the experimentally observed decrease in temperature with angle (Figure V-21). If the hot region is assumed to cool toward the compound nucleus as the rest of the nucleus warms then T_0 should be taken as the compound nucleus temperature, $T_0 = T_{cn} \simeq 3$ MeV. In Figure V-22 it is shown that if one considers only the region where the relative contribution from peripheral processes is insignificant (i.e. beyond about 30°), the quantity $\ln(T_\Theta - T_0)$ is linearly related to Θ for all light particles. Moreover, for deuterons, tritons and alpha-particles the slope and intercept are very similar. For protons a flatter slope and smaller intercept are obtained which might be due to a larger compound nucleus contri-bution. The observed slope corresponds to $\omega\tau = 45.5$ degrees. Assuming a rotational velocity corresponding to a grazing collision with the moment of inertia of two touching spheres we obtain a decay time of the order of $\tau = 3 \times 10^{-22}$ sec. This is about an order of magnitude shorter than observed at lower incident energy [Ho 77]. The corresponding relaxation time of the "hot spot" is then of the order $\tau_R \simeq 10^{-21}$ sec which is in rough agreement with other estimates [Bl 76].

The rotating hot spot model fits the experimental data
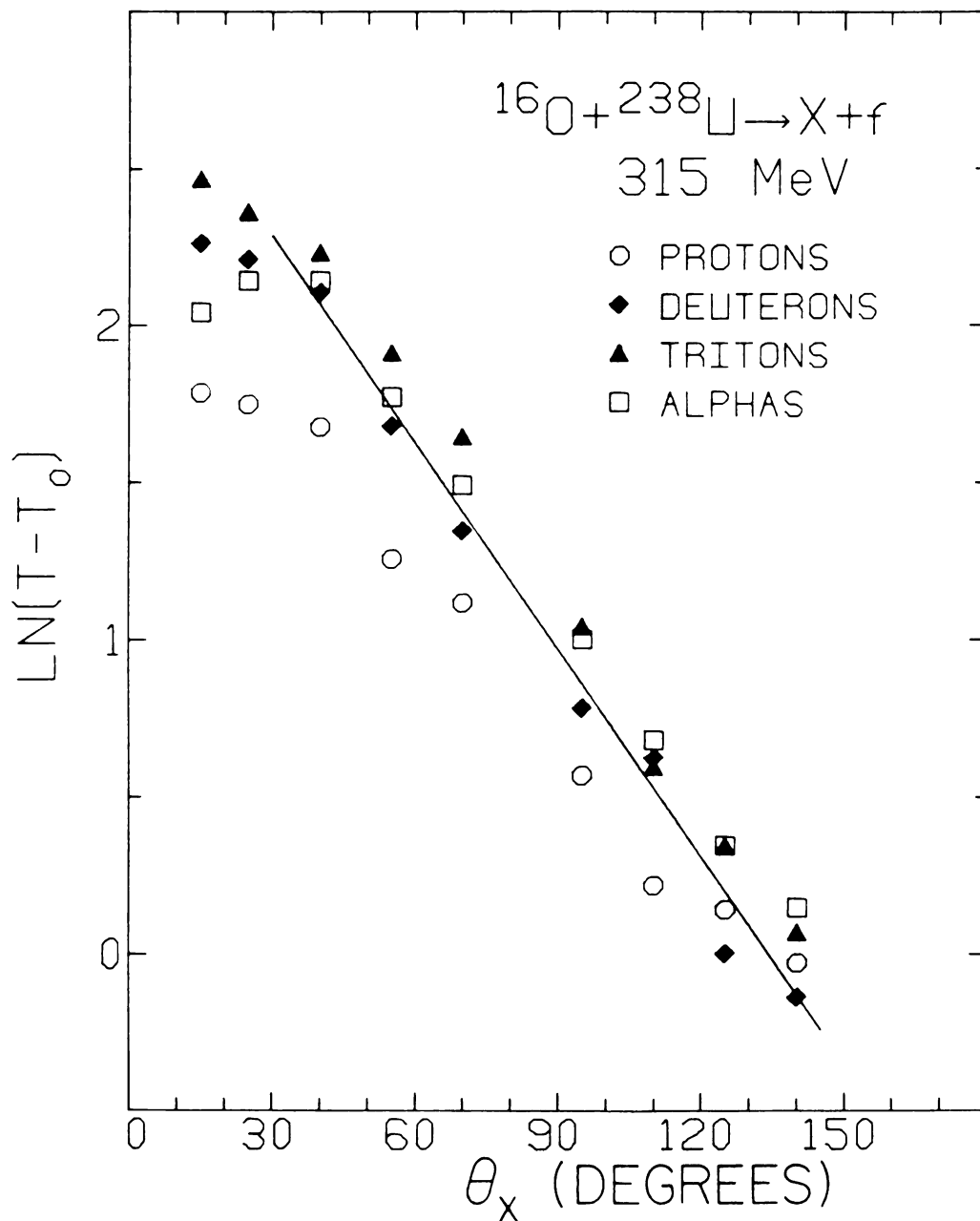
Figure V-22. Angular dependence of ln (T_Θ - T_o), where
T_o = T_{cn} = 3 MeV and T_Θ is the temperature in
MeV (Figure V-21) obtained by fitting the p,d,
t, and α energy spectra according to the
rotating hot spot model. The curve shown has
a slope of -0.022 deg.$^{-1}$ and an intercept
corresponding to T_i = 22 MeV.

quite well and offers a physical explanation for several
features of the data. However, in order to explain the
experimental fact that the greatest temperatures are
observed in the forward direction it was necessary to assume
that the light particles are emitted tangentially from the
hot spot. The physical justification for such an
assumption is not clear. If the target and projectile are
assumed to stick together as they rotate, then due to
absorption in the perpendicular directions the light
particles should be emitted primarily in the tangential
plane between the two nuclei. In this picture, the light
particle energy spectra should display an angle dependent
temperature which is symmetric about 90°. Instead, the
observed light particle energy spectra display temperatures
which decrease continuously beyond 90°. Alternatively, the
tangential emission might be a result of the rotational
motion of the hot spot. However, in the present experiment
the rotational energy at the nuclear surface is not
expected to exceed about one MeV per nucleon and therefore
will not dominate the thermal emission. (If very high
rotational velocities of the hot spot could occur,
Eq. (V-3) would have to be modified to take the effect of
rotation into account explicitly. Similar to Nomura et. al.
[No 78] we have ignored this rotational velocity of the
source with the result that the local nuclear temperature
might be somewhat overestimated.)

E. Moving Source Model

1. Energy Distributions

After having doubts about the justification for the rotating hot spot model, we search for an alternative explanation for the light particle emission. Some qualitative insight on the overall trends of the light particle spectra may be obtained by presenting the Lorentz invariant cross sections, $E\frac{d^3\sigma}{d^3p}$, as a contour plot in the velocity plane. By means of such a diagram one can easily determine whether or not a rest frame exists from which the emission appears isotropic. If such a frame existed the contours of constant cross section would appear as circles centered on the velocity of that frame. For emission from the compound nucleus in the reaction $^{16}O + ^{238}U$ at 315 MeV, these circular contours would be centered on the compound nucleus velocity, $v_{cn} = 0.013c$. For emission from the projectile the contours would be centered on the beam velocity $v_B = 0.205c$. A contour diagram of the Lorentz invariant proton cross sections is shown in Figure V-23. Levels of constant invariant cross sections are indicated by the solid and open points. The points of equal cross section fall approximately on circles which are slightly flattened in the 90° region and are centered on a velocity of slightly less than half of the beam velocity.

We first investigate the question of whether it is possible that the protons are emitted from both the
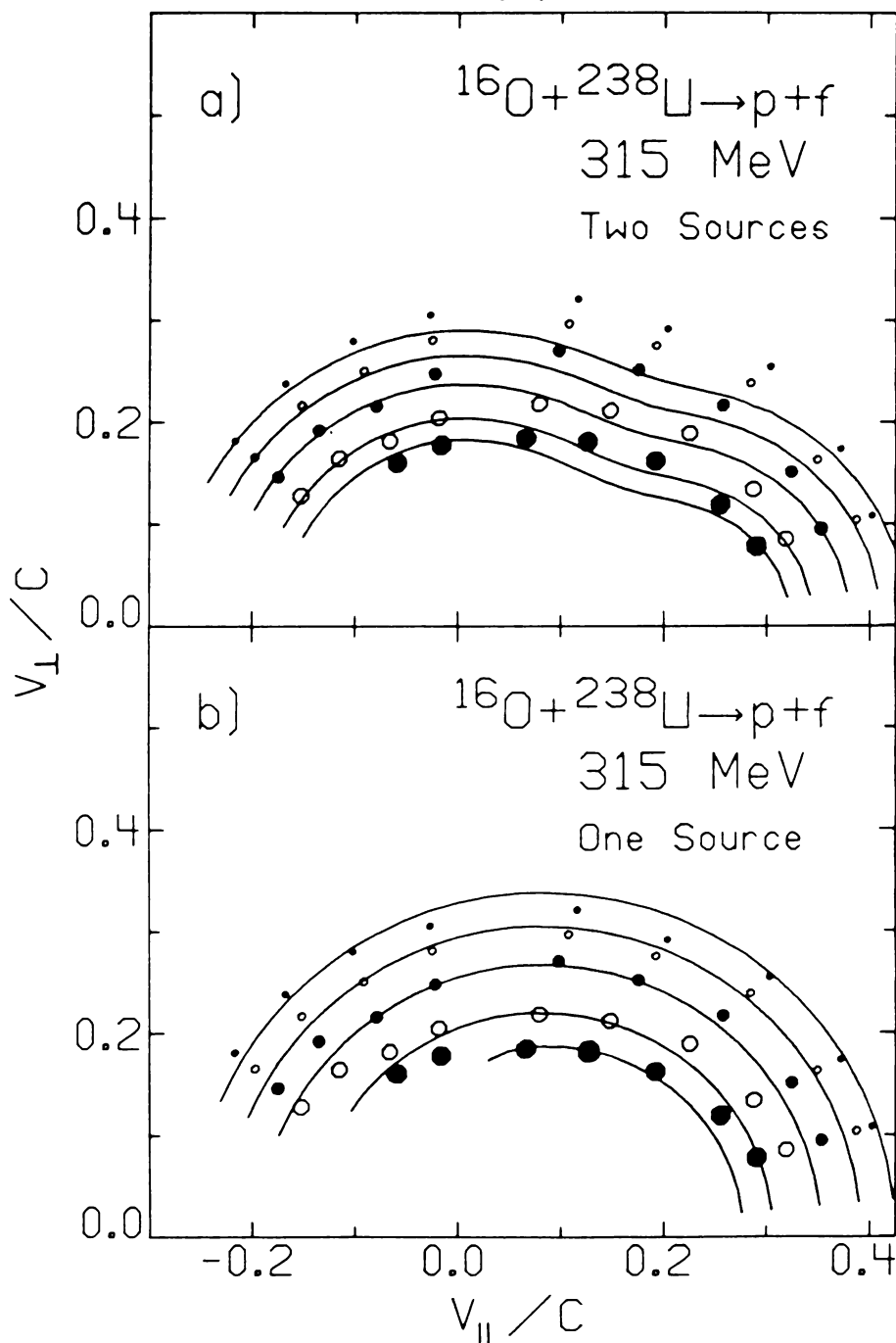
Figure V-23. Contour plot of the Lorentz invariant proton
cross section. The contours are in the ratios
1:4:4:4:2. The experimental data are given by
circles. The curves in part (a) represent the
cross sections calculated for thermal emission
from two sources, one moving with the beam
velocity and the other moving with the
compound nucleus velocity (see also solid
curves in Figure V-25). The curves in part
(b) describe the emission from a single
thermal source moving with slightly less than
half the beam velocity (see solid curves in
Figure V-26).

projectile and the compound nucleus giving a sum distribution which has the appearance of nearly isotropic emission from a single source at an intermediate velocity. In Figure V-24 we present contours of the Lorentz invariant proton cross sections gated on central or peripheral collisions. One might expect that such a gate should separate the compound nucleus contribution (central component) and the projectile contribution (peripheral component). It is evident from the figure that the gated contours do not follow these expectations, although the weaker peripheral component does exhibit a slight enhancement of emission from the projectile. The dominant feature of the Lorentz invariant contours, however, indicates nearly isotropic emission from a source which moves at slightly less than half of the beam velocity.

To be more precise, we assume that light particles are emitted with a Maxwellian distribution in the rest frame of a source [Sy 80] which is at temperature T.

$$N(E) \propto E^{\frac{1}{2}} \exp (-E/T). \qquad (V-9)$$

(Note that we use the $E^{\frac{1}{2}}$ factor corresponding to volume emission [Go 78] instead of the factor E corresponding to surface emission. The difference between the two expressions would hardly be discernible except at low energies.) Transforming into the laboratory and correcting for the Coulomb repulsion of the light particle from the

129
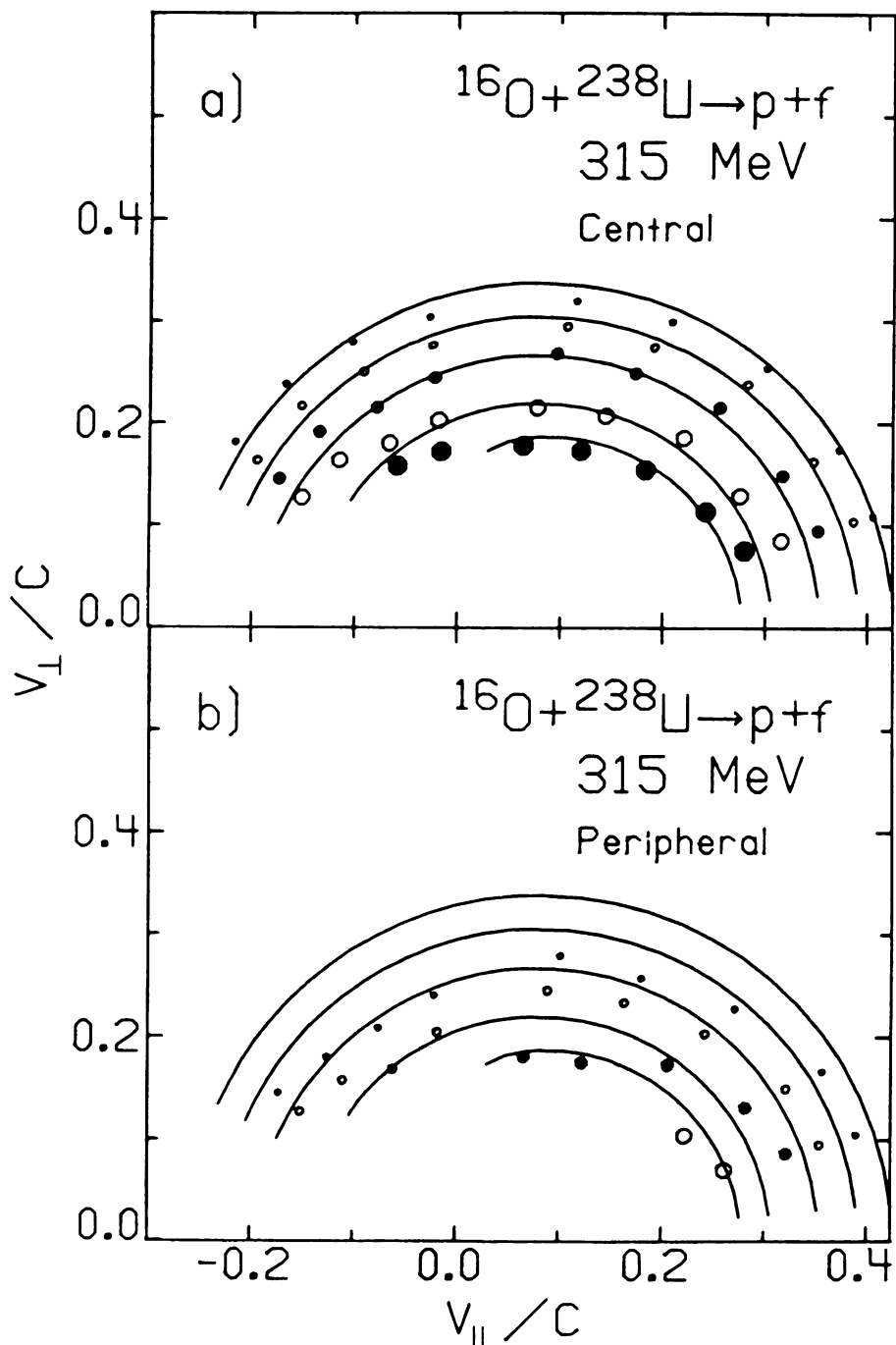
Figure V-24. Contour plot of the Lorentz invariant proton
cross section. The contours are in the ratios
1:4:4:4:2. The curves describe the emission
from a single thermal source moving with
slightly less than half the beam velocity.
The cross sections for "central" collisions
are shown in part (a), the ones for
"peripheral" collisions are shown in part (b).

target residue we obtain non-relativistically

$$\frac{d^2N}{d\Omega dE} = N_o f(v,T,E_c) = N_o (E - ZE_c)^{\frac{1}{2}}$$

$$x \exp \{-[(E - ZE_c) + E_1 - 2E_1^{\frac{1}{2}}(E - ZE_c)^{\frac{1}{2}}\cos\theta]/T\} \qquad (V-10)$$

where $E_1 = \frac{1}{2}mv^2$ is the kinetic energy of a particle at rest in the frame of the moving source, θ is the laboratory angle, N_o is an overall normalization constant, and ZE_c is the Coulomb energy of the light particle with charge Z.

The curves in Figure V-23a represent contours which were produced assuming contributions from two sources

$$\frac{d^2N}{d\Omega dE} = N_{cn}f(v_{cn},T_{cn},E_{c,cn}) + N_p f(v_p,T_p,E_{c,p}) \qquad (V-11)$$

One source was assumed to correspond to emission from the compound nucleus; the corresponding parameters are $v_{cn} = 0.013c$ and $E_{c,cn} = 10$ MeV. The other source was assumed to correspond to emission from the fully accelerated projectile fragments which were assumed to move with the projectile velocity, $v_p = 0.205c$, and have negligible Coulomb barrier, $E_{c,p} = 0$. At the most backward angles, $\theta = 140°$, emission from the projectile is negligible and the parameters for emission from the compound nucleus can be determined rather unambiguously as $T_{cn} = 4.58$ MeV and $N_{cn} = 319$. (This temperature is, of course, too high for true compound nucleus emission). Correspondingly, emission from the compound nucleus gives only minor

contributions to the most forward angles. Here the parameters for projectile emission can be determined rather unambiguously as $T_p = 3.85$ MeV and $N_p = 309$. The resulting energy and angle integrated relative contribution from the projectile-like source was found to be 75% of the compound nucleus source contribution. The calculation reproduces the data very well at forward and backward angles but significantly underestimates the cross section in the 90° region. Furthermore, the overall shapes of the contour lines predicted by this calculation are not observed experimentally.

A better description of the experimental data may be obtained by assuming isotropic emission in a rest frame which moves with a velocity intermediate between projectile and target. The temperature of such a source as well as its velocity are treated as free parameters to give an optimum description of the data. The results of such a calculation, obtained with Eq. (V-10), are shown in Figure V-23b (and, for comparison, also in Figures V-24a and V-24b). The Coulomb energy was fixed at $E_c = 10$ MeV and the source which best reproduced the proton energy spectra at all angles was determined to have a temperature of $T = 7.0$ MeV and a velocity of slightly less than half of the beam velocity ($v = 0.091c$). The single source calculation gives satisfactory fits for large transverse momenta but becomes slightly worse in the forward and backward directions. The overall agreement is seen to be surprisingly good.

To make the discussion more quantitative we compare these calculations with the measured energy spectra for reactions of $^{16}O + ^{238}U$ at 315 MeV. In Figure V-25 the proton energy spectra are shown with the cross sections calculated using Eq. (V-11) for two moving sources. The solid curves were obtained with the same parameters as were used for the calculated contours of Figure V-23a. The dashed curves correspond to emission from the projectile at the distance of closest approach to the target. The projectile-like source was assumed to move with the velocity, $v_p = 0.18c$, corresponding to the velocity of the ^{16}O nuclei after deceleration in the Coulomb field of the target nucleus. A Coulomb barrier of $E_{c,p} = 10$ MeV was chosen and a temperature of $T = 3.94$ MeV was obtained by fitting the proton data at 15°. In this case the integrated contribution from the projectile-like source was 59% of the compound nucleus source contribution. With either calculation the agreement with the data is quite good at both forward and backward angles but disagrees by as much as an order of magnitude in the intermediate angle region.

In Figure V-26 the solid curves have been calculated using Eq. (V-10) with the same parameters as for the calculated contours of Figure V-23b. The overall agreement with the proton data is seen to be remarkably good assuming only a single moving source. The agreement is certainly no worse than for the two source calculation.
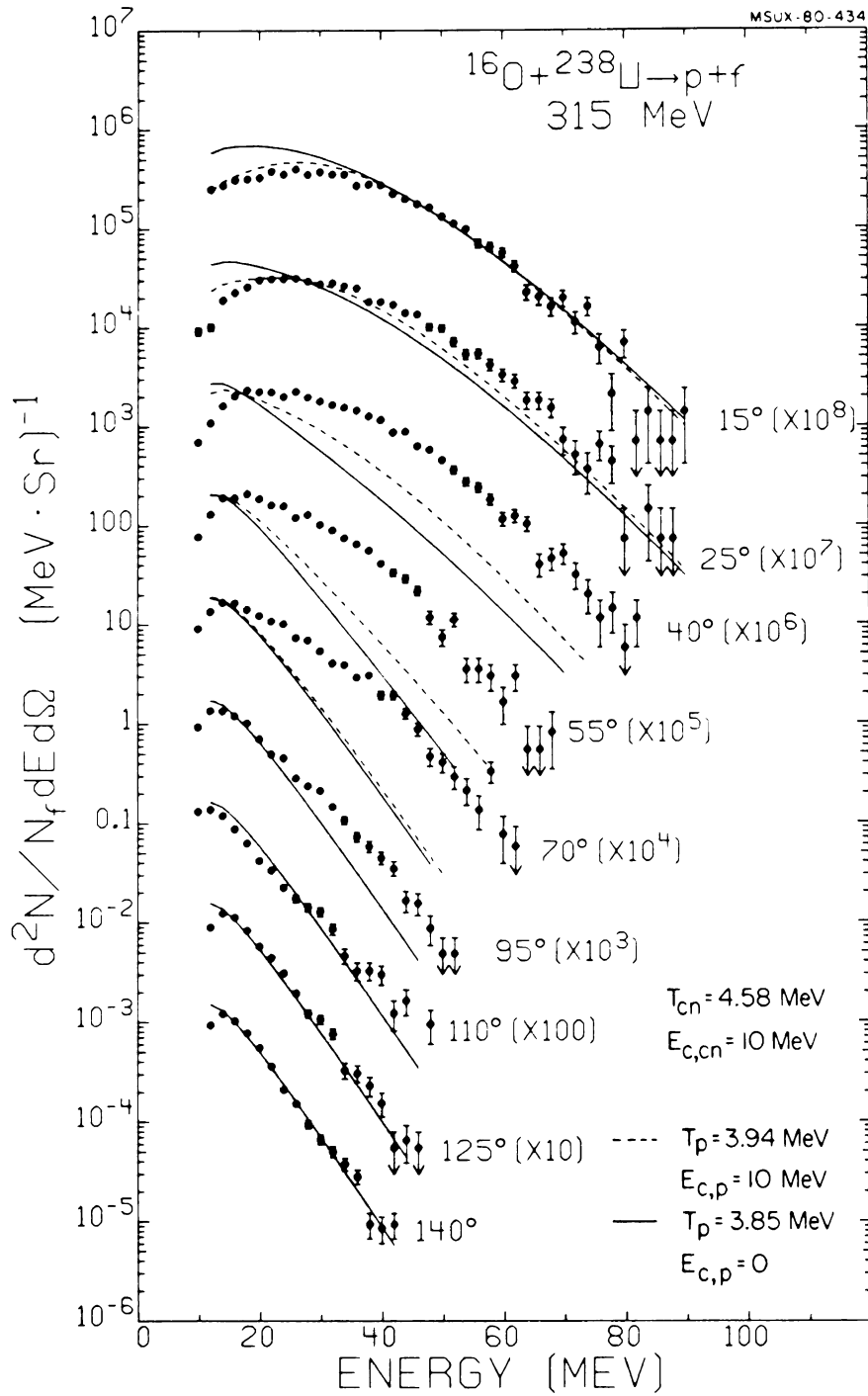
Figure V-25. Energy spectra of protons detected in the reaction ^{238}U (^{16}O, pf) at 315 MeV. The curves have been calculated by assuming contributions from two sources, each given by Eq. (V-10). One source is associated with a projectile-like fragment and the other with a target residue.
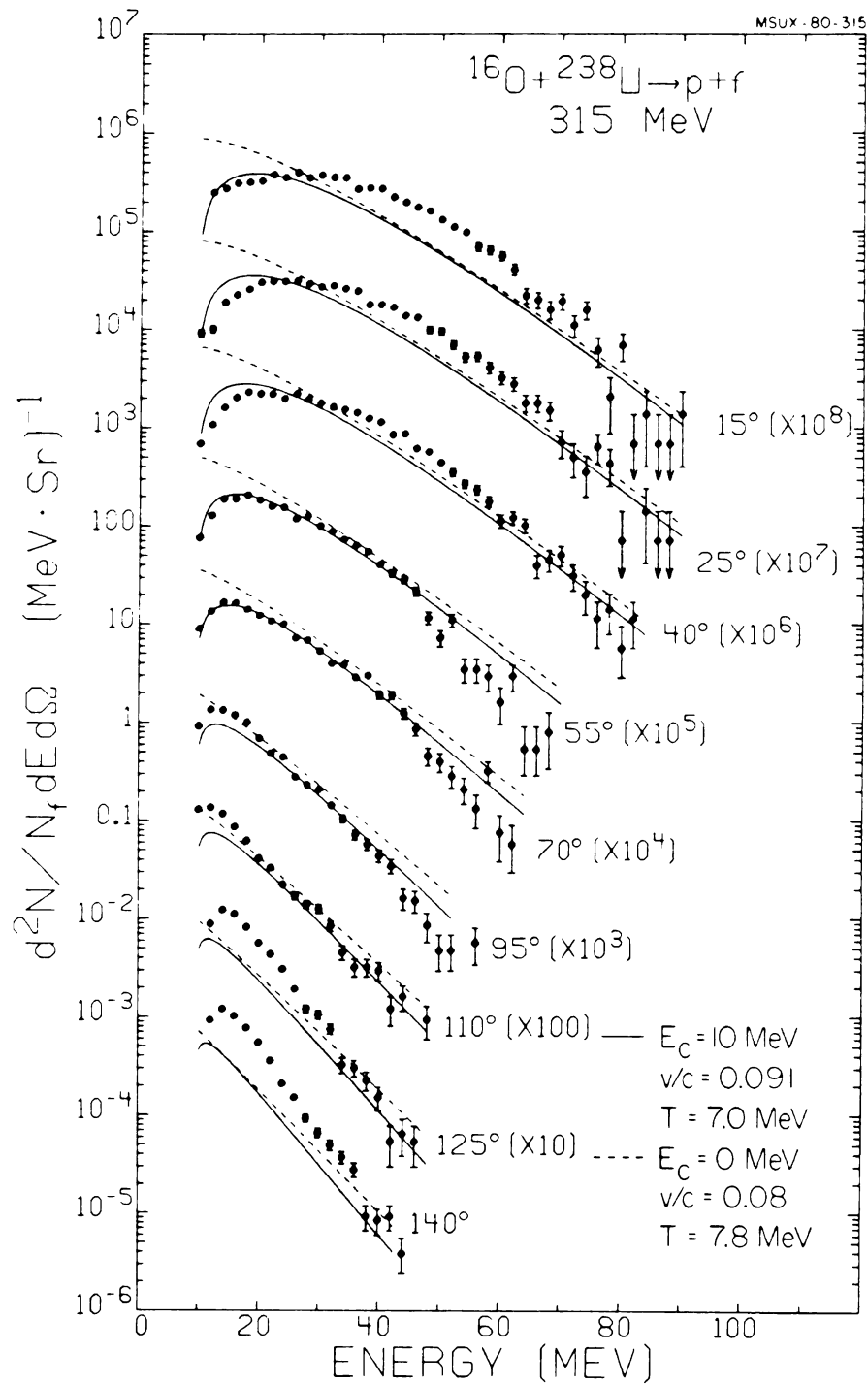
Figure V-26. Energy spectra of protons detected in the
reaction ^{238}U (^{16}O, pf) at 315 MeV. The
curves have been calculated with the moving
source model of Eq. (V-10). The laboratory
angles and moving source parameters are
indicated.

Obviously, better reproduction of the data could be obtained by using two sources in which both source velocities were allowed to vary or by using three sources with one source allowed to vary freely and the other two fixed at the compound nucleus and projectile velocities. At this point such a procedure would lead to complications and uncertainties of interpretation. Therefore, we proceed using the single source model and try to assess the significance of the resulting parameters.

It must be remembered that the dominant process of light particle emission involves the transfer of nearly the entire beam momentum to the target residue (see Sections V.A.2 and V.B.1). As a consequence, any substantial source of nucleons must ultimately be absorbed by the target nucleus. This observation would preclude the existence of an independently moving thermal source as suggested by the fireball [We 76] and firestreak [My 78] models for collisions at relativistic energies. The successful application of the moving source parameterization should not, therefore, be taken as evidence for thermal emission from a hot gas of nucleons separated from the target nucleus. Instead, it simply indicates that the light particle velocities are randomized in a rest frame different from the compound nucleus frame.

In Figures V-26, V-27, V-28, and V-29 the curves were calculated by a least-squares minimization using Eq. (V-10)
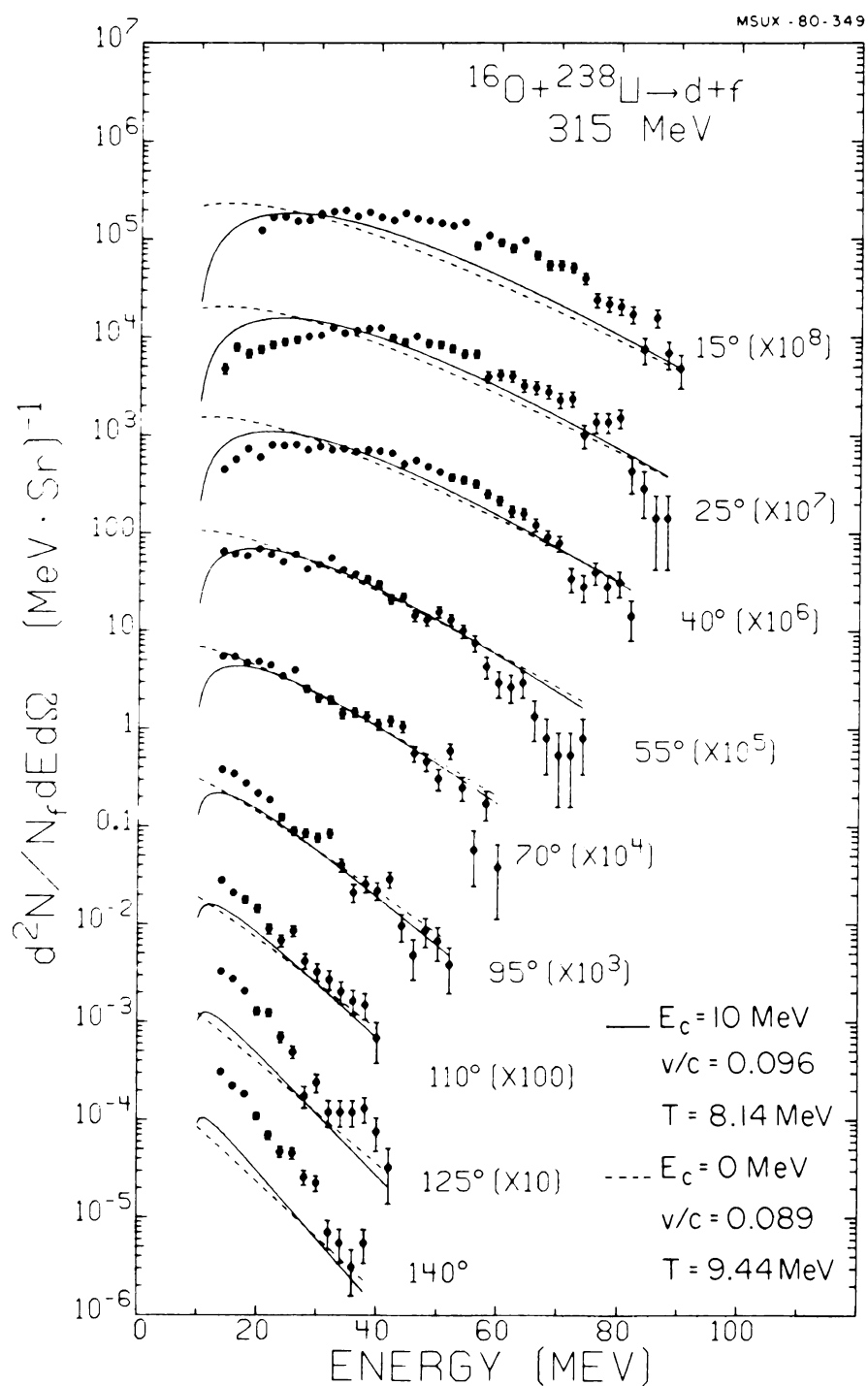
Figure V-27. Energy spectra of deuterons detected in the reaction ^{238}U (^{16}O, df) at 315 MeV. The curves have been calculated with the moving source model of Eq. (V-10). The laboratory angles and moving source parameters are indicated.
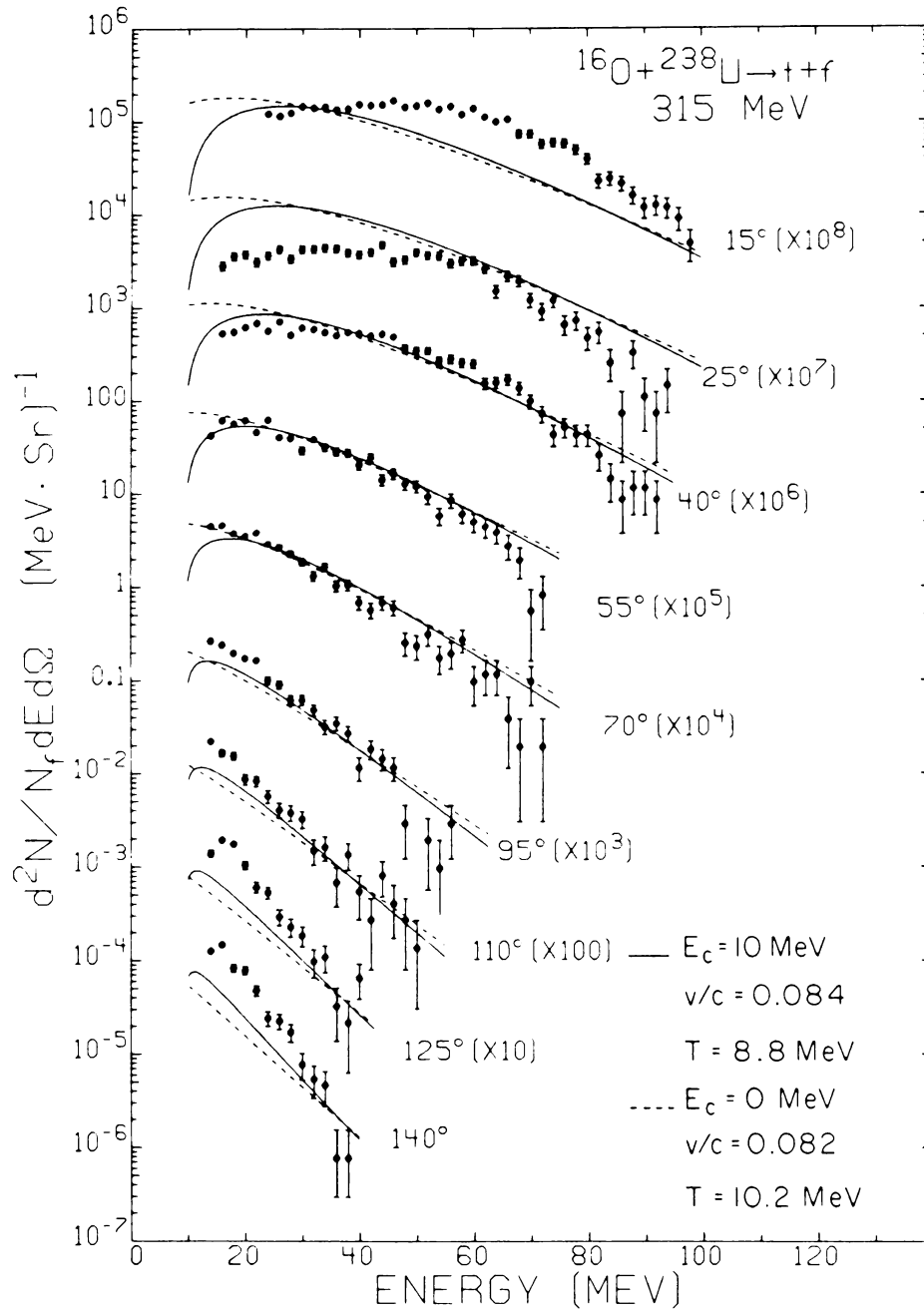
Figure V-28. Energy spectra of tritons detected in the
reaction ^{238}U (^{16}O, tf) at 315 MeV. The
curves have been calculated with the moving
source model of Eq. (V-10). The laboratory
angles and moving source parameters are
indicated.
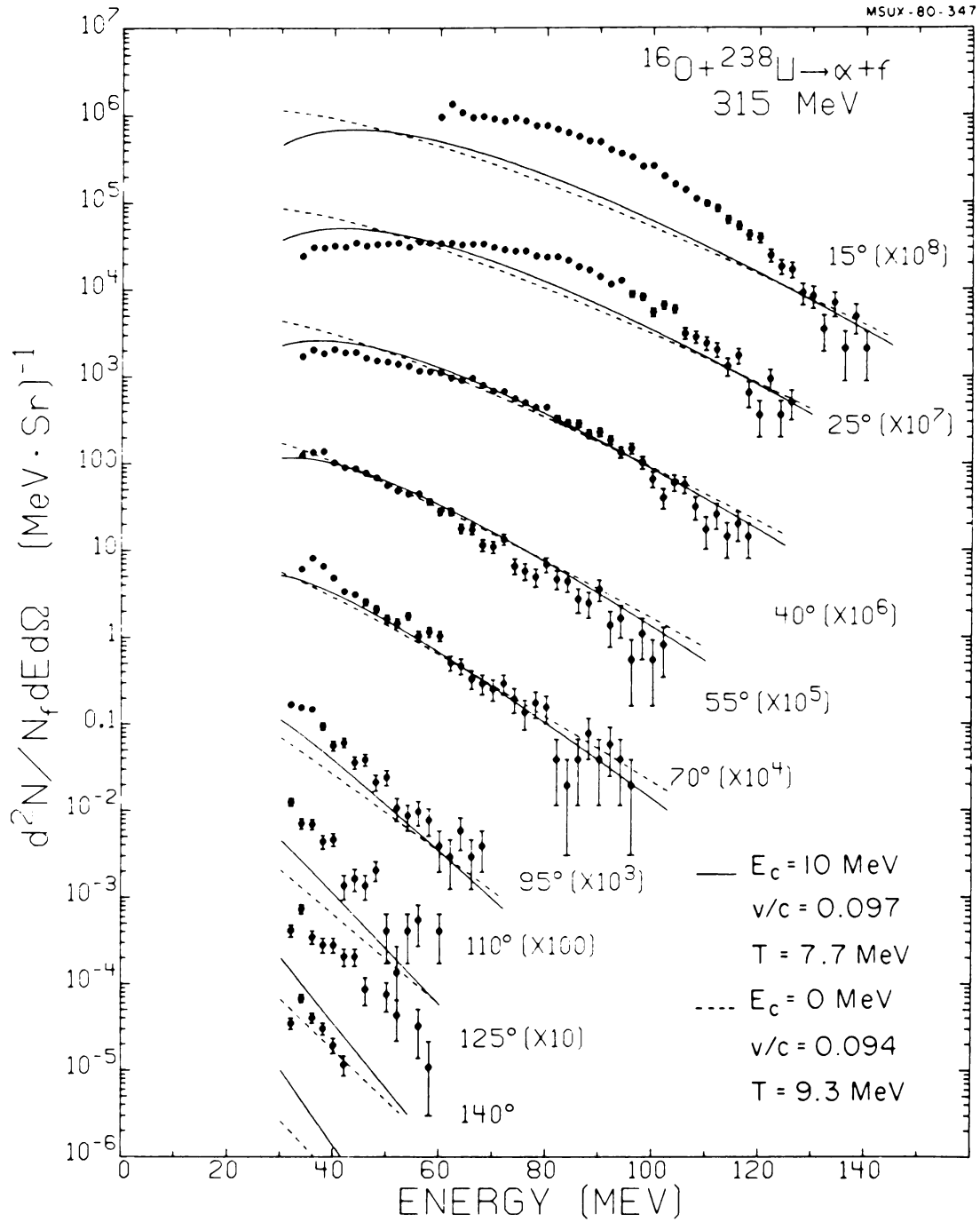
Figure V-29. Energy spectra of alpha-particles detected in the reaction ^{238}U (^{16}O, αf) at 315 MeV. The curves have been calculated with the moving source model of Eq. (V-10). The laboratory angles and moving source parameters are indicated.

for a single moving source. The solid curves were obtained using a Coulomb repulsion per unit charge which had been chosen as $E_C = 10$ MeV. The dashed curves have been calculated by neglecting the Coulomb repulsion from the target residue. Clearly, the description of the data in the low energy region is better when the Coulomb effects are taken into account.

The thermal sources which best describe the light particle spectra are found to have very similar velocities and temperatures. The rest frames in which the light particle emission appears isotropic have velocities of $v/c = 0.091$, 0.096, 0.084, and 0.097 for p,d,t, and α-particles, respectively. It is interesting that these velocities closely coincide with the velocity, $v = 0.089c$, of the nucleon-nucleon center of mass frame if the slowing down of the ^{16}O nuclei in the Coulomb field of the ^{238}U target nuclei is taken into account. Source temperatures of $T = 7.0$, 8.14, 8.8 and 7.7 MeV are determined for p,d,t, and α-particles, respectively. These temperatures are significantly larger than the temperature $T_{cn} \simeq 3$ MeV expected for the compound nucleus.

In order to better assess the significance of the moving source parameters we have also used the moving source model to describe the inclusive light particle spectra. As seen by the solid curves of Figures V-30, V-31, and V-32, this parameterization provides a good description of the
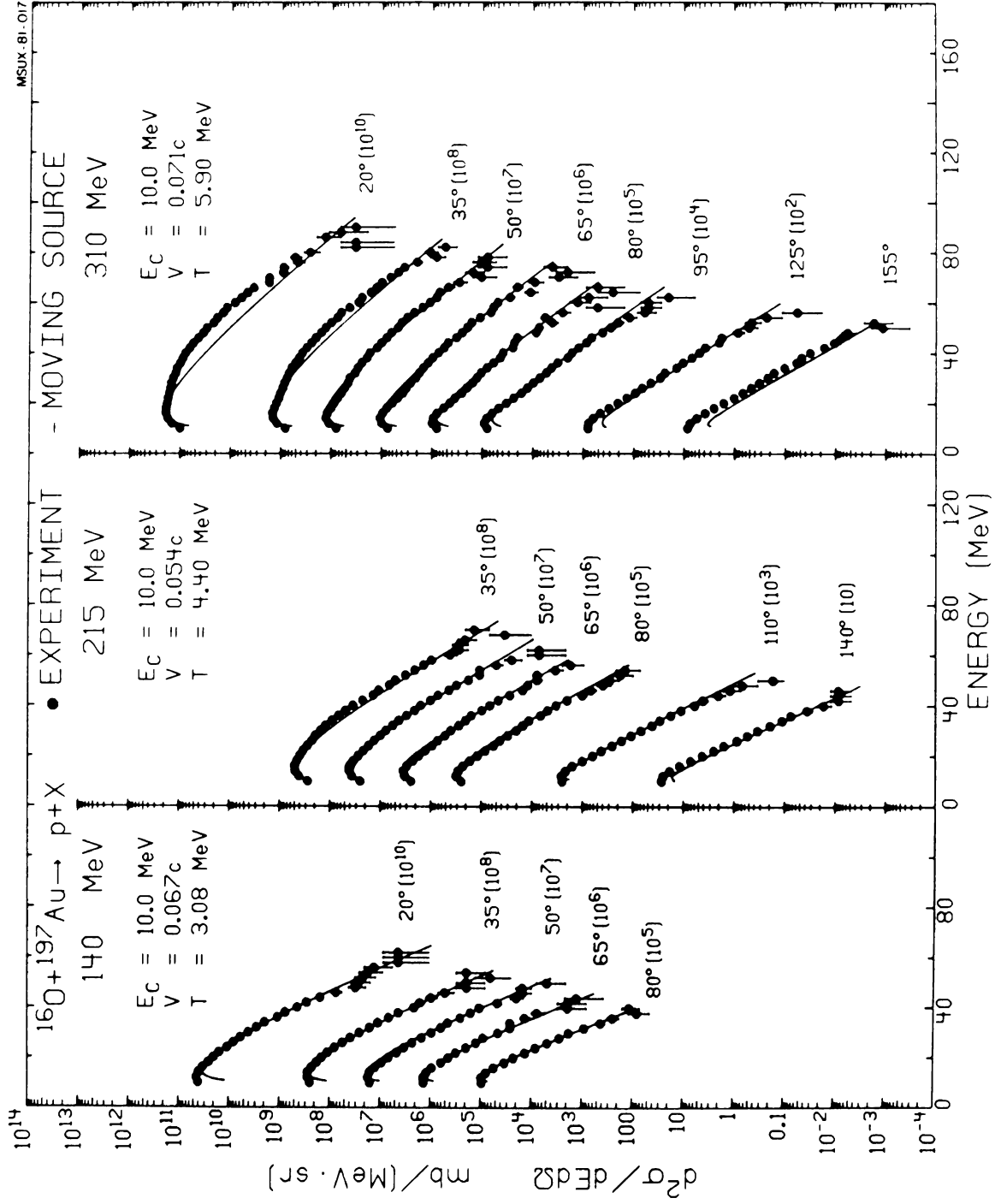
Figure V-30. Energy spectra of protons in the ^{197}Au $(^{16}O, p)$ reaction. The data are fitted with the moving source model of Eq. (V-10). The laboratory angles and the moving source parameters are indicated.
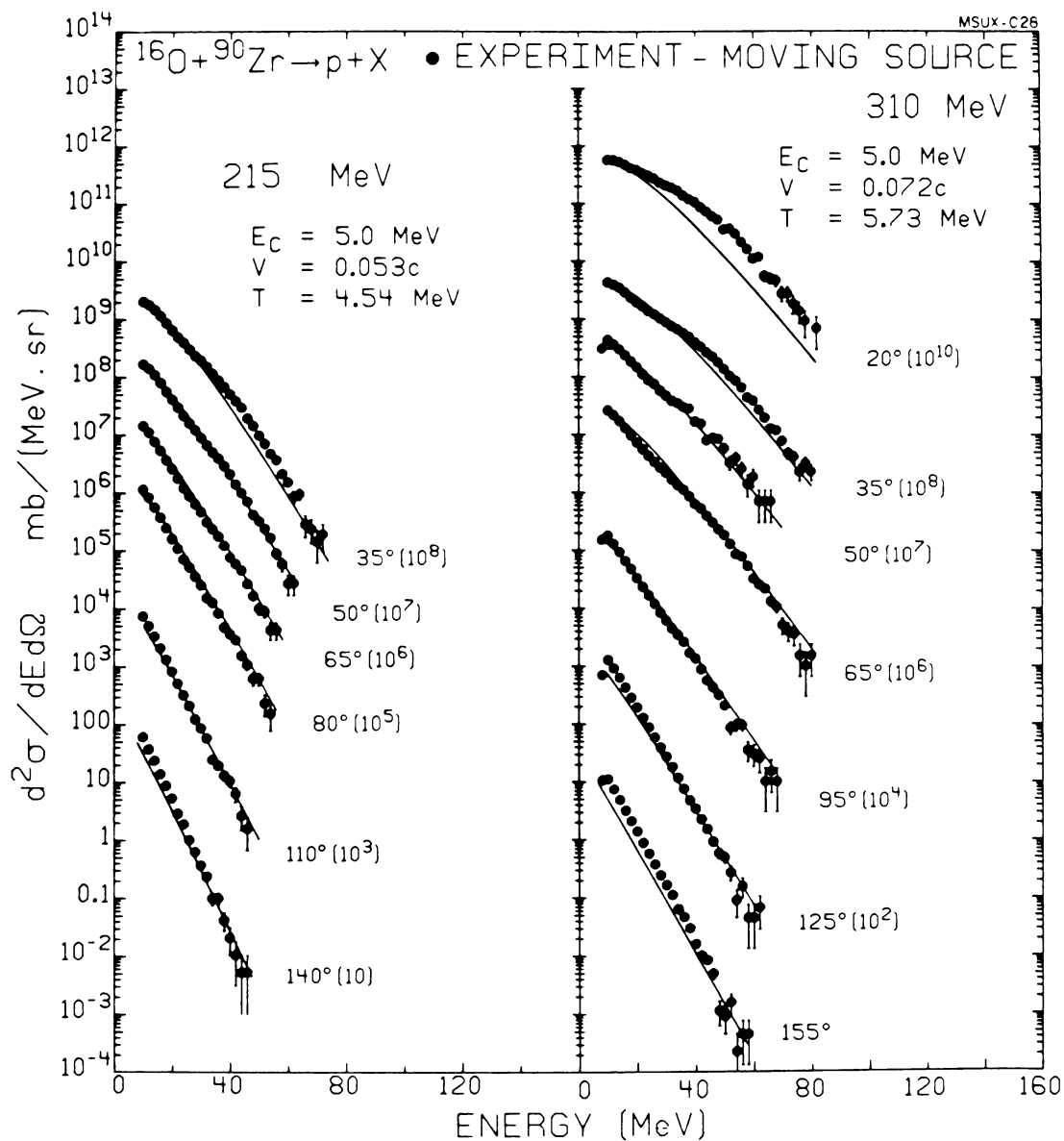
Figure V-31. Energy spectra of protons in the ^{90}Zr (^{16}O, p) reaction. The data are fitted with the moving source model of Eq. (V-10). The laboratory angles and the moving source parameters are indicated.
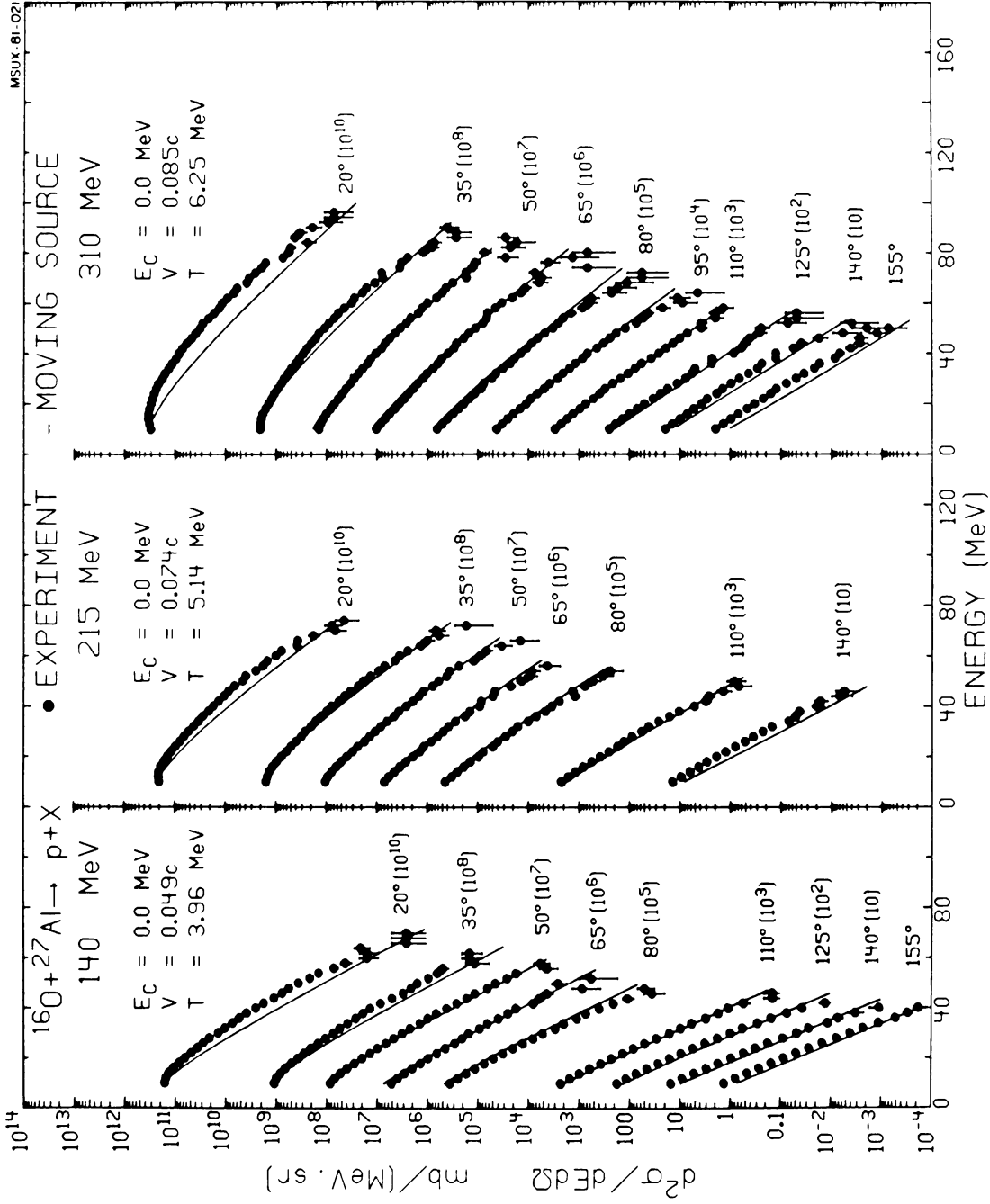
Figure V-32. Energy spectra of protons in the ^{27}Al (^{16}O, p) reaction. The data are fitted with the moving source model of Eq. (V-10). The laboratory angles and the moving source parameters are indicated.

proton spectra for all targets and incident energies. The temperatures obtained are typically greater than those of the compound nucleus and the velocities are intermediate between the projectile and compound nucleus velocity. In this analysis, the temperature and velocity parameters have been determined by a least-squares minimization while the Coulomb threshold parameters E_C have been chosen at values of $E_C = 0$, 5, and 10 MeV for the Al, Zr, and Au targets, respectively. In the fitting procedure each data point was given an additional 10% error to reduce the statistical weight of the low energy regions of the spectra. As a result, the high energy regions of the inclusive spectra are fit better than the high energy regions of the spectra from the $^{16}O + ^{238}U$ reaction. This also explains the differences in the extracted temperature parameters between the similar reactions $^{16}O + ^{238}U$ at 315 MeV and $^{16}O + ^{197}Au$ at 310 MeV (see for example, Figures V-26 and V-30). An example of the shape of the x^2-minima is shown in Figure V-33 for the $^{197}Au(^{16}O,p)$ reaction at 310 MeV. Here the reduced x^2-values are shown for variations in the temperature, velocity and Coulomb parameters. In general, changes of about 5% in the temperature or about 10% in the velocity parameter increase the reduced x^2-values by about 20%. In addition, the velocity parameter is found to be quite sensitive to the angular range over which the data are fit. For example, by considering only the region
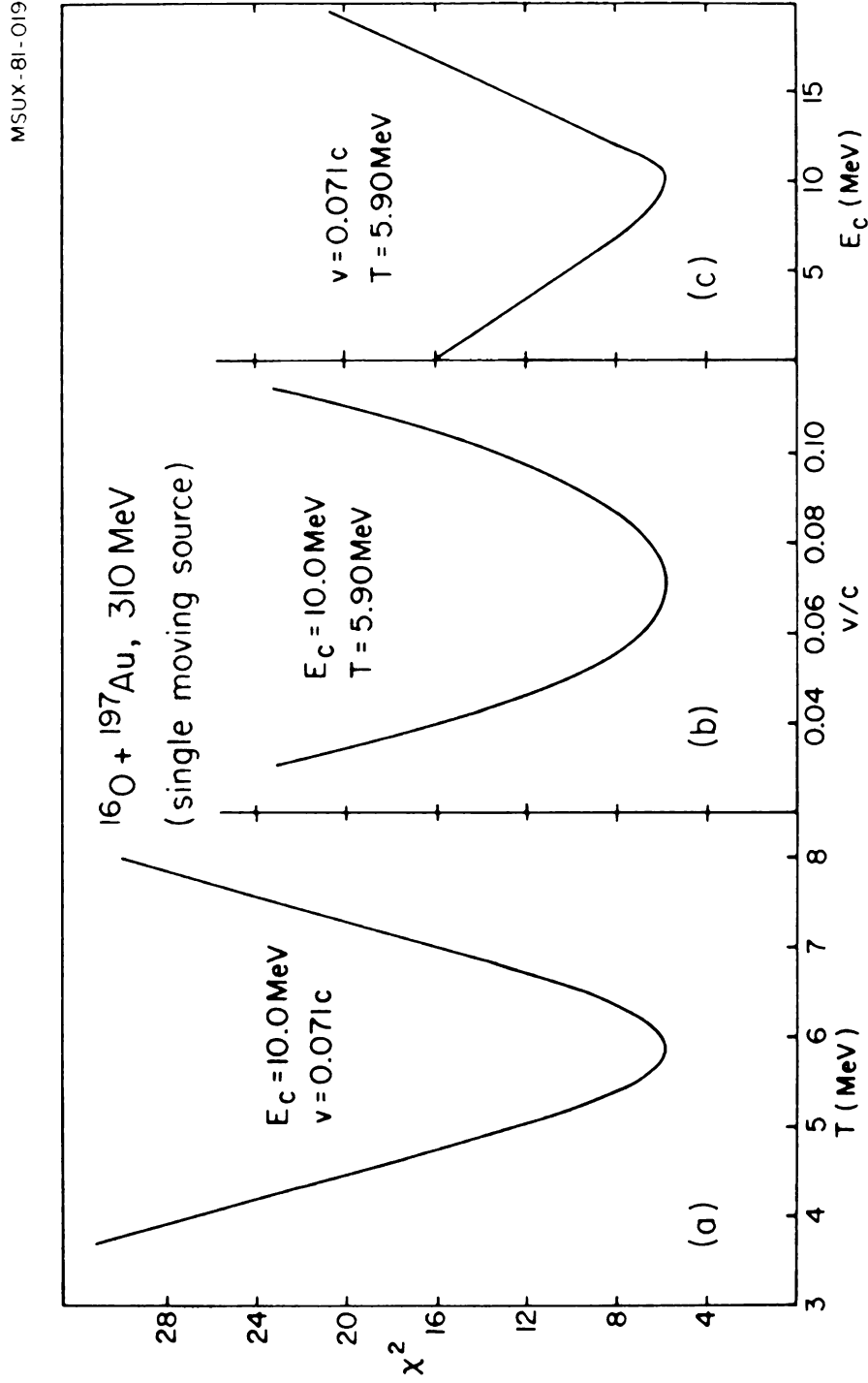
Figure V-33. Parameter dependence of the reduced χ^2-value for the moving source fit of the reaction ^{197}Au (^{16}O, p) at 310 MeV (see Figure V-30). The variations of the reduced χ^2-value for independent variations of the temperature, velocity, and Coulomb parameters of Eq. (V-10) are shown.

from 20° - 80° for the $^{27}Al(^{16}O,p)$ reaction at 140 MeV, values of v = 0.071c and T = 3.84 MeV were obtained as compared to the values of v = 0.049c and T = 3.96 MeV obtained by considering the full angular range. This observation explains the comparatively large source velocity extracted for reactions on the ^{197}Au target at 140 MeV where only a restricted angular range of data was measured.

Energy spectra and moving source calculations for deuteron, triton, and alpha-particle emission are presented in Figures V-34, V-35, V-36, Figures V-37, V-38, V-39, and Figures V-40, V-41, V-42, respectively. The moving source parameterization gives quite a reasonable description of the composite particle energy spectra although the reproduction of the angular dependence becomes somewhat worse with increasing mass of the outgoing composite particle. The most persistent discrepancy between the moving source model and experiment occurs at forward angles for the higher incident energies. Here the increasing contributions from direct processes such as projectile breakup are likely to become significant [Na 81, Na 81a].

A summary of the moving source parameters extracted from the inclusive light particle energy spectra is given in Table V-4. From this table it is observed that, for each reaction, the extracted velocity parameters are very similar for all light particle species whereas the tempera-ture parameters are slightly lower for protons than for
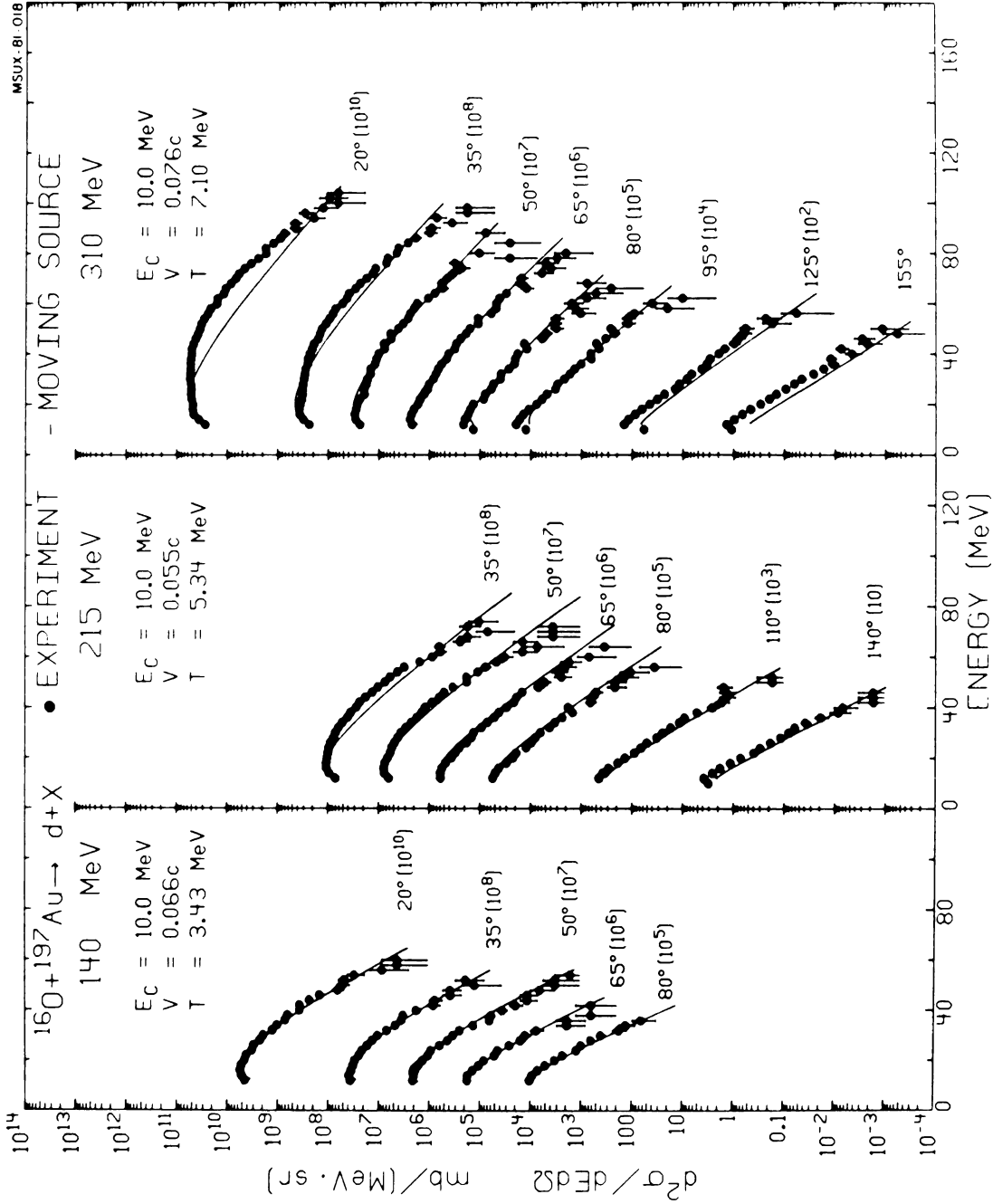
Figure V-34. Energy spectra of deuterons in the ^{197}Au (^{16}O, d) reaction. The data are fitted with the moving source model of Eq. (V-10). The laboratory angles and the moving source parameters are indicated.

147
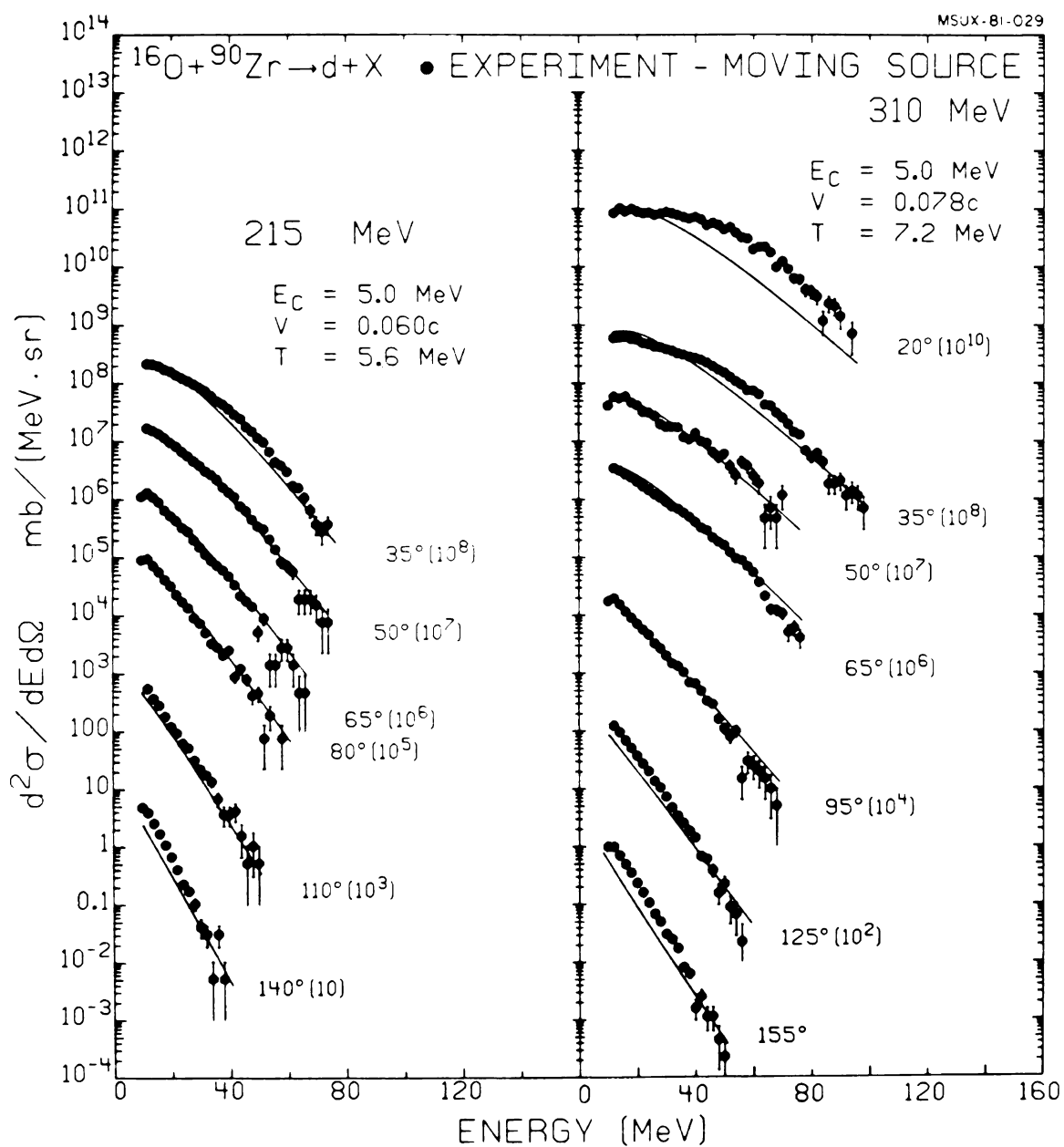
Figure V-35.   Energy spectra of deuterons in the
                ^{90}Zr (^{16}O, d) reaction. The data are fitted
                with the moving source model of Eq. (V-10).
                The laboratory angles and the moving source
                parameters are indicated.
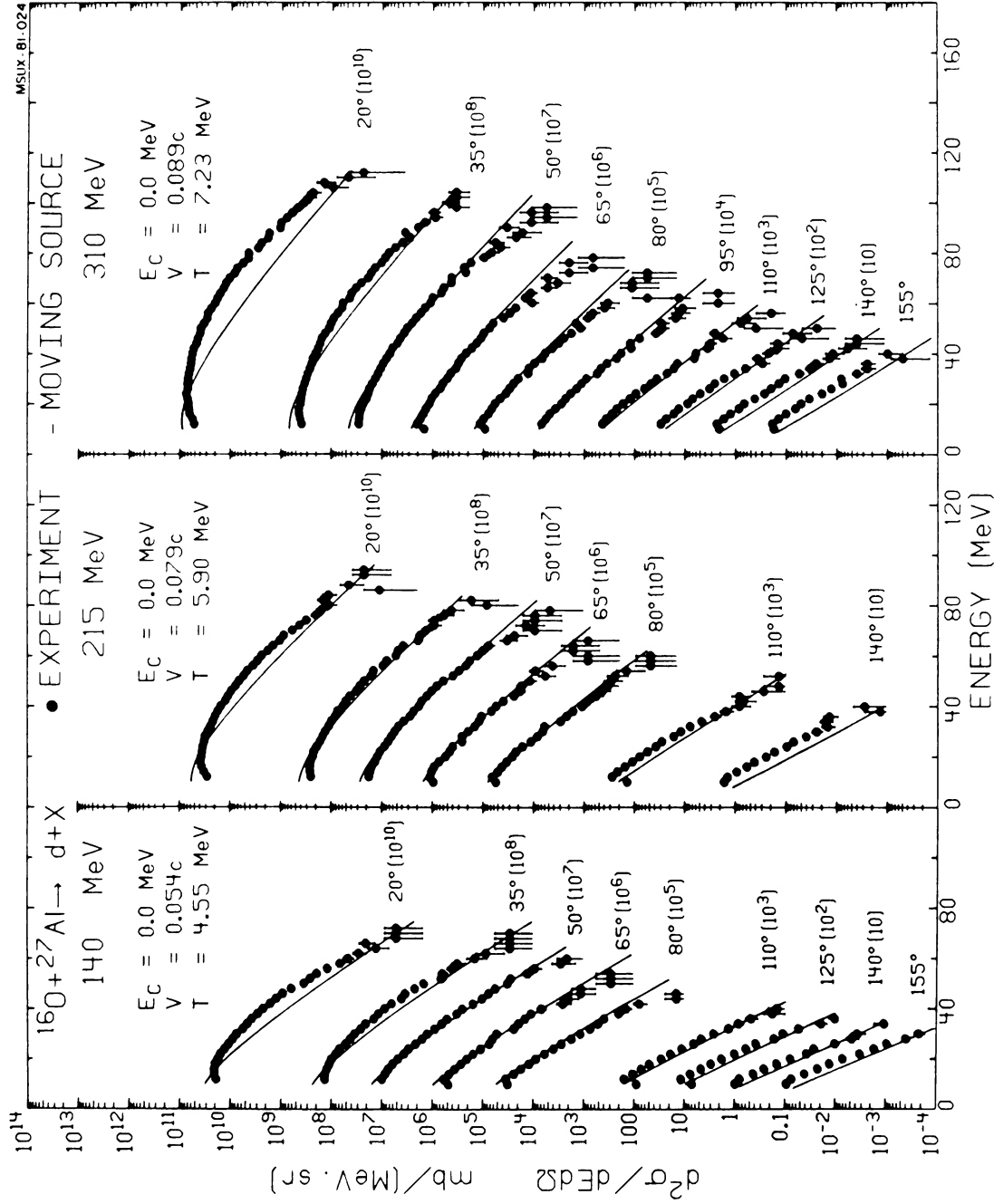
Figure V-36. Energy spectra of deuterons in the ^{27}Al (^{16}O, d) reaction. The data are fitted with the moving source model of Eq. (V-10). The laboratory angles and the moving source parameters are indicated.
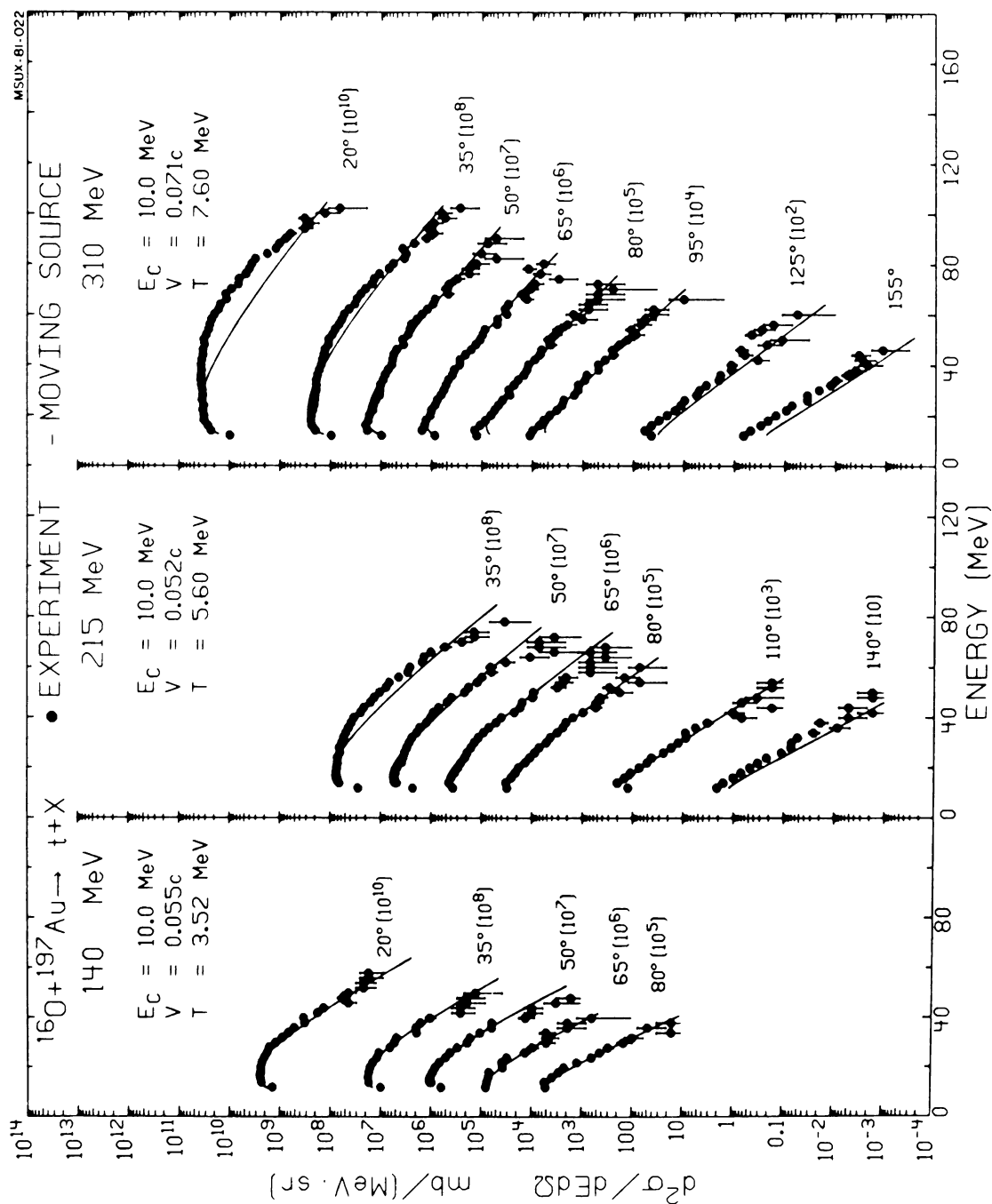
Figure V-37. Energy spectra of tritons in the ^{197}Au $(^{16}O, t)$ reaction. The data are fitted with the moving source model of Eq. (V-10). The laboratory angles and the moving source parameters are indicated.

MSUX-81-027

$^{16}O + ^{90}Zr \rightarrow t + X$ • EXPERIMENT - MOVING SOURCE

310 MeV

E_c = 5.0 MeV
V = 0.073c
T = 8.2 MeV

215 MeV

E_c = 5.0 MeV
V = 0.059c
T = 6.2 MeV

$20°$ (10^{10})

$35°$ (10^8)

$50°$ (10^7)

$65°$ (10^6)

$80°$ (10^5)

$95°$ (10^4)

$110°$ (10^3)

$125°$ (10^2)

$140°$ (10)

$155°$

$d^2\sigma/dEd\Omega$ mb/(MeV·sr)

ENERGY (MeV)
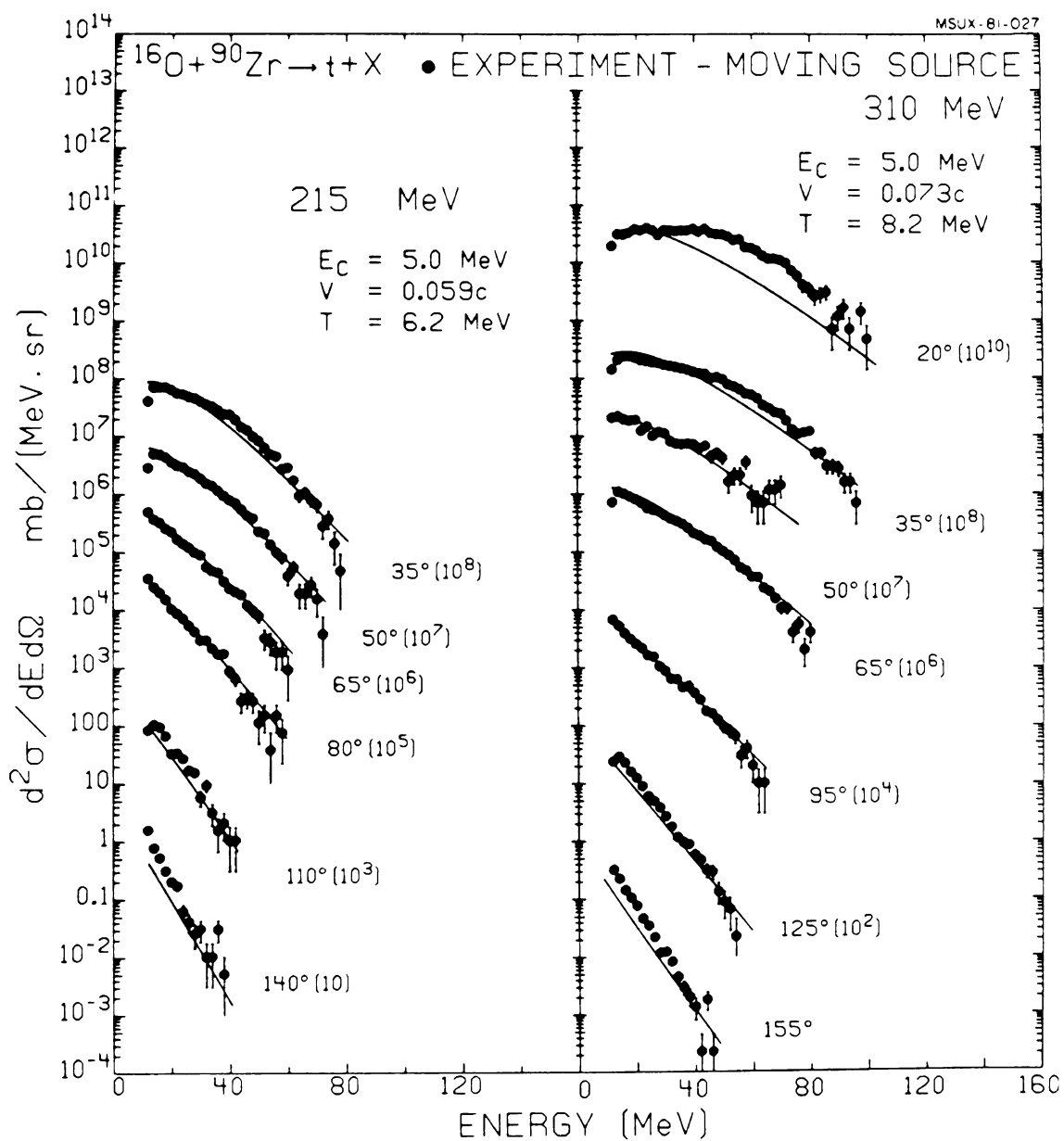
Figure V-38. Energy spectra of tritons in the ^{90}Zr (^{16}O, t) reaction. The data are fitted with the moving source model of Eq. (V-10). The laboratory angles and the moving source parameters are indicated.
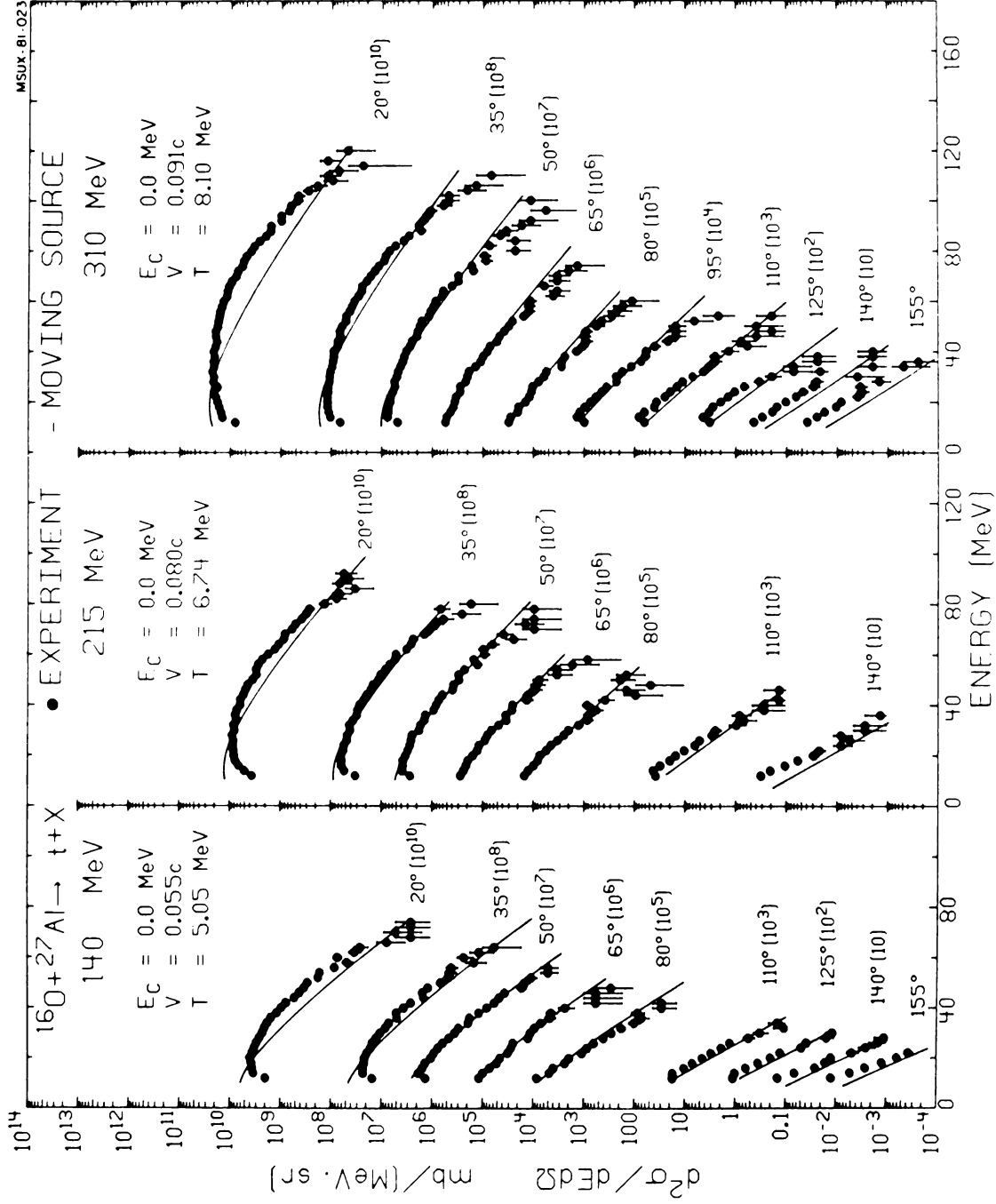
Figure V-39. Energy spectra of tritons in the ^{27}Al (^{16}O, t) reaction. The data are fitted with the moving source model of Eq. (V-10). The laboratory angles and the moving source parameters are indicated.
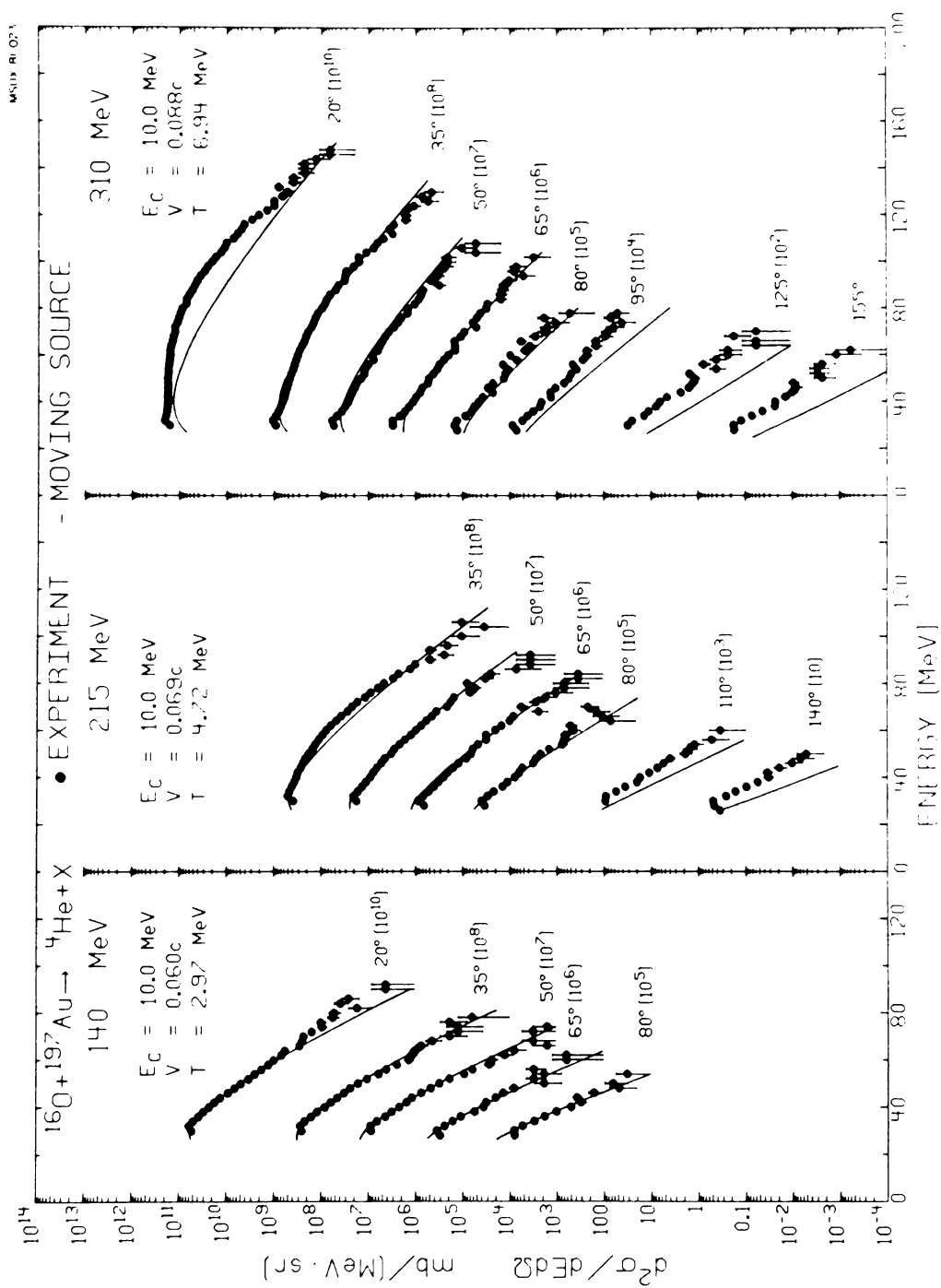
Figure V-40. Energy spectra of alpha-particles in the ^{197}Au $(^{16}$O, $\alpha)$ reaction. The data are fitted with the moving source model of Eq. (V-10). The laboratory angles and the moving source parameters are indicated.

Figure V-41. Energy spectra of alpha-particles in the ^{90}Zr (^{16}O, α) reaction. The data are fitted with the moving source model of Eq. (V-10). The laboratory angles and the moving source parameters are indicated.
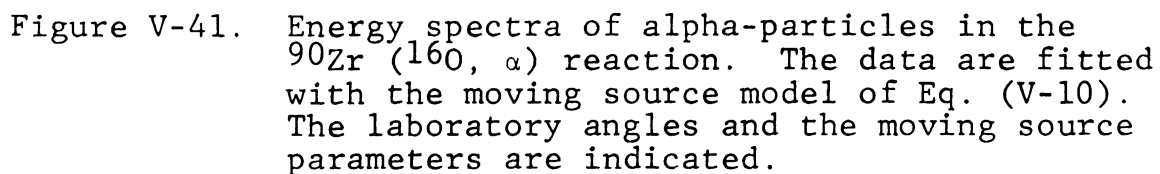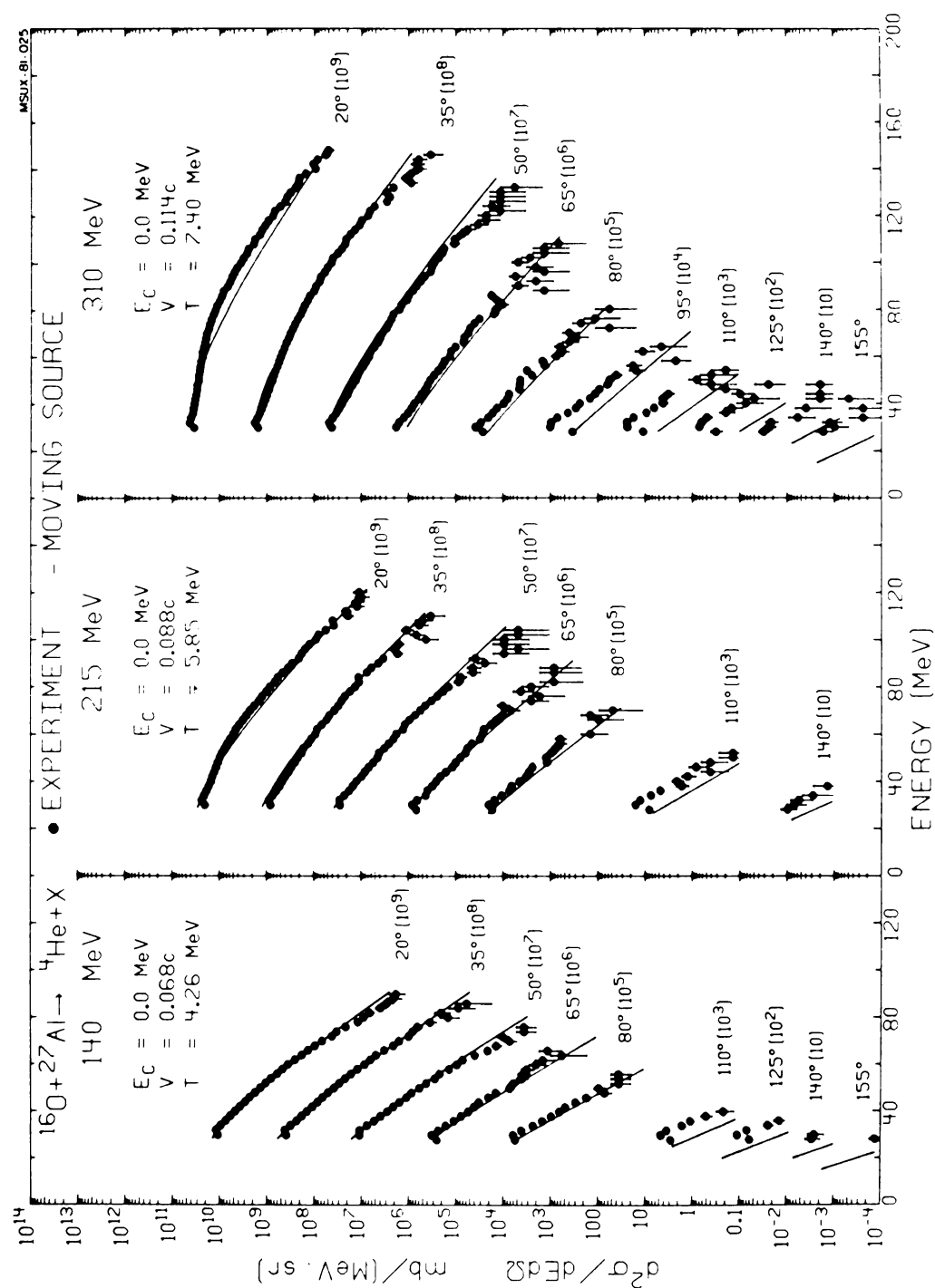
Figure V-42. Energy spectra of alpha-particles in the ^{27}Al $(^{16}O, \alpha)$ reaction. The data are fitted with the moving source model of Eq. (V-10). The laboratory angles and the moving source parameters are indicated.

Table V-4. Moving source parameters used in calculations of Figures V-30 through V-42.

Target	Energy(MeV)	Particle	N_0[a)	v/c[b)	$T(MeV)$[c)	$\sigma(mb)$[d)
^{197}Au	140	p	2.01	.067	3.08	121
	140	d	.28	.066	3.43	20
	140	t	.146	.055	3.52	11
	140	α	2.74	.060	2.97	156
	215	p	4.32	.054	4.40	444
	215	d	.71	.055	5.34	98
	215	t	.519	.052	5.60	77
	215	α	3.04	.069	4.72	347
	310	p	9.62	.071	5.90	1535
	310	d	2.28	.076	7.10	480
	310	t	1.34	.071	7.60	313
	310	α	4.38	.088	6.94	892
^{90}Zr	215	p	12.7	.053	4.54	1368
	215	d	1.47	.060	5.62	218
	215	t	.474	.059	6.23	82

Table V-4. (con't.)

Target	Energy(MeV)	Particle	N_o^a	v/c^b	$T(MeV)^c$	$\sigma(mb)^d$
^{90}Zr	215	α	4.02	.066	5.67	604
	310	p	22.4	.072	5.73	3421
	310	d	3.86	.078	7.23	836
	310	t	1.34	.073	8.16	348
	310	α	6.47	.087	8.22	1698
^{27}Al	140	p	19.0	.049	3.96	1667
	140	d	1.91	.054	4.55	206
	140	t	.284	.055	5.05	36
	140	α	14.7	.068	4.26	1439
	215	p	13.3	.074	5.14	1726
	215	d	2.40	.079	5.90	383
	215	t	.460	.080	6.74	90
	215	α	11.7	.088	5.85	1844
	310	p	15.2	.085	6.25	2645
	310	d	3.33	.089	7.23	721

Table V-4. (con't.)

Target	Energy(MeV)	Particle	N_o [a]	v/c [b]	$T(MeV)$ [c]	$\sigma(mb)$ [d]
^{27}Al	310	t	.834	.091	8.10	214
	310	α	13.6	.114	7.39	3042

a) Units of mb/((MeV)$^{3/2}$sr).
b) Typically ±10% uncertainty.
c) Typically ±5% uncertainty.
d) Calculated using Eq. (V-13) of text.

the composite particles. These features, as well as the dependence of the parameters on target and incident energy, will be discussed in detail in Section V.E.3.

2. Angular Distributions

The angular distribution expected within the moving source parameterization can be obtained by integrating Eq. (V-10) over energy. With a low-energy threshold, E_T, the following expression for the moving source angular distribution is obtained

$$\frac{d\sigma}{d\Omega} = \frac{N_o}{2\pi} (\pi T)^{3/2} e^{-E_1 \sin^2\Theta/T} \{ (1+2x^2)$$

$$+ [(1+2x^2) \mathrm{erf}(x-y) + \frac{2}{\pi^{\frac{1}{2}}} (x+y) e^{-(x-y)^2}] \} \qquad (V-12)$$

where $x = (E_1/T)^{\frac{1}{2}}\cos\Theta$ and $y = [(E_T-E_c)/T]^{\frac{1}{2}}$. For $E_T = E_c$ we have $y = 0$ and observe that the first term in Eq. (V-12) is symmetric in x about 90° while the second term is anti-symmetric and accounts for the observed forward peaking of the angular distributions. The calculated moving source angular distributions are shown by the dashed curves in Figures V-10, V-11, and V-12. These curves have been calculated at 310 MeV incident energy for all light particles with the indicated low-energy thresholds and using the proton velocity and temperature parameters (see Table V-4). The differences in the angular distributions of the various light particles are essentially accounted for by the kinematic effect of the differing

masses. This is reflected in the dependence of Eq. (V-12)
on the ratio of $E_1/T = \frac{1}{2}mv^2/T$ which reduces to a pure mass
dependence due to the similarity of the velocity and
temperature parameters for all particle types in a
particular reaction (see Table V-4). Within this model,
one expects the source velocity to be the same for all
light particles while the thermal velocity should be
inversely proportional to the particle mass. As a conse-
quence, the angular distributions exhibit steeper slopes
with increasing mass of the emitted particles.

The moving source light particle cross sections can be
calculated by integrating Eq. (V-10) over energy from
$E = E_c$ and over angles to obtain

$$\sigma = 2N_o(\pi T)^{3/2}. \qquad\qquad (V-13)$$

These calculated cross sections have been included in
Table V-4 and should be compared with those listed in
Table V-1 as an indication of the amount of cross section
falling below the low-energy cut-offs introduced in
Table V-1.

3. Systematics of Moving Source Parameters

The dependence of the moving source parameters on
target and incident energy is shown in Figure V-43. The
temperature and velocity parameters exhibit an approxi-
mately linear dependence on $[(E-V_c)/A]^{\frac{1}{2}}$, or equivalently, on
the relative velocity of target and projectile at the
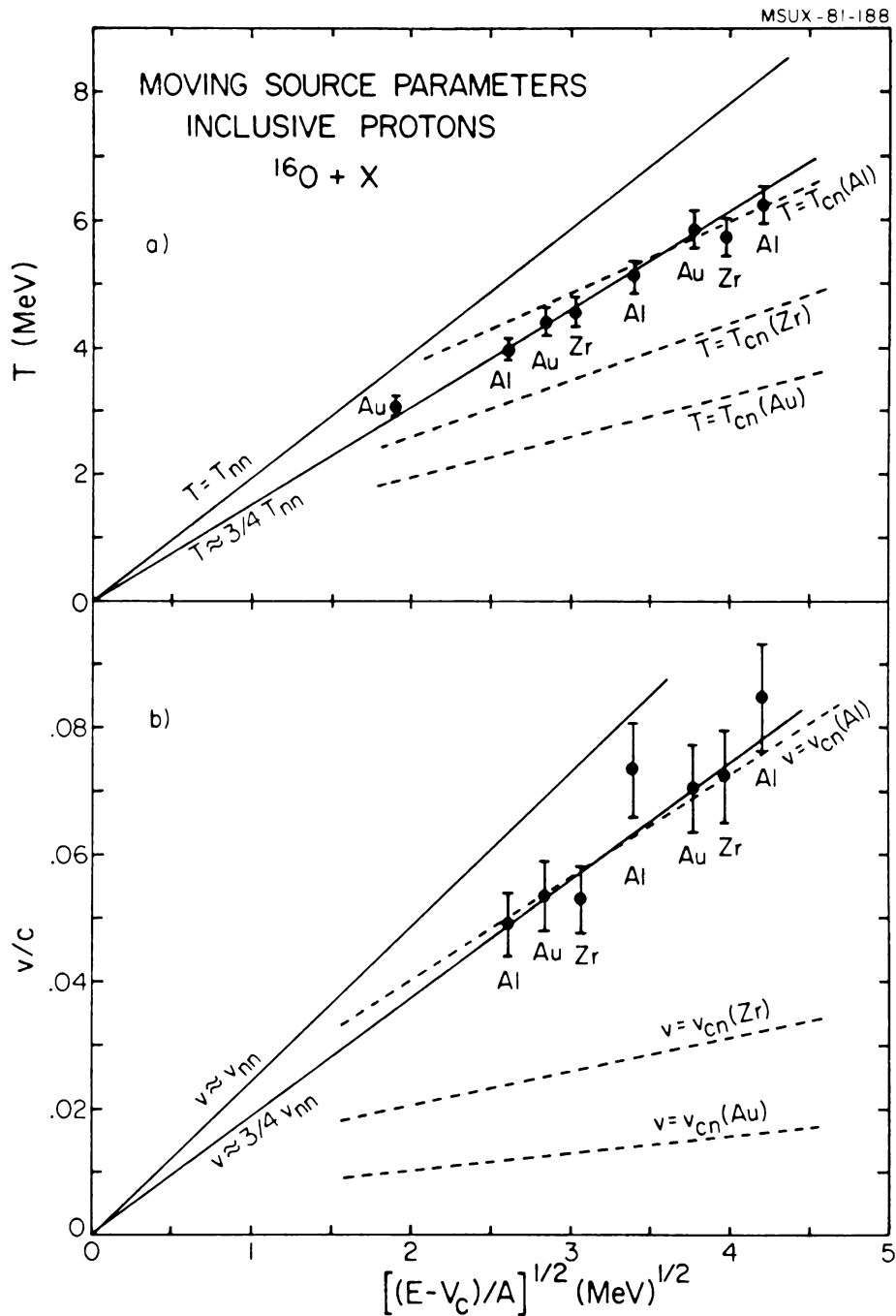
Figure V-43. Incident energy and target dependence of the moving source temperature and velocity parameters are shown in parts (a) and (b), respectively. The Coulomb barrier, V_c, has been calculated using Eq. (V-1). The dependence expected for compound nucleus emission is indicated by the dashed curves. The solid curve in part (a) denoted by $T = T_{nn}$ was calculated according to Eq. (V-16). The solid curve marked $v = v_{nn}$ in part (b) was calculated using Eq. (V-17).

point of contact. Here, V_c is the recoil-corrected Coulomb barrier calculated according to Eq. (V-1) and A is the mass number of the projectile. As indicated by the dashed curves of Figure V-43, such a dependence cannot be explained by compound nucleus emission. Instead it suggests more rapid processes such as knock-out or the formation of a hot subsystem of nucleons. In fact, the observed linear dependence on the relative velocity can be understood if one assumes the formation of a hot Fermi gas consisting of equal nucleon contributions from target and projectile [GFBe].

For an ideal Fermi gas, the internal energy per nucleon, U/N, is given to lowest order in T by the relation [Pa 72]

$$\frac{U}{N} = \frac{3}{5}\ \varepsilon_F\ \left[1 + \frac{5\pi^2}{12}\left(\frac{T_{nn}}{\varepsilon_F}\right)^2 \right] \qquad (V-14)$$

where ε_F is the Fermi energy. For a system of N nucleons consisting of equal contributions from target and projectile nuclei, $N_t = N_p = N/2$, the internal energy per nucleon for the system can alternatively be written as

$$\frac{U}{N} = \frac{3}{5}\ \varepsilon_F + \frac{E^*}{N} = \frac{3}{5}\ \varepsilon_F + \frac{m_o}{2}\left(\frac{v_{rel}}{2}\right)^2 \qquad (V-15)$$

where E^* is the excitation energy of the N nucleons, m_o is the nucleon mass, and $v_{rel} = [2(E-V_c)/m_oA]^{\frac{1}{2}}$ is the relative velocity between target and projectile at the point of contact. From Eqs. (V-14) and (V-15) the

temperature of such a system is given by

$$T_{nn} = \left(\frac{m_0 \epsilon_F}{2\pi^2}\right)^{\frac{1}{2}} v_{rel} . \qquad (V-16)$$

Furthermore, due to equal target and projectile contributions, nucleon emission should be isotropic in the nucleon-nucleon rest frame. The velocity of this frame after accounting for target recoil, is given by

$$v_{nn} = \frac{v_{rel}}{2} + \frac{A_p}{(A_t + A_p)} (v_B - v_{rel}) \simeq \frac{v_{rel}}{2} \qquad (V-17)$$

where v_B is the beam velocity and A_p and A_t are the mass numbers of projectile and target. According to the solid curves of Figure V-43 the temperature and velocity parameters are 25% lower than the equal contributions limit given by Eqs. (V-16) and (V-17).

It is interesting to investigate whether the observed trends can be extrapolated toward relativistic energies where similar thermal models [We 76, Go 77, Na 81] have been used to describe the light particle spectra. With this in mind we have determined temperature and velocity parameters for the reaction ^{20}Ne + NaF → p at incident energies of E/A = 400 and 800 MeV [Na 81]. This has been done in a manner consistent with our low energy treatment by using the relativistic generalization of Eq. (V-10) for the Lorentz-invariant cross section

$$\frac{E}{p^2} \frac{d^2\sigma}{dpd\Omega} = N_0 \gamma (E - \beta p\cos\theta) \exp[-\gamma(E - \beta p\cos\theta)/T] \qquad (V-18)$$

where β is the velocity of the source (c=1), $\gamma=(1-\beta^2)^{-\frac{1}{2}}$, and $E=(p^2+m_o^2)^{\frac{1}{2}}$. In order to minimize the contribution from fragmentation and knockout [Na 81] we have restricted our consideration to the data at large transverse momenta ($\Theta \geq 45°$). Despite the simplicity of the present parameterization, it provides an acceptable description of the experimental data (as seen in Figure V-44).

The trend of the temperature parameter observed at low energies may be connected smoothly to the temperatures obtained for the Ne + NaF reaction at relativistic energies. This is shown in Figure V-45 where, for orientation, the solid and dashed curves have been calculated for relativistic Fermi and Boltzmann gases consisting of equal nucleon contributions from target and projectile. In this case, the excitation energy per nucleon, ϵ^*, is related to the incident kinetic energy per nucleon above the Coulomb barrier, $(E-V_c)/A$, according to

$$\epsilon^* = [m_o^2 + \tfrac{1}{2}m_o(E-V_c)/A]^{\frac{1}{2}} - m_o \ , \qquad (V-19)$$

where m_o is the nucleon rest mass. Alternatively, the excitation energy per nucleon of the gas may be written as

$$\epsilon^* = <\epsilon(T)> - <\epsilon(T=0)> \ , \qquad (V-20)$$

where $<\epsilon(T)>$ is the average kinetic energy per nucleon at temperature T with $<\epsilon(T=0)>=0$ for a Boltzmann gas and $<\epsilon(T=0)>=3/5\epsilon_F$ for a Fermi gas. Combining Eqs. (V-19) and
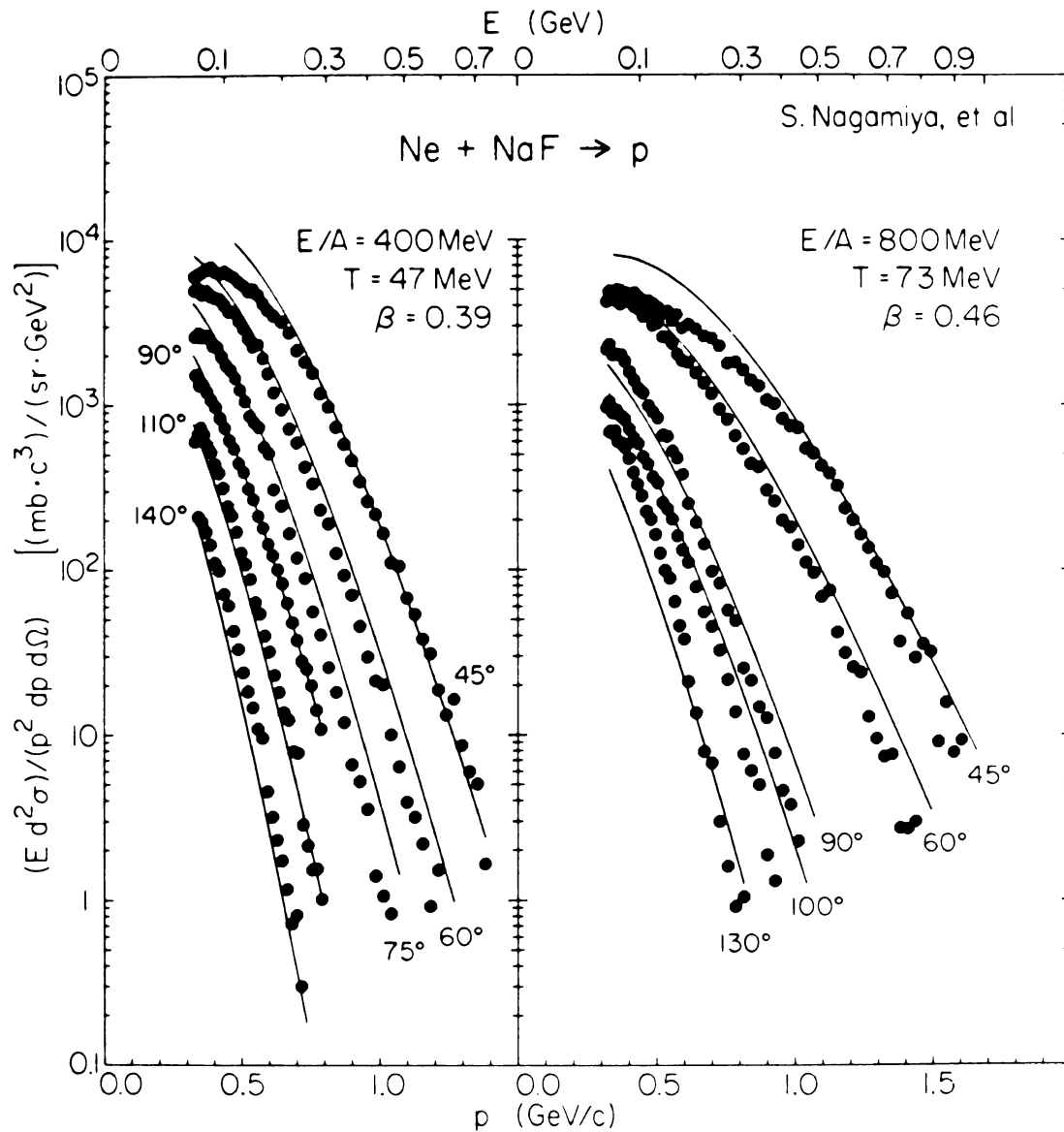
Figure V-44. Energy spectra of protons in the Ne + NaF reaction at incident energies of E/A = 400 and 800 MeV. The data (from Nagamiya et. al. [Na 81]) are fitted with the relativistic moving source of Eq. (V-18). The laboratory angles and the moving source parameters are indicated.
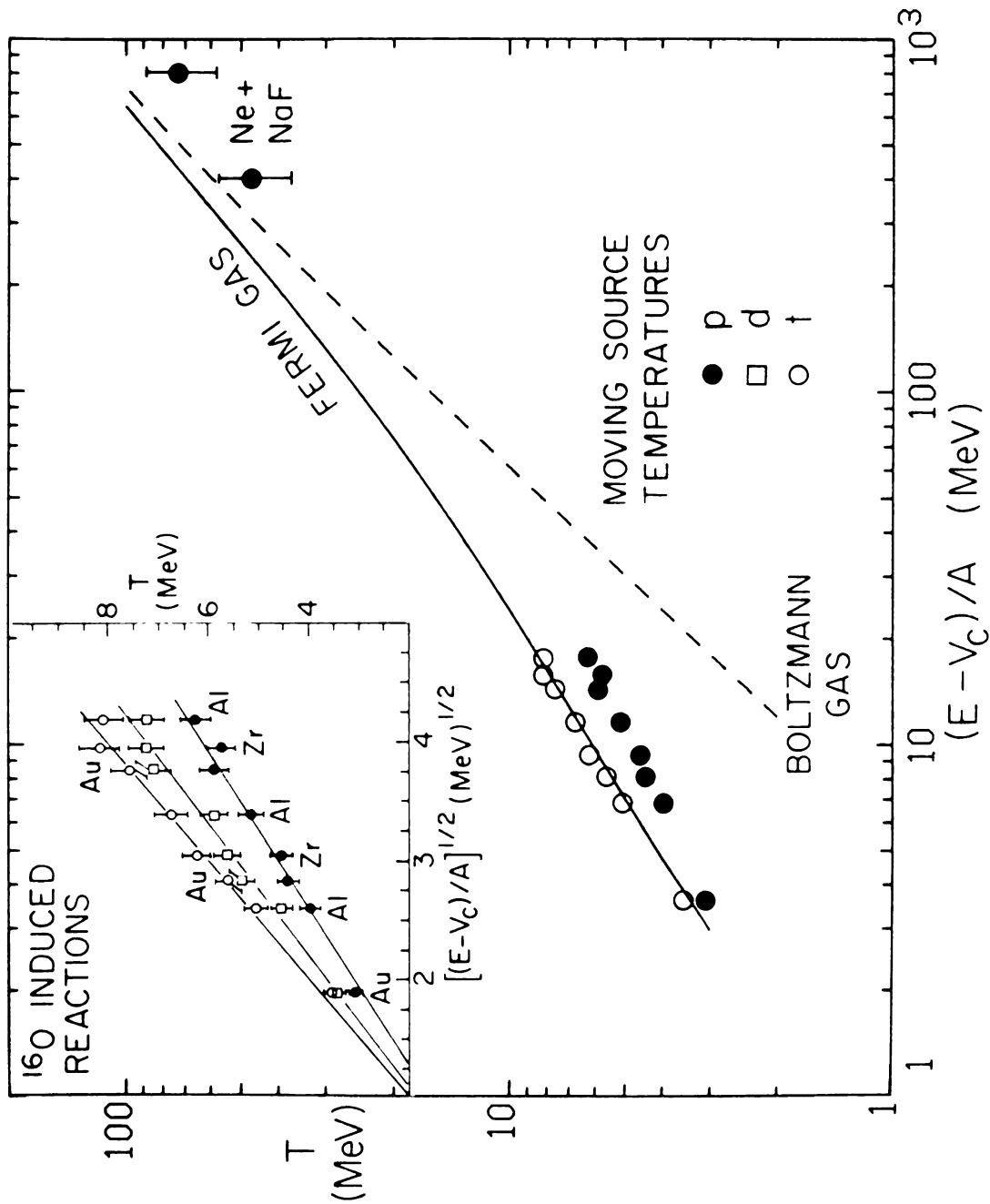
Figure V-45. Moving source temperature parameters for the proton, deuteron, and triton spectra in 16o-induced reactions of the present study and for the reaction Ne+NaF→p at 400 and 800 MeV/A. The solid and dashed curves are described in the text.

(V-20) one obtains the desired relation between temperature and incident kinetic energy.

The average kinetic energy is calculated using

$$<\varepsilon(T)> = \frac{V}{N} \frac{g}{2\pi^2\hbar^3} \int_0^\infty E(p)f(p,T)p^2 dp \; . \qquad (V-21)$$

Here g is the spin-isospin degeneracy factor, $E(p) = (p^2 + m_0^2)^{\frac{1}{2}} - m_0$ is the kinetic energy of the nucleon and $f(p,T)$ is the distribution function given by

$$f(p,T) = \frac{1}{\alpha + \exp\{[E(p) - \mu(T)]/T\}} \qquad (V-22)$$

with $\alpha = 0$ for Boltzmann statistics and $\alpha = 1$ for Fermi statistics. The chemical potential $\mu(T)$ is determined from

$$\frac{N}{V} = \frac{g}{2\pi^2\hbar^3} \int_0^\infty f(p,T)p^2 dp \; , \qquad (V-23)$$

by assuming normal nuclear density, $N/V = 0.17$ fm^{-3}. We note that, at low energies, the temperature will be given by Eq. (V-16) for a Fermi gas and by $T = 2/3 \; \varepsilon^*$ for a Boltzmann gas.

The general trend of the experimental temperature parameters is seen to follow approximately that depicted by the Fermi gas calculation. Recent inclusive measurements for ^{12}C on ^{60}Ni at several energies confirm our low-energy temperature dependence [RLAu]. Other recent measurements (^{20}Ne + Ni, Ag, and Ta at E/A = 43 MeV [Na 81a], ^{12}C + C, Al, Cu, Ag, and Au at E/A = 58 and 86 MeV [Ja 81], and ^{4}He + Al

and Ta at E/A = 180 MeV [Co 81]) follow the trend of the Fermi gas curve in the intermediate energy region with temperatures of 13 - 16 MeV, 11 MeV, 11 - 16 MeV, and 26 MeV at incident energies of E/A = 43, 58, 86, and 180 MeV, respectively. These values deviate somewhat from a smooth trend but this is most likely because the various authors have used different approaches to extract the temperatures. Taken literally, the observed trend suggests the thermalization of a subset of nucleons. However, because features of inclusive measurements may be reproduced by models having rather different assumptions [Sy 80, Sa 80, Co 81, Na 81] it should be investigated whether the observed trend can be reproduced by alternative approaches such as single-scattering or precompound models. We will consider this question in the following two sections.

As a final comment, we draw attention to the insert of Figure V-45 which demonstrates that the temperatures extracted for deuterons and tritons are systematically larger than those for protons. This may be because the proton spectra contain larger contributions from more equilibrated processes such as compound nucleus evaporation. Further investigations with different target projectile combinations and at higher energies are necessary to elucidate the origin of this systematic temperature difference.

F. Knock-out Model

The results of the previous two sections suggest that many of the features of the light particle spectra may be interpreted as evidence for thermal emission from a hot subsystem of nucleons. However, before adopting such an interpretation we must investigate whether the observed characteristics can be explained by alternative methods. Our motivation derives from the moving source analysis of Section V.E which suggested that equal contributions of nucleons from target and projectile were involved in the production of light particles. This analysis also demonstrated that the proton emission was nearly isotropic in the nucleon-nucleon rest frame. These properties are very suggestive of a single-scattering knock-out process for the production of energetic protons. At relativistic energies it is observed that while many features of the proton spectra can be explained by fully thermal models [We 76, My 78], it is also possible to explain several features as resulting from single nucleon-nucleon scattering processes [Ko 77, Ha 79]. In this section a schematic single-scattering knock-out model is considered [Ch 79] to determine whether the inclusive proton energy and angular distributions might result from such a process.

At the incident energies of the present study, we envision a peripheral reaction in which a single nucleon of the projectile scatters in a quasi-free manner with a

nucleon in the surface of the target. Following this inter-
action, one of the nucleons escapes and, as suggested by
the rather low nucleon multiplicities observed
(see Table V-1), the other nucleon is absorbed by the
target or projectile. Describing the incoming and outgoing
particles by plane waves, and using a zero-range nucleon-
nucleon interaction, the differential cross section
[Ch 79] for observing the emitted nucleon with energy E is
(see Appendix C)

$$\frac{d^2\sigma}{dEd\Omega} \sim \frac{k}{K_0} \int d^3K \left[\frac{1}{A} |F_A(\tilde{A}(\vec{K}_0+\vec{K}+\vec{k}))|^2 P_B(-\tilde{B}\vec{K}_0-\vec{K}) \right.$$

$$\left. + \frac{1}{B} |F_B(\tilde{B}(-\vec{K}_0+\vec{K}+\vec{k}))|^2 P_A(\tilde{A}\vec{K}_0-\vec{K}) \right] \delta(E_f-E_i) \ . \tag{V-24}$$

In this expression $\vec{K}_0$ is the incoming momentum of the
projectile in the center of mass and $\vec{k}$ is the momentum of
the knocked out nucleon. The quantities $\tilde{A}$ and $\tilde{B}$ are given
by $\tilde{A} = (A-1)/A$ and $\tilde{B} = (B-1)/B$ where A and B are the mass
numbers of the projectile and target, respectively. The
first term in Eq. (V-24) represents knock-out from the
target (see Figure C-1) with $P_B(\vec{q})$ being the momentum
distribution of a nucleon in the target

$$P_B(\vec{q}) = \sum_{\beta} |\phi_{\beta}(\vec{q})|^2 \tag{V-25}$$

and $F_A(\vec{q})$ is the form factor of the density distribution,
$\rho_A(\vec{r})$, of the projectile

$$F_A(\vec{q}) = \int d^3r \ e^{-i(\vec{q}\cdot\vec{r})}\rho_A(\vec{r}) \ . \qquad (V-26)$$

Similarly, the second term of Eq. (V-24) represents knock-out from the projectile.

To evaluate $P(\vec{q})$ and $F(\vec{q})$ we use the harmonic oscillator s- and p-shell wavefunctions for ^{16}O to obtain

$$P_{16}(\vec{q}) = 4\left[\frac{6}{\pi^{\frac{1}{2}}}\right]^3 (1+2b^2q^2)e^{-b^2q^2} \qquad (V-27)$$

$$F_{16}(\vec{q}) = 4(4-\tfrac{1}{2}b^2q^2)e^{-b^2q^2/4} \qquad (V-28)$$

with size parameter b=1.84 fm. Because the interactions are assumed to occur in the nuclear surface, the function $P(\vec{q})$ and $F(\vec{q})$ for the target nuclei should be similar to those for ^{16}O. Therefore, we have used the above functions for the target nuclei as well as for the ^{16}O projectile.

The knock-out calculation for the $^{197}Au(^{16}O,p)$ reaction (solid curves in Figure V-46) is found to reproduce the observed angular distribution in the low-energy region but falls off slightly faster than experiment in the high-energy region. The curves have been calculated using Eq. (C-23) of Appendix C with $P(\vec{q})$ and $F(\vec{q})$ as described above. In addition, the calculated curves have been shifted by 8 MeV to approximate the Coulomb repulsion of the emitted proton from the target residue.

Although the similarity between knock-out calculation and experiment for the ^{197}Au target is encouraging, the
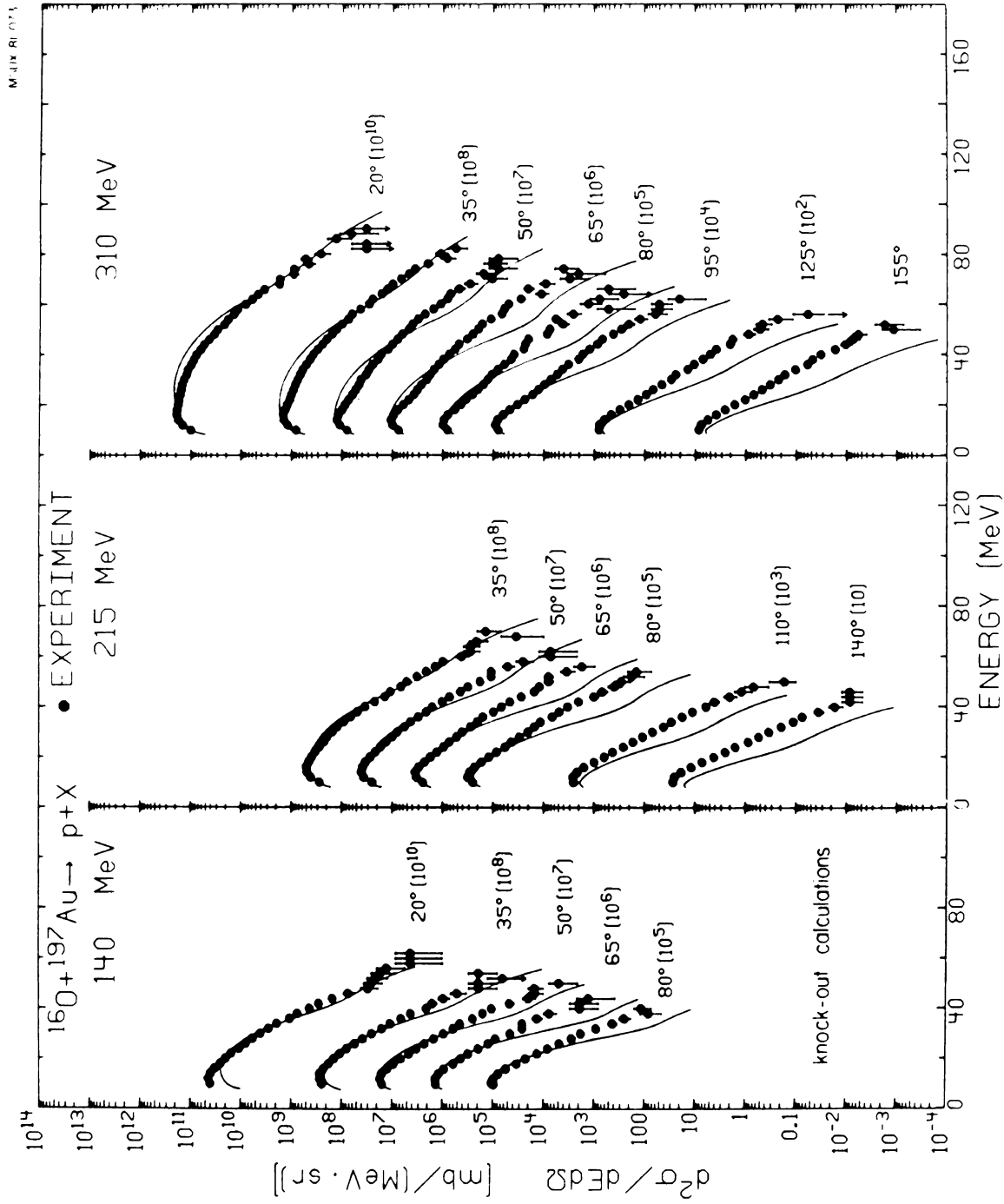
Figure V-46. Energy spectra of protons in the ^{197}Au (^{16}O, p) reaction at 140, 215, and 310 MeV incident energy. The curves are the result of knock-out calculations described in the text.

knock-out model gives much steeper energy spectra than found experimentally for the $^{27}Al(^{16}O,p)$ reactions, see Figure V-47. Furthermore, when seemingly more realistic calculations were made by including all of the filled harmonic oscillator orbitals in $P(\vec{q})$ and $F(\vec{q})$ for the target nuclei, the calculated energy spectra were observed to fall-off much faster than experiment and showed an enhanced oscillatory structure (due primarily to $F(\vec{q})$) which is not observed in the experimental data. Qualitatively similar results were obtained by using Woods-Saxon wavefunctions instead of the harmonic oscillator wavefunctions described above. Much steeper energy spectra were also obtained when both nucleons were assumed to escape. We conclude that although the above schematic knock-out model cannot rule out a single-scattering interpretation of the proton spectra, it makes such an interpretation unlikely. It will be necessary to perform a more detailed analysis including distorted waves in the final state to determine the overall magnitude and details of the knock-out process.

G. Precompound Calculation

In the previous two sections we have considered two extreme explanations for the light particle emission. At one extreme a completely thermal model was applied and at the other a single-scattering model. In this section we
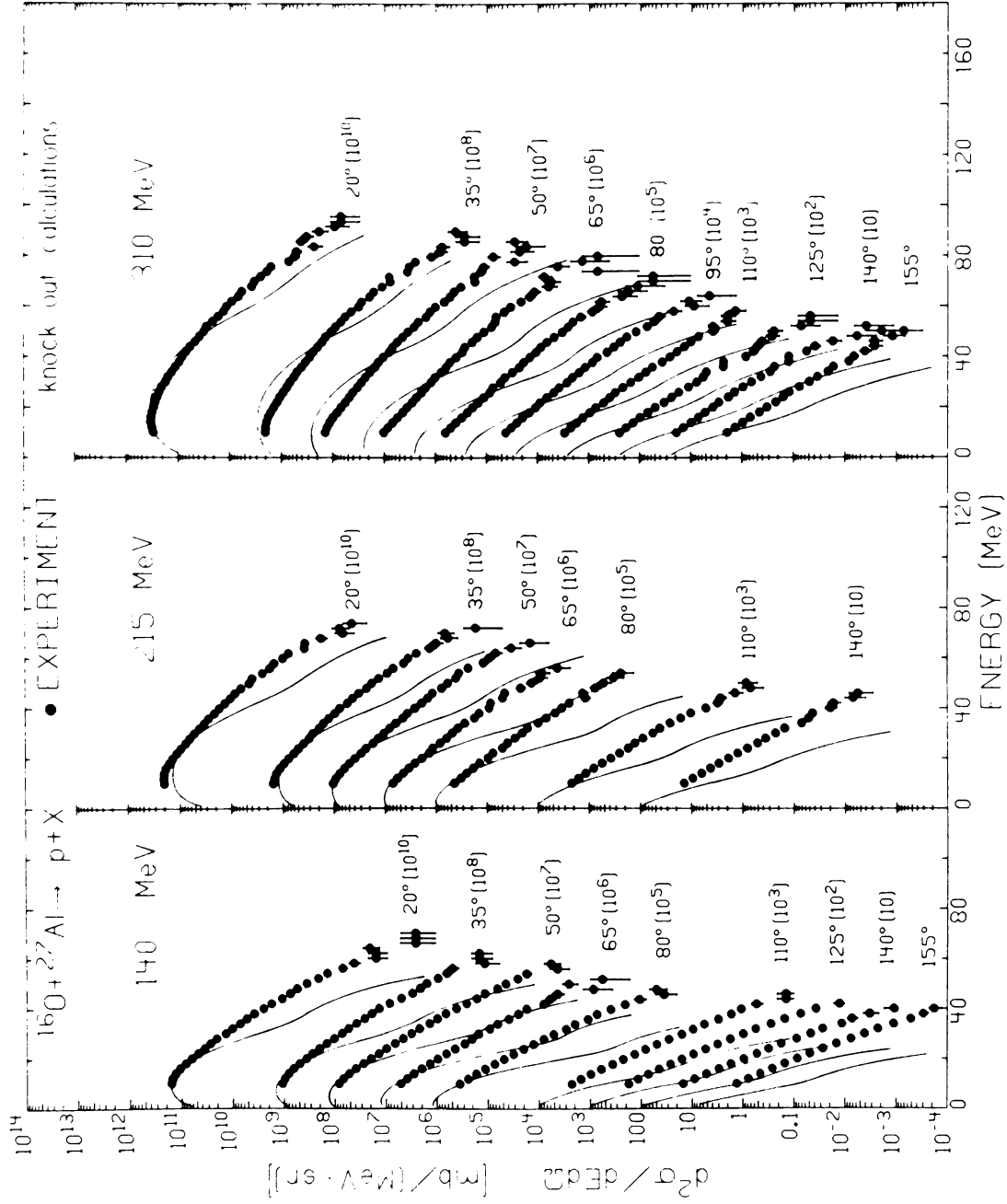
Figure V-47. Energy spectra of protons in the 27Al (16o, p) reaction at 140, 215, and 310 MeV incident energy. The curves are the result of knock-out calculations described in the text.

consider a compromising viewpoint and allow both direct and thermal contributions. At relativistic energies models which include both contributions either explictly [Ch 80] or by following the development of the collision process, as in cascade calculations [Hü 77, Ra 78, Ya 79a, Cu 80, Cu 81, Ya 81] have been most successful in reproducing the experimental light particle spectra [Na 81]. At low energies, the preequilibrium [Bl 75] and cascade [Be 76] calculations which follow the time development of the system toward equilibrium have been quite successful in reproducing the light particle spectra resulting from light-ion induced reactions. Until now, however, there have not been sufficient inclusive light particle measurements to adequately test the recent generalization [Bl 81] of the preequilibrium model to heavy-ion induced reactions.

In the generalization of the precompound model to heavy-ion collisions the Boltzmann master equation approach of Harp, Miller, and Berne [Ha 68, Ha 71] is applied with an additional term included to represent the time dependent addition of projectile nucleons to the equilibrating system as the fusion process develops. The master equation for a one-fermion type gas is represented by the set of differential equations

$$\frac{d(n_i g_i)}{dt} = \sum_{j,k,l} \omega_{kl \rightarrow ij} \; g_k n_k g_l n_l (1-n_i)(1-n_j) g_i g_j$$

$$- \sum_{j,k,l} \omega_{ij \rightarrow kl} \; g_i n_i g_j n_j (1-n_k)(1-n_l) g_k g_l \qquad \text{(V-29)}$$

$$- n_i g_i \omega_{i \rightarrow i'} g_{i'} + \frac{d}{dt} (n_i g_i)_{fus}$$

where n_i the average occupation number and g_i the number of
single particle states per MeV in an energy interval
centered at i MeV above the bottom of the nuclear well.
The well of the compound nucleus is assumed. The $\omega_{ab \rightarrow cd}$
are the transition rates for nucleons in initial states
a and b to scatter to final states c and d, and are
evaluated from free nucleon-nucleon scattering cross
sections. The $\omega_{i \rightarrow i'}$ gives the rate for a particle at energy
i within the nucleus to go to an energy i' outside the
nucleus. The first two terms of Eq. (V-29) give the rates
for scattering particles into and out of the energy
interval i by two-body collisions. The fractional occupa-
tion numbers $(1-n_m)$ take into account the Pauli blocking
of the final states. The third term in this equation gives
the rate of emission into the continuum. The rate of
precompound emission at the early stages of the reaction
as well as the rate of equilibrium emission at later
stages follows from this term as

$$\frac{dN_{i'}}{dt} = n_i g_i \omega_{i \rightarrow i'} g_{i'} \quad . \qquad \text{(V-30)}$$

The fourth term of Eq. (V-29) is the modification of the master equation for heavy ion reactions. It represents the time-dependent addition of nucleons from the coalescing projectile to the energy interval i of the composite system. The number of projectile nucleons n_t which enter the reaction region at each time interval is calculated from the geometrical volume of the projectile which passes through the tangential plane between target and projectile at the initial point of contact. Only S-wave collisions are considered, and the fusion rate is determined by the relative velocity at the point of contact. The n_t projectile nucleons entering the system in a given time interval are assumed to be distributed according to

$$N(U) \Delta U = n_t \frac{[U^{n_o-1} - (U - \Delta U)^{n_o-1}]}{(E^*)^{n_o-1}} \qquad (V-31)$$

where $N(U) \Delta U$ represents the number of nucleons in an excitation interval ΔU centered at U MeV of excitation, E^* is the compound nucleus excitation, and n_o is the number of degrees of freedom over which the excitation energy is partitioned. In light ion induced reactions n_o corresponds to the initial number of particles and holes, or excitons, and is typically equal to the projectile mass number plus one particle and one hole in the target. In heavy-ion reactions it might also be expected that the projectile nucleons partition all of the excitation energy and so we

should have $n_o \approx 16 - 18$ for ^{16}O-induced reactions. However
this is likely to underestimate the true degrees of
freedom since nucleons could transfer from the target
nucleus to the projectile or part of the excitation energy
could go into collective modes. In either event, we expect
that n_o should be rather independent of incident energy.
In the actual calculations Eqs. (V-29), (V-30), and (V-31)
are generalized to a two-fermion type gas of neutrons and
protons. This model does not calculate angular distribu-
tions nor composite particle emission although it might be
generalized to do so with further assumptions [Ma 76, Ma 79,
Ma 80, Sy 80, Bl 81].

The angle-integrated energy distributions as observed
in the center-of-mass system for the $^{197}Au(^{16}O,p)$ reaction
at 140, 215 and 310 MeV incident energies are compared in
Figure V-48 with results of the heavy-ion precompound
model [Bl 81]. The precompound calculations have been
normalized using the total reaction cross sections of
Table V-1 instead of the fusion cross sections and therefore
are an overestimate of the expected proton cross sections.
The calculations were performed using 60 steps over a
relaxation interval of 1.3×10^{-21} sec (following Blann
[Bl 81]) and assuming available excitation energies of
$E^* = 97$, 162 and 254 MeV at the three incident energies,
respectively. In one case, the parameter n_o which
determines the distribution function (we will call n_o the
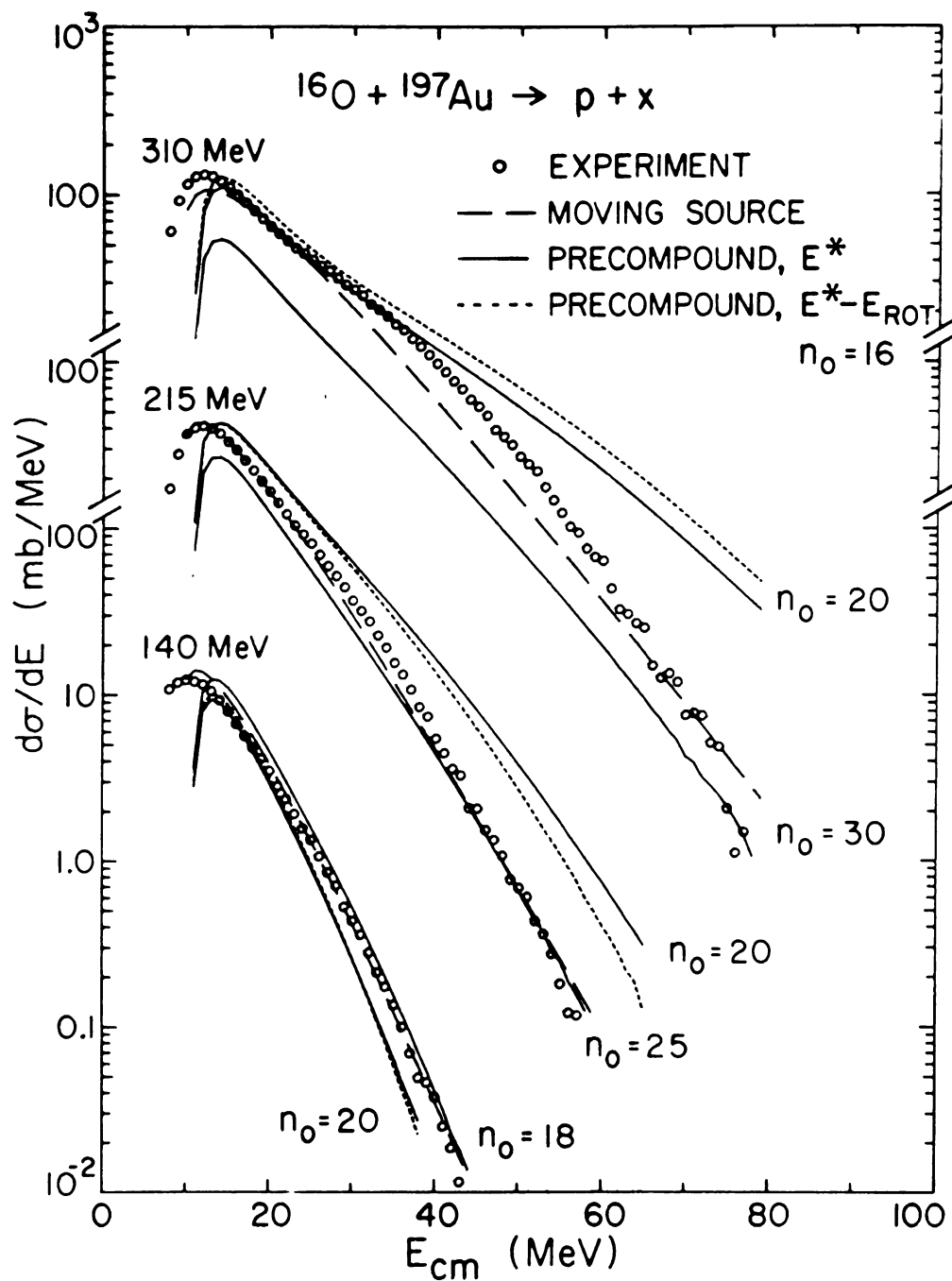
Figure V-48. Angle-integrated proton spectra in the compound nucleus rest frame for the ^{197}Au (^{16}O, p) reaction at 140, 215, and 310 MeV incident energies. The calculated curves are described in the text.

exciton number although it may include collective degrees of freedom) has been arbitrarily chosen at $n_o = 20$ and was assumed to be independent of energy. This calculation (see solid curves of Figure V-48 labelled $n_o = 20$) is seen to yield energy slopes which are too steep at 140 MeV and too flat at 215 and 310 MeV. In order to reproduce the observed spectral shapes, exciton numbers of about $n_o \approx 18$, 25, and 30 must be assumed at the energies of 140, 215, and 310 MeV (solid curves Figure V-48 labelled $n_o = 18$, 25, 30). Under the present assumptions of the model it is not possible to describe the proton spectra with an exciton number parameter which is independent of the incident energy.

In order to investigate those assumptions of the model which might be improved we have made two additional calculations which illustrate the effects governing the fusion process. Because evidence from deeply inelastic scattering suggests that the intermediate complex may be rather long-lived we have performed a calculation in which the fusion process is assumed to occur at one fifth of the rate expected from the relative velocities. This calculation yielded results which were virtually identical to the above results implying that the model is rather insensitive to the time scale of the fusion process. This suggests that the interactions of an excited nucleon with cold nucleons are much more important than the interactions with other

excited nucleons. The assumption of only S-wave collisions has been investigated by decreasing the available excitation energy by the rotational energy for fusion occurring at the angular momentum limit. Following the classical model of Bass [Ba 74a] we have used rotational energies of $E_{rot} = 17$, 34, and 34 MeV, respectively. These calculations, using an initial exciton number of $n_0 = 16$, are shown by the dotted curves in Figure V-48. Removing the rotational energy from the available excitation energy has the same effect as sharing the excitation energy among more excitons. However, it is still necessary to vary the number of excitons with incident energy in order to fit the data.

In order to improve the agreement of the precompound model and remove the strong energy dependence of the exciton number, we should use the information available in the proton angular distributions. As we have noted previously, the angular distributions imply that the protons are emitted from the nucleon-nucleon rest frame rather than the compound nucleus frame. The excitation energy in this frame would be lower and hence lower values of n_0 would be obtained. Although we have demonstrated that the precompound results are independent of the rate at which nucleons are added to the equilibrating system, it appears to be important to account for the local velocity of the fusing system. Further work will be necessary in order to

understand the energy dependence of n_o.

Also shown by the dashed curves in Figure V-48 are the energy distributions expected from the moving source model. These distributions were calculated according to

$$\frac{d\sigma}{dE} = \frac{2\pi N_o T}{E_1^{\frac{1}{2}}} \exp[-(E-E_c+E_1)/T]\sinh[2(E_1)^{\frac{1}{2}}(E-E_c)^{\frac{1}{2}}/T] \quad (V-32)$$

which is obtained by integrating Eq. (V-10) over solid angle. The calculations were performed using the parameters listed in Table V-4 which fit the double differential cross sections (Figure V-30). With the exception of the 310 MeV data the agreement with experiment is excellent. Here an additional component is observed in the experimental spectra at proton energies of about 50 MeV. This is the same component which was observed at forward angles in the double differential cross sections (Figure V-30) and is most likely due to a direct contribution.

CHAPTER VI

COMPOSITE PARTICLE PRODUCTION

A.   Light Particle Ratios

It has been suggested that the relative production of protons and composite particles provides information about the bulk properties of nuclei in relativistic heavy ion collisions. If the protons and composite particles in the region of interaction are assumed to be in chemical equilibrium then it has been proposed that the relative abundances of the various light particle species may be used to determine the entropy produced in the reaction [Si 79] and hence to investigate the equation of state of nuclear matter and search for possible phase transitions. Alternatively, it has been proposed that the relative abundances may be used to determine the volume of the region of interaction [Me 77, Me 78, Me 80, Sa 81a]. In this section we present the energy dependence of the relative light particle yields and in the following section we discuss the implications toward entropy production.

The proton to deuteron ratios of the present study are shown by the solid points in Figure VI-1 as a function of the incident energy per nucleon above the Coulomb barrier. The ratios were calculated using the cross sections of Table V-1 with a low-energy cut-off of 12 MeV. With this rather high cut-off the p to d ratio is found to be rather independent of target. As the solid curve indicates, the ratio decreases smoothly from a value of 5 at the lowest energies to about 2.5 at the highest energies. This value is very similar to the values obtained at 400 MeV/nucleon incident energies which vary between 2 and 3 depending on the target-projectile system [Na 81].

The open circles in Figure VI-1 show the proton to deuteron ratios with the low-energy cut-offs lowered to near the detector thresholds at 8 and 10 MeV for proton and deuterons, respectively. The corresponding p/d-ratios, therefore, include larger contributions from possible compound nucleus evaporation. Including these contributions removes the degeneracy between the various targets. The reactions on the ^{90}Zr target contain the largest low-energy proton component (indicating the largest compound nucleus contribution), and the ^{197}Au target gives the smallest low-energy contribution due to its large Coulomb barrier. The proton to deuteron ratios are observed to increase toward lower incident energies which we may interpret as due to the increasing importance of compound
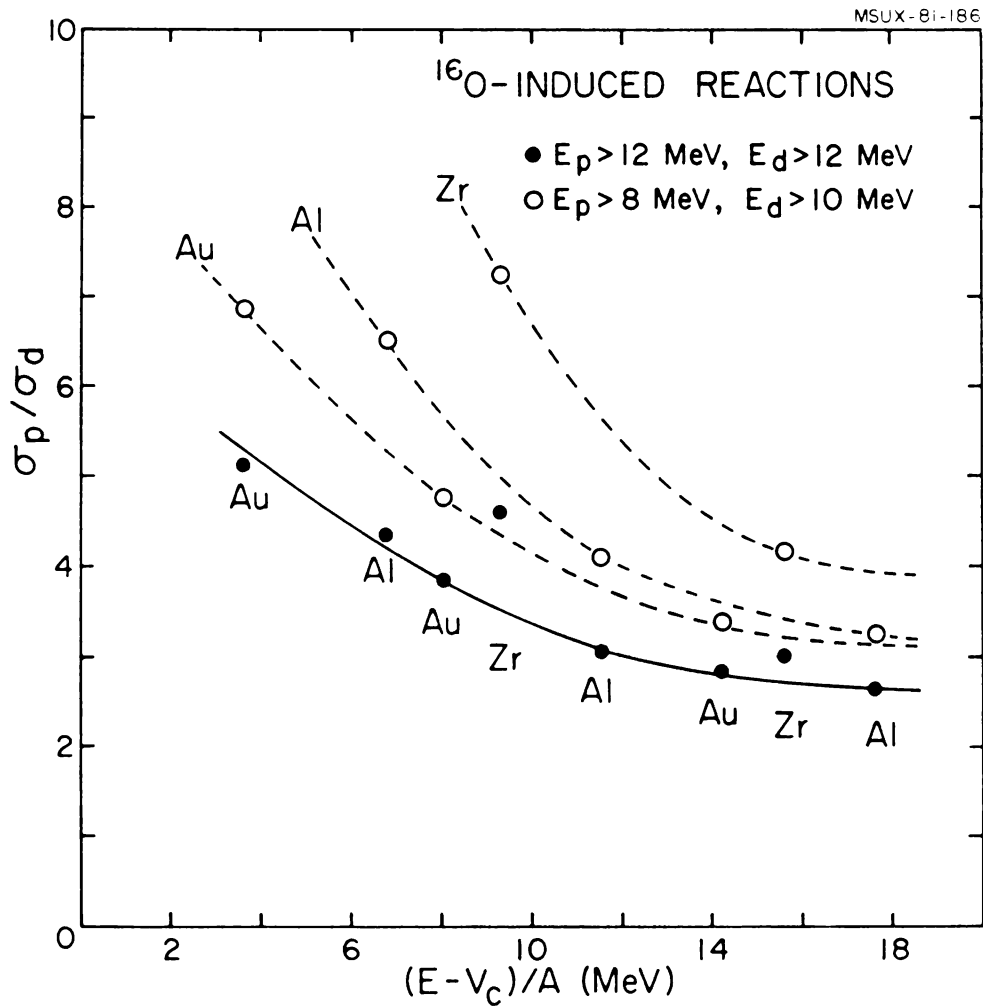
Figure VI-1. Incident energy and target dependence of the
proton to deuteron ratio. The solid points
were calculated with a common low-energy cut-
off of 12 MeV. The open points were calcu-
lated with low-energy cut-offs near the
detector threshold. The solid and dashed
curves have been drawn to guide the eye.

nucleus reactions for which proton evaporation will be favored over deuteron emission [Pü 77].

The proton to composite particle ratios are summarized in Table VI-1. The p/t and p/α-ratios show an increase toward low bombarding energies similar to the trend of the p/d-ratio. These ratios also show a clear target dependence. Like the p/d-ratios, the p/t-ratios are rather similar to those observed at relativistic energies [Na 81]. In contrast, the p/α-ratios of relativistic energies are larger by 1 to 2 orders of magnitude than the present values.

B. Entropy Production

It has been suggested that the proton to deuteron ratio might offer a means of determining the amount of entropy produced in the region of overlap in relativistic heavy-ion reactions [Si 79]. An excess production of entropy over that expected might provide an indication for an abnormal process such as a pion condensate or a phase transition to quark matter [Si 79, Mi 80]. With increasing incident energy one expects the system to access more degrees of freedom and hence produce more entropy. Therefore, since composite particles have fewer degrees of freedom than the sum of their constituent nucleons, one would expect an increase in the ratio of nucleon emission to composite particle production as the bombarding energy is increased.

Table VI-1. Proton to composite particle ratios[†] of the present study.

Energy(MeV)	Target	$\sigma(p)/\sigma(d)$	$\sigma(p)/\sigma(t)$	$\sigma(p)/\sigma(\alpha)$
140	Al	4.4	18.1	1.81
	Au	5.1	9.5	1.06
215	Al	3.1	10.2	1.01
	Zr	4.6	11.1	2.85
	Au	3.8	5.0	1.36
310	Al	2.6	7.3	0.65
	Zr	3.0	6.5	1.36
	Au	2.8	4.2	1.22
315	U	2.2	2.6	0.89

[†]Calculated using the integrated cross sections of Table V-1 and the multiplicities of Section V.B.2. For the Al, Zr, and Au targets the low energy thresholds were at 12 MeV for hydrogen isotopes and at 30 MeV for alpha-particles. For the U target a fission coincidence was required and the low energy thresholds were at 15 MeV for hydrogen isotopes and at 35 MeV for alpha-particles.

On a quantitative basis, it is assumed that the heated gas of nucleons expands after the initial stage of the reaction. During this expansion phase, chemical and thermal equilibrium are assumed to persist until the composite particle freeze-out density is reached. If the system of nucleons can be described in terms of an ideal gas then the entropy per nucleon is given by the Sackur-Tetrode equation

$$S/N = 5/2 - \mu_p/T \qquad\qquad \text{(VI-1)}$$

where μ_p is the proton chemical potential. The chemical potential of a composite particle of A nucleons, μ_A, is given by [Pa 72]

$$\mu_A = T \ln \left[\frac{n_A}{n_A^c} \right] - \varepsilon_A \qquad\qquad \text{(VI-2)}$$

where n_A and ε_A are the density and binding energy of species A and n_A^c is the critical density or inverse cube of the thermal wavelength for species A

$$n_A^c = g_A \left(\frac{m_A T}{2\pi\hbar^2} \right)^{3/2} . \qquad\qquad \text{(VI-3)}$$

Here g_A and m_A are the spin degeneracy and the mass of the composite particle. Assuming that all nucleons and composite particles are in chemical equilibrium, $\mu_A = A\mu_p$, the entropy per nucleon follows as [Si 79, Mi 80]

$$S/N(A\!:\!p) = 5/2 + \frac{1}{(A-1)} \left\{ \varepsilon_A/T + \ln\left[\frac{g_A}{g_p} \left(\frac{m_A}{m_p} \right)^{3/2} \right] - \ln\ (N_A/N_p) \right\}$$

$$\text{(VI-4)}$$

where N_A/N_p is the ratio of composite particles of A nucleons to protons. If the expansion of the fireball is further assumed to be nearly isentropic this entropy then corresponds to the entropy produced in the early stages of the reaction. Neglecting the deuteron binding energy Eq. (VI-4) becomes

$$S/N(d:p) = 3.95 - \ln (\sigma_d/\sigma_p) \qquad \text{(VI-5)}$$

with the deuteron to proton ratio σ_d/σ_p.

An entropy of $S/N(d:p) = 5.0$ is obtained from Eq. (VI-5) using the p/d-ratio of Table VI-1 for the $^{16}O + ^{197}Au$ reaction at 310 MeV incident energy. This value is shown in Figure VI-2. It is very similar to values observed at relativistic energies and is much larger than the expected entropy production [Si 79, Mi 80, St 80]. The entropy per nucleon should not depend on which composite particle species is used in Eq. (VI-4). However, by using our particle ratios for the $^{16}O + ^{197}Au$ reaction at 310 MeV (Table VI-1) we obtain $S/N(d:p) = 5.4$, $S/N(t:p) = 4.8$, and $S/N(\alpha:p) = 4.6$. Although these discrepancies appear to be rather small, they imply that the observed particle ratios deviate significantly (due to the logarithmic dependence of Eq. (VI-4) on N_A/N_p) from the ratios which would be expected for an ideal gas in chemical equilibrium.

A possible reason why the predicted entropy production (see curves marked S_η and S_S in Figure VI-2) is not
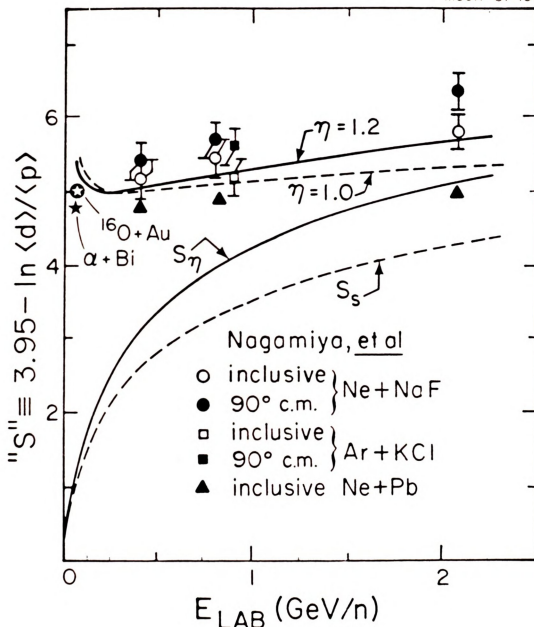
Figure VI-2. The bombarding energy dependence of the entropy (taken from Stöcker [St 80]) as calculated for a viscous (S_η) and an inviscid fluid (S_s). Also shown are the "entropy" values, "S", calculated using the measured d/p-ratios via Eq. (VI-5). The measured values are taken from Nagamiya et. al. [Na 81], Wu et. al. [Wu 79] (α + Bi at E/A = 25 MeV) and from the present study (^{16}O + Au at E/A = 20 MeV). The solid (dashed) lines denoted by η = 1.2 (η = 1.0) represent the viscous (inviscid) calculation of "S" from the calculated d/p-ratios.

obtained using Eq. (VI-4) with the observed particle ratios is that the ideal gas approximation used in the derivation is unjustified. In order to justify a treatment in terms of an ideal gas, the density of the system of nucleons must be much less than the critical density

$$n \ll g \left(\frac{m_o T}{2\pi \hbar^2} \right)^{3/2} \qquad \text{(VI-6)}$$

where m_o is the nucleon mass, T the temperature of the system, and g is the nucleon degeneracy factor. In the present analysis, with $T \simeq 10$ MeV we must have $n \ll 0.09 n_o$ where $n_o = 0.17$ fm^{-3} is the normal nuclear density. This condition is unlikely to be satisfied. Even at temperatures of $T = 50$ MeV, as observed at incident energies of $E/A = 400$ MeV, the strong condition $n \ll n_o$ might not be well fulfilled. As a consequence, thermodynamic treatments which use the ideal gas formalism such as the present model should be treated with care at relativistic energies and, probably, should not be applied in the nonrelativistic regime.

It has recently been shown [St 80] that large proton to deuteron ratios can be obtained in a hydrodynamic calculation which includes nucleon decay from excited states of composite particles. These decays effectively increase the proton to deuteron ratio to give good agreement with the experimentally observed ratios over the full range of

incident energies. This is indicated by the curves marked $\eta = 1.2$ and $\eta = 1.0$ in Figure VI-2 in which the quantity "S" of Eq. (VI-5) (not necessarily the entropy) has been determined from the calculated proton to deuteron ratio.

It is also likely that final state interactions might have a large effect on the observed composite particle ratios. In fact, it has recently been proposed that the deuterons result from pickup in the nuclear surface [Ha 80] and, therefore, have little relation to the concepts of chemical equilibrium or entropy production.

C. Coalescence Model

As discussed in Chapter V, the slopes of the energy spectra of the various light particle species are very similar for a given target and energy. In the context of the moving source model discussed in Section V.E, this implied particle emission from a source of rather well defined temperature. As a consequence one expects the validity of a simple power law relating composite particle spectra to the proton spectra according to

$$e^{-E/T} \sim (e^{-E/AT})^A. \qquad \text{(VI-7)}$$

Similar observations [Gu 76, Go 77, Le 79, Na 81] have been made for light particles emitted in relativistic heavy ion collisions. As a result, several models have

been proposed which relate the emission of composite particles to proton emission via a power law [Bu 63, Sc 63, Gu 76, Bo 77, Go 77, Me 77, Me 78, Ka 80, Me 80, Sa 81a]. In the coalescence model the complex particles are assumed to be synthesized by the coalescence of free nucleons which happen to occupy the same region of momentum space [Sc 63]. This model is a pure phase space approach and makes no assumption about the dynamics of the reaction. It involves a single free parameter, the coalescence radius, P_0, which is the radius of the sphere in momentum space within which the coalescence occurs. There have been several attempts [Bo 77, Me 77, Me 78, Ka 80, Me 80, Sa 81a] to arrive at a dynamical understanding of the coalescence relation but at present the question of its dynamical basis must be considered open.

Since the coalescence prescription has had great success in reproducing the composite particle spectra at relativistic energies, it is interesting to investigate the validity of the model at non-relativistic energies. However, at lower energies the influence of the Coulomb field of the target residue cannot be neglected as has been done at relativistic energies (see Section V.E). If the effect of the Coulomb repulsion of the charged particles from the target residue is taken into account one obtains a generalized coalescence relation

$$\frac{d^2N(Z,N,E_A)}{dE_A d\Omega} = \left(\frac{N_t + N_p}{Z_t + Z_p}\right)^N \frac{A-1}{N!Z!} \left\{\frac{\frac{4\pi}{3} P_o^3}{\{2m_o^3(E-E_c)\}^{\frac{1}{2}}}\right\}^{A-1} \left[\frac{d^2N(1,0,E)}{dEd\Omega}\right]^A \quad (VI-8)$$

The derivation of this relation is given in Appendices D and E. Here N_t, N_p and Z_t, Z_p are the neutron and proton numbers of target and projectile respectively, m_o is the nucleon rest mass, $d^2N(Z,N,E_A)/dE_A d\Omega$ is the differential multiplicity of nuclei composed of Z protons and N=A-Z neutrons, and E_A=AE-NE$_c$ where E_c is the Coulomb repulsion per unit charge.

The differential multiplicity for a given event is not a measured quantity. In practice, it is approximated by the average differential multiplicity [Gu 76, Go 77]

$$\frac{d^2N(Z,N)}{dE_A d\Omega} = \frac{1}{\sigma_R} \frac{d^2\sigma(Z,N)}{dE_A d\Omega} \quad (VI-9)$$

where σ_R is the total reaction cross section. In the analysis of the inclusive light particle results we use Eq. (VI-9) with the total reaction cross sections listed in Table V-1. For the analysis of the fission coincidence results we use the corresponding approximation

$$\frac{d^2N(Z,N)}{dE_A d\Omega} = \frac{1}{N_f} \frac{d^2N_f(Z,N)}{dE_A d\Omega} , \quad (VI-10)$$

where $N_f(Z,N)$ is the number of light particles observed in coincidence with fission and N_f is the total number of fission events.

The physical picture underlying Eq. (VI-8) is that the coalescing neutrons and protons are emitted with the same energy distributions in the vicinity of the target residue. The light particles of charge Z then receive a Coulomb boost of energy ZE_c as they roll down the Coulomb barrier of the target residue. More explicitly, it is assumed that the neutron energy distribution is related to the proton distribution according to

$$\frac{d^2N(0,1,E)}{dEd\Omega} = \left[\frac{N_t + N_p}{Z_t + Z_p}\right] \frac{d^2N(1,0,E+E_c)}{dEd\Omega} \quad . \qquad (VI-11)$$

We shall demonstrate that this assumption provides an adequate description of the composite particle spectra for reactions on ^{238}U, ^{197}Au, and ^{27}Al at all energies of the present study.

In Figure VI-3 the energy spectra of deuterons (solid points) are compared with the predictions of the coalescence model which has not been modified to take Coulomb effects into account (dashed lines). Without the Coulomb modifications the coalescence model is unable to relate the composite particle cross sections to the proton cross sections.

In Figure VI-3, VI-4, and VI-5 the energy spectra of deuterons, tritons and alphas (solid points) are compared with the predictions of the Coulomb-modified coalescence relation (open squares). For deuterons and tritons the
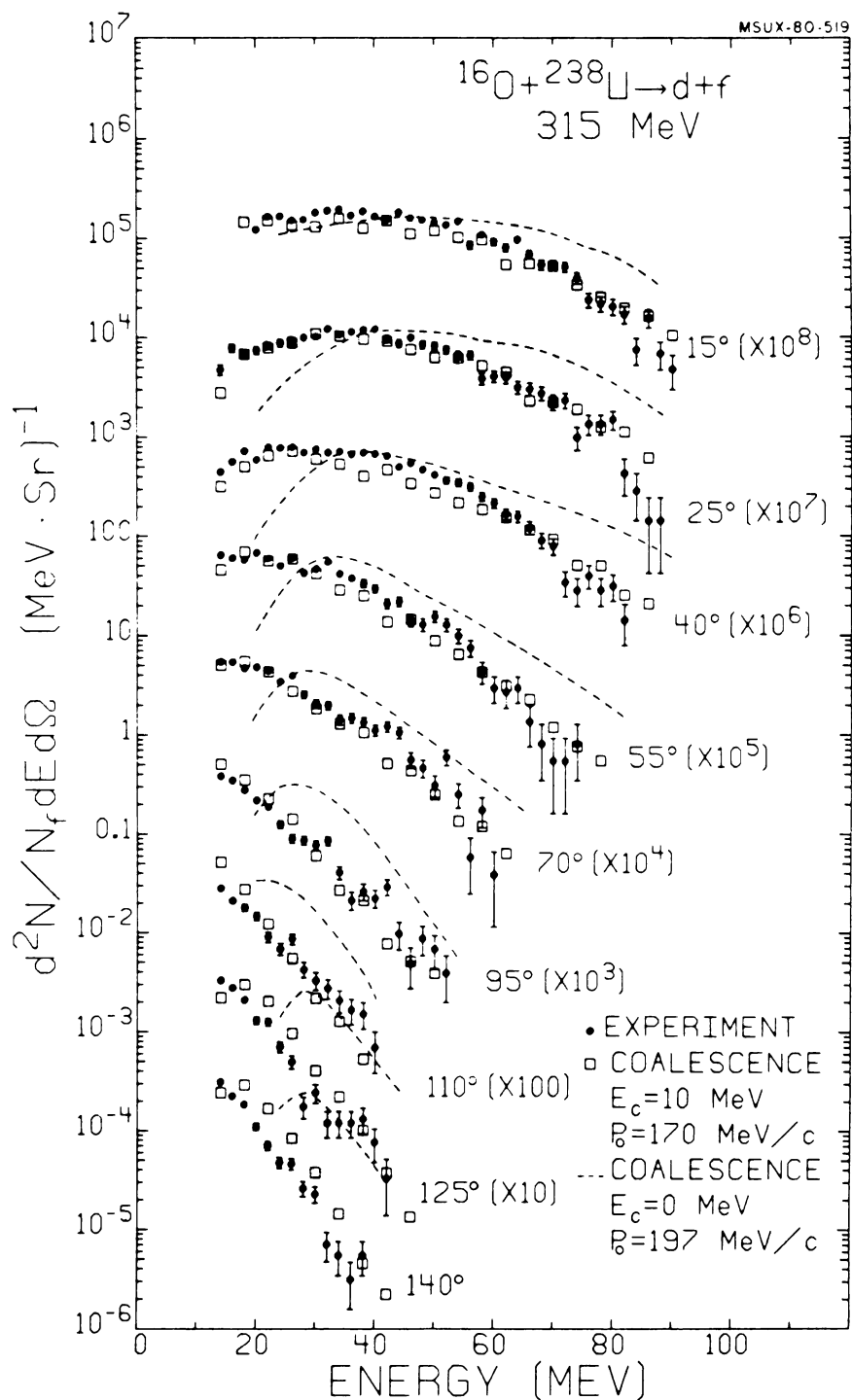
Figure VI-3. Energy spectra of deuterons (solid points) detected in the reaction ^{238}U (^{16}O, df) at 315 MeV. The open squares are spectra predicted by the Coulomb-modified coalescence model; the dashed curves are the predictions of the coalescence model if Coulomb effects are neglected.
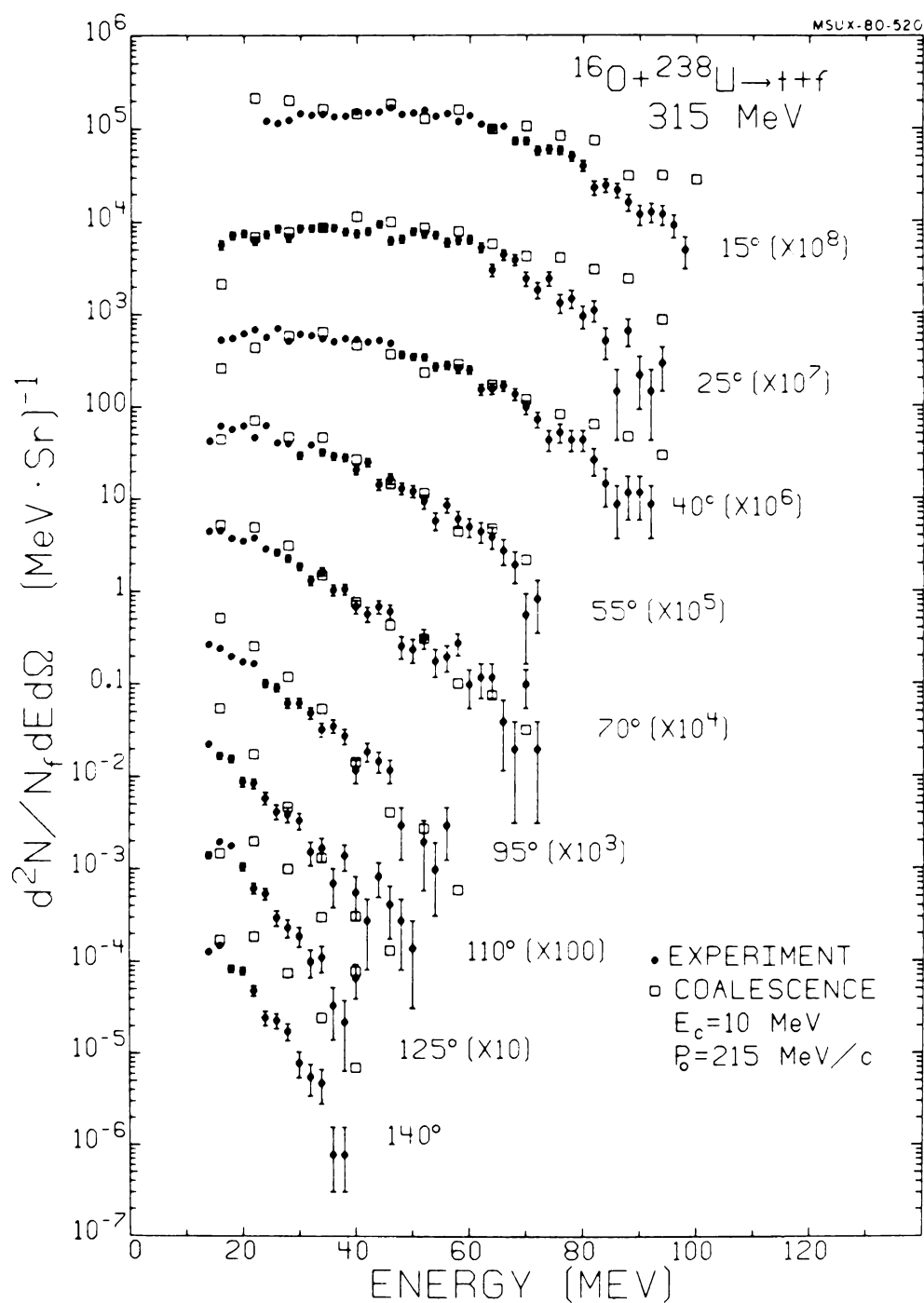
Figure VI-4.   Energy spectra of tritons (solid points) detected in the reaction ^{238}U (^{16}O, tf) at 315 MeV.   The open squares are spectra predicted by the Coulomb-modified coalescence model of Eq. (VI-8).
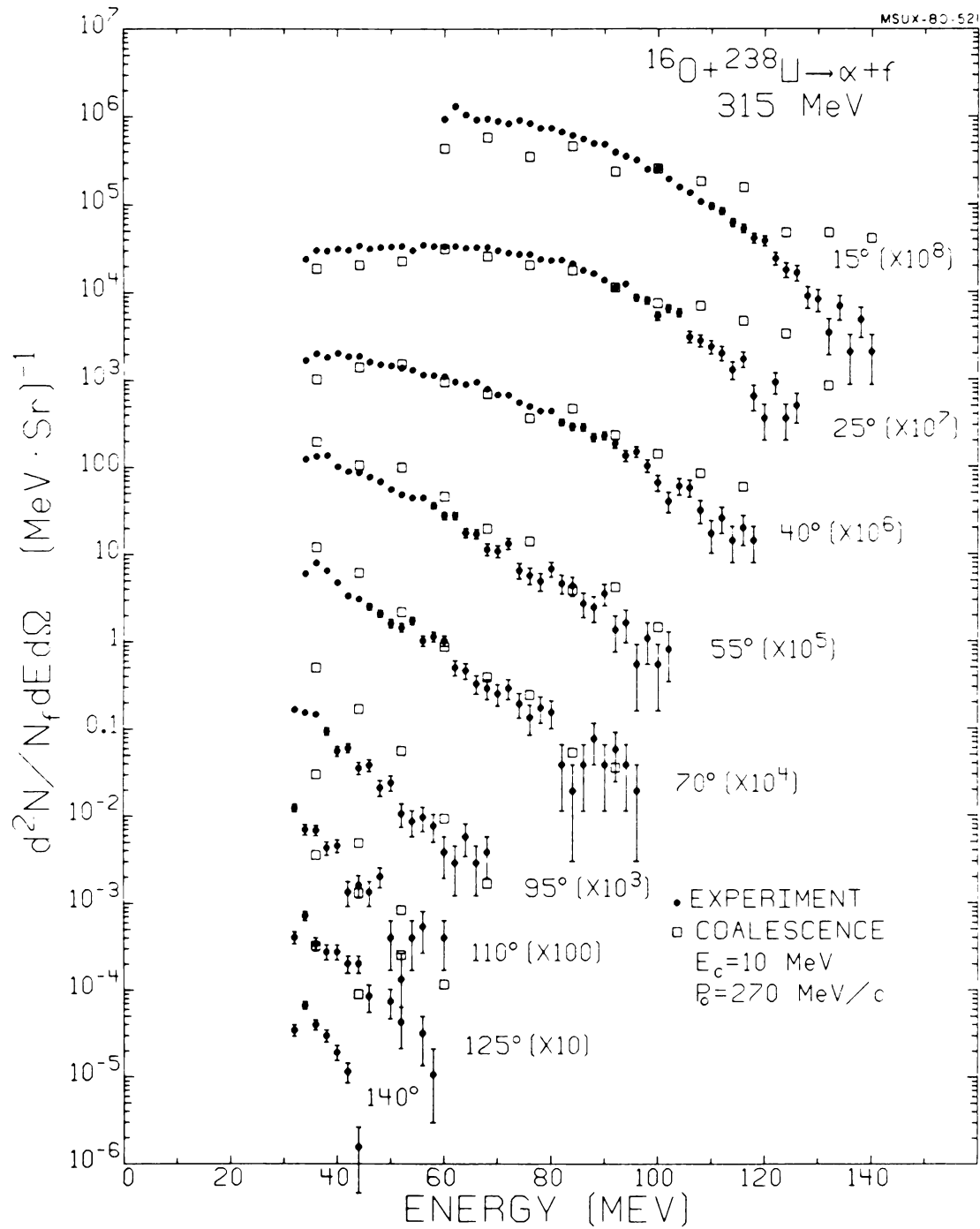
Figure VI-5.   Energy spectra of alpha-particles (solid
                points) detected in the reaction
                ^{238}U (^{16}O, αf) at 315 MeV.   The open squares
                are spectra predicted by the Coulomb-modified
                coalescence model of Eq. (VI-8).

agreement with the data is excellent except at the most backward angles. For the alpha-particle spectra (Figure VI-5) the coalescence predictions are also in fair agreement with the data. Here discrepancies are expected to occur also at forward angles, because of the enhanced contributions from projectile breakup reactions.

In Figure VI-6 the energy spectra of light particles (solid points) are shown for reactions on ^{197}Au at 140 MeV. The spectra of the composite particles are compared with the predictions of the coalescence model (open squares) obtained from the experimental proton spectra shown in the upper left quadrant of the figure. The coalescence relation can reproduce the high energy tails of the composite particle spectra very well but becomes somewhat worse in the low energy region, especially for tritons. At incident energies of 215 and 310 MeV (see Figures VI-7 and VI-8, respectively) the coalescence relation describes the composite particle spectra from reactions on ^{197}Au quite well, although the general agreement becomes slightly worse with increasing incident energy.

The composite particle spectra are compared to the coalescence relation for reactions on ^{27}Al at 140, 215, and 310 MeV in Figures VI-9, VI-10, and VI-11. The agreement between experiment and calculation is qualitatively similar to that observed for reactions on ^{197}Au.

The energy spectra of deuterons and tritons for
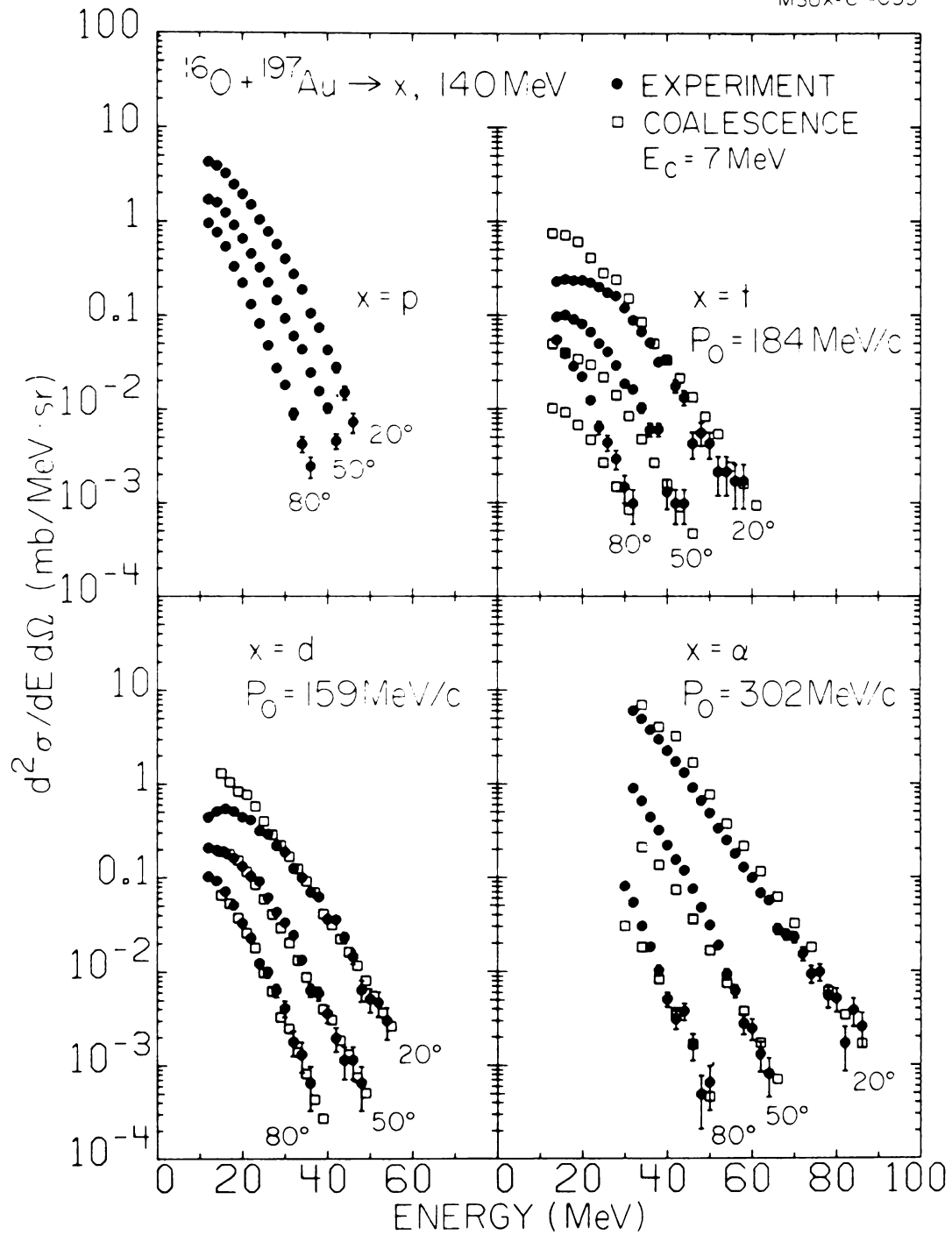
Figure VI-6. Energy spectra of light particles in reactions of 140 MeV ^{16}O on ^{197}Au. The open squares are spectra predicted by the coalescence model of Eq. (VI-8).
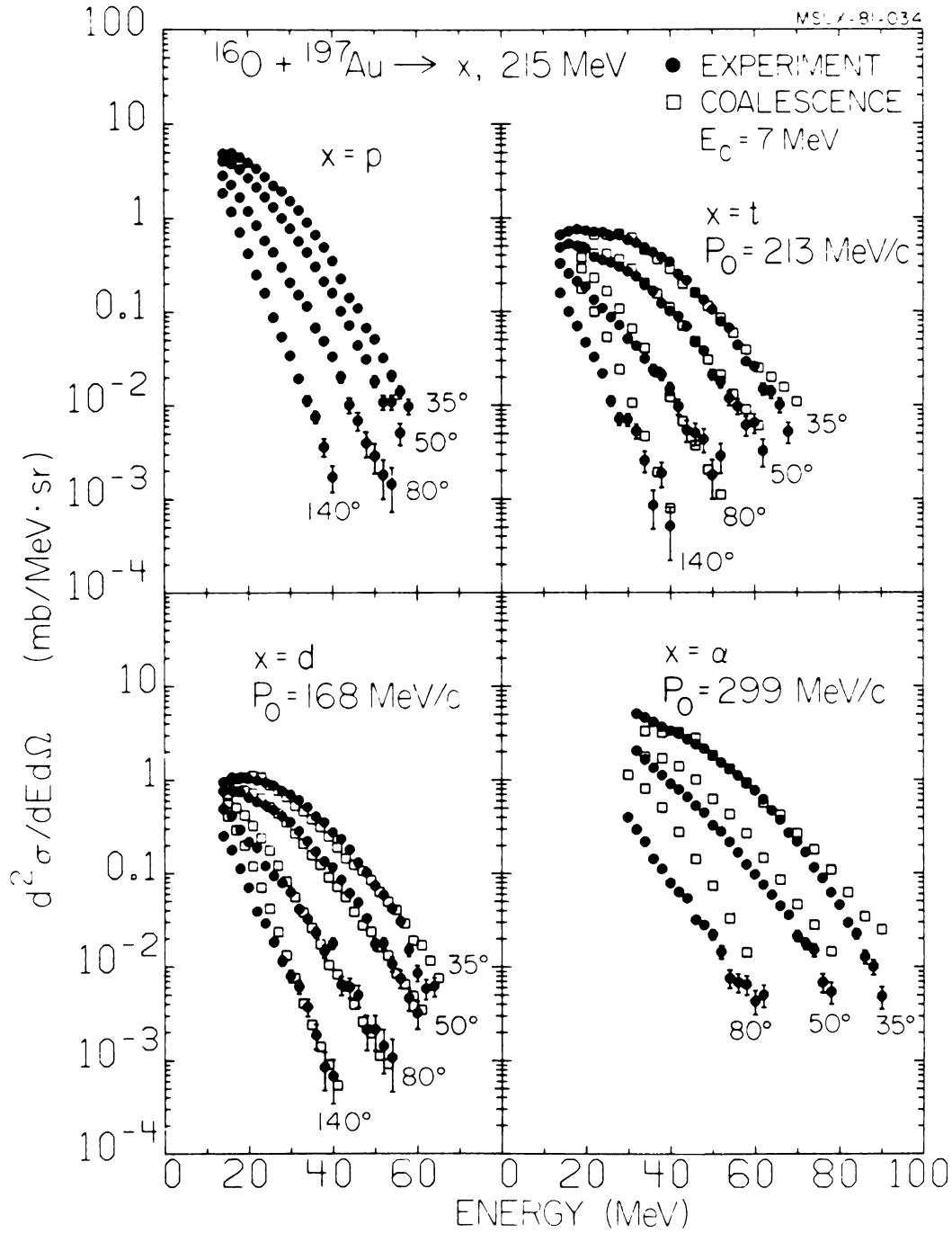
Figure VI-7. Energy spectra of light particles in reactions
of 215 MeV ^{16}O on ^{197}Au. The open squares are
spectra predicted by the coalescence model of
Eq. (VI-8).
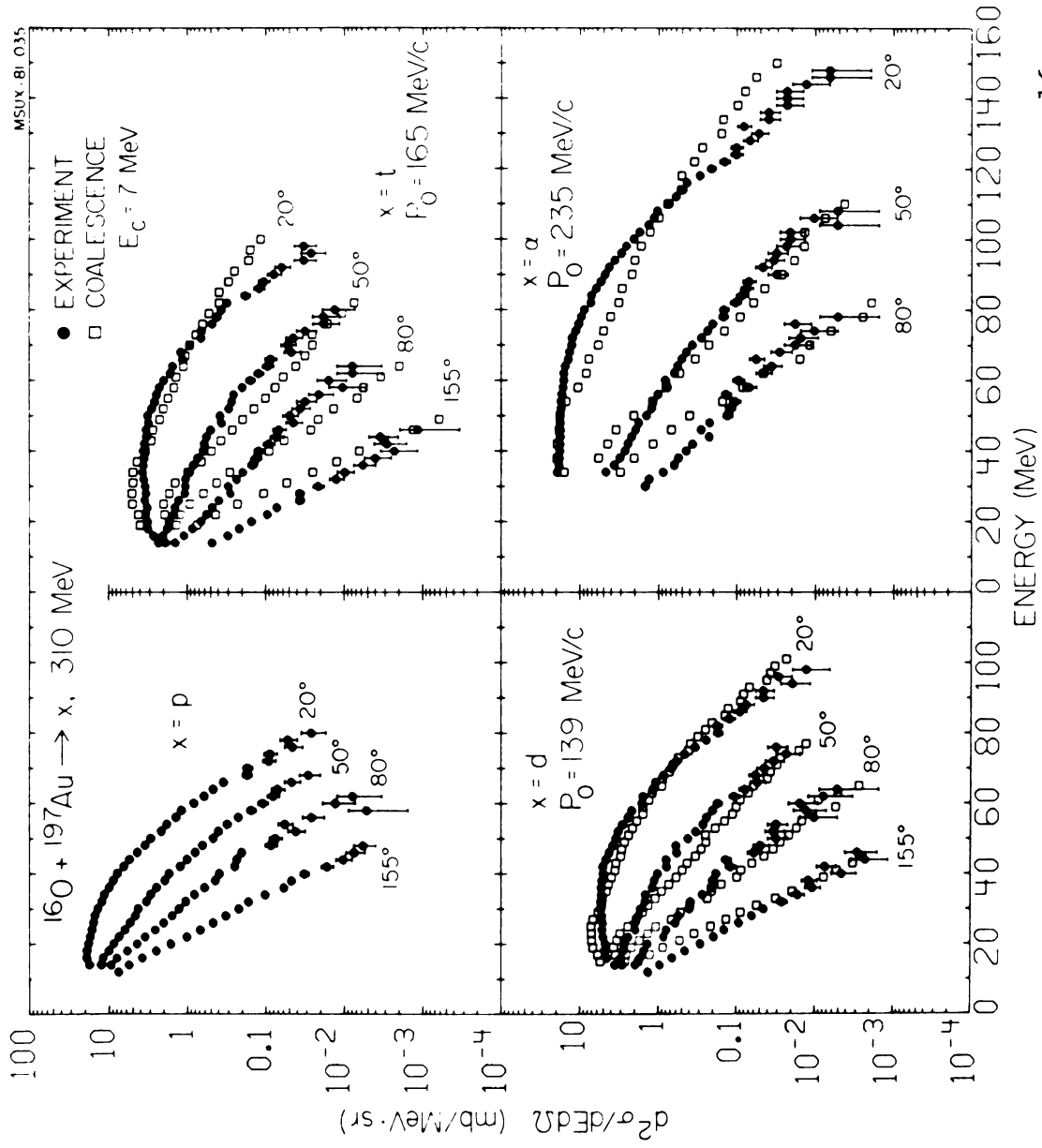
Figure VI-8. Energy spectra of light particles in reactions of 310 MeV 16O on 197Au. The open squares are spectra predicted by the coalescence model of Eq. (VI-8).
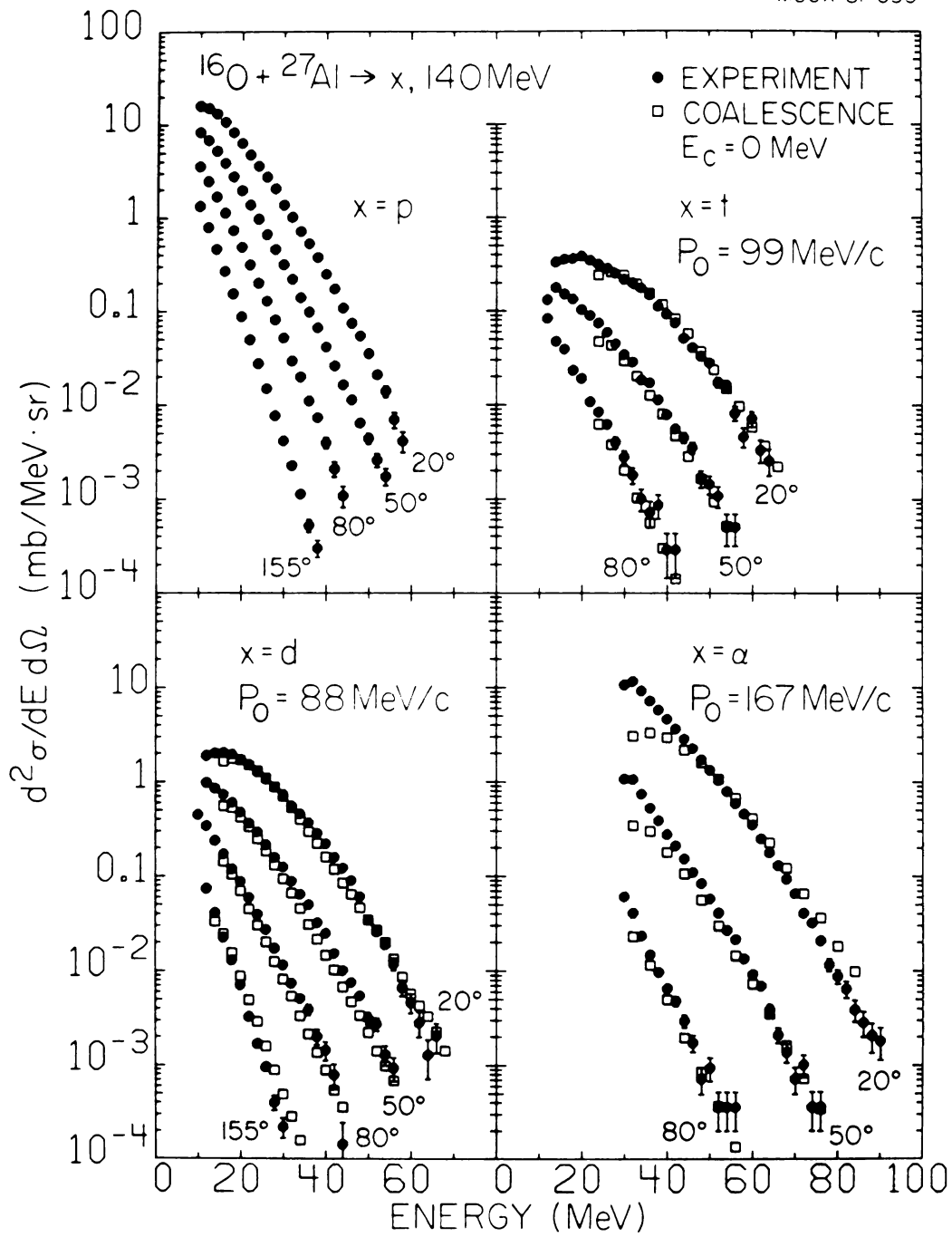
Figure VI-9. Energy spectra of light particles in reactions of 140 MeV ^{16}O on ^{27}Al. The open squares are spectra predicted by the coalescence model of Eq. (VI-8).
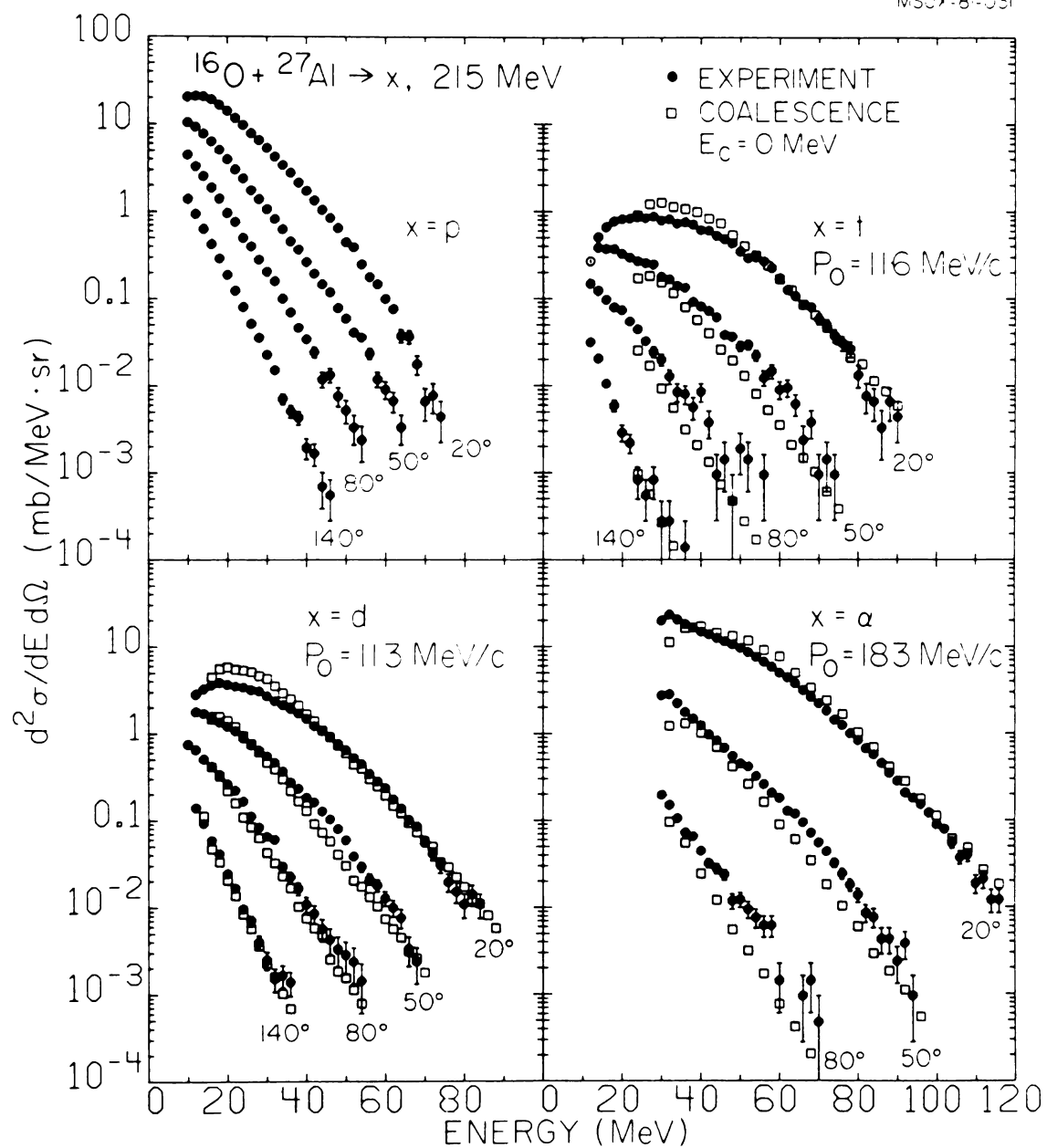
Figure VI-10. Energy spectra of light particles in reactions of 215 MeV ^{16}O on ^{27}Al. The open squares are spectra predicted by the coalescence model of Eq. (VI-8).

204
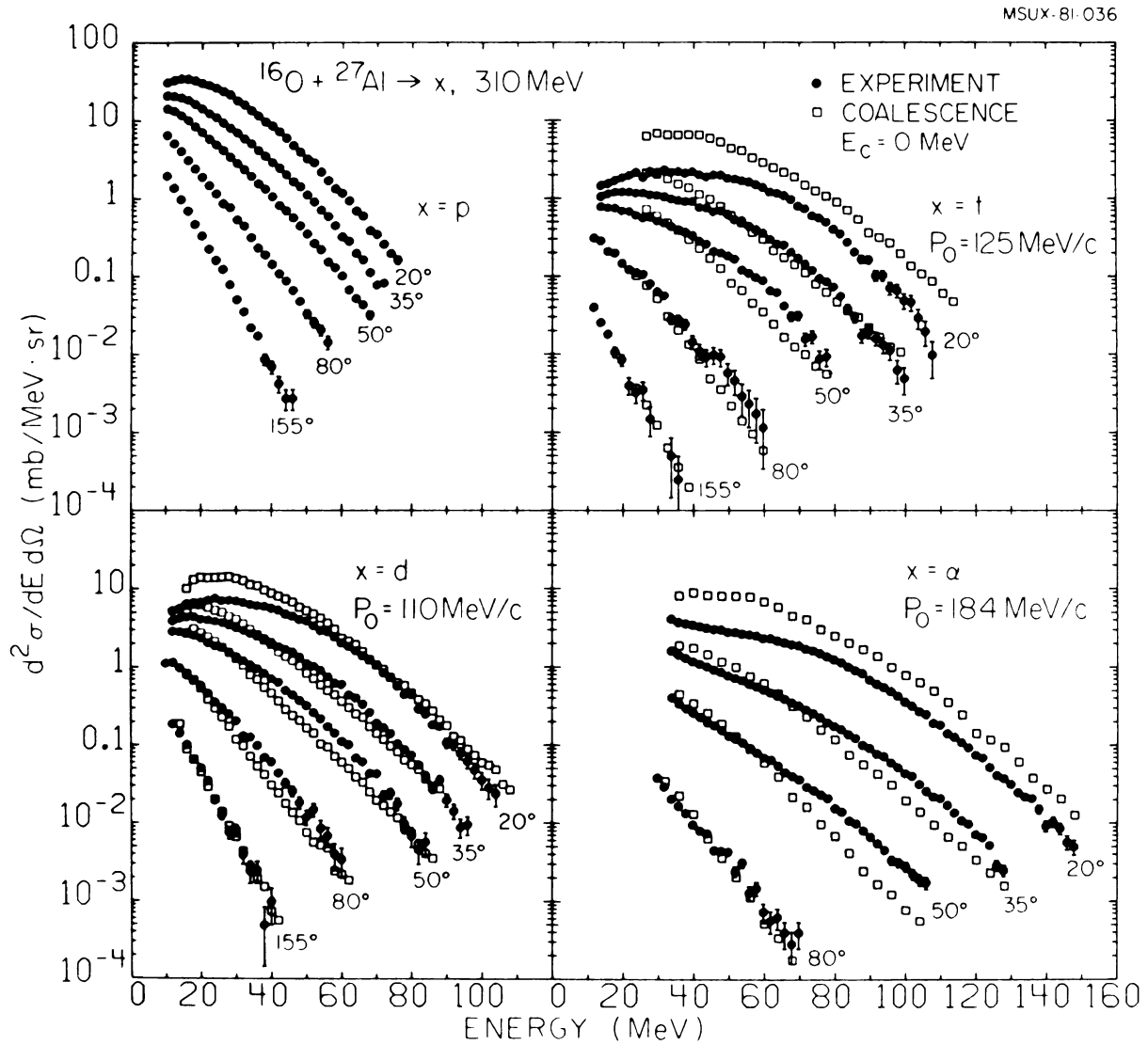
Figure VI-11. Energy spectra of light particles in reactions of 310 MeV ^{16}O on ^{27}Al. The open squares are spectra predicted by the coalescence model of Eq. (VI-8).

reactions of ^{16}O on ^{90}Zr at 215 and 310 MeV incident energies are shown in Figure VI-12. The coalescence results with $E_C = 0$ MeV are shown by the solid curves. The coalescence model is seen to give a poor reproduction of the experimental spectra, especially at low energies where the calculated spectra appear to have the wrong slope. This discrepancy at low energies is due to the relatively large low-energy compound nucleus component in the proton spectra which has no counterpart in the composite particle spectra, (see also the discussion of Figure VI-1). In fact, if we ignore the low-energy region of the proton spectra below 20 MeV then we should compare coalescence calculation and experiment in the region above 40 MeV for deuterons and above 60 MeV for tritons. The agreement between coalescence calculation and experiment is much better in this region.

A summary of the coalescence radii obtained in the present study is given in Table VI-2. Allowing for the 10% uncertainty in the coalescence radii due to the 35% uncertainty in the absolute cross sections (see Eq. (VI-8)) we cannot present conclusive evidence for an incident energy dependence of the coalescence parameter. The order of magnitude of the coalescence radii and the quality of the fits are similar to those obtained at relativistic energies [Le 79]. However, in contrast to the general trends observed at relativistic energies [Le 79, Na 81] we extract smaller coalescence radii P_O for reactions on the
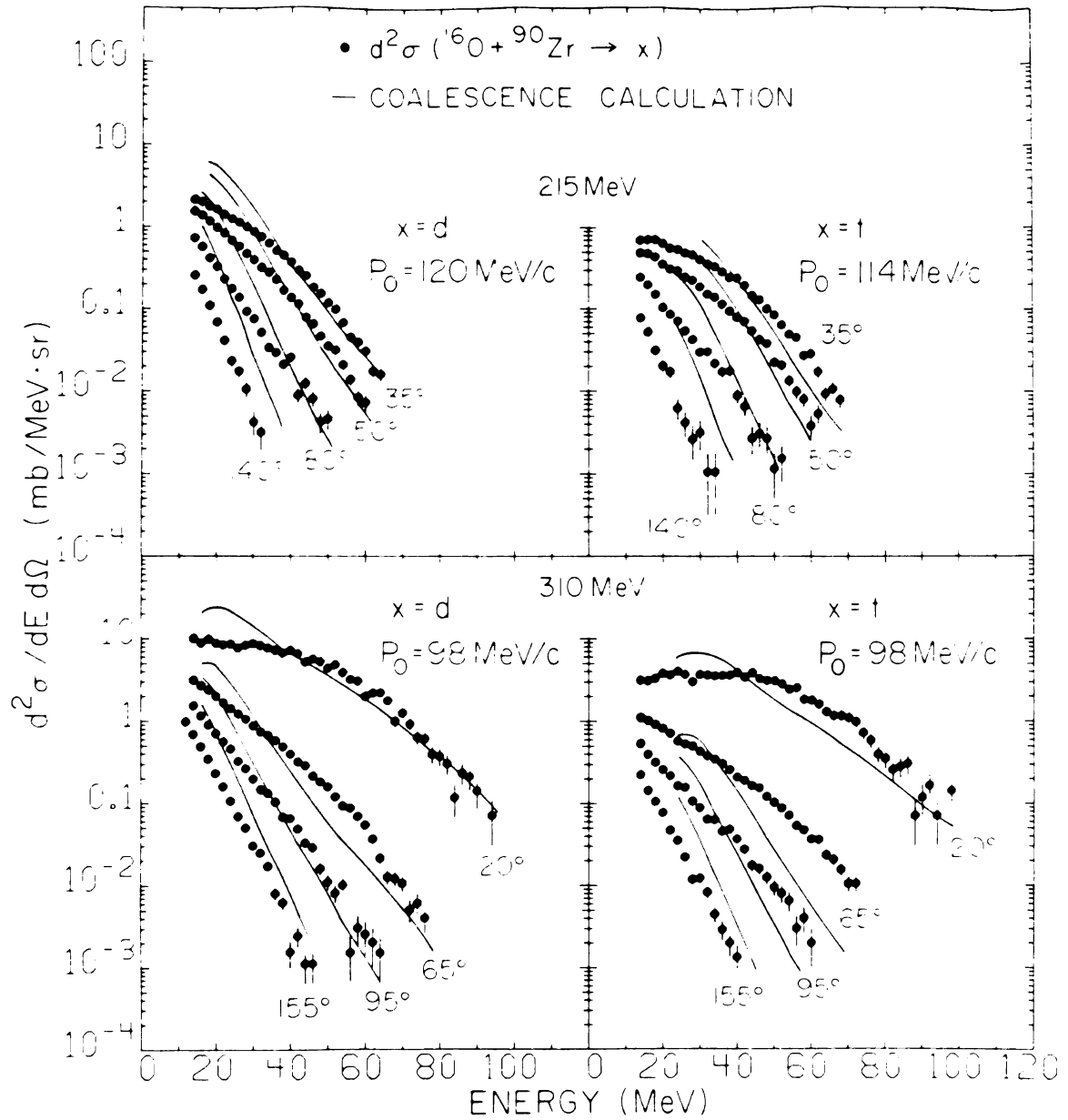
Figure VI-12. Energy spectra of deuterons and tritons in reactions of 16O on 90Zr at 215 and 310 MeV incident energy. The solid curves are spectra predicted by the coalescence model of Eq. (VI-8).

Table VI-2. Summary of coalescence radii[†], P_o, and freeze-out radii[††], R.

Energy	Target	Deuterons P_o(MeV/c)	R(fm)	Tritons P_o(MeV/c)	R(fm)	Alpha-particles P_o(MeV/c)	R(fm)
140	Al	88	11.8	99	10.6	167	8.6
	Au	159	6.9	184	6.3	302	6.0
215	Al	113	8.8	116	8.3	183	6.5
	Zr	(120)	(8.5)	(114)	(8.8)	-	-
	Au	168	6.1	213	4.8	299	4.4
310	Al	110	8.8	125	7.3	184	5.8
	Zr	(98)	(10.0)	(98)	(9.6)	-	-
	Au	139	7.1	165	5.7	235	4.7
315	U	170	5.7	215	4.2	270	3.8

[†]Systematic errors in P_o are about ±10% due to the ±35% uncertainty in the absolute cross sections (see Eq. VI-8}. For Zr there is an additional uncertainty of about ±30% due to the poor quality of the coalescence fits (see Figure VI-12). The coalescence radii for the U target have been normalized to inclusive fission events rather than to the total reaction cross section (see Eq. (VI-10)) and therefore should not be compared directly with the other coalescence radii.

[††]Calculated according to Eq. (VI-12) with $g_d = 3$, $\epsilon_d = 2.2$ MeV, $g_t = 2$, $\epsilon_t = 8.5$ MeV, and $g_\alpha = 1$, $\epsilon_\alpha = 28.3$ MeV. The proton moving source temperatures of Section V.E were used for T.

light target Al than for the heavy Au target.

If the thermodynamic interpretation of the coalescence
model applies, the momentum radius P_O can be related to the
volume of the thermal system at the freeze-out density where
formation and breakup of composite particles ceases [Me 77,
Me 78, Le 79, Me 80]

$$V = \left[\frac{Z!N!A^3}{2^A} \, g_A \, \exp(\epsilon_A/T) \right]^{1/(A-1)} \frac{3h^3}{4\pi P_o^3} \, . \qquad (VI-12)$$

Here ϵ_A is the binding energy and g_A is the spin degeneracy
factor of the composite particle. Expressing the volume V
in terms of an equivalent sphere, the spatial radius is seen
to be inversely proportional to the coalescence radius. In
the density matrix formulation [Sa 81a] a similar inverse
relationship is also expected. The spatial radii calculated
according to Eq. (VI-12) have been included in Table VI-2.
Since the interaction radius should increase with increasing
target mass, we would expect decreasing values of P_O. This
target dependence is observed at high energies. The smaller
values of P_O observed for the lighter target in the present
study might indicate a change in the mechanism of composite
particle production at low energies such as to a mechanism
of nucleon pickup from the nuclear surface [Ha 80]. Alterna-
tively, the different target dependence at low incident
energies might be an artifact of the Coulomb modification of
the coalescence relation. Further experimental and theoreti-
cal studies of the energy, projectile and target dependence
of composite light particle emission will be necessary to

clarify the underlying reaction mechanism.

In performing the coalescence calculations Coulomb para-
meters of $E_c = 7$ and 10 MeV were found to give the best agree-
ment with experiment for reactions on ^{197}Au and ^{238}U,
respectively. These values are significantly smaller than
expected for emission of the charged particle from the sur-
face of the composite nucleus. The low values of E_c may be
due to large deformations of the target residue or to
emission from the surface of the ^{16}O. However, the Coulomb
parameter might not strictly reflect the difference in the
proton and neutron distributions. In order to assess the
validity of the Coulomb modifications of Eq. (VI-8) we have
made a direct comparison of the energy spectra of protons
and neutrons emitted in coincidence with fission fragments
in the reaction ^{16}O + ^{238}U at 310 MeV incident energy.

The differential neutron multiplicities per fission
event, $d^2N/N_f dEd\Omega$, are shown in Figure VI-13. At low
energies, the spectra are dominated by a low temperature
component which has no apparent counterpart in the proton
spectra (see Section V.E.1). This component is consistent
with the statistical evaporation of neutrons from
equilibrated target residues and fission fragments. At
higher neutron energies the energy spectra fall off less
rapidly with increasing energy than expected of statistical
emission from fully equilibrated heavy nuclei. The high
energy regions of the neutron spectra exhibit characteris-
tics that are qualitatively similar to those observed for
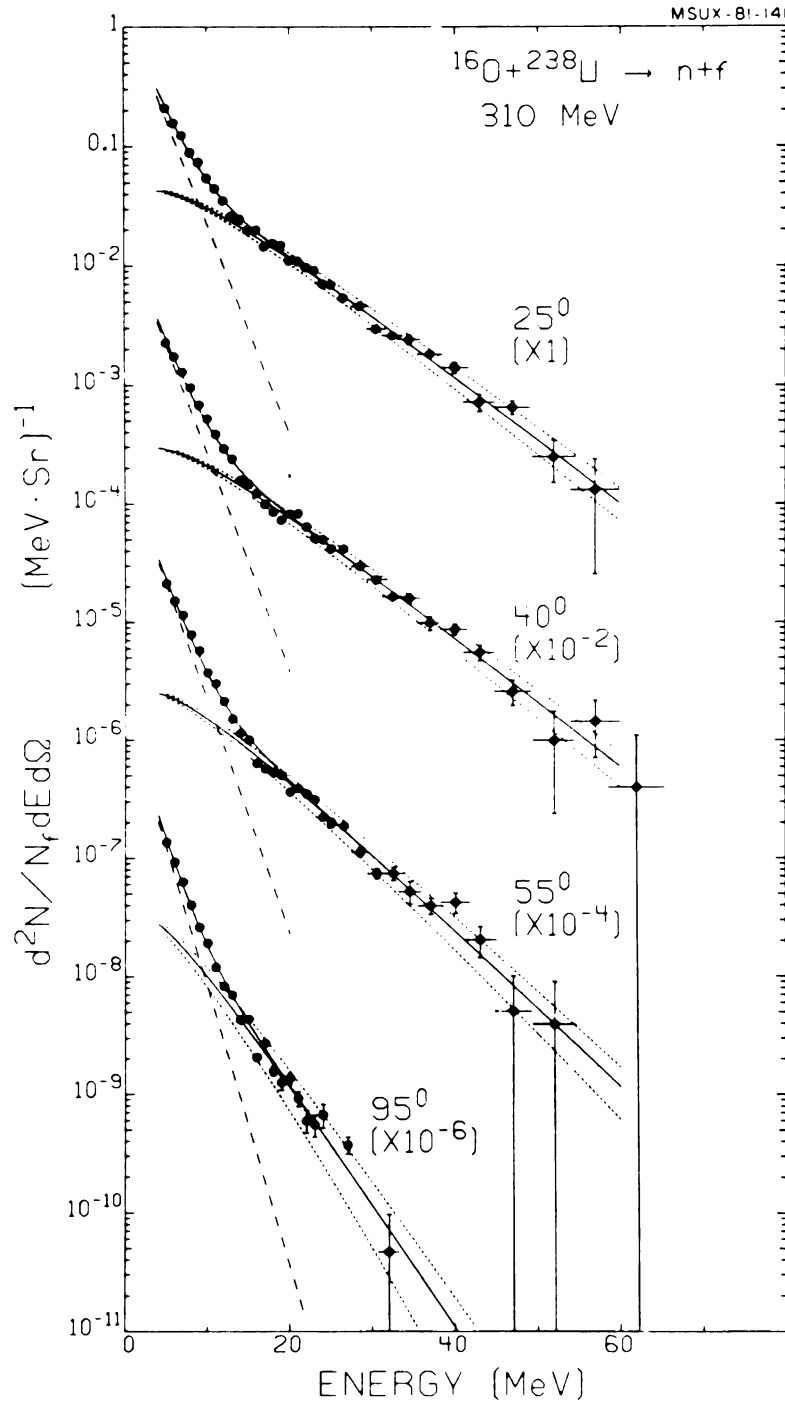
Figure VI-13. Differential neutron multiplicities per fission event measured for the reaction ^{238}U $(^{16}O, nf)$ at 310 MeV. The solid and dashed lines show the decomposition into equilibrium and nonequilibrium components, respectively. The dotted lines indicate the estimated errors within which the high energy regions of the neutron spectra are established. These limits are used for the comparison with the proton spectra in Figure VI-14.

the emission of energetic charged particles: with increas-
ing scattering angle the cross sections decrease and the
energy spectra become steeper.

In order to facilitate the comparison of proton and
neutron cross sections, we have decomposed each neutron
spectrum into two components by fitting the energy spectra
with the following function

$$\frac{d^2N(E)}{N_f dEd\Omega} = N_o \ e^{-E/T_o} + N_1 E^{\frac{1}{2}} e^{-E/T_1} \ . \tag{VI-13}$$

The first term, which omits an energy factor, adequately
represents the low energy component, and the second term
describes the high energy component which we associate with
preequilibrium processes. The constants N_o, T_o, N_1, T_1 are
adjustable parameters. This decomposition is shown in
Figure VI-13 by the solid and dashed curves. The correspond-
ing parameters are given in Table VI-3. The dotted lines
included in the figure show the uncertainties within which
the high energy regions of the neutron spectra are believed
to be established. The limits defined by these dotted lines
will be used for the comparison with the proton cross
sections shown in Figure VI-14.

The proton cross sections measured with the same
experimental geometry are compared to the corresponding
neutron cross sections in Figure VI-14. The proton data are
represented by solid points and the preequilibrium neutron
components are given by the shaded area in Figure VI-14a.

Table VI-3. Parameters of Eq. (VI-13) used for the decomposition of equilibrium and non-equilibrium components shown in Figure VI-13.

Θ_n	$N_o (MeV \cdot sr)^{-1}$	$T_o (MeV)$	$N_1 (MeV^{3/2} \cdot sr)^{-1}$	$T_1 (MeV)$
25°	1.35	2.45	0.036	7.60
40	1.85	2.35	0.025	7.4
55	2.00	2.20	0.024	6.2
95	1.78	1.85	0.038	4.0

MSUX-81-142

^{16}O + ^{238}U → p + f

310 MeV

25^0
(X1)

55^0
(X10^{-2})

(a)

25^0
(X1)

55^0
(X10^{-2})

(b)

ENERGY (MeV)

$(MeV \cdot Sr)^{-1}$

$d^2N/N_f dE d\Omega$
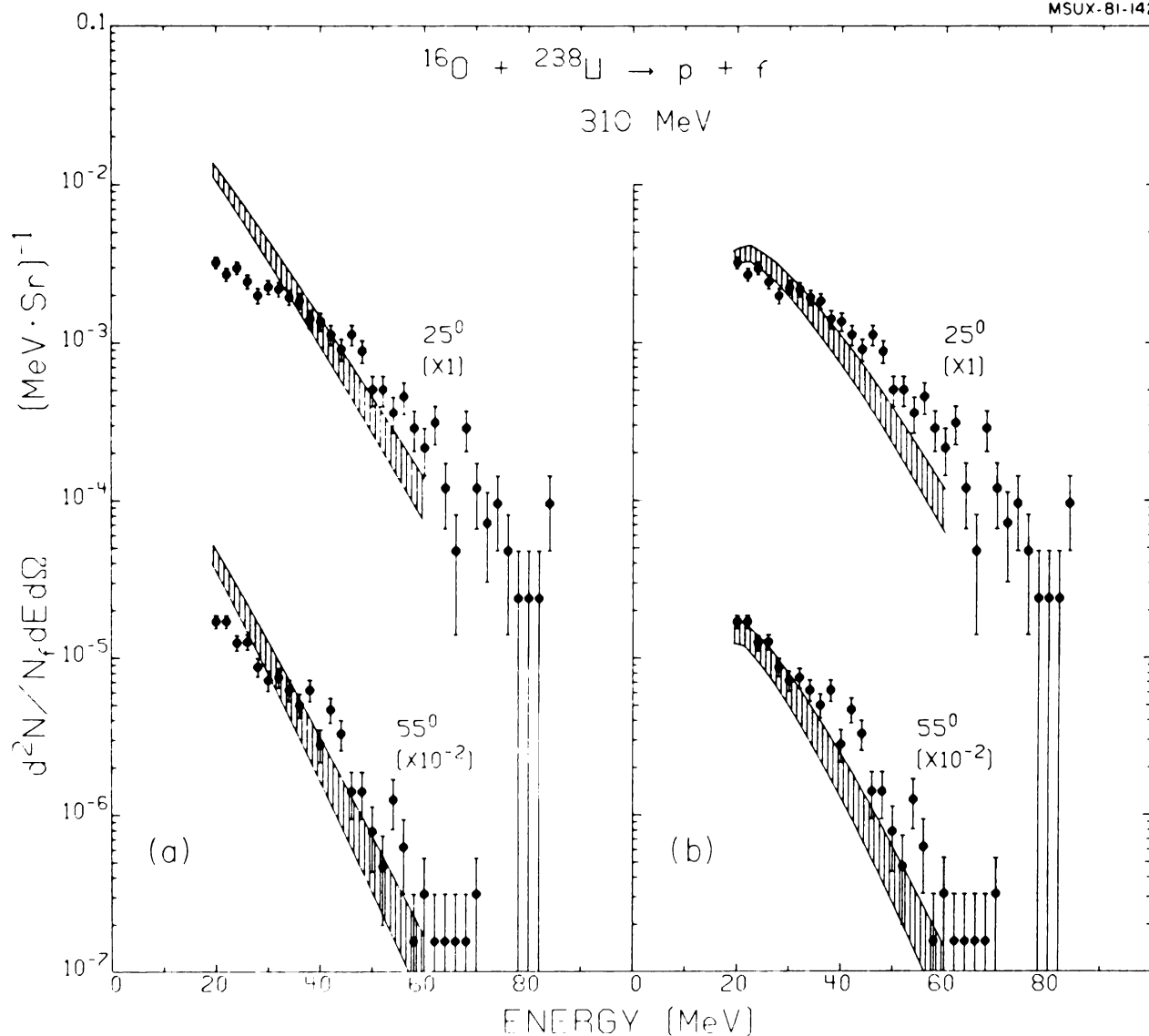
Figure VI-14. Differential proton multiplicities per
fission event measured for the reaction
^{238}U (^{16}O, nf) at 310 MeV. The shaded areas
represent the measured pre-equilibrium
neutron multiplicities (part a) and their
predicted transformation into proton multi-
plicities according to Eq. (VI-14) of the
text (part b).

The shapes of the proton and neutron spectra exhibit signif-
icant differences. Steeper slopes are observed for the
neutron spectra than for the proton spectra. At lower
energies ($E \lesssim 30$ MeV) the neutron cross sections exceed the
proton cross sections. However, the neutron cross section
drops below the proton cross section at higher energies
($E \gtrsim 30$ MeV).

The differences between the low energy part of the
proton and neutron spectra are most likely due to barrier
penetration effects. To illustrate this point, we have
transformed the neutron spectra of Figure VI-14a according
to the relation

$$\frac{d^2 N(E)}{N_f dE d\Omega} = \frac{\sigma_{inv}^{(p)}(E)}{\sigma_{inv}^{(n)}(E)} \frac{d^2 N(E)}{N_f dE d\Omega} \quad . \qquad \text{(VI-14)}$$

Here, the inverse reaction cross sections, $\sigma_{inv}(E)$,
were calculated from the optical model by using the
potentials of Becchetti and Greenlees [Be 69]. The use of
Eq. (VI-14) implies that the partial waves are added
incoherently and have the same statistical weight as for the
inverse reactions. Although these assumptions may not be
entirely correct, they should illustrate the penetrability
effect in the low-energy region. The resulting cross
sections are shown by the shaded areas in Figure VI-14b.
Reasonable agreement with the proton cross sections is
obtained at low neutron energies. The high energy part of

the spectrum is only slightly modified since $\sigma_{inv}(p) \simeq \sigma_{inv}(n)$

at high energies. Therefore, a simple barrier penetration

effect cannot explain the depletion of high energy neutrons.

Precompound model calculations [Bl 81] are able to

obtain qualitative agreement with our data. In Figure VI-15,

the (angle-integrated) neutron spectrum predicted for ^{16}O

induced reactions on ^{197}Au at 310 MeV incident energy is

compared with the experimental proton spectrum of the

present study and the calculated precompound proton spectrum

(see Section V.G). The calculation predicts lower neutron

cross sections in the high energy tail of the spectrum

and larger neutron cross sections in the low energy part of

the spectrum when compared to the proton spectrum. While

these features are in qualitative agreement with the data

of Figure IV-14a they are not predicted by recent "hot spot"

calculations [Mo 80] of nucleon emission from the interface

of the colliding nuclei. This calculation predicts that the

neutron-to-proton cross section ratio should scale with the

neutron-to-proton ratio of the emitting system.

It is clear from Figure VI-14a that the assumption of

Eq. (VI-11) is inconsistent with the observed neutron

spectra. The neutron spectra are not equivalent to the

proton spectra after Coulomb shifting and weighting by the

N/Z-ratio of the composite system. Similar observations

have been made at relativistic energies [Sc 79]. As a

result, a coalescence calculation in which the deuteron
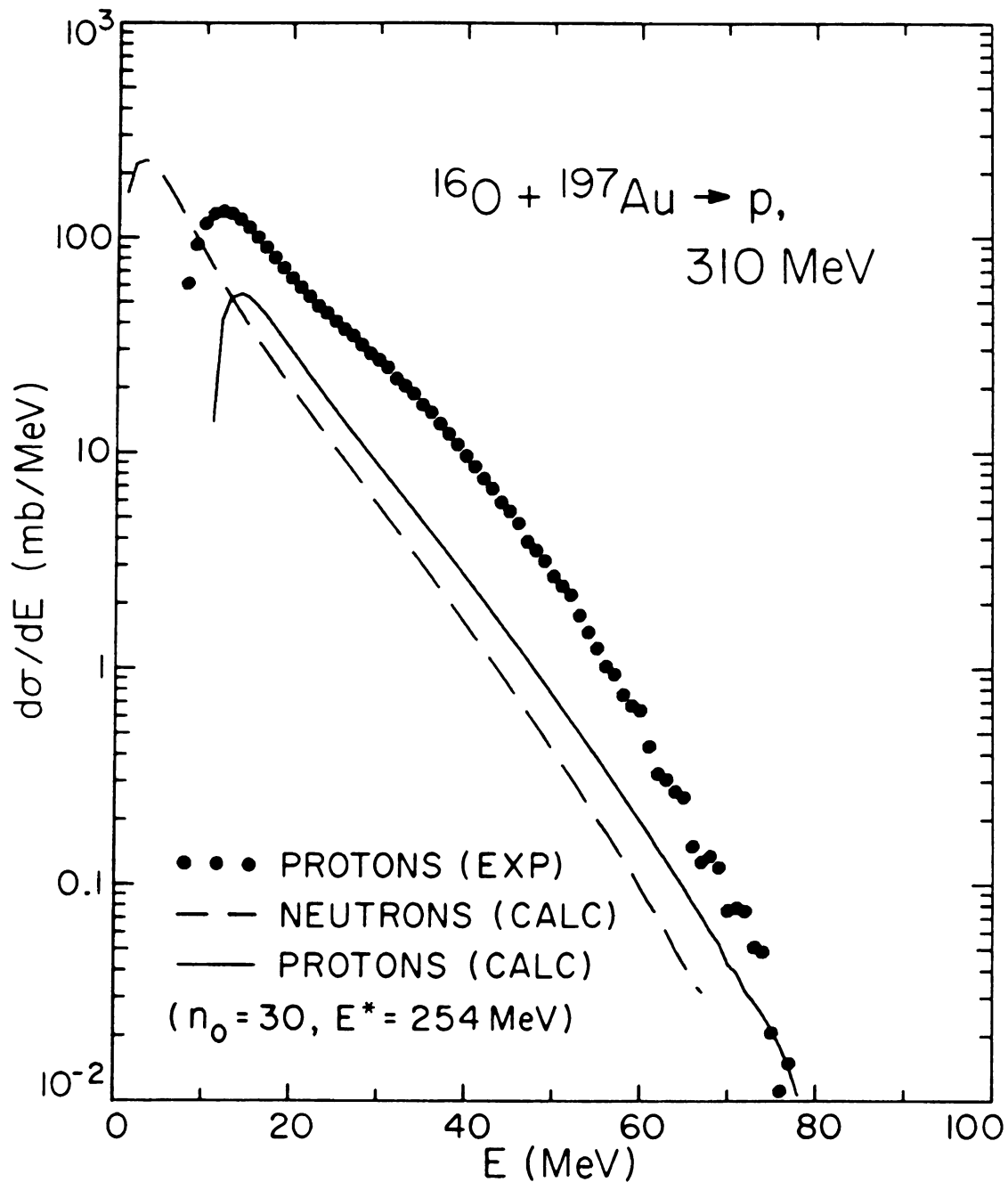
Figure VI-15. Comparison of neutron and proton angle-
integrated spectra in the compound nucleus
frame calculated with the precompound model
of Blann [Bl 81]. The calculation and the
experimental data are the same as shown in
Figure V-48 for $n_0 = 30$ and $E^* = 254$ MeV.

cross section is calculated as a product of the proton and neutron cross sections will not reproduce the data. Therefore, we have yet to understand the success of the coalescence formula of Eq. (VI-8) which uses the assumption of Eq. (VI-11). Investigating possible alternative explanations for composite particle formation remains an interesting subject for future research.

CHAPTER VII

SUMMARY AND CONCLUSIONS

A. Summary of Results

The emission of projectile residues and light particles in coincidence with fission fragments has been studied in ^{16}O-induced reactions on ^{238}U at $E/A = 20$ MeV incident energy. The measured folding-angle between the two coincident fission fragments was used to estimate the amount of linear momentum transferred to the target residue prior to fission. This information has been used to provide a simple operational classification of the reaction into "central" and "peripheral" collisions corresponding to large and small momentum transfers to the target residue.

A kinematical estimate of the unobserved momentum and of the fission fragment mass distributions observed in coincidence with projectile residues near the grazing angle has provided clear evidence for the inadequacy of the assumption of two-body kinematics. The emission of light particles into the forward direction is an important aspect of the mechanism of projectile residue emission. The light

particle emission is not, however, due to a quasi-elastic breakup process where the target nucleus acts as a mere spectator. Instead, large amounts of linear momentum and excitation energy are transferred to the target nucleus during the collision. Such information could not be obtained from the study of single particle inclusive energy spectra, which could be rather well described by quasi-elastic projectile breakup processes [Ge 77, Ud 79, Mc 80]. Future extensions of models for heavy ion breakup reactions will have to include this large inelasticity of the reaction. It will be interesting to perform similar coincidence measurements at higher incident energies where the participant-spectator models have been most successfully applied to the single particle inclusive cross sections.

Although light particle emission is an important aspect of peripheral collisions in which projectile-like fragments are emitted, it has been shown that most energetic light particles are associated with central collisions in which nearly the entire beam momentum is transferred to the target residue. The angular distributions of light particles emitted in central collisions are not as sharply forward peaked as those of peripheral reactions. On the other hand, the energy spectra have been shown to be rather similar for the two processes. The similarity of the energy spectra suggests a reaction mechanism in which the light particles are emitted at an early stage of the reaction.

The energy and target dependence of the inclusive light particle cross sections has been studied in ^{16}O-induced reactions on targets of ^{197}Au, ^{90}Zr, and ^{27}Al at incident energies of 140, 215, and 310 MeV. The light particle spectra can be parameterized in terms of a single thermal source which moves with slightly less than half of the beam velocity. The extracted velocity and temperature parameters do not follow the trend expected of compound nucleus emission, but instead, exhibit a systematic variation with the incident energy per nucleon above the Coulomb barrier. The trend of the temperature parameter can be extrapolated to temperatures observed in relativistic heavy-ion collisions. This systematic behavior follows the trend expected for the formation of a Fermi gas consisting of about equal contributions of nucleons from target and projectile. At present it is not clear why deuterons and tritons exhibit larger temperature parameters than protons.

Since the temperature and velocity parameters of the moving source model suggested an interpretation in which each interacting nucleon of the projectile was paired with a nucleon of the target, a single-scattering knock-out model has been investigated. These calculations, which involved a plane wave approximation, demonstrated that a direct mechanism is unlikely to account for all of the features of the energy distributions. It will be necessary to perform more detailed calculations with distorted waves

in order to determine the magnitude and details of the knock-out contribution.

The proton energy spectra for reactions on ^{197}Au have also been compared with the results of precompound calculations. It was shown that the spectra could not be described with a single energy-independent exciton number. Although the energy dependence of the exciton number was not due to assumptions on the rate of the fusion process, it might be explained by accounting for the local velocity and excitation of the system as the fusion process develops.

The light particle multiplicities were observed to increase smoothly with incident energy approaching unity at the highest energies. On the other hand, the proton to deuteron ratio was observed to decrease with energy to a value very similar to that observed at relativistic energies. This observation might indicate that the proton to deuteron ratio is largely determined by final state effects rather than by chemical equilibrium. Future theoretical and experimental investigations will be necessary to clarify whether this ratio can be used to extract information about the entropy produced in heavy-ion collisions.

It has been shown that the composite particle spectra may be understood in terms of the proton spectra via a coalescence relation which has been modified to include the effects of Coulomb distortion. With this modification the coalescence model has been extended to incident energies of

less than E/A = 10 MeV with values of the coalescence para-
meter similar to those obtained at relativistic energies.
However, a large low-energy contribution in the proton
spectra prohibited a satisfactory application of the
coalescence relation to the composite particle spectra for
reactions on the ^{90}Zr target. It was found that the ^{197}Au
target resulted in the largest coalescence radii. This
appears to be in contrast to the situation at relativistic
energies where the coalescence radii generally decrease with
increasing target mass. However, this new trend may be a
simple result of the Coulomb modification of the coalescence
relation which was necessary at the energies of the present
study. At present, the details of the production of
composite light particles are not fully understood. In
particular, a direct comparison of neutron and proton spectra
has shown that the assumption underlying the Coulomb-modified
form of the coalescence relation cannot be supported. On the
other hand, a simple multiplication of the proton and neutron
spectra, as the coalescence model would suggest, will not
reproduce the observed deuteron spectra. Clarification of
the mechanism responsible for composite particle emission
remains an interesting topic for future investigations.

B.   Conclusions

In the present study, a large portion of the linear
momentum lost by the projectile residue was observed to be

transferred to the target residue. This is not consistent with a pure projectile breakup reaction in which all out-going fragments are emitted as free particles. Instead, it indicates a strong interaction between target and projectile with a large probability for absorbing a portion of the projectile. Although inclusive measurements were well described by quasi-free breakup processes [Ge 78, Wu 78, Wu 79, Ud 79, Mc 80], the observations of the present study are consistent with other recent results which indicate, instead, that breakup reactions are dominated by "inelastic" and "absorptive" breakup for light ion induced reactions [Bu 78, Ko 79, Sh 79, Ca 80], and by "breakup-fusion" reactions in heavy ion induced reactions [Ke 79, Ta 81].

The observation that light particles with very similar energy spectra result from "peripheral" collisions accompanied by projectile residues, as well as from "central" collisions in which a large portion of the projectile is absorbed by the target nucleus, suggests that a common reaction mechanism might underlie all of these phenomena. This mechanism might involve the breakup of the projectile accompanied by a strong interaction with the target nucleus. The interaction could occur via absorption of one of the projectile fragments, by inelastic excitation of the target or by nucleon transfer. The successful application and systematic behavior of the moving source parameterization suggests that the reaction is of a

localized nature and that the mechanism evolves smoothly
with incident energy and independently of the target
characteristics. Furthermore, the success of the
coalescence relation for describing composite particle
emission indicates that the mechanism of composite particle
production is closely tied to that of nucleon emission.
Incorporating these observations into a suitable model of
the heavy ion reaction mechanism presents a challenging
theoretical problem for the future.

APPENDICES

APPENDIX A: CORRECTION FOR SYSTEMATIC FOLDING-ANGLE ERRORS

The small size (8 x 47 mm) of commercially available
(ORTEC) position sensitive solid state detectors demands
a close geometry of the experimental set-up in order to
facilitate a complete coverage of the folding-angle
distributions. This, in turn, renders the experimental
determination of the folding-angles very susceptible to
alignment errors. Two main contributions to the
systematic folding-angle error arise from the fact that
1) the target plane might be slightly offset from the
center of the chamber by an amount x and 2) the beam
misses the true center of the chamber by an amount y. A
possible geometry is shown in Figure A-1. The actual
intercept of the beam with the target is denoted I and is
located at a distance r and angle ϕ with respect to the
true center, C, of the scattering chamber. The quantities
r and ϕ are related (see Figure A-1) to the target offset
x, the beam offset y, and the target angle Θ_t according to
the relations

$$r \sin \phi = y \qquad\qquad\qquad (A-1)$$

and

$$r \cos \phi = \frac{x + y \cos \Theta_t}{\sin \Theta_t} \quad . \qquad\qquad (A-2)$$
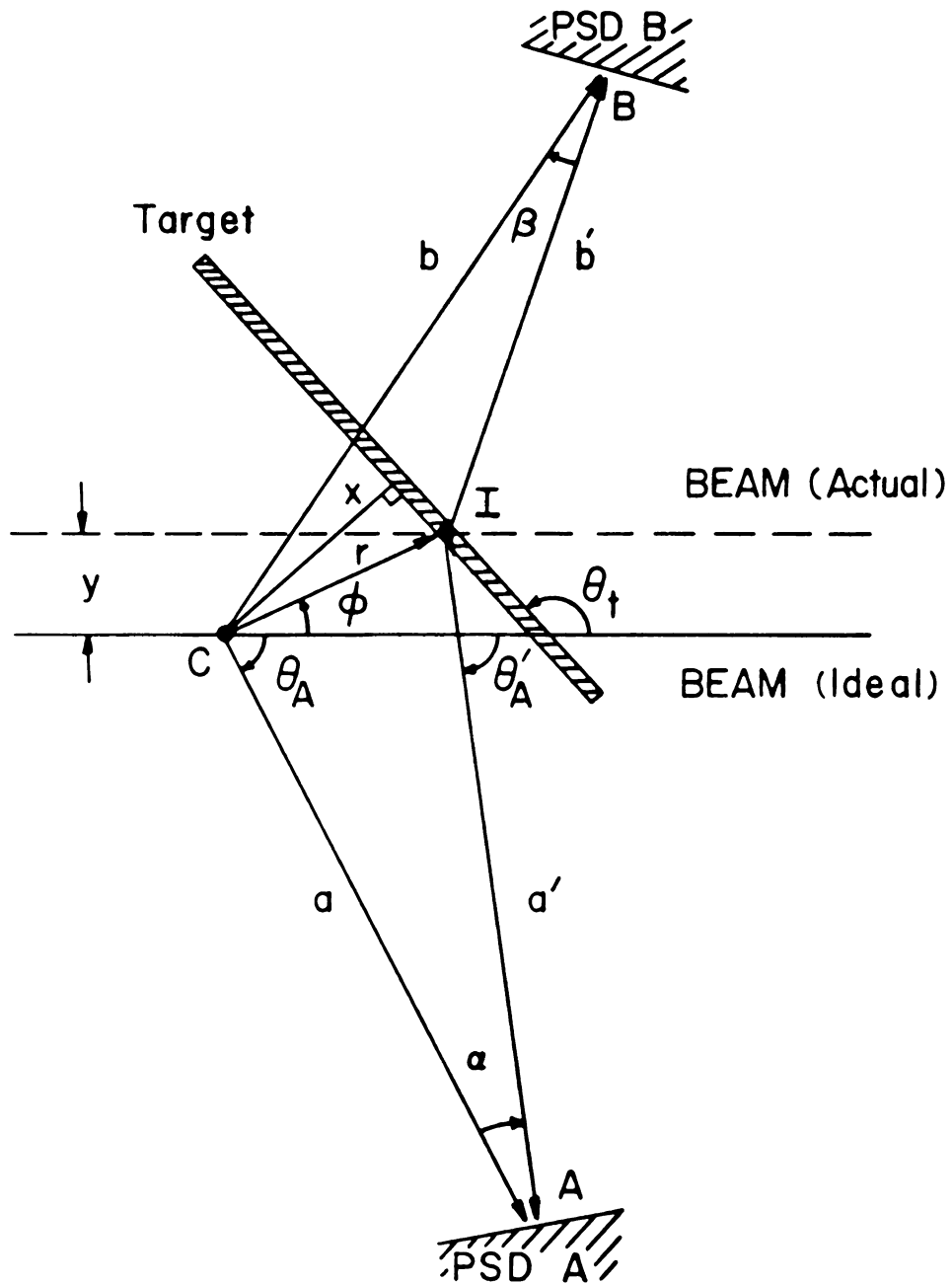
Figure A-1. Illustration of the effects of beam spot off-
sets. Trigonometric relations used to derive
the angle corrections are discussed in the
text.

For fission fragment A the true emission angle, Θ_A', is related to the measured angle, Θ_A, by

$$\Theta_A' = \Theta_A + \alpha \ .$$ (A-3)

The correction term α can be obtained from trigonometric relations between quantities pertaining to the triangle ACI of Figure A-1. Here the point A denotes the position where the fragment is detected in the PSD. The unknown distance, a', is related to the calibrated distance, a, according to

$$a'^2 = a^2 + r^2 - 2ar \cos (\Theta_A + \phi) \ .$$ (A-4)

With the relation

$$a' \sin \alpha = r \sin (\Theta_A + \phi)$$ (A-5)

the correction term is obtained as

$$\alpha = \arcsin \left(\frac{r \sin (\Theta_A + \phi)}{[a^2 + r^2 - 2ar \cos (\Theta_A + \phi)]^{\frac{1}{2}}} \right) \ .$$ (A-6)

The solution in the interval $[-\pi/2, \pi/2]$ should be used. For fission fragment B the true emission angle is

$$\Theta_B' = \Theta_B + \beta \ .$$ (A-7)

The correction β can similarly be written as

$$\beta = \arcsin \left(\frac{r \sin (\Theta_B - \phi)}{[b^2 + r^2 - 2br \cos (\Theta_B - \phi)]^{\frac{1}{2}}} \right) \ .$$ (A-8)

Again only the solution in the interval $[-\pi/2, \pi/2]$ is to be used.

By measuring the inclusive folding-angle distributions for four angles of the target with respect to the beam axis, for example at θ, $\pi-\theta$, $\pi+\theta$, and $2\pi-\theta$ we can determine the two contributions to the systematic error rather accurately by requiring the corrected folding-angle distributions to remain independent of target angle. Three settings of the target angle are in fact sufficient for a determination of the two offsets and the true folding-angle distribution, and consequently the fourth target angle setting serves as a consistency check of the measurement.

To check this correction procedure as well as the calibration of the PSDs, measurements were made of the inclusive fission fragment folding-angle distribution resulting from reactions of 140 MeV ^{16}O ions incident on ^{238}U. At this energy, complete fusion of target and projectile is expected to be a dominant reaction mechanism. In addition, the previous measurements of Sikkeland et. al. [Si 62] for the same system were available for comparison.

The inclusive folding-angle distribution obtained in the present study is shown in Figure A-2. These data, which are the sum of four target settings, have
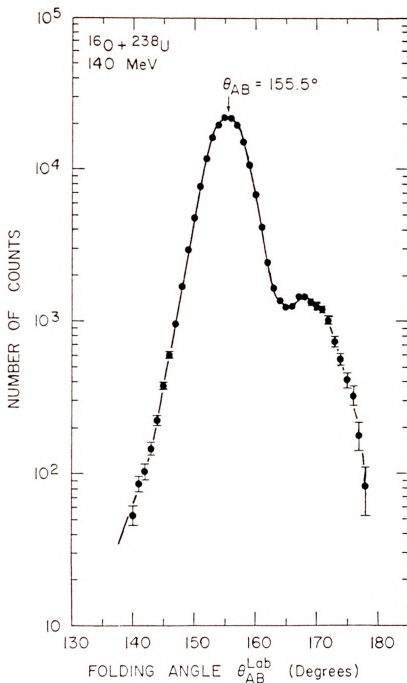
Figure A-2. Inclusive fission fragment folding-angle distribution for 140 MeV ^{16}O on ^{238}U. Data have been corrected for systematic errors due to imperfect beam and target positions, as well as the folding-angle dependent detection efficiency.

been corrected for systematic errors due to target and beam offsets. The maximum in the distribution is located at $\Theta_{AB} = 155.5°$. This is in good agreement with a theoretical estimate of $\Theta_{AB}^{theo} = 155.8°$ obtained by assuming full momentum transfer to the compound nucleus, ^{254}Fm, folllowed by asymmetric fission at the most probably mass division and at the measured total kinetic energy release of 195.1 MeV [Gi 77].

In the previous measurements of Sikkeland et. al. [Si 62] the maximum in the fission yield curve was located at a folding-angle of $\Theta_{AB} = 156.6°$. The discrepancy between this result and our measurement is a consequence of using different experimental geometries for the fission detectors (for an example of the consequences of different experimental geometries see Figures V-1 and V-2). A calculation of the expected most probable folding-angle under these experimental circumstances (see Appendix B) accounts for the ∿1° discrepancy between the two experimental results. We therefore conclude that the folding-angle measurements of the present study are accurate to within ±1°.

APPENDIX B: SIMULATION OF FISSION COINCIDENCE

EXPERIMENTS

When performing coincidence studies it is important
to understand the kinematic bias which is introduced in
the result as a consequence of the location and geometry
of the various detectors. For this purpose, a computer
program called EFFY has been written in order to simulate
the experimental situation of the present fission
coincidence measurements. The program simulates the
detection of both fission fragments which result from the
sequential fission decay of the target residue, and in
addition, allows for the possibility of detecting a
coincident projectile residue. As input, the program
requires the specification of the location and geometry
of the two position-sensitive fission fragment detectors,
the mass distribution of the fission products, and the
average total kinetic energy release for a given fission
fragment mass division. In the fission-inclusive mode,
in which a projectile-like fragment is not observed, the
recoil momentum is specified in the beam direction and
the efficiency for detecting both fragments and the
average folding-angle, $<\theta_{AB}>$, between them are calculated.
This allows a determination of the detection efficiency
as a function of the average folding-angle (see Figure III-1)
which can then be used to perform the efficiency correction

231

to the observed folding-angle distributions. It also allows a determination of the expected relationship between the recoil momentum and average folding-angle and an investigation of the dependence of this relationship on experimental geometry and on the identity of the system assumed to be fissioning (see Figure III-5, III-6, and V-2). In the coincidence mode, an initial two-body reaction is assumed followed by the sequential fission decay of the target residue. In this case, the mass and energy of the incident projectile, the mass and scattering angle of the projectile-like fragment, and the Q-value of the reaction are all specified. From this information the recoil momentum, detection efficiency, average folding-angle, and average mass asymmetry between the two fission detectors, $<M_B - M_A>$, can be calculated. These quantities can be compared to those obtained from the fission-inclusive calculation to determine whether they are biased as a result of the asymmetry of the recoil directions imposed by detecting the projectile-like fragment. For the present study, this calculation reveals that there is little kinematic bias as a result of detecting the projectile residue due to the fact that it was observed at a forward angle of 15°.

Details of the equations and calculational procedure used in the program EFFY are as follows:

1. CALCULATE DETECTOR GEOMETRY. Input the distances a, d_A, and d_A' and the angles Θ_A^o and ϕ_A defined in Figure B-1 for detector A. The angular acceptance of the detector is calculated as

$$\Theta_A^{min} = \Theta_A^o - \arctan\left(\frac{d_A \sin\phi_A}{a + d_A \cos\phi_A}\right) \qquad \text{(B-1a)}$$

$$\Theta_A^{max} = \Theta_A^o + \arctan\left(\frac{d_A' \sin\phi_A}{a - d_A' \cos\phi_A}\right) . \qquad \text{(B-1b)}$$

The angular acceptance of detector B is calculated in a similar fashion.

2. CALCULATE THE RECOIL MOMENTUM $\vec{P}_R$. This is done in either a fission-inclusive mode or in a coincidence mode:

   a. Fission-inclusive mode. The target residue is assumed to recoil into zero degrees and the magnitude of $|\vec{P}_R|$ is input.

   b. Coincidence mode. Specify m_1, E_1, m_3, Θ_3, m_R, and Q, that is, the mass and energy of the projectile, the mass and scattering angle of the projectile residue, the recoil mass and the reaction Q-value, respectively. From energy conservation

$$\frac{P_1^2}{2m_1} = \frac{P_R^2}{2m_R} + \frac{P_3^2}{2m_3} - Q \qquad \text{(B-2)}$$
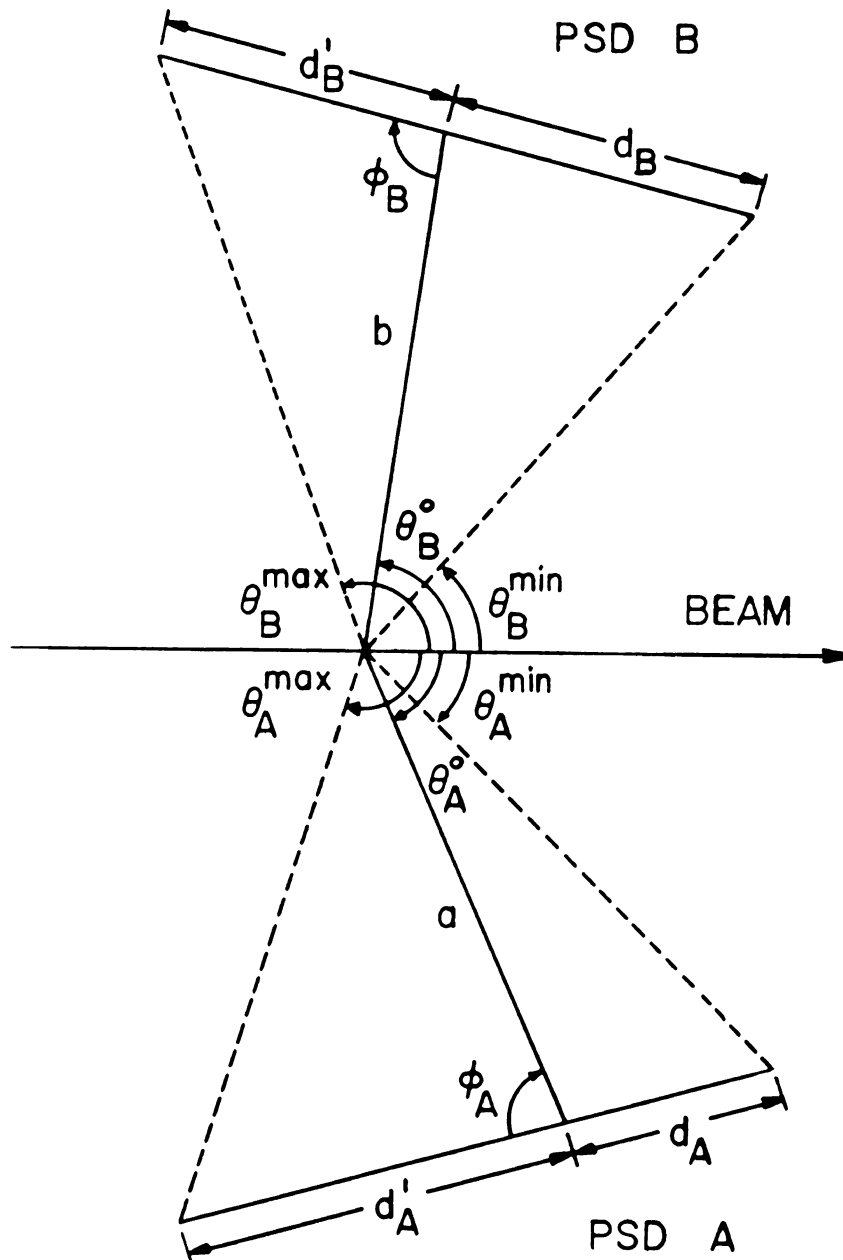
Figure B-1. Illustration of the quantities which define
the geometry of the position sensitive fission
fragment detectors.

and from momentum conservation

$$\vec{P}_1 = \vec{P}_R + \vec{P}_3 \tag{B-3}$$

where $\vec{P}_1$ is the momentum of the beam and $\vec{P}_R$ and $\vec{P}_3$ are the momenta of the recoiling target and projectile fragment, respectively. These equations can be combined to yield the quadratic equation

$$\left(\frac{1}{m_3} + \frac{1}{m_R}\right) P_3^2 - \left(\frac{2P_1}{m_R} \cos\theta_3\right) P_3 - \left[2Q + \left(\frac{1}{m_1} - \frac{1}{m_R}\right) P_1^2\right] = 0. \tag{B-4}$$

Here, the positive root for P_3 is to be taken. The recoil momentum $\vec{P}_R$ follows from Eq. (B-3).

3. CALCULATE CENTER OF MASS VELOCITIES. In the present study we have simulated fission of the target nucleus ^{238}U, as expected for the most peripheral collisions, using the experimental fission fragment mass and total kinetic energy distributions observed for proton-induced fission of ^{238}U [Bi 70]. At the other extreme of complete fusion reactions we have used either the experimental distributions for spontaneous fission of ^{254}Fm [Gi 77] or the more symmetric distributions for spontaneous fission of ^{257}Fm [Ba 71]. From the chosen mass distribution a fragment of mass m_A is assumed to be emitted toward detector A and a fragment of mass $m_B = m_R - m_A$ toward detector B. Using the average total

kinetic energy release $\overline{TKE}$ corresponding to this mass division calculate

$$p^2 = \frac{2m_A m_B}{(m_A + m_B)} \overline{TKE} \qquad (B-5)$$

from which the fission fragment velocities in the center of mass of the target recoil are calculated as

$$v_A^{cm} = \frac{p}{m_A} \qquad (B-6a)$$

and

$$v_B^{cm} = \frac{p}{m_B} . \qquad (B-6b)$$

4. CALCULATE LABORATORY ANGLES OF FISSION FRAGMENTS. For a particular angle of emission of fragment A in the recoil frame, Θ_A^{cm}, the laboratory angles of fragments A and B are seen from Figure B-2 to be given by

$$\Theta_A = \arctan\left(\frac{v_A^{cm} \sin\Theta_A^{cm}}{v_R + v_A^{cm}\cos\Theta_A^{cm}}\right) + \Theta_R \qquad (B-7a)$$

and

$$\Theta_B = \arctan\left(\frac{v_B^{cm} \sin\Theta_A^{cm}}{v_R - v_B^{cm}\cos\Theta_A^{cm}}\right) - \Theta_R \qquad (B-7b)$$

where we have used the fact that $\Theta_B^{cm} = \pi - \Theta_A^{cm}$.

5. CALCULATE THE DETECTION EFFICIENCY $\varepsilon(m_A, \Theta_A^{cm})$. The relative out of plane width, $w_A(\Theta_A)$, of detector A at the angle Θ_A is given by
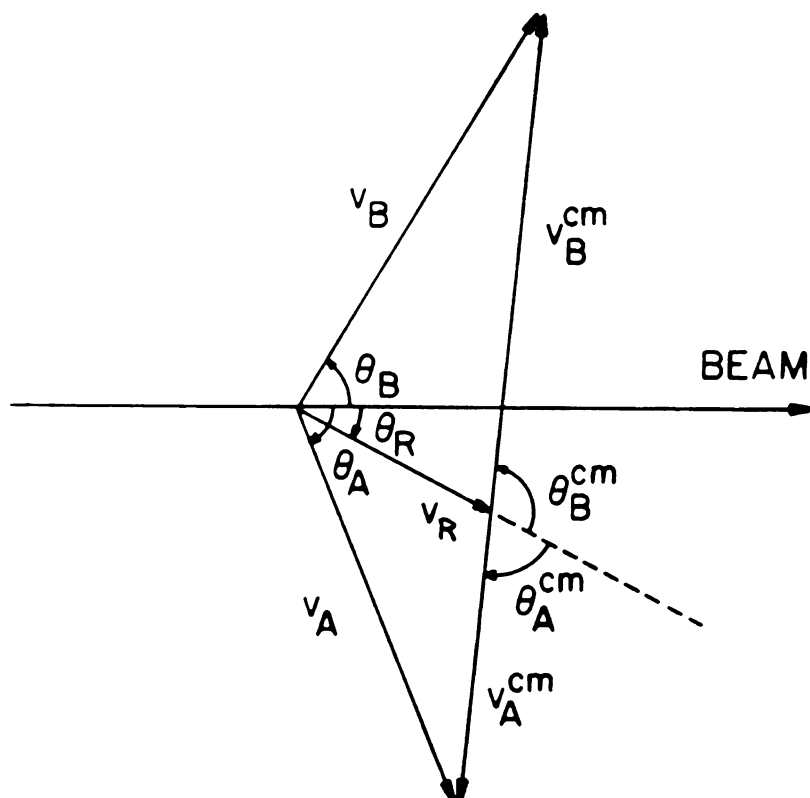
Figure B-2. Relationship between the angles and velocities of the fission fragments in the rest frame of the recoiling target residue and in the laboratory frame.

$$w_A(\Theta_A) = \begin{cases} w_A^o \sin(\Theta_A^o + \phi_A - \Theta_A)/\sin\phi_A & \text{for } \Theta_A^{min} \le \Theta_A \le \Theta_A^{max} \\ 0 & \text{otherwise} \end{cases} \qquad \text{(B-8)}$$

where w_A^o is the width of the fission detector. A similar expression applies for the relative out of plane width, $w_B(\Theta_B)$, of detector B. (Note for $\phi_A = 90°$ we have $\sin(\Theta_A^o + \phi_A - \Theta_A)/\sin\phi_A = \cos(\Theta_A^o - \Theta_A)$). Accounting for the angular acceptance and out of plane width of the fission detectors, the efficiency for simultaneously observing both fission fragments is then defined as the minimum width at the two locations struck

$$\varepsilon(m_A, \Theta_A^{cm}) = \min[w_A(\Theta_A), w_B(\Theta_B)] \ . \qquad \text{(B-9)}$$

6. AVERAGE OVER EMISSION ANGLES Θ_A^{cm} . Repeat steps 4 and 5 for N increments of Θ_A^{cm} over the interval $[0, 2\pi]$. Evaluate the efficiency for detecting a coincident fragment of mass m_A in detector A as

$$\varepsilon(m_A) = \sum_{\Theta_A^{cm}} \varepsilon(m_A, \Theta_A^{cm}) \ . \qquad \text{(B-10)}$$

The angle-averaged value of a quantity $f(m_A, \Theta_A^{cm})$ (for example, $f(m_A, \Theta_A^{cm}) = \Theta_{AB} = \Theta_A + \Theta_B$ or $f(m_A, \Theta_A^{cm}) = m_B - m_A$) is defined as

$$f(m_A) = \left[\sum_{\Theta_A^{cm}} f(m_A, \Theta_A^{cm}) \cdot \varepsilon(m_A, \Theta_A^{cm})\right] \Big/ \varepsilon(m_A) \quad . \qquad (B-11)$$

And finally,

7. AVERAGE OVER FISSION PRODUCTS. Repeat steps 3 through 6 for each mass, m_A, in the fission mass distribution. Corresponding to the recoil momentum, $\vec{P}_R$, the average value of the quantity $f(m_A)$ is

$$<f> = \sum_{m_A} f(m_A) \cdot P(m_A) \qquad (B-12)$$

where $P(m_A)$ is the relative yield of fission fragments of mass m_A satisfying

$$\sum_{m_A} P(m_A) = 1. \qquad (B-13)$$

The efficiency for observing the recoil momentum $\vec{P}_R$ is obtained according to Eq. (B-12) as

$$<\varepsilon> = \sum_{m_A} \varepsilon(m_A) \cdot P(m_A) \quad . \qquad (B-14)$$

There are at least two shortcomings in the simulation procedure described here. In the first place, it neglects neutron evaporation from the fission fragments which might result in a non-colinear emission of the fragments in the center of mass frame. Due to the resulting loss of

coplanarity in the laboratory this would most likely decrease the overall detection efficiency but would do so uniformly for all recoil momenta (or folding-angles). However, neutron emission increases with excitation energy of the fissioning system and so this would give rise to an excitation energy dependent efficiency correction. The neglect of neutron emission probably has only a minor effect on the calculated average quantities. The simulation program also neglects the possibility of target recoils out of the plane of the fission detectors. These transverse momentum transfers would also decrease the detection efficiency but in a non-uniform manner. For complete fusion reactions there could be no transverse momentum transfer and so the efficiency would be calculated accurately, however in peripheral reactions, the neglect of transverse components of the momentum transfer would result in an overestimate of the detection efficiency.

The accuracy of the calculation is subject to additional uncertainties due to the assumed mass and energy distributions of the fission fragments. For a given fissioning nucleus the mass distribution can range from very asymmetric at low excitation energy to quite symmetric at large excitations (cf. Figure IV-15). Depending on the choice of fission distributions this can result in an uncertainty in the average folding-angle of about $\Delta\Theta = \pm 1°$ at full momentum transfer.

APPENDIX C: KNOCK-OUT MECHANISM IN LOW-ENERGY HEAVY-ION
COLLISIONS

We wish to investigate the role of a knock-out
mechanism in heavy-ion reactions at incident energies of
about 20 MeV/nucleon.   At these energies we envision a
peripheral process in which a single nucleon from the
projectile scatters in a quasi-free manner with a nucleon
of the target.   This is followed by the escape of one
nucleon and the subsequent absorption of the other nucleon
by either the target (Figure C-1a) or the projectile
(Figure C-1b).   A simple plane wave approximation is applied
in order to determine whether such a single-scattering
process can account for the observed shapes of the energy
and angular distributions.

We consider first the process of nucleon knock-out
from the target (Figure C-1b).   The incoming projectile of
mass number A and target of mass number B are described by
plane waves of momenta $\vec{K}_0$ and $-\vec{K}_0$, respectively.   The final
state is similarly approximated by plane waves with wave
vectors $\vec{k}, \vec{K}_A$, and $\vec{K}_B$ for the emitted nucleon, the outgoing
projectile, and the target residue of mass number B-1,
respectively.   The initial and final wavefunctions |i> and
|f> are written as

$$|i> = \frac{1}{V} e^{i\vec{K}_0 \cdot (\vec{R}_A - \vec{R}_B)} \phi_\alpha (\vec{r}_a - \vec{R}_a) \ \phi_\beta \ (\vec{r}_b - \vec{R}_b) \quad (C-1)$$
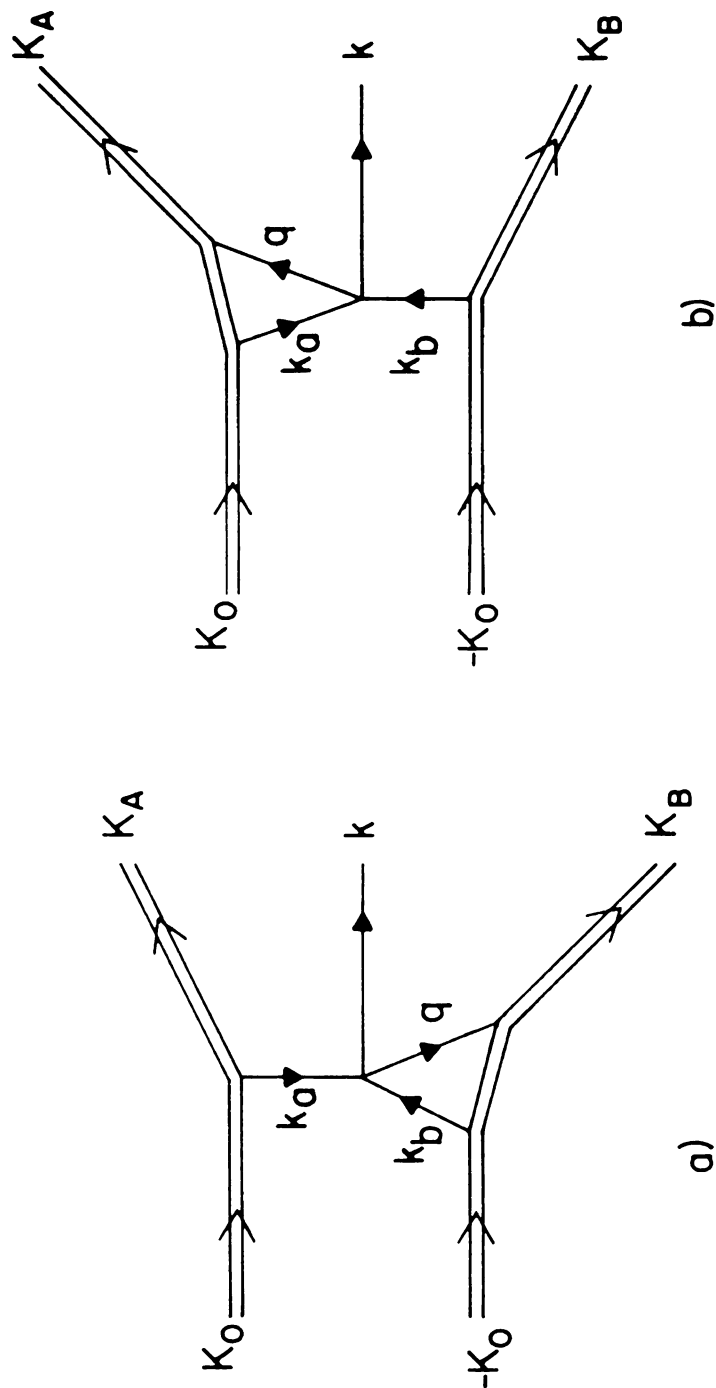
Figure C-1. Processes calculated in knock-out model. Part (a) represents knock-out from the projectile. Knock-out from the target is represented in part (b).

and

$$|f> = \frac{1}{V^{3/2}} e^{i\vec{K}_A \cdot \vec{R}_A} e^{i\vec{K}_B \cdot \vec{R}_b} e^{i\vec{k} \cdot \vec{r}_b} \phi_{\alpha'}(\vec{r}_a - \vec{R}_a) \qquad (C-2)$$

where V is the normalization volume of the plane waves and ϕ_α and ϕ_β are the wavefunctions for the relative motion of the interacting nucleon within the projectile and target nucleus, respectively. Here $\vec{R}_A$ and $\vec{R}_B$ are the coordinates of projectile and target, $\vec{r}_a$ and $\vec{r}_b$ are the coordinates of the interacting projectile and target nucleons, and $\vec{R}_a$ and $\vec{R}_b$ are the coordinates of the projectile and target residues consisting of A-1 and B-1 nucleons, respectively. These coordinates are related by

$$A\vec{R}_A = (A - 1)\vec{R}_a + \vec{r}_a \qquad (C-3a)$$

$$B\vec{R}_B = (B - 1)\vec{R}_b + \vec{r}_b \qquad (C-3b)$$

Using $\vec{R}_a$, $\vec{R}_b$, $\vec{r}_a$, and $\vec{r}_b$ as independent variables and expressing the bound state wavefunctions in terms of their Fourier components the initial and final state wavefunctions become

$$|i> = \frac{1}{(2\pi)^3 V} e^{i\vec{K}_o \cdot \left[\frac{(A-1)}{A}\vec{R}_a + \frac{\vec{r}_a}{A}\right]} e^{-\vec{K}_o \cdot \left[\frac{(B-1)}{B}\vec{R}_b + \frac{\vec{r}_b}{B}\right]}$$

$$\times \int d^3 k_a d^3 k_b \phi_\alpha(\vec{k}_a) \phi_\beta(\vec{k}_b) e^{i\vec{k}_a \cdot (\vec{r}_a - \vec{R}_a)} e^{i\vec{k}_b \cdot (\vec{r}_b - \vec{R}_b)} \qquad (C-4)$$

and

$$|f\rangle = \frac{1}{(2\pi)^{3/2}V^{3/2}} \, e^{i\vec{K}_A \cdot \left[\frac{(A-1)}{A} \, \vec{R}_a + \frac{\vec{r}_a}{A}\right]} e^{i\vec{K}_B \cdot \vec{R}_b} \, e^{i\vec{k} \cdot \vec{r}_b}$$

$$\times \int d^3q \; e^{i\vec{q} \cdot (\vec{r}_a - \vec{R}_a)} \phi_{\alpha'}(\vec{q}) \; . \tag{C-5}$$

The interaction matrix element $\langle f|v|i\rangle$ is evaluated by assuming a zero range interaction, $v(\vec{r}_a, \vec{r}_b) = v_0 \delta (\vec{r}_a - \vec{r}_b)$, between the interacting nucleons. Using Eqs. (C-4) and (C-5) one obtains

$$\langle f|v|i\rangle = \frac{1}{(2\pi)^{9/2}} \frac{v_0}{V^{5/2}} \int d^3q \, d^3k_a \, d^3k_b \, \phi_{\alpha'}^*(\vec{q}) \, \phi_\alpha(\vec{k}_a) \, \phi_\beta(\vec{k}_b)$$

$$\times \int d^3R_a \; e^{i\left[\vec{K}_o \frac{(A-1)}{A} - \vec{k}_a - \vec{K}_A \frac{(A-1)}{A} + \vec{q}\right] \cdot \vec{R}_a}$$

$$\times \int d^3R_b \; e^{i\left[-\vec{K}_{.,} \frac{(B-1)}{B} - \vec{k}_b - \vec{K}_B\right] \cdot \vec{R}_b}$$

$$\times \int d^3r_a \; e^{i\left[\vec{k}_a + \vec{k}_b + \frac{\vec{K}_o}{A} - \frac{\vec{K}_o}{B} - \frac{\vec{K}_A}{A} - \vec{k} - \vec{q}\right] \cdot \vec{r}_a} \; . \tag{C-6}$$

By rewriting the spatial integrals in terms of δ-functions and integrating over d^3k_a and d^3k_b the following expression is obtained

$$\langle f|v|i\rangle = \frac{(2\pi)^{9/2} v_0}{V^{5/2}} \int d^3q \, \phi_{\alpha'}^*(\vec{q}) \, \phi_\alpha(\tilde{A}(\vec{K}_o - \vec{K}_A) + \vec{q}) \, \phi_\beta(-\tilde{B}\vec{K}_o - \vec{K}_B)$$

$$\times \; \delta(\vec{K}_A + \vec{K}_B + \vec{k}) \; . \tag{C-7}$$

Here we have introduced the quantities $\tilde{A} = (A-1)/A$ and $\tilde{B} = (B-1)/B$. The δ-function in Eq. (C-7) insures momentum
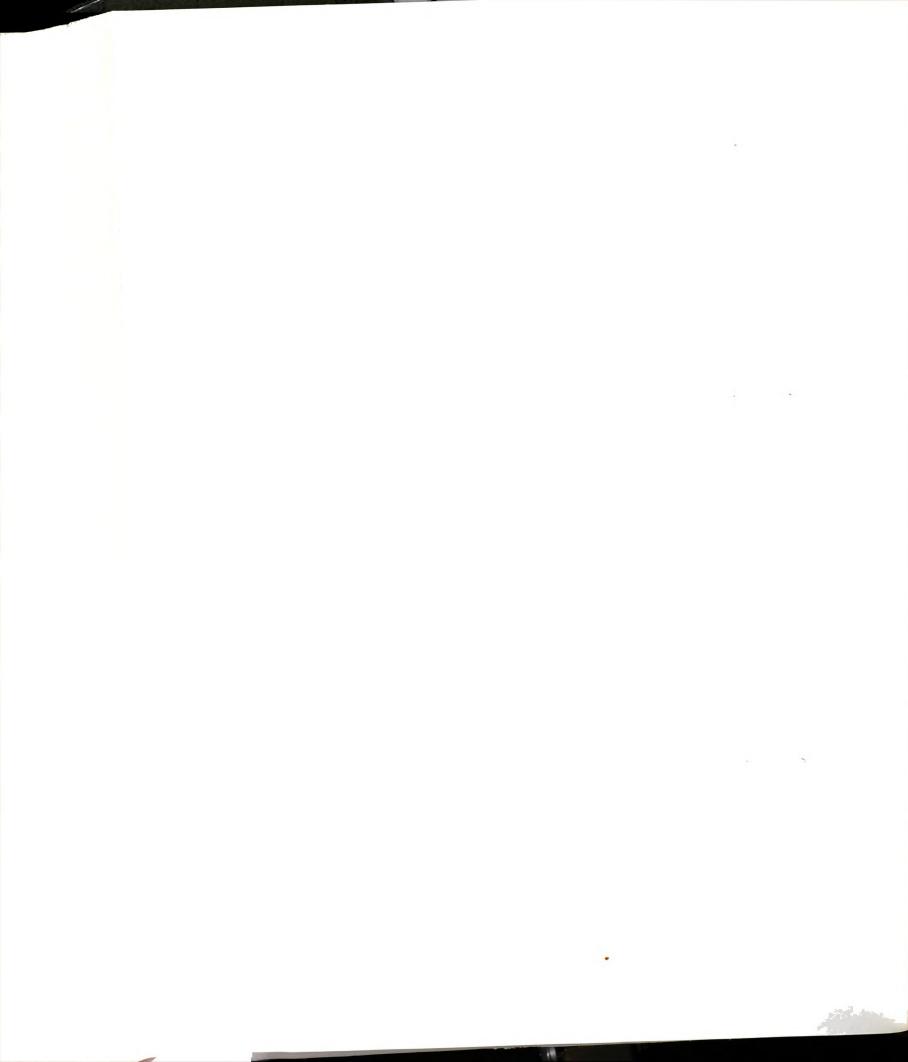
conservation. We make the replacement

$$\int d^3q \phi^*_{\alpha'}(\vec{q}) \phi_\alpha (\vec{q} + \vec{K}) = \int d^3r \, e^{-i\vec{K}\cdot\vec{r}} \phi^*_{\alpha'}(\vec{r}) \phi_\alpha(\vec{r}) = \rho_{\alpha'\alpha}(\vec{K}) . \quad (C-8)$$

With this substitution Eq. (C-7) becomes

$$<f|v|i> = \frac{(2\pi)^{9/2} v_0}{V^{5/2}} \, \rho_{\alpha'\alpha} \, (\tilde{A}(\vec{K}_o - \vec{K}_A)) \phi_\beta (-\tilde{B}\vec{K}_o - \vec{K}_B) \delta (\vec{K}_A + \vec{K}_B + \vec{k}) \quad .$$

$$(C-9)$$

The transition rate is given according to Golden rule No. 2 by

$$d\Gamma = \frac{2\pi}{\hbar} \, |<f|v|i>|^2 \, dN \; \delta(E_f - E_i) \qquad (C-10)$$

where dN is the density of final states. For three free particles in the final state

$$dN = \frac{V^3}{(2\pi)^9} \, d^3K_A d^3K_B d^3k \quad . \qquad (C-11)$$

Therefore the transition rate for emitting a nucleon of momentum $\vec{k}$ within the momentum element d^3k is

$$\frac{d\Gamma}{d^3k} = \frac{2\pi}{\hbar} \, |<f|v|i>|^2 \, \frac{V^3}{(2\pi)^9} \, d^3K_A d^3K_B \; \delta(E_f - E_i) \quad . \qquad (C-12)$$

Substituting Eq. (C-9) into Eq. (C-12) yields

$$\frac{d\Gamma}{d^3k} = \frac{2\pi}{\hbar} \, \frac{v_0^2}{V^2} \, d^3K_A d^3K_B |\rho_{\alpha'\alpha} \, (\tilde{A}(\vec{K}_o - \vec{K}_A))|^2 |\phi_\beta(-\tilde{B}\vec{K}_o - \vec{K}_B)|^2$$

$$x \, \delta (\vec{K}_A + \vec{K}_B + \vec{k}) \delta (\vec{K}_A + \vec{K}_B + \vec{k}) \delta (E_f - E_i) \quad . \qquad (C-13)$$

We sum over final states $\int d^3K_A d^3K_B$ and assume that the absorbed nucleon is reabsorbed into the same state $\alpha'=\alpha$. Performing the integration over d^3K_A gives

$$\frac{d\Gamma}{d^3k} = \frac{2\pi}{\hbar} \frac{v_o^2}{V^2} \int d^3K_B |\rho_{\alpha\alpha}(\tilde{A}(\vec{K}_o + \vec{K}_B + \vec{k}))|^2 |\phi_\beta(-\tilde{B}\vec{K}_o - \vec{K}_B)|^2 \delta(\vec{0})$$

$$\times \delta(E_f - E_i) \; . \tag{C-14}$$

But $\delta(\vec{0})$ is evaluated as

$$\delta(\vec{0}) = \frac{1}{(2\pi)^3} \int d^3r = \frac{V}{(2\pi)^3} \tag{C-15}$$

The transition rate then becomes

$$\frac{d\Gamma}{d^3k} = \frac{v_o^2}{(2\pi)^2 \hbar V} \int d^3K_B |\rho_{\alpha\alpha}(\tilde{A}(\vec{K}_o + \vec{K}_B + \vec{k}))|^2$$

$$\times |\phi_\beta(-\tilde{B}\vec{K}_o - \vec{K}_B)|^2 \delta(E_f - E_i) \; . \tag{C-16}$$

We average over initial states α and β noting that since the target and projectile are initially in their ground states the scattering can occur from A possible orbits in the projectile and B possible orbits in the target. Furthermore, we make a coherent average over the initial projectile states α since these states cannot be observed due to the reabsorption. The transition rate is then

$$\frac{d\Gamma}{d^3k} = \frac{v_o^2}{(2\pi)^2 \hbar V} \int d^3K_B |\frac{1}{A}\sum_\alpha \rho_{\alpha\alpha}(\tilde{A}(\vec{K}_o + \vec{K}_B + \vec{k}))|^2$$

$$\times \frac{1}{B}\sum_\beta |\phi_\beta(-\tilde{B}\vec{K}_o - \vec{K}_B)|^2 \delta(E_f - E_i) \; . \tag{C-17}$$

We then introduce the momentum distribution $P_B(\vec{q})$ of the target nucleons

$$P_B(\vec{q}) = \sum_\beta |\phi_\beta(\vec{q})|^2 \qquad\qquad (C-18)$$

and the density form factor $F_A(\vec{q})$ of the projectile nucleus

$$F_A(\vec{q}) = \sum_\alpha \rho_{\alpha\alpha}(\vec{q}) = \int d^3r \, e^{-i\vec{q}\cdot\vec{r}} \sum_\alpha |\phi_\alpha(\vec{r})|^2 \ . \qquad\qquad (C-19)$$

Dividing the transition rate by the incident flux density

$$|\vec{j}_{inc}| = \frac{(A+B)}{AB} \frac{\hbar K_o}{mV} \qquad\qquad (C-20)$$

yields the differential cross section for the knock-out of a nucleon from the target nucleus

$$\frac{d^2\sigma}{dEd\Omega} = \frac{m^2}{\hbar^4} \frac{k}{K_o} \frac{v_o^2}{(2\pi)^2} \frac{(A+B)^{-1}}{A} \int d^3K_B |F_A(\tilde{A}(\vec{K}_o + \vec{K}_B + \vec{k}))|^2$$

$$\times \ P_B(-\tilde{B}\vec{K}_o - \vec{K}_B)\delta(E_f - E_i) \ . \qquad\qquad (C-21)$$

The contribution of knock-out from the projectile (Figure C-1a) is similarly found to be

$$\frac{d^2\sigma}{dEd\Omega} = \frac{m^2}{\hbar^4} \frac{k}{K_o} \frac{v_o^2}{(2\pi)^2} \frac{(A+B)^{-1}}{B} \int d^3K_A |F_B(\tilde{B}(-\vec{K}_o + \vec{K}_A + \vec{k}))|^2$$

$$\times \ P_A(\tilde{A}\vec{K}_o - \vec{K}_A)\delta(E_f - E_i) \ . \qquad\qquad (C-22)$$

Combining Eqs. (C-21) and (C-22) the total differential cross section for single nucleon knock-out is given by

$$\frac{d^2\sigma}{dEd\Omega} = \frac{m^2}{\hbar^4} \frac{k}{K_o} \frac{v_o^2}{(2\pi)^2} (A+B)^{-1} \int d^3K \left[\frac{1}{A} |F_A(\tilde{A}(\vec{K}_o + \vec{K} + \vec{k}))|^2 \right.$$

$$x \, P_B(-\tilde{B}\vec{K}_o - \vec{K})\delta(E_f^B - E_i) + \frac{1}{B} |F_B(\tilde{B}(-\vec{K}_o + \vec{K} + \vec{k}))|^2$$

$$\left. x \, P_A(\tilde{A}\vec{K}_o - \vec{K})\delta(E_f^A - E_i) \right] \tag{C-23}$$

where the initial energy E_i is given by

$$E_i = \frac{(A+B)}{AB} \frac{\hbar^2 K_o^2}{2m} \tag{C-24}$$

and the final energies E_f^A and E_f^B are given as

$$E_f^A = \frac{\hbar^2}{2m} \left[\frac{K^2}{(A-1)} + \frac{(\vec{K}+\vec{k})^2}{B} + k^2 \right] + E_o^A \tag{C-25a}$$

and

$$E_f^B = \frac{\hbar^2}{2m} \left[\frac{(\vec{K}+\vec{k})^2}{A} + \frac{K^2}{(B-1)} + k^2 \right] + E_o^B \tag{C-25b}$$

where E_o^A and E_o^B are the binding energies of the nucleon removed from the projectile and target, respectively.

Equation (C-23) can be evaluated after the momentum distribution $P(\vec{k})$ and the density form factor $F(\vec{q})$ are obtained within the framework of a suitable model of nuclear structure. It should be clear that $P(\vec{k})$ enters at the vertex of Figure C-1 where the nucleon is removed from the nucleus while $|F(\vec{q})|^2$ enters at the vertex where the other nucleon is removed but absorbed again.

APPENDIX D: COALESCENCE MODEL FOR POISSON

MULTIPLICITY DISTRIBUTION

The basic assumption of the coalescence model is that complex particles are formed by the coalescence of nucleons which happen to share the same volume element of momentum space [Sc 63]. The critical radius, P_o, within which coalescence occurs is treated as a free parameter. The probability, P, for finding one primary nucleon in the coalescence volume centered at a momentum per nucleon, $\vec{p}$, is given by the product of this volume with the single nucleon momentum density

$$P = \frac{4\pi}{3} P_o^3 \frac{1}{\bar{m}} \frac{d^3N(\vec{p})}{dp^3} \,, \tag{D-1}$$

where $\frac{d^3N(\vec{p})}{dp^3}$ represents the differential nucleon multiplicity and $\bar{m}$ is the average nucleon multiplicity.

For a given multiplicity, m, i.e. when m nucleons are produced in an event, the probability of finding n of them ($n \leq m$) in the coalescence volume will be given by the binomial distribution

$$P(n|m) = \binom{m}{n} P^n (1 - P)^{m-n} \,. \tag{D-2}$$

In actuality, each multiplicity will have a probability $f(m)$ of occurrence. Summing over this distribution of multiplicities we obtain the average probability for finding n nucleons in the coalescence volume.

$$\langle P(n) \rangle = \sum_{m \geq n} f(m) P(n|m) = \sum_{m \geq n} f(m) \binom{m}{n} P^n (1 - P)^{m-n} \ . \qquad \text{(D-3)}$$

In the case of low average multiplicities, $\bar{m}$, as in the present experiment, it is reasonable to assume a Poisson distribution of multiplicities

$$f(m) = \frac{(\bar{m})^m}{m!} e^{-\bar{m}} \qquad \text{(D-4)}$$

Substituting Eq. (D-4) into Eq. (D-3) we obtain an average probability given by

$$\langle P(n) \rangle = \sum_{m \geq n} \frac{(\bar{m})^m}{m!} e^{-\bar{m}} \frac{m!}{n!(m-n)!} P^n (1 - P)^{m-n}$$

$$= \frac{(\bar{m}P)^n e^{-\bar{m}}}{n!} \sum_{\nu \geq 0} \frac{1}{\nu!} ((1 - P)\bar{m})^\nu \qquad \text{(D-5)}$$

$$= \frac{(\bar{m}P)^n e^{-\bar{m}P}}{n!}$$

Eq. (D-5) is exact for a Poisson multiplicity distribution. In the case of a non-Poisson multiplicity distribution it is assumed that Eq. (D-3) can be approximated by

$$\langle P(n) \rangle \simeq P(n|\bar{m}) = \binom{\bar{m}}{n} P^n (1 - P)^{\bar{m}-n} \qquad \text{(D-6)}$$

Then if $P \ll 1$ and $\bar{m} \gg n$ the binomial distribution becomes Poisson in form which again results in Eq. (D-5).

Typically, the exponential term in Eq. (D-5) can be ignored since $\bar{m}P$ is small. This gives the average

probability for having N neutrons and Z protons in the
coalescence sphere to be

$$\langle P(N,Z) \rangle = \frac{(\bar{m}_Z P_Z)^Z}{Z!} \frac{(\bar{m}_N P_N)^N}{N!} , \tag{D-7}$$

where we have assumed that the probabilities for the
observation of neutrons and protons are independent. In
the context of the coalescence model $P(N,Z)$ represents
the probability of forming a composite particle with
momentum per nucleon $\vec{p}$.

Since the neutron distributions typically are not
measured, we assume that they have the same shape as the
proton distributions but are weighted by the N/Z ratio
of the composite system

$$\frac{d^3N(0,1)}{dp^3} = \left(\frac{N_t + N_p}{Z_t + Z_p}\right)\frac{d^3N(1,0)}{dp^3} . \tag{D-8}$$

Substituting Eqs. (D-1) and (D-8) into Eq. (D-7) and
dividing by the coalescence volume we obtain the composite
particle momentum distribution in the form of the usual
coalescence relation [Gu 76, Go 77, Le 79] used at
relativistic energies

$$\frac{d^3N(Z,N)}{dp^3} = \left(\frac{N_t + N_p}{Z_t + Z_p}\right)^N \frac{1}{N!Z!} \left(\frac{4\pi}{3} P_o^3\right)^{A-1} \left(\frac{d^3N(1,0)}{dp^3}\right)^A \tag{D-9}$$

It is important to note that the differential nucleon

multiplicity per event, d^3N/dp^3, is chosen by normalizing
the experimentally observed momentum distribution to the
class of events of interest

$$\frac{d^3N}{dp^3} = \frac{1}{\sigma_o} \frac{d^3\sigma}{dp^3} \ .$$
(D-10)

At relativistic energies this class of events has been
chosen to consist of all possible reactions [Gu 76, Go 77,
Le 79]. Therefore, the total reaction cross section, σ_R,
is substituted for σ_o. In the fission coincidence
experiment of this study, we have analogously chosen to
normalize our momentum distributions to inclusive fission
events (see Eq. (VI-10)). It should be clear from
Eqs. (D-9) and (D-10) that this choice of normalization
enters directly into the interpretation of P_o.

APPENDIX E: MODIFICATION OF COALESCENCE

RELATION BY COULOMB FIELD

We calculate the modification to the coalescence relation of Appendix D (Eq. D-9) which results when the coalescence occurs in the vicinity of a stationary Coulomb source [Gy 81] such as at the nuclear surface. The energy balance for a particle of charge Z and mass number A can be written as

$$\frac{p_A^2}{2mA} = \frac{p_{A_0}^2}{2mA} + ZE_c \qquad (E-1)$$

where E_c is the Coulomb energy per unit charge of the composite particle, p_{A_0} is the momentum of the composite particle at the nuclear surface, and p_A is the momentum of the particle in the laboratory. Eq. (E-1) can be rewritten as

$$p_{A_0} = p_A(1 - \frac{2mAZE_c}{p_A^2})^{\frac{1}{2}} . \qquad (E-2)$$

From Eq. (E-1) we see that

$$p_A dp_A = p_{A_0} dp_{A_0} \qquad (E-3)$$

Then using Eq. (E-2) we obtain

$$p_{A_0}^2 dp_{A_0} = p_{A_0} p_A dp_A = (1 - \frac{2mAZE_c}{p_A^2})^{\frac{1}{2}} p_A^2 dp_A \qquad (E-4)$$

253

Analogously for a proton we have $Z = A = 1$ which gives

$$p_o^2 dp_o = (1 - \frac{2mE_c}{p^2})^{\frac{1}{2}} p^2 dp \qquad \text{(E-5)}$$

We then assume that

$$p_{A_o} = Ap_o \qquad \text{(E-6)}$$

and also that the Coulomb field does not change the angular directions

$$d\Omega_A = d\Omega_{A_o}, \quad d\Omega = d\Omega_o \qquad \text{(E-7)}$$

The coalescence relation of Eq. (D-9) then states that, at the nuclear surface, the composite particle cross section is related to the proton cross section according to

$$\frac{d^3 N(Z,N)}{dp_o^3} = C \left(\frac{d^3 N(1,0)}{dp_o^3} \right)^A \qquad \text{(E-8)}$$

where

$$C = \left(\frac{N_t + N_p}{Z_t + Z_p} \right)^N \frac{1}{N!Z!} (\frac{4\pi}{3} p_o^3)^{A-1} \qquad \text{(E-9)}$$

Transforming the light particle cross sections into the laboratory by using Eqs. (E-4), (E-5), and (E-7) we obtain the Coulomb modified coalescence relation in momentum space

$$\frac{d^2N(Z,N)}{p_A^2 dp_A d\Omega} = CA^{-3} \frac{(1 - 2mAZE_c/p_A^2)^{\frac{1}{2}}}{(1 - 2mE_c/p^2)^{A/2}} \left(\frac{d^2N(1,0)}{p^2 dp d\Omega}\right)^A \tag{E-10}$$

We now transform Eq. (E-10) into energy space by first rewriting it as

$$\frac{d^2N(Z,N)}{p_A dp_A d\Omega} = CA^{-3} \frac{(p_A^2 - 2mAZE_c)^{\frac{1}{2}}}{(p^2 - 2mE_c)^{A/2}} \left(\frac{d^2N(1,0)}{p dp d\Omega}\right)^A \tag{E-11}$$

and then using

$$p_A^2 = 2mAE_A, \quad p^2 = 2mE \tag{E-12}$$

and

$$p_A dp_A = mAdE_A, \quad pdp = mdE \tag{E-13}$$

This gives

$$\frac{d^2N(Z,N)}{mAdE_A d\Omega} = \frac{CA^{-3}}{(2m)^{(A-1)/2}} \frac{(AE_A - ZAE_c)^{\frac{1}{2}}}{(E-E_c)^{A/2}} \left(\frac{d^2N(1,0)}{mdE d\Omega}\right)^A \tag{E-14}$$

or

$$\frac{d^2N(Z,N)}{dE_A d\Omega} = \frac{CA^{-1}}{(2m^3)^{(A-1)/2}} \frac{((E_A - ZE_c)/A)^{\frac{1}{2}}}{(E - E_c)^{A/2}} \left(\frac{d^2N(1,0)}{dE d\Omega}\right)^A \tag{E-15}$$

Finally noting that

$$E_A - ZE_c = E_{A_o} = AE_o = A(E - E_c) \tag{E-16}$$

we obtain a coalescence relation which is valid when
the coalescence occurs in the vicinity of a Coulomb field

$$\frac{d^2N(Z,N,E_A)}{dE_A d\Omega} = \left(\frac{N_t + N_p}{Z_t + Z_p}\right)^N \frac{A^{-1}}{N!Z!} \left[\frac{\frac{4\pi}{3}P_o^3}{(2m^3(E-E_c))^{\frac{1}{2}}}\right]^{A-1} \left(\frac{d^2N(1,0,E)}{dEd\Omega}\right)^A \quad (E-17)$$

LIST OF REFERENCES

LIST OF REFERENCES

A

[Al 79]   Y. Alhassid, R.D. Levine, J.S. Karp, and S. Steadman, Phys. Rev. C$\underline{20}$, 1789 (1979).

[Ar 73]   A.G. Artukh, G.F. Gridnev, V.L. Mikheev, V.V. Volkov, and J. Wilczyński, Nucl. Phys. $\underline{A215}$, 91 (1973).

[RLAu]   R.L. Auble, J.B. Ball, F.E. Bertrand, R.L. Ferguson, C.B. Fulmer, I.Y. Lee, R.L. Robinson, G.R. Young, J.R. Wu, J.C. Wells, and H. Yamada (unpublished).

[Aw 79]   T.C. Awes, C.K. Gelbke, B.B. Back, A.C. Mignerey, K.L. Wolf, P. Dyer, H. Breuer, and V.E. Viola, Jr., Phys. Lett. $\underline{87B}$, 43 (1979).

[Aw 80]   T.C. Awes, C.K. Gelbke, G. Poggi, B.B. Back, B. Glagola, H. Breuer, V.E. Viola, Jr., T.J.M. Symons, Phys. Rev. Lett. $\underline{45}$, 513 (1980).

[Aw 81]   T.C. Awes, G. Poggi, C.K. Gelbke, B.B. Back, B.G. Glagola, H. Breuer, and V.E. Viola, Jr., Phys. Rev. C$\underline{24}$, 89 (1981).

[Aw 81a]   T.C. Awes, G. Poggi, S. Saini, C.K. Gelbke, R. Legrain, and G.D. Westfall, Phys. Lett. $\underline{103B}$, 417 (1981).

[Aw 82]   T.C. Awes, S. Saini, G. Poggi, C.K. Gelbke, D. Cha, R. Legrain, and G.D. Westfall, (to be published in Phys. Rev. C (1982)).

B

[Ba 71]   J.P. Balagna, G.P. Ford, D.C. Hoffman, and J.D. Knight, Phys. Rev. Lett. $\underline{26}$, 145 (1971).

[Ba 74]   R. Bass, Nucl. Phys. $\underline{A231}$, 45 (1974).

[Ba 75]   J.B. Ball, C.B. Fulmer, E.E. Gross, M.L. Halbert,
           D.C. Hensley, C.A. Ludemann, M.J. Saltmarsh, and
           G.R. Satchler, Nucl. Phys. A252, 208 (1975).

[Ba 78]   J.B. Ball, C.B. Fulmer, M.L. Mallory, and R.L.
           Robinson, Phys. Rev. Lett. 40, 1698 (1978).

[Ba 80]   B.B. Back, K.L. Wolf, A.C. Mignerey, C.K. Gelbke,
           T.C. Awes, H. Breuer, V.E. Viola, Jr., and P.
           Dyer, Phys. Rev. C22, 1927 (1980).

[Ba 80a]   J.H. Barker, J.R. Beene, M.L. Halbert, D.C.
           Hensley, M. Jääskeläinen, D.G. Sarantites, and R.
           Woodward, Phys. Rev. Lett. 45, 424 (1980).

[Be 38]   H.A. Bethe, Phys. Rev. 53, 675 (1938).

[Be 69]   F.D. Becchetti, Jr., and G.W. Greenlees, Phys.
           Rev. 182, 1190 (1969).

[Be 76]   H.W. Bertini, R.T. Santoro, and O.W. Hermann, Phys.
           Rev. C14, 590 (1976).

[Be 81]   J.R. Beene, M.L. Halbert, D.C. Hensley, R.A.
           Dayras, K. Geoffroy Young, D.G. Sarantites, and
           J.H. Barker, Phys. Rev. C23, 2463 (1981).

[GFBe]   G.F. Bertsch, private communication.

[Bh 79]   R.K. Bhowmik, E.C. Pollacco, N.E. Sanderson, J.B.A.
           England, G.C. Morrison, Phys. Rev. Lett. 43, 619
           (1979).

[Bi 70]   C.J. Bishop, R. Vandenbosch, R. Aley, R.W. Shaw,
           Jr., and I. Halpern, Nucl. Phys. A150, 129 (1970).

[Bi 80]   M. Bini, C.K. Gelbke, D.K. Scott, T.J.M. Symons, P.
           Doll, D.L. Hendrie, J.L. Laville, J. Mahoney, M.C.
           Mermaz, C. Olmer, K. Van Bibber, and H.H. Wieman,
           Phys. Rev. C22, 1945 (1980).

[Bl 75]   M. Blann, Ann. Rev. Nucl. Sci. 25, 123 (1975).

[Bl 76]   M. Blann, A. Mignerey, W. Scobel, Nukleonika 21,
           335 (1976).

[Bl 81]   M. Blann, Phys. Rev. C23, 205 (1981).

[Bo 77]   R. Bond, P.J. Johansen, S.E. Koonin and S.
           Garpman, Phys. Lett. 71B, 43 (1977).

[Bo 79]   J.P. Bondorf, J.N. De, A.O.T. Karvinen, G. Fái,
          B. Jakobsson, Phys. Lett. 84B, 162 (1979).

[Bo 80]   J.P. Bondorf, J.N. De, G. Fái, A.O.T. Karvinen,
          B. Jacobsson, and J. Randrup, Nucl. Phys. A333,
          285 (1980).

[Br 61]   H.C. Britt and A.R. Quinton, Phys. Rev. 124, 877
          (1961).

[Bu 63]   S.T. Butler and C.A. Pearson, Phys. Rev. 129, 836
          (1963).

[Bu 78]   A. Budzanowski, G. Baur, C. Alderliesten, J.
          Bojowald, C. Mayer-Böricke, W. Oelert, P. Turek,
          F. Rösel, and D. Trautmann, Phys. Rev. Lett. 41,
          635 (1978).

                          C

[Ca 80]   C.M. Castaneda, H.A. Smith, Jr., P.P. Singh, and
          H. Karwowski, Phys. Rev. C21, 179 (1980).

[Ch 67]   A.J. Chapman, in Heat Transfer (The Macmillan Co.,
          1967).

[Ch 79]   D. Cha and G. Bertsch, Annual Report, Michigan
          State University (1979-80).

[Ch 80]   M. Chemtob and B. Schürmann, Nucl. Phys. A336, 508
          (1980).

[Co 61]   L.J. Colby, Jr., Mary LaSalle Shoaf, and J.W.
          Cobble, Phys. Rev. 121, 1415 (1961).

[Co 81]   K.R. Cordell, S.T. Thornton, L.C. Dennis, R.R.
          Doering, R.L. Parks, and T.C. Schweizer, Nucl.
          Phys. A362, 431 (1981).

[Cr 76]   J.G. Cramer, R.M. DeVries, D.A. Goldberg, M.S.
          Zisman, and C.F. Maguire, Phys. Rev. C14, 2158
          (1976).

[JGCr]   J.G. Cramer, (unpublished).

[Cu 80]   J. Cugnon, Phys. Rev. C22, 1885 (1980).

[Cu 81]   J. Cugnon, J. Knoll, and J. Randrup, Nucl. Phys.
          A360, 444 (1981).

D

[Dy 79]   P. Dyer, T.C. Awes, C.K. Gelbke, B.B. Back, A. Mignerey, K.L. Wolf, H. Breuer, and V.E. Viola, Jr., Phys. Rev. Lett. $\underline{42}$, 560 (1979).

E

[Eg 81]   Ch. Egelhaaf, G. Bohlen, H. Fuchs, A. Gamp, H. Homeyer, and H. Kluge, Phys. Rev. Lett. $\underline{46}$, 813 (1981).

[Er 60]   T. Erickson, Adv. Phys. $\underline{9}$, 425 (1960).

[Ey 78]   Y. Eyal, A. Gavron, I. Tserruya, Z. Fraenkel, Y. Eisen, S. Wald, R. Bass, G.R. Gould, G. Kreyling, R. Renfordt, K. Stelzer, R. Zitzmann, A. Gobbi, A. Lynen, H. Stelzer, I. Rode, and R. Bock, Phys. Rev. Lett. $\underline{41}$, 625 (1978).

F

[Fr 81]   W.A. Friedman and D. Saloner, Phys. Rev. C$\underline{23}$, 2532 (1981).

G

[Ga 78]   A. Gamp, J.C. Jacmart, N. Poffe´, H. Doubre, J.C. Roynette, and J. Wilczyński, Phys. Lett. $\underline{74B}$, 215 (1978).

[Ga 80]   S.I.A. Garpman, D. Sperber, and M. Zielinska-Pfabe, Phys. Lett. $\underline{90B}$, 53 (1980).

[Ga 80a] S.I.A. Garpman, S.K. Samaddar, D. Sperber, and M. Zielinska-Pfabe, Phys. Lett. $\underline{92B}$, 56 (1980).

[Ga 81]   A. Gavron, R.L. Ferguson, Felix E. Obenshain, F. Plasil, G.R. Young, G.A. Petitt, K. Geoffroy Young, D.G. Sarantites, and C.F. Maguire, Phys. Rev. Lett. $\underline{46}$, 8 (1981).

[Ge 77]   C.K. Gelbke, D.K. Scott, M. Bini, D.L. Henrie, J.L. Laville, J. Mahoney, M.C. Mermaz, and C. Olmer, Phys. Lett. $\underline{70B}$, 415 (1977).

[Ge 77a] C.K. Gelbke, M. Bini, C. Olmer, D.L. Hendrie, J.L. Laville, J. Mahoney, M.C. Mermaz, D.K. Scott, and H.H. Wieman, Phys. Lett. $\underline{71B}$, 83 (1977).

[Ge 78]   C.K. Gelbke, C. Olmer, M. Buenerd, D.L. Hendrie, J. Mahoney, M.C. Mermaz and D.K. Scott, Phys. Reports $\underline{42}$, 311 (1978).

[Ge 80]   H. Gemmeke, P. Netter, Ax. Richter, L. Lassen, S. Lewandowski, W. Lücking, and R. Schrek, Phys. Lett. $\underline{97B}$, 213 (1980).

[Gi 77]   J.E. Gindler, K.F. Flynn, L.E. Glendenin, and R. K. Sjoblom, Phys. Rev. C$\underline{16}$, 1483 (1977).

[Go 74]   A.S. Goldhaber, Phys. Lett. $\underline{53B}$, 306 (1974).

[Go 75]   F.S. Goulding and B.G. Harvey, Ann. Rev. Nucl. Sci. $\underline{25}$, 167 (1975).

[Go 77]   J. Gosset, H.H. Gutbrod, W.G. Meyer, A.M. Poskanzer, A. Sandoval, R. Stock, and G.D. Westfall, Phys. Rev. C$\underline{16}$, 629 (1977).

[Go 77a]   P.A. Gottschalk, and M. Weström, Phys. Rev. Lett. $\underline{39}$, 1250 (1977).

[Go 78]   A.S. Goldhaber, Phys. Rev. C$\underline{17}$, 2243 (1978).

[Go 79]   P.A. Gottschalk, and M. Weström, Nucl. Phys. $\underline{A314}$, 232 (1979).

[Go 80]   A. Gobbi and W. Nörenberg, Chapt. 3, p. 128 in Heavy Ion Collisions, Vol. 2, Edited by R. Bock, (North Holland Publishing Co., 1980).

[Go 80a]   C.R. Gould, R. Bass, J.v. Czarnecki, V. Hartmann, K. Stelzer, R. Zitzmann, and Y. Eyal, Z. Phys. $\underline{A294}$, 323 (1980).

[Gr 75]   D.L. Greiner, P.J. Lindstrom, H.H. Heckman, B. Cork, and F.S. Bieser, Phys. Rev. Lett. $\underline{35}$, 152 (1975).

[Gu 76]   H.H. Gutbord, A. Sandoval, P.J. Johansen, A.M. Poskanzer, J. Gosset, W.G. Meyer, G.D. Westfall, and R. Stock, Phys. Rev. Lett. $\underline{37}$, 667 (1976).

[Gy 81]   M. Gyulassy and S.K. Kauffmann, Nucl. Phys. $\underline{A362}$, 503 (1981).

H

[Ha 68]   G.D. Harp, J.M. Miller, and B.J. Berne, Phys. Rev. $\underline{165}$, 1166 (1968).

[Ha 71]   G.D. Harp and J.M. Miller, Phys. Rev. C3, 1847
           (1971).

[Ha 77]   J.W. Harris, T.M. Cormier, D.F. Gesaman, L.L. Lee,
           Jr., R.L. McGrath, and J.P. Wurm, Phys. Rev. Lett.
           38, 1460 (1977).

[Ha 79]   R.L. Hatch and S.E. Koonin, Phys. Lett. 81B, 1
           (1979).

[Ha 80]   F. Hachenberg, H.C. Chiang, and J. Hüfner, Phys.
           Lett. 97B, 183 (1980).

[Hi 78]   D.L. Hillis, O. Christensen, B. Fernandez, A.J.
           Ferguson, J.D. Garrett, G.B. Hagemann, B. Herskind,
           B.B. Back, and F. Folkmann, Phys. Lett. 78B, 405
           (1978).

[Hi 79]   D. Hilscher, J.R. Birkelund, A.D. Hoover, W.U.
           Schröder, W.W. Wilcke, J.R. Huizenga, A.C.
           Mignerey, K.L. Wolf, H.F. Breuer, and V.E. Viola,
           Jr., Phys. Rev. C20, 576 (1979).

[Ho 77]   H. Ho, R. Albrecht, W. Dünnweber, G. Graw, S.G.
           Steadman, J.P. Wurm, D. Disdier, V. Rauch, and F.
           Scheibling, Z. Phys. A283, 235 (1977).

[Ho 80]   H. Ho, P. Gonthier, M.N. Namboodiri, J.B. Natowitz,
           L. Adler, S. Simon, K. Hagel, R. Terry, and A.
           Khodai, Phys. Lett. 96B, 51 (1980).

[Hü 77]   J. Hüfner and J. Knoll, Nucl. Phys. A290, 460
           (1977).

                              I

[In 77]   T. Inamura, M. Ishihara, T. Fukuda, T. Shimoda,
           and H. Hiruta, Phys. Lett. 68B, 51 (1977).

                              J

[Ja 81]   B. Jakobssson, L. Carlén, P. Kristiansson, J.
           Krumlinde, A. Oskarsson, I. Otterlund, B. Schrøder,
           H.Å. Gustafsson, T. Johansson, H. Ryde, G. Tibell,
           J.P. Bondorf, G. Fái, A.O.T. Karvinen, O.B.
           Nielsen, M. Buenerd, J. Cole, D. Lebrun, J.M.
           Loiseaux, P. Martin, R. Ost, P. De Saintignon, C.
           Guet, E. Monnand, J. Mougey, H. Nifenecker, P.
           Perrin, J. Pinston, C. Ristori, and F. Schussler,
           Phys. Lett. 102B, 121 (1981).

K

[Ka 80]   J.I. Kapusta, Phys. Rev. C21, 1301 (1980).

[Ka 81]   J. Kasagi, S. Saini, T.C. Awes, A. Galonsky, C.K.
            Gelbke, G. Poggi, D.K. Scott, K.L. Wolf, and R.L.
            Legrain, Phys. Lett. 104B, 434 (1981).

[Ke 79]   A.K. Kerman and K.W. McVoy, Ann. Phys. (N.Y.)
            122, 197 (1979).

[Ko 77]   S.E. Koonin, Phys. Rev. Lett. 39, 680 (1977).

[Ko 79]   R.W. Koontz, C.C. Chang, H.D. Holmgren, and J.R.
            Wu, Phys. Rev. Lett. 43, 1862 (1979).

[RJKu]   R.J. Kurz, UCRL-11339 (1964), unpublished.

L

[Le 79]   M.-C. Lemaire, S. Nagamiya, S. Schnetzer, H.
            Steiner, and I. Tanihata, Phys. Lett. 85B, 38
            (1979).

[Lu 68]   A.V. Luikov, in Analytical Heat Diffusion Theory
            (Academic Press, 1968).

M

[Ma 76]   G. Mantzouranis, H.A. Weidenmüller, and D. Agassi,
            Z. Phys. A276, 145 (1976).

[Ma 79]   H. Machner, Phys. Lett. 86B, 129 (1979).

[Ma 80]   H. Machner, Phys. Rev. C21, 2695 (1980).

[CMap]   C. Maples, Program LZY, unpublished.

[Mc 80]   K.W. McVoy and M.C. Nemes, Z. Phys. A295, 177
            (1980).

[Me 77]   A. Mekjian, Phys. Rev. Lett. 38, 640 (1977).

[Me 78]   A. Mekjian, Phys. Rev. C17, 1051 (1978).

[Me 80]   A. Mekjian, Phys. Lett. 89B, 177 (1980).

[Mi 80]   I.M. Mishustin, F. Myhrer, and P.J. Siemens, Phys.
            Lett. 95B, 361 (1980).

[Mo 80]   W.W. Morison, S.K. Samaddar, D. Sperber, and M. Zielinska-Pfabe, Phys. Lett. 93B, 379 (1980).

[Mo 81]   P. Mooney, W.W. Morison, S.K. Samaddar, D. Sperber, and M. Zielinska-Pfabe, Phys. Lett. 98B, 240 (1981).

[My 78]   W.D. Myers, Nucl. Phys. A296, 177 (1978).

N

[Na 81]   S. Nagamiya, M.-C. Lemaire, E. Moeller, S. Schnetzer, G. Shapiro, H. Steiner, and I. Tanihata, Phys. Rev. C24, 971 (1981).

[Na 81a] J.B. Natowitz, M.N. Namboodiri, L. Adler, R.P. Schmitt, R.L. Watson, S. Simon, M. Berlanger, and R. Choudhury, Phys. Rev. Lett. 47, 1114 (1981).

[No 78]   T. Nomura, J. Delaunay, C. Tosello, and N. Bendjaballah, Nucl. Phys. A305, 262 (1978).

P

[Pa 72]   R.K. Pathria, in Statistical Mechanics (Pergamon Press, 1972).

[Pü 77]   F. Pühlhofer, Nucl. Phys. A280, 267 (1977).

R

[Ra 78]   J. Randrup, Phys. Lett. 76B, 547 (1978).

[Re 75]   K.E. Rehm, J.J. Körner, M. Richter, H.P. Rother, J.P. Schiffer, and H. Spieler, Phys. Rev. C12, 1945 (1975).

S

[Sa 80]   A. Sandoval, H.H. Gutbrod, W.G. Meyer, R. Stock, Ch. Lukner, A.M. Poskanzer, J. Gosset, J.-C. Jourdain, C.H. King, G. King, Nguyen Van Sen, G.D. Westfall, and K.L. Wolf, Phys. Rev. C21, 1321 (1980).

[Sa 81]   F. Saint-Laurent, M. Conjeaud, R. Dayras, S. Harar, C. Volant, and H. Oeschler, Proc. of Versailles Conf. (1981).

[Sa 81a]   H. Sato and K. Yazaki, Phys. Lett. 98B, 153 (1981).

[Sc 63]   A. Schwarzschild and Č. Zupančič, Phys. Rev. 129, 854 (1963).

[Sc 65]   H.W. Schmitt, W.E. Kiker, C.W. Williams, Phys. Rev. 137, B837 (1965).

[Sc 77]   W.U. Schröder and J.R. Huizenga, Ann. Rev. Nucl. Sci. 27, 465 (1977).

[Sc 78]   D.K. Scott, Lectures delivered at the NATO/NSF Advanced Studies Institute on Theoretical Methods in Medium-Energy and Heavy-Ion Physics, Madison, Wisconsin, June 12 - 23, 1978.

[Sc 79]   W. Schimmerling, J.W. Kast, D. Ortendahl, R. Madey, R.A. Cecil, B.D. Anderson, and A.R. Baldwin, Phys. Rev. Lett. 43, 1985 (1979).

[Sc 81]   R.P. Schmitt, G.J. Wozniak, G.U. Rattazzi, G.J. Mathews, R. Regimbart, and L.G. Moretto, Phys. Rev. Lett. 46, 522 (1981).

[Sc 81a]   D.K. Scott, Nucl. Phys. A354, 375c (1981).

[Sh 79]   R. Shyam, G. Baur, F. Rösel, and D. Trautmann, Phys. Rev. C19, 1246 (1979).

[Sh 81]   A.C. Shotter, A.N. Bice, J.M. Wouters, W.D. Rae, and J. Cerny, Phys. Rev. Lett. 46, 12 (1981).

[Si 62]   T. Sikkeland, E.L. Haines, and V.E. Viola, Jr., Phys. Rev. 125, 1350 (1962).

[Si 79]   P.J. Siemens and J.I. Kapusta, Phys. Rev. Lett. 43, 1486 (1979).

[Si 79a]   K. Siwek-Wilczyńska, E.H. du Marchie van Voorthuysen, J. van Popta, R.H. Siemssen, and J. Wilczyński, Phys. Rev. Lett. 42, 1599 (1979); Nucl. Phys. A330, 150 (1979).

[Sp 74]   P. Sperr, H. Spieler, M.R. Mair, and D. Evers, Nucl. Instr. and Meth. 116, 55 (1974).

[St 80]   H. Stöcker, Lawrence Berkeley Laboratory Preprint, LBL-12302 (1980).

[Sy 80]   T.J.M. Symons, P. Doll, M. Bini, D.L. Hendrie, J. Mahoney, G. Mantzouranis, D.K. Scott, K. Van Bibber, Y.P. Viyogi, H.H. Wieman, and C.K. Gelbke, Phys. Lett. 94B, 131 (1980).

T

[Ta 79]   B. Tamain, R. Chechik, H. Fuchs, F. Hanappe, M.
           Morjean, C. Ngô, J. Péter, M. Dakowski, B. Lucas,
           C. Mazur, M. Ribrag, and C. Signarbieux, Nucl.
           Phys. A330, 253 (1979).

[Ta 81]   E. Takada, T. Shimoda, N. Takahashi, T. Yamaya,
           K. Nagatani, T. Udagawa, and T. Tamura, Phys.
           Rev. C23, 772 (1981).

[Ts 81]   I. Tserruya, A. Breskin, R. Chechik, Z. Fraenkel,
           S. Wald, N. Zwang, R. Bock, M. Dakowski, A. Gobbi,
           H. Sann, R. Bass, G. Kreyling, R. Renfordt, K.
           Stelzer, and U. Arlt, Phys. Rev. Lett. 47, 16
           (1981).

U

[Ud 79]   T. Udagawa, T. Tamura, T. Shimoda, M. Fröhlich,
           M. Ishihara, and K. Nagatani, Phys. Rev. C20,
           1949 (1979).

[Ut 80]   H. Utsunomiya, T. Nomura, T. Inamura, T. Sugitate,
           and T. Motobayashi, Nucl. Phys. A334, 127 (1980).

V

[Va 73]   R. Vandenbosch and J.R. Huizenga, in Nuclear
           Fission , Academic Press, New York 1973, p. 339.

[Vi 76]   V.E. Viola, Jr., R.G. Clark, W.G. Meyer, A.M.
           Zebelman, and R.G. Sextro, Nucl. Phys. A261, 174
           (1976).

[Vo 78]   V.V. Volkov, Phys. Reports 44, 93 (1978).

W

[Wa 60]   N.S. Wall, p. 31 in Nuclear Spectroscopy, Part A
           (Academic Press, N.Y. and London, 1960).

[We 76]   G.D. Westfall, J. Gosset, P.J. Johansen, A.M.
           Poskanzer, W.G. Meyer, H.H. Gutbrod, A. Sandoval,
           and R. Stock, Phys. Rev. Lett. 37, 1202 (1976).

[We 77]   R. Weiner and M. Weström, Nucl. Phys. A286, 282
           (1977).

[We 78]   L. Westerberg, D.G. Sarantites, D.C. Hensley, R.A. Dayras, M.L. Halbert, and J.H. Barker, Phys. Rev. C18, 796 (1978).

[Wu 78]   J.R. Wu, C.C. Chang, and H.D. Holmgren, Phys. Rev. Lett. 40, 1013 (1978).

[Wu 79]   J.R. Wu, C.C. Chang, and H.D. Holmgren, Phys. Rev. C19, 659 (1979).

Y

[Ya 79]   H. Yamada, D.R. Zolnowski, S.E. Cala, A.C. Kahler, J. Pierce, and T.T. Sugihara, Phys. Rev. Lett. 43, 605 (1979).

[Ya 79a] Y. Yariv and Z. Fraenkel, Phys. Rev. C20, 2227 (1979).

[Ya 81]   Y. Yariv and Z. Fraenkel, Phys. Rev. C24, 488 (1981).

[Yo 80]   G.R. Young, R.L. Ferguson, A. Gavron, D.C. Hensley, Felix E. Obenshain, F. Plasil, A.H. Snell, M.P. Webb, C.F. Maguire, and G.A. Petitt, Phys. Rev. Lett. 45, 1389 (1980).

[Yo 81]   K. Geoffroy Young, D.G. Sarantites, J.R. Beene, M.L. Halbert, D.C. Hensley, R.A. Dayras, and J.H. Barker, Phys. Rev. C23, 2479 (1981).

Z

[Zo 78]   D.R. Zolnowski, H. Yamada, S.E. Cala, A.C. Kahler, and T.T. Sugihara, Phys. Rev. Lett. 41, 92 (1978).